



Université d'Aix–Marseille

École doctorale : ED 251 – Sciences de l'environnement
CEREGE UM34

Thèse présentée pour obtenir le grade universitaire de docteur

Discipline : Géosciences de l'environnement

Dawin H. BADEN

Caractérisation des propriétés élastiques d'un réservoir
carbonaté hétérogène et fracturé

Characterization of elastic properties of a heterogeneous and fractured
carbonate reservoir

Soutenue le 21 Décembre 2017 devant le jury:

Prof. Dr. Yves Guglielmi	Aix–Marseille Université/LBNL (Berkeley)	Directeur
Dr. Pierre Henry	CNRS–CEREGE	Co-directeur
Dr. Ginette Saracco	CNRS–CEREGE	Co-directeur
Prof. Dr. Stéphane Garambois	Université Grenoble Alpes	Rapporteur
Dr. Jérôme Fortin	CNRS–ENS Paris	Rapporteur
Dr. Renaud Toussaint	CNRS–Université de Strasbourg	Examineur
Dr. Gérard Massonnat	Total	Examineur
Dr. Sophie Viseur	Aix–Marseille Université	Invité

Numéro national de thèse/suffixe local : 2017AIXM0581/045ED251

Résumé

Les réservoirs carbonatés contiennent l'essentiel des réserves pétrolières du Moyen-Orient et représentent plus de la moitié des réserves mondiales d'hydrocarbures. Ils sont également intensément exploités pour leur réserve d'eau potable, de ressource géothermique, ou le stockage géologique du dioxyde de carbone. Dans le bassin méditerranéen au climat exceptionnellement sec, ils constituent une ressource vitale en eau souterraine. Ces réservoirs sont difficiles à caractériser à cause de la variabilité des faciès, en raison d'une architecture et d'une histoire diagénétique souvent complexes. Il en résulte en particulier une faible résolution des méthodes de sismique réflexion dans les carbonates.

Depuis les années 2000, les chercheurs d'Aix-Marseille Université conduisent une série de travaux visant à caractériser les propriétés pétrophysiques, mécaniques, et élastiques des calcaires Urgoniens de Provence. Le travail présenté dans cette thèse offre de nouvelles perspectives sur cette thématique. Une approche intégrée est proposée pour caractériser les propriétés pétrophysiques et élastiques des carbonates, de l'échelle centimétrique (plug) à multi-métrique (crosshole). Cette étude s'est effectuée en deux étapes. La première partie de la thèse comprend plusieurs expériences menées en laboratoire, sur des échantillons d'échelles variables mais toujours comparables. Cela inclut des mesures de vitesse d'ondes P et S, ainsi que des mesures d'anisotropie sur plugs ($\varnothing=2.54$ ou 3.81 cm) et sur carottes ($\varnothing=12.5$ cm), en utilisant différentes fréquences centrales ultrasonores de 500 ou 1000 kHz (plugs) à ~ 250 kHz (carottes). Les mesures acoustiques ont été menées conjointement avec une caractérisation détaillée de la roche à des échelles comparables aux longueurs d'onde utilisées (c'est-à-dire 4–26 mm). Les mesures sur plugs ont été interprétées en fonction des caractéristiques géologiques observées sur lames-minces et des images issues de Microscopie Électronique à Balayage. Les mesures effectuées sur les carottes ont été comparées aux données de tomodynamométrie qui permettent d'imager des réseaux de fractures complexes et la géométrie des hétérogénéités (fossiles). Le second volet de l'approche a été conduit à l'échelle du terrain en développant une méthode d'acquisition acoustique inter-puits au sein du Laboratoire Souterrain à Bas Bruit de Rustrel (LSBB). Deux sondes ont été construites afin de conduire des mesures acoustiques aux fréquences ultrasonores (~ 50 kHz) entre deux puits verticaux et distants de 2 m, sur une profondeur d'environ 14.5 m, et avec une résolution de 10 cm.

Les principaux résultats de cette approche montrent que les vitesses moyennes d'ondes P et S sont similaires indépendamment de l'échelle de mesure, car elles sont dictées par la porosité. Cependant, des variations significatives sont observées autour des vitesses moyennes, avec des significations différentes selon l'échelle de mesure. L'échelle du plug (centimétrique) est pertinente pour estimer les propriétés élastiques de la matrice intacte. Ainsi, les variations de vitesse obtenues pour un faciès dépendent de l'hétérogénéité plus que de l'anisotropie, surtout pour les carbonates hétérogènes. À l'échelle des carottes (décimétrique), une anisotropie (apparente) peut être mesurée. Cette anisotropie peut être liée à une distribution inégale de certaines propriétés pétrophysiques, ou aux micro-fractures, ou aux fractures ouvertes. Ces travaux de thèse montrent que l'anisotropie azimutale causée par des fossiles (>5 cm) non-poreux et empaquetés dans une matrice poreuse peut atteindre jusqu'à 5%. L'anisotropie causée par des familles de fractures non-uniformes peut atteindre 10–15%. Les hétérogénéités observées sur les carottes sont de taille supérieure aux plugs conventionnels. Par conséquent, l'échelle du plug n'est pas pertinente pour déterminer si ces carbonates sont anisotropes ou non. L'échelle des carottes discutée dans cette étude semble plus appropriée, mais d'autres cas d'étude seront nécessaires pour le confirmer. À l'échelle du terrain (multi-métrique) une faible anisotropie est détectée, variant de +10% (axe lent perpendiculaire aux strates) et -2% (axe lent parallèle aux strates). Cette anisotropie résulte de la combinaison des effets des hétérogénéités et des fractures. Enfin, ces travaux ont mis en exergue la dépendance entre la localisation de la source, les vitesses d'ondes P et l'anisotropie dans un réservoir carbonaté stratifié et hétérogène. Cela pourrait expliquer la différence entre les valeurs d'anisotropie de cette étude et celles obtenues sur le même site mais à une autre échelle (hectométrique) et avec une distribution des sources sismiques différente.

En conclusion, l'approche adoptée durant ces travaux de thèse a permis de définir les interactions entre les propriétés de la matrice, les hétérogénéités, les fractures, et les propriétés élastiques des roches carbonatées. Elle a montré que les propriétés élastiques tout comme les structures géologiques varient en fonction de l'échelle. Plus précisément l'anisotropie dans les carbonates hétérogènes semble difficile à caractériser à partir de mesures à des échelles inférieures au décimètre.

Mots clés : Réservoirs carbonatés, hétérogénéité, fractures, vitesses d'ondes P et S, anisotropie

Abstract

Carbonate reservoirs contain most of the Middle-East oil and gas reserves which count for more than one half of the world's hydrocarbon reserves. They are also exploited for water production, geothermal energy, and carbon geological storage. In the Mediterranean basin where the climate is particularly dry, carbonate reservoirs are the main groundwater reserves. Geophysical characterization of carbonate formations remains challenging because they have complex facies distribution, related to both their deposit environment and their diagenetic history. It results in a relatively poor resolution of seismic reflection data.

Since the early 2000s researchers from Aix-Marseille University have carried out studies of the petrophysical, mechanical, and elastic properties of the Urganian limestones in the Provence region. The work presented in this thesis offers new insights into this topic. An integrated multi-scale approach is proposed to characterize carbonate rocks petrophysical and elastic properties at different scales ranging from the centimeter-sized sample (plug) to multi-meter scale (crosshole). The study is divided in two main parts. The first part of the work consisted in several experiments carried out on samples with different, but still comparable, sizes in the laboratory. It included P- and S-wave velocity and anisotropy measurements on plugs ($\varnothing=2.54, 3.81$ cm), and on cores ($\varnothing=12.5$ cm), using different ultrasonic frequencies of 500–1000 kHz for plugs, and ~ 250 kHz for cores. The acoustic measurements were coupled to a detailed characterization of the rock at a scale comparable to the wavelength (i.e., 4–26 mm). The plug scale measurements were compared to geological features observed on thin-sections and on Scanning Electron Micrograph images, whereas the core scale measurements were compared to Computed Tomography data, which enabled imaging complex fractures network and the geometry of heterogeneities (e.g. fossils). The second part of the work has been carried out at the field scale using acoustic crosshole logging. Two probes have been developed to carry out acoustic measurements at ultrasonic frequencies (~ 50 kHz) between two vertical boreholes located 2 m apart and over 14.5 m depth, with a 10 cm resolution. The study took place in the Low Noise Underground Laboratory of Rustrel (LSBB, France).

The main results of this approach show that the ranges of P- and S-wave velocity are in average the same regardless to the scale, but significant fluctuations around the average values are observed. Depending on the measurement, these fluctuations appear to have different meanings. Plug (centimeter) scale is generally relevant to estimate the elastic properties of the intact-matrix. The velocity variations for a given facies are related to its heterogeneity rather than to its anisotropy especially in platform-type carbonates. At the core (decimeter) scale, anisotropy (at least apparent) can be measured in carbonates. This anisotropy can be related to a patchy distribution of some petrophysical properties, local cracks distribution, and “thick” single fractures. It is shown that azimuthal-anisotropy caused by inclusion of large and non-porous fossils (>5 cm) embedded in a porous matrix can reach up to 5%, while azimuthal-anisotropy caused by non-uniform fracture-sets reaches up to 10–15%. Since the heterogeneities observed at the core scale were larger than laboratory-sized samples, the plug scale is not suitable to characterize if whether or not platform-carbonates are seismically anisotropic. However, the core scale discussed in this thesis seems to be more relevant, but further case studies will be needed to generalize our conclusion. At the field (multi-meter) scale, a weak anisotropy is detected in our experiments, varying between +10% (slow axis perpendicular to strata) and -2% (slow axis parallel to strata). This anisotropy likely results from combination of centimeter-to-decimeter heterogeneities and of fractures effects. We noticed that our measurements may be impacted by source location. Through comparison with larger scale seismic anisotropy characterizations conducted on the same site by other research groups, we discuss this as a potential bias in interpreting crosshole surveys with sparse data, especially in carbonate formations.

In conclusion, the approach adopted during this PhD work has enabled to scope out the interplay between matrix properties, heterogeneity, fracturing, and elastic properties in carbonate rocks. The scale plays a major role on the significance of the apparent anisotropy. Similar anisotropy strengths are found to be related either to heterogeneity or fracturing, despite the signal is dominated by the latter at larger scale. Anisotropy is hard to detect from plug to decimeter scales where heterogeneity dominates.

Keywords: Carbonate reservoirs, heterogeneity, fractures, P- and S-wave velocity, anisotropy

Remerciements

Avant de rentrer dans les détails des remerciements, et au cas où vous ne voudriez pas lire cette page jusqu'à la fin, je tiens à remercier grandement toutes les personnes qui m'ont soutenu durant ces quatre années et qui ont participé directement et indirectement à l'achèvement de cette thèse.

Mes premiers remerciements vont à ma famille, sur qui j'ai toujours pu compter : ma mère, mes frères, mon père ainsi que Marika. Je vous remercie pour votre soutien indéfectible.

Je remercie aussi sincèrement mes directeurs de thèse : Yves, Pierre, Ginette, Lionel, Sophie. Ils m'ont fait confiance dès le début. Leurs précieux conseils ainsi que leur disponibilité m'ont accompagné tout au long de ces quatre années.

Je tiens aussi à exprimer ma reconnaissance à tous ceux qui ont rendu mon intégration à l'Université d'Aix Marseille beaucoup plus facile : Gilles, Jocelyne, Alain, Didier et Thierry.

Je remercie aussi TOTAL pour le support dans le développement de la sonde et le LSBB de nous avoir ouvert leurs portes pour mener cette étude. Merci aussi au consortium autour du projet H Cube tout d'abord de m'avoir donné l'opportunité de faire cette thèse, mais aussi pour tous les échanges enrichissants autour de la modélisation du stockage du CO₂.

Je remercie enfin particulièrement tous mes collègues doctorants pour leur bonne humeur. J'ai été très content de travailler avec vous tous, et vous souhaite le meilleur pour la suite. Les remerciements au cas par cas viendront dans la version finale.

Table of content

Résumé	3
Abstract	4
Remerciements	5
Table of content	7
Table of figures	11
Section 1: Introduction générale –FRENCH–	13
1.1 Avant-propos	13
1.2 Contexte scientifique	14
1.2.1 Projet H-CUBE	14
1.2.2 Projet ALBION-HPMSCa	15
1.2.3 Partenaires	17
1.3 Objectifs de la thèse	20
1.4 Organisation du Manuscrit	20
Section 2: Synthèse des travaux –FRENCH–	23
2.1 Enjeux scientifiques	23
2.1.1 Généralités sur les propriétés des carbonates	24
2.1.2 Propagation des ondes dans les carbonates	26
2.2 Objectifs et problématiques	28
2.3 Méthodes employées	31
2.3.1 Philosophie de l’approche	31
2.3.2 Investigation multi-échelle en laboratoire	32
2.3.3 Investigation multi-échelle sur le terrain	35
2.4 Principaux résultats	37
2.5 Conclusion et perspectives	43
Section 3: Experimental settings	45
3.1 Abstract	45
3.2 A new crosshole acoustic survey to explore carbonates at the multi-meter scale	45
3.2.1 Introduction	45
3.2.2 Guidelines and specifications	46
3.2.3 Acquisition workflow	51
3.2.4 Calibration	54
3.3 Acoustic characterization of 5” diameter water-saturated cores	59
3.3.1 Overview of the semi-automatized acquisition system	59

3.3.2	Acquisition workflow	61
3.3.3	Calibration	62
3.4	Other methods used in this work	65
Section 4: Field scale investigation of a carbonate series assuming seismic isotropy		67
4.1	Abstract	67
4.2	Introduction	68
4.3	Geological context	70
4.3.1	The Urganian platform in Rustrel area	70
4.3.2	Geology of the study site	72
4.4	Material and method	77
4.4.1	Plug-scale velocity measurements	77
4.4.2	Field-scale velocity measurements	78
4.4.3	Tomographic reconstruction using SIPPI	80
4.5	Results	82
4.5.1	Porosity-Velocity relationship at the plugs scale	82
4.5.2	Crosshole velocity logging	86
4.5.3	Tomography	88
4.5.4	Fractures set vs. crosshole velocities	90
4.6	Discussion	93
4.6.1	Crosshole acoustics vs. existing methods	93
4.6.2	Impact of diagenesis and pores geometry	94
4.6.3	Effects of fractures on the P-wave velocity	96
4.7	Conclusion	97
Section 5: Scale dependency of velocity anisotropy in heterogeneous carbonates		99
5.1	Abstract	99
5.2	Introduction	99
5.3	Material and methods	100
5.3.1	Rock material	100
5.3.2	Experimental settings	101
5.3.3	Processing the cores data	106
5.4	Results and discussion	109
5.4.1	General properties of the matrix	109
5.4.2	Comparison of the elastic properties at two scales	114
5.4.3	Lessons from this two-scale approach	120
5.5	Conclusion	122
Section 6: Anisotropy in porous and fractured carbonates at field-scale		124
6.1	Abstract	124
6.2	Introduction	124
6.3	Geological setting	127
6.4	Material and methods	130

6.4.1	Probes characteristics	130
6.4.2	Acoustic logging and data acquisition	133
6.4.3	Data processing	135
6.5	Results	137
6.5.1	P-wave travel-times	137
6.5.2	P- and S-waves velocity	138
6.5.3	Characterization of the apparent-anisotropy	141
6.5.4	Stiffness tensor assuming TI symmetry	143
6.5.5	Forward modelling	148
6.6	Discussion	152
6.7	Conclusion	155
	Conclusions and perspectives	157
	References	163
	Appendix	173
Articles		173
	Dawin Baden, Yves Guglielmi, Pierre Henry, Ginette Saracco, Lionel Marié, and Seiji Nakagawa (2017- <i>under 2nd round of review</i>), Scale dependency of velocity anisotropy in heterogeneous carbonates , <i>submitted in Geophysics</i> . [cf. Chapter 4]	173
	Dawin Baden, Yves Guglielmi, Pierre Henry, Ginette Saracco, and Lionel Marié (2017- <i>under revision after a 1st round of review</i>), Field characterization of a fractured-carbonate formation using crosshole acoustic waves anisotropy , <i>submitted in Journal of Geophysical Research Solid Earth</i> . [cf. Chapter 5]	173
	Dawin Baden, Yves Guglielmi, Pierre Henry, Ginette Saracco, Lionel Marié, (<i>in preparation</i>), Anisotropy and effects of heterogeneities in fractured carbonate reservoirs , <i>Targeted journal: Geophysical Research Letters</i>	173
Proceedings		175
	Dawin Baden, Pierre Henry, Ginette Saracco, Lionel Marié, Alain Tonetto, Yves Guglielmi, Seiji Nakagawa, Gérard Massonnat, and Jean-Paul Rolando (2017) How seismic anisotropy changes with scale . SEG Technical Program Expanded Abstracts 2017: pp. 305-309. https://doi.org/10.1190/segam2017-17587710.1	175
	Dawin Baden, Pierre Henry, Ginette Saracco, Lionel Marié, and Yves Guglielmi (2017), Investigation of anisotropy in non-saturated and heterogeneous carbonate series using crosshole acoustic techniques . SEG Technical Program Expanded Abstracts 2017: pp. 310-315. https://doi.org/10.1190/segam2017-17587284.1	181
Abstracts		189
	Dawin Baden, Yves Guglielmi, Ginette Saracco, Sophie Viseur, and Lionel Marié (2014), High density ultrasonic characterization of carbonates heterogeneities , in <i>Résumés de la 24e Réunion des Sciences de la Terre</i> , p. 309.	189
	Dawin Baden, Yves Guglielmi, Ginette Saracco, Lionel Marié, and Sophie Viseur (2015). 3D modeling of carbonates petro-acoustic heterogeneities . Geophysical Research Abstracts, Vol 17, EGU2015-9838. EGU General Assembly 2015.	191

Dawin Baden, Yves Guglielmi, Lionel Marié (2016), **Acoustic Characterization of Sub-Seismic Scaled Heterogeneities in Carbonate Reservoirs: Example of Barremian Microporous Limestone from SE France, an Analog of Middle East Hydrocarbon Reservoirs.** in *AAPG Annual Convention & Exhibition 2016, Calgary, Alberta, Canada.*

193

Table of figures

Figure 2.1. Analyse multi-échelle des propriétés pétrophysiques et élastiques en laboratoire....	34
Figure 2.2. Acquisition des données acoustiques sur le terrain.	36
Figure 2.3. Propriétés élastiques et pétrophysiques à l'échelle de la matrice.	38
Figure 2.4. Exemples d'hétérogénéités et leurs conséquences sur le signal acoustique.	40
Figure 2.5. Considération des hypothèses d'isotropie et d'anisotropie.	42
Figure 3.1. Photographs, and schematic overview of the experimental set up.	48
Figure 3.2. Photographs and schematic view of the reception-probe.	50
Figure 3.3. Simplified flow chart of the acoustic logging.	52
Figure 3.4. Extract of the probes orientation logs.	53
Figure 3.5. The output signal through air at 20°C.	55
Figure 3.6. Results of a wavelet transform onto the source signal.	56
Figure 3.7. Radiation pattern of the couple emitter-receiver through air at 20°C.	57
Figure 3.8. Time delay introduced by the probes design.	58
Figure 3.9. Photographs and schematic view of the laboratory experimental set. [Core-scale]..	60
Figure 3.10. Simplified flow chart and schematic view of the acquisition in the acoustic tank..	62
Figure 3.11. Results of a wavelet transform onto a recorded signal.	63
Figure 3.12. Source signal compared to the recorded signal in water at 20°C.	64
Figure 4.1. Localization GAS-gallery in the LSBB, and disposition of the boreholes.	71
Figure 4.2. Synthetic lithology and porosity logs of studied formations.	74
Figure 4.3. Microscopic images of studied facies.	76
Figure 4.4. Schematic view of the experimental set-up. [Plug-scale measurements].....	78
Figure 4.5. Schematic view of one section logging. [Field-scale measurements]	79
Figure 4.6. Poroelastic data measured on plugs.	84
Figure 4.7. Log and histogram of the crosshole P-wave velocities.	87
Figure 4.8. Tomography of inter-borehole space.	89
Figure 4.9. Modeling the P-wave travel times using SIPPI.	90
Figure 4.10. Summary of the structural analysis based on the borehole imagery (OPTV).	92
Figure 5.1. Experimental set-up used for the cores characterization.	104

Figure 5.2. Stained thin-sections and SEM-images of cores.	111
Figure 5.3. A selection of slices from the cores CT-scan.	112
Figure 5.4. Cross-plot of the P and S-wave velocity against porosity at plug scale.	113
Figure 5.5. Maps of modeled P-wave velocity.	116
Figure 5.6. Comparison between waveforms and CT-images.	118
Figure 5.7. P-wave anisotropy (ϵ') at the cores scale.	119
Figure 6.1. Overview of the geological setting.	129
Figure 6.2. Design of the acoustic-probes, and experimental setup during acoustic logging.	134
Figure 6.3. Rays' coverage, assuming straight-rays' geometry.	135
Figure 6.4. Examples of waveforms recorded for one shot.	136
Figure 6.5. P-wave travel-times versus raypath angle.	138
Figure 6.6. P- and S-wave velocity as a function of raypath angle.	139
Figure 6.7. Velocity models computed using the stiffness coefficients.	147
Figure 6.8. Synthetic examples of apparent-anisotropy caused by heterogeneities.	151

Section 1: Introduction générale

1.1 Avant-propos

L'ensemble de ces travaux de thèse ont été réalisés au sein du Centre de Recherche et d'Enseignement de Géosciences de l'Environnement (CEREGE UM34), principalement dans les locaux du site de la Faculté des Sciences de Saint-Charles à Marseille, mais aussi dans ceux du site de l'Arbois à Aix-en-Provence, notamment dans le laboratoire d'acoustique. Les mesures de terrain ont été réalisées entre Mars et Avril 2015 dans les locaux du Laboratoire Sous-terrain à Bas Bruit (LSBB) de Rustrel.

Ces travaux ont été menés dans le cadre d'un projet de Recherche intitulé **H-CUBE** « *Hydrodynamique, Hétérogénéité et Homogénéisation dans la modélisation du stockage géologique du dioxyde de carbone dans les aquifères salins* », financé par l'Agence Nationale de la Recherche ([Projet-ANR-12-SEED-0006](#)). Ce projet qui a débuté en Janvier 2013 pour s'achever en Janvier 2017 a entre autres, permis de financer ma bourse doctorale à partir d'Octobre 2013.

La partie expérimentale de ces travaux de thèse a également bénéficié de la contribution d'un partenaire industriel, à savoir Total E&P France, dans le cadre d'un vaste programme de Recherche intitulé « *Analogue Laboratory to Build Images of Onsite Networks* » (ALBION), et plus précisément du projet intitulé « *Predicting Hydraulic, Petrophysical, Mechanical and Seismic Properties of Carbonates* » (HPMSCa). Le projet ALBION-HPMSCa a débuté en Septembre 2014.

1.2 Contexte scientifique

1.2.1 Projet H-CUBE

En 2009 une directive de la Commission Européenne sur le stockage géologique du carbone a mis en exergue l'importance de l'usage de la modélisation hydrodynamique en amont et pendant l'exploitation des sites destinés au stockage du dioxyde de carbone (CO₂) à une échelle commerciale. La modélisation doit permettre d'une part de prédire le déplacement du panache de CO₂ injecté, une meilleure interprétation des données issues du monitoring et d'autre part fournir des informations générales sur l'hydrodynamisme au sein de l'aquifère.

La problématique de l'intégration de l'hétérogénéité dans l'évaluation des écoulements multiphasiques dans les milieux poreux est connue depuis de nombreuses années. Durant les dernières décennies, les effets du réchauffement climatique se sont accentués et la réduction des émissions de gaz à effet de serre est devenue une priorité. Plusieurs solutions sont évoquées, offrant un nouveau contexte propice à la recherche sur les écoulements multiphasiques en milieu poreux. En effet, après injection du CO₂ sous forme de fluide supercritique dans un réservoir géologique en sub-surface tel qu'un aquifère salin ou un réservoir d'hydrocarbures en déclin, le CO₂ s'écoule et se mélange à la saumure présente dans le réservoir. Étant donné que l'injection de CO₂ à l'échelle industrielle doit durer plusieurs décennies sur un même site pour être économiquement viable, cela peut modifier ou interférer durablement sur l'hydrodynamisme au sein du réservoir. Dans ce contexte, l'impact des hétérogénéités sédimentaires est prépondérant et peut avoir une incidence critique sur l'évolution du panache de CO₂, à savoir sur la migration et la répartition du champ de pression dans le réservoir.

Le projet H-CUBE visait à caractériser l'impact des hétérogénéités sédimentaires sur les prévisions des modèles, en particulier le comportement hydrodynamique du panache de CO₂ sur

les sites de stockage, les augmentations de pression et le déplacement de la saumure. Le projet proposait de nouvelles méthodes pour évaluer l'hydrodynamisme des réservoirs hétérogènes. Les échelles considérées varient du décimètre au kilomètre, et des modèles d'écoulements multiphasiques ont été testés sur des réservoirs aussi bien terrigènes que carbonatés. Des outils géophysiques et de nouveaux protocoles expérimentaux ont été développés, principalement dans le cadre de ces travaux de thèse, pour affiner la caractérisation des réservoirs carbonatés.

Parmi les contributions majeures du projet H-CUBE, on peut citer la réalisation de modèles théoriques et numériques pour l'évaluation du comportement hydrodynamique du CO₂ sur les sites de stockage. L'accent a été mis sur l'écoulement du mélange CO₂–saumure sous les effets de la gravité et de la dissolution. La méthodologie d'évaluation de l'hétérogénéité des formations géologiques à différentes échelles a permis de caractériser l'impact des hétérogénéités sur l'écoulement du CO₂ à proximité immédiate du puits d'injection (~2m) et à l'échelle du bassin (~100 km). Parmi les principaux résultats, on peut citer : (1) l'optimisation de la simulation des écoulements (« upscaling », et techniques d'homogénéisation) ; (2) de nouvelles routines de travail (routines de modélisation et de traitements statistiques des incertitudes liées aux contextes géologiques) ; (3) un cadre complet allant de l'observation de la géologie sur le terrain aux modèles statiques géologiques.

1.2.2 Projet ALBION-HPMSCa

Le projet ALBION-HPMSCa vise à fournir une caractérisation « exhaustive » d'une série carbonatée fracturée en se basant sur l'étude des processus géologiques, des propriétés hydrauliques et mécaniques de la formation, et d'observations « hydro-géophysiques ». Le projet repose principalement sur deux approches, la première est essentiellement géologique et vise à caractériser la séquence diagénétique en tenant compte des paramètres environnementaux, du type

de roche réservoirs, et de la fracturation. Cette approche est en cours de mise en œuvre dans le cadre de la thèse de Jean Cochard. Elle se focalise plus particulièrement sur la caractérisation des ciments calcaïques au sein de la matrice et des fractures et sur leur impact sur la porosité et la perméabilité des carbonates. La seconde approche concerne la quantification de l'impact de la porosité à plusieurs échelles allant de quelques microns (porosité matricielle) à plusieurs centimètres (karst, fractures), sur les propriétés mécaniques et hydrauliques des carbonates. Cette approche est menée par des mesures couplées hydromécaniques (travaux de thèse de Simon Seguy) et géophysiques en laboratoire et in situ dans les forages recoupant des calcaires fracturés et stratifiés de faciès Urgoniens. La partie « mesures géophysiques » fait l'objet de cette thèse.

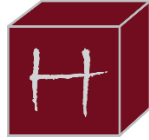
Les objectifs du projet ALBION-HPMSCa concernent d'une part certains aspects fondamentaux, par exemple en s'interrogeant sur les méthodes d'identification des relations entre la diagénèse des carbonates et la fracturation ; d'autre part des aspects pratiques, en proposant des solutions intégrées en vue de la modélisation de la « Physique » des roches carbonatées. L'un des problèmes clés auquel ce projet tente d'apporter une réponse concerne la relation existante entre les descriptions pétrophysiques à l'échelle du micromètre et les propriétés statiques et hydrauliques à l'échelle macroscopique. La réponse à cette question est essentielle pour améliorer la simulation des ondes sismiques dans des réservoirs carbonatés complexes et fracturés. Les enjeux sont une meilleure imagerie de la porosité et perméabilité des carbonates poreux fracturés. Une autre problématique à laquelle s'adresse le projet concerne l'inférence de paramètres pétrophysiques à l'échelle micrométrique à partir d'observations à plus grande échelle (vitesses sismiques, atténuation et paramètres anisotropes). Cette approche de réduction d'échelle nécessite une description théorique des milieux multiphasiques ou des descriptions calibrées extraites d'expériences en laboratoire et in situ.

1.2.3 Partenaires

Je remercie l'ensemble des partenaires institutionnels et privés pour leurs contributions à mes travaux de thèse, que ce soit de façon matérielle par le biais de financements ou de mise à disposition de ressources technologiques et/ou d'infrastructures ; ou de façon immatérielle par le biais des échanges scientifiques que j'ai pu avoir avec leurs représentants respectifs à l'occasion de nos nombreuses réunions.

Projet H-CUBE

Logo officiel du projet H-CUBE



Hydrodynamics
Heterogeneity
Homogenization

Financier



Leader du projet



Géosciences pour une Terre durable

brgm

Université et laboratoire hôtes de la thèse



Autres Partenaires



LSCE

LABORATOIRE DES SCIENCES DU CLIMAT
& DE L'ENVIRONNEMENT



Terra3E

Energy Environment Expertise

Projet ALBION-HPMSCa

Financier et leader du projet



Leader du sous-projet HPMSCa



Laboratoire d'accueil des expériences in situ



Autres Partenaires



1.3 Objectifs de la thèse

L'objectif de cette thèse est de caractériser un réservoir carbonaté microporeux et fracturé par l'estimation des propriétés pétrophysiques et élastiques à partir de mesures des variations de vitesses d'ondes sismiques à différentes fréquences. Cette finalité requiert plusieurs étapes intermédiaires comme : (1) la caractérisation géologique de la formation ; (2) la détermination des facteurs influençant les propriétés élastiques depuis l'échelle des mesures (laboratoire) jusqu'à l'échelle d'intérêt (réservoir) ; (3) la caractérisation des effets d'échelle sur les propriétés physiques ou géologiques mesurées ; (4) l'établissement de liens entre les propriétés pétrophysiques et élastiques avec les caractéristiques géologiques.

1.4 Organisation du Manuscrit

Ce mémoire s'articule autour de six grandes sections. La première section introduit et replace cette thèse dans le cadre des deux programmes de recherche (H-CUBE et ALBION-HPMSCa) qui ont motivé l'étude. Après une brève synthèse des problématiques liées aux propriétés élastiques des formations carbonatées, la seconde section résume en français l'ensemble du travail réalisé durant la thèse. Les travaux y sont décrits de façon générale, commentés et replacés dans le contexte global de l'étude. La troisième section est essentiellement méthodologique et revient en détail sur la conception et la mise en œuvre des dispositifs expérimentaux développés (sondes acoustiques) ou améliorés (cuve acoustique) durant la thèse. Les sections 4, 5 et 6, détaillent et discutent les résultats issus des différentes approches choisies pour aborder l'étude des propriétés élastiques du même réservoir carbonaté, à savoir : (1) une approche « conventionnelle » basée sur un traitement simple des données (à l'échelle du plug et du terrain), c'est-à-dire en ignorant les effets d'échelle et l'impact de l'anisotropie ; (2) une approche multi-échelle en laboratoire où l'anisotropie et les effets d'échelle sont pris en compte ; enfin (3) une approche à l'échelle du

terrain qui tient compte de l'anisotropie, des effets d'échelle (dans l'interprétation) et de l'hétérogénéité du réservoir.

La section 4 présente et discute les variations des vitesses d'ondes P et S observées en laboratoire sur des plugs de 3.81 cm et sur le terrain à l'échelle inter-puits. Le choix fait dans cette section est d'analyser les vitesses en fonction de la géologie de la formation étudiée et en ignorant une quelconque influence de l'anisotropie. Ce choix arbitraire est souvent celui fait par défaut dans des études de laboratoire basées uniquement sur de « petits » échantillons. Cette approche montre son efficacité dans l'établissement de relations entre les vitesses moyennes d'onde P ou S avec la porosité. Dans le cadre des faciès étudiés, la relative monotonie des types poreux se traduit par des relations quasi-linéaires qui peuvent facilement être modélisées par des polynômes du second degré. En revanche, cette approche montre ses limites quand il s'agit d'expliquer les variations de 10–20% autour de la vitesse moyenne en se basant sur des arguments géologiques.

La section 5 traite de la problématique de la variation des propriétés élastiques en fonction de l'échelle. Pour ce faire, des échantillons de tailles différentes mais comparables sont caractérisés à l'aide d'ondes P et S. Contrairement à la section précédente, l'éventualité de l'anisotropie est considérée. Les vitesses sont ensuite comparées aux données géologiques observées à des échelles comparables aux longueurs d'ondes utilisées pour la caractérisation. Cette section démontre la nécessité d'employer des échantillons aux dimensions supérieures aux standards actuels pour pouvoir être en mesure de caractériser des faciès poreux de plateforme carbonatée, car ces derniers présentent des tailles d'hétérogénéités (macro-fossiles, horizons diagénétiques) susceptibles d'affecter la propagation des ondes sismiques, soit en modifiant les vitesses moyennes soit en générant de l'anisotropie qui peut atteindre le même niveau que celle causée par une fracturation diffuse (cracks). Cette section pointe également certaines limites concernant « l'upscaling » des

vitesses mesurées sur plugs. L'hétérogénéité des faciès poreux se traduit par des variations significatives des données pétrophysiques (porosité) pour deux échantillons issus du même faciès, ce qui implique que l'up-scaling de ces propriétés dépend fortement de la lecture que fait l'interpréteur.

La section 6 traite de l'impact de la distribution irrégulière des fractures et de la stratification (de la porosité) sur l'anisotropie observée à l'échelle du terrain. Une double approche de la modélisation est proposée pour estimer les modules d'élasticité, et déterminer l'origine de cette anisotropie. Dans un premier temps, les vitesses d'ondes P et S sont « modélisées » à l'aide de fonctions périodiques (cosinus) afin de simuler les données manquantes à cause de la faible couverture angulaire de notre dispositif. Les modules d'élasticité sont estimés à l'aide des équations exactes de la propagation des ondes P et S dans un milieu transverse isotrope. Dans un second temps des modèles synthétiques simples (cf. « forward modeling ») et d'une échelle comparable à celle de nos conditions expérimentales, sont utilisés pour comparer l'impact de la stratification à celui de la distribution non-homogène des fractures sur les vitesses. Enfin l'ensemble de ces résultats est comparé aux données publiées dans la littérature à l'échelle du plug et de la sismique.

Section 2: Synthèse des travaux

2.1 Enjeux scientifiques

Les réservoirs géologiques contiennent non seulement l'ensemble des réserves énergétiques fossiles telles que le pétrole et le gaz naturel mais également une grande partie des réserves d'eau potable. Même dans le cas des aquifères salins, dont l'eau est impropre à la consommation, on trouve un intérêt économique et/ou sociétal dans le cadre de l'utilisation de l'énergie géothermique et le stockage du dioxyde de carbone (CO₂). En effet, les réservoirs géologiques sont la cible désignée pour permettre, dès aujourd'hui et d'avantage dans le futur, le stockage durable de la production excédentaire de gaz à effet de serre liée à l'activité anthropique. Ces réservoirs sont donc un enjeu majeur qu'il convient de caractériser et de monitorer au mieux pour en permettre une gestion durable. Pour ce faire, une bonne caractérisation, en amont, des propriétés pétrophysiques telles que la porosité et la perméabilité est essentielle. Dans le cas de la porosité, il en va de la justesse de l'estimation de la capacité de stockage du réservoir. La perméabilité détermine le taux auquel un fluide pourra être extrait ou injecté dans le réservoir. Ces deux paramètres sont primordiaux, *a priori* simples à comprendre et à évaluer. Cependant, ces données sont difficilement accessibles car le plus souvent les réservoirs géologiques se trouvent en profondeur. Les données disponibles sont toujours discutables, soit parce qu'elles sont locales comme les données de puits (données en 1D ou de 1.5D), soit parce qu'elles ne sont pas représentatives des conditions en profondeur, comme dans le cas d'études d'affleurements rocheux analogues (données en 2D ou 3D). L'étude d'affleurement par des méthodes géophysiques peut

partiellement résoudre ce problème, en offrant l'accès à des objets géologiques peu profonds (*shallow subsurface*) et exposés quelques mètres plus loin.

Les formations carbonatées de Provence sont de bons analogues des réservoirs producteurs d'hydrocarbures du Moyen-Orient car elles présentent des similitudes en termes d'âge, de paléo-environnement et de faciès (Borgomano et al. 2013). De plus les calcaires Urgoniens de Provence présentent des propriétés réservoirs en tous points similaires à ces derniers, à l'exception du fait que les hydrocarbures n'ont pu être stockés en raison d'une histoire diagénétique et d'un contexte tectonique régional différent.

2.1.1 Généralités sur les propriétés des carbonates

Les roches sédimentaires sont des matériaux composites qui résultent de la consolidation de sédiments carbonatés, terrigènes ou un mélange de ces derniers. Les propriétés élastiques des roches sédimentaires dépendent de leurs constituants (grains, pores). Dans les grès, la minéralogie des grains, leur organisation spatiale et la porosité contrôlent la vitesse de propagation des ondes élastiques. Dans les carbonates, il faut ajouter aux facteurs précédents : le type et la forme des pores, et la diagénèse qui vient complexifier la relation entre les vitesses et les propriétés élastiques des constituants (pris individuellement). En effet, tandis que la porosité est restreinte à l'espace inter-granulaire dans les grès, elle peut se retrouver presque partout dans les carbonates (espace inter- ou intra-granulaire, structure minérale d'un test d'organisme). Dans les grès, la dimension des pores est dictée par la granulométrie, le tri des grains et parfois la profondeur (souvent corrélée au degré de cimentation). En revanche, ce type de relation est moins évident dans les carbonates, compte tenu de la nature biogénétique des constituants et de la diagénèse plus complexe. Par exemple, des pores macroscopiques peuvent coexister avec des pores inter-cristallins microscopiques au sein du même faciès. La nature métastable des minéraux carbonatés tels que

l'aragonite et la calcite magnésienne ou encore la précipitation de ciments liés à l'activité biologique font que la diagenèse peut débuter très précocement dans les carbonates (Tucker and Wright 1990). Ainsi on peut retrouver des couches de sédiments carbonatés complètement lithifiées à même le plancher marin (profondeur nulle). De plus, la diagenèse des carbonates se poursuit durant toutes les phases de l'enfouissement (~cimentation), mais aussi lors de l'exhumation où l'exposition aux fluides météoriques peut recréer ou augmenter la porosité.

La relative simplicité des grès par rapport aux carbonates leur a souvent valu la préférence des auteurs quand il était question de caractériser le phénomène de propagation d'ondes en milieu poreux. En effet, du point de vue de la Physique un grès peut être modélisé par un volume contenant des billes de verre. Alors, les propriétés élastiques ne dépendent que de celles des billes et des propriétés des contacts bille-bille, par exemple une réduction de porosité se traduira simplement par une augmentation de la surface de contact entre les grains (Kuster and Toksoz 1974; Winkler 1983; Yin et al. 1995; Tutuncu et al. 1997; Manificat and Guéguen 1998; Zimmer et al. 2007a, 2007b). Aucune analogie de ce type n'est possible dans les carbonates. Tandis que des avancées majeures sur la propagation des ondes dans les grès sont publiées depuis les années 50 (Wyllie et al. 1956), peu d'auteurs se sont intéressés aux carbonates avant les années 90. On peut citer les travaux pionniers de *Kisslinger*, (1950, 1953), *Gardner et al.*, (1974), *Rafavich et al.*, (1984) qui ont permis d'établir que, contrairement aux grès, les propriétés élastiques des carbonates dépendaient moins de la minéralogie (hors dolomie) que de la porosité. En effet, les minéraux carbonatés présentent peu de variabilité de densité, notamment parce qu'ils ont la même composition atomique et que seuls leurs réseaux cristallins diffèrent. Depuis les années 90, de nombreux travaux ont contribué à affiner la connaissance des propriétés des carbonates. Ces travaux ont montré le rôle prépondérant des caractéristiques du réseau poreux qui dépend

directement de la diagénèse (cimentation, dissolution), au détriment d'autres caractéristiques pétrographiques tels que le faciès, le type de grains, etc. (Anselmetti and Eberli 1993, 2001; Kenter, Podladchikov, et al. 1997; Anselmetti et al. 1998; Melim et al. 2001; Kenter et al. 2002, 2007; Assefa et al. 2003; Eberli et al. 2003; Baechle et al. 2008; Fournier et al. 2011). En effet, la diagénèse influence directement les propriétés élastiques à l'échelle de la matrice. Par exemple, une réduction de la porosité du fait de la cimentation, provoque une augmentation du module d'élasticité et donc de la vitesse de propagation des ondes. Une augmentation de la porosité suite à de la dissolution aura l'effet inverse.

2.1.2 Propagation des ondes dans les carbonates

Les propriétés pétrophysiques des roches carbonatées telles que la porosité, la perméabilité ainsi que leurs modules d'élasticité évoluent avec le temps et en réponse aux diverses altérations diagénétiques. Une bonne compréhension des relations qui existent entre les propriétés pétrophysiques et élastiques est essentielle pour la modélisation et l'inversion des données sismiques (Gardner et al. 1974; Christensen and Szymanski 1991; Stafleu et al. 1994; Anselmetti, Eberli, et al. 1997; Eberli et al. 2001; Huuse and Feary 2005; Zampetti et al. 2005; Verwer et al. 2008; Xu and Payne 2009). Depuis les travaux pionniers de Biot (1956a, 1956b) ou de Wyllie et al. (1956), il est admis que la porosité est le facteur principal influençant la vitesse de propagation des ondes élastiques dans les milieux poreux. Dès lors de nombreuses lois théoriques et empiriques ont été proposées pour expliquer cette relation. La WTA « Wyllie Time Average » qui estime le temps de trajet total d'une onde acoustique dans une roche sédimentaire comme étant la somme des temps de trajet dans les différentes phases solide et fluide de cette roche fut l'une des premières du genre. Elle fut ensuite améliorée et revisitée à de nombreuses reprises (Gardner et al. 1974; Raymer et al. 1980; Nur and Dvorkin 1998; Saleh and Castagna 2004). Néanmoins ces relations

ne donnent qu'une estimation grossière des vitesses et de nombreux auteurs ont montré les limites de la WTA en ce qui concerne les roches carbonatées. En effet, cette relation ne tenant pas compte de la diversité et de l'inhomogénéité des pores dans les carbonates sous-estime généralement les vitesses d'ondes P et S, et ne parvient pas à expliquer les variations de vitesse observées pour une valeur de porosité donnée (Anselmetti and Eberli 1993, 1999; Anselmetti, Salis, et al. 1997; Verwer et al. 2008; Baechle et al. 2009; Fournier and Borgomano 2009; Fournier et al. 2011, 2014). Ces études sont souvent menées à l'échelle du laboratoire, sur des échantillons supposés homogènes et en faisant l'hypothèse que les roches testées soient isotropes. Dans ce contexte, les variations de vitesses d'ondes P et S observées pour un échantillon donné sont souvent interprétées comme résultant, soit de l'alignement préférentiel des pores et de certains minéraux soit de la présence de microfissures liées à l'extraction (Nur and Simmons 1969; Todd and Simmons 1972). L'anisotropie à cette échelle n'est que très rarement considérée pour les carbonates ou bien les auteurs se focalisent sur des échantillons relativement peu poreux et homogènes (Z. Wang 2002a, 2002b; Martínez and Schmitt 2013). Pourtant certains auteurs ont observé des variations relatives de vitesse correspondant aux effets d'hétérogénéités sédimentaires telles que des lamines présentant des contrastes de porosité, du grano-classement induisant une orientation préférentielle des pores ou encore les stylolites etc. (Z. Wang 2002b; Louis et al. 2005; Adam et al. 2009). Ces éléments montrent que sous certaines conditions, de l'anisotropie pourraient exister dans les carbonates et ce même à l'échelle du laboratoire. Bien que l'anisotropie soit le plus souvent négligée en laboratoire, elle est omniprésente à l'échelle de la sismique (Helbig and Thomsen 2005). À grande échelle, les auteurs attribuent le plus souvent l'anisotropie soit aux propriétés de la matrice (cf. marnes) soit à la fracturation (Backus 1962; Crampin 1981; Berryman et al. 1999; Bakulin et al. 2000a; Grechka and Kachanov 2006). Dans le premier cas, l'anisotropie peut

théoriquement être calibrée à partir de mesures en laboratoire, tandis que cela s'avère plus compliqué dans le second cas, l'échelle des sets de fractures étant supérieure à celle des échantillons de laboratoire. Certains auteurs ont montré que les vitesses mesurées en laboratoire étaient significativement supérieures à celles mesurées in situ sur des formations fracturées (Stierman and Kovach 1979; Moos and Zoback 1983). Pour cette raison, la modélisation demeure le moyen privilégié pour faire avancer les connaissances concernant l'impact de la fracturation sur les propriétés élastiques des roches. Néanmoins ces modèles sont basés sur des hypothèses fortes qui conditionnent le résultat final (nombre de fractures, leur géométrie souvent simpliste, leur orientation etc...) et ne représentent souvent que des cas très particuliers et peu probables dans la nature (Hudson 1981; Bakulin et al. 2000a, 2000b; Grechka and Kachanov 2006; Berryman 2008). Bien que les informations issues de la modélisation soient précieuses quand il s'agit d'estimer l'anisotropie, il est souvent difficile de déterminer les contributions respectives de la matrice et de la fracturation sur cette anisotropie observée ou estimée. Cette problématique peut être solutionnée en étudiant les propriétés élastiques des formations carbonatées à l'échelle métrique ou multi-métrique car il serait alors possible d'évaluer quantitativement les signatures de la matrice et de la fracturation (McCann et al. 1975; Lubbe and Worthington 2006; Worthington and Lubbe 2007; Bereš et al. 2013; C. Matonti et al. 2015).

2.2 Objectifs et problématiques

L'objectif de cette thèse est de caractériser un réservoir carbonaté en utilisant les propriétés des ondes acoustiques. Pour y parvenir, il faut comprendre l'effet des hétérogénéités sédimentaires ou structurales sur les propriétés élastiques du réservoir, comme la vitesse de propagation des ondes de compression (onde P) et/ou de cisaillement (onde S), ainsi que l'anisotropie. Le second objectif

est de caractériser l'effet d'échelle sur les propriétés élastiques mesurées, afin de discuter son impact sur l'exploration sismique à grande échelle.

Caractériser les propriétés d'un réservoir inclut non seulement la caractérisation des dimensions et de l'architecture du réservoir, mais aussi la détermination de la distribution spatiale et des ordres de grandeur des propriétés pétrophysiques. La vitesse des ondes P, qui est une donnée acquise de façon continue et qui peut être calculée en tout point du réservoir peut être corrélée à la porosité qui est une propriété acquise de façon discontinue à partir des carottes de forages. Cette approche est couramment réalisée pour estimer la distribution de la porosité à l'échelle du réservoir. Cependant, il est primordial de pouvoir calibrer au mieux cette corrélation, ce qui n'est pas évident dans les roches carbonatées.

La notion d'anisotropie qui traduit la variation des vitesses d'ondes P ou S en fonction de la direction dans l'espace permet de caractériser l'effet des fractures ou d'autres types d'hétérogénéités. L'anisotropie des vitesses d'ondes acoustiques au sein du réservoir doit être déterminée très en amont, souvent par des mesures en laboratoire car elle intervient dans les toutes premières phases du traitement des données sismiques. Une calibration insuffisante peut être lourde de conséquence sur la qualité des données et l'interprétation qui pourra en être faite. Prenons l'exemple de la correction du « *normal moveout* » qui consiste à corriger le décalage temporel observé entre des traces sismiques illuminant un même point (« *common midpoint* »). Ce décalage est provoqué par une augmentation de la distance source–récepteur (« *offset* ») et donc une augmentation de la distance parcourue par l'onde sismique (« *raypath* »). Il se traduit en théorie par une relation hyperbolique de forme $t^2 = t_0^2 + x^2/v^2$ où t et t_0 sont le temps d'arrivée et le temps d'arrivée à l'« *offset nul* », x est l'offset, et v la vitesse de propagation dans le milieu (cf. Tsvankin (2012) pour plus d'informations sur les traitements des données sismiques anisotropes).

En réalité cette relation hyperbolique ne s'applique que si le milieu est homogène et isotrope. Quand le milieu est anisotrope, cette relation n'est jamais hyperbolique (Tsvankin and Thomsen 1994). Or, d'autres étapes du traitement des données sismiques telles que le moyennage des traces correspondant à un « *common midpoint* » afin d'améliorer le rapport signal/bruit (« *stacking* ») ou la correction du pendage des réflecteurs (« *dip moveout* »), dépendent entièrement de la correction du « *normal moveout* ». Par conséquent l'anisotropie peut induire une marge d'erreur importante sur les vitesses au sein d'un intervalle, une mauvaise conversion temps-profondeur et la détérioration de la qualité des sections « *stackées* » (Tsvankin and Thomsen 1994; Tsvankin et al. 2010).

Les roches carbonatées présentent de faibles contrastes d'impédance acoustique et produisent peu ou pas de réflecteurs sismiques exploitables. Les réservoirs carbonatés sont souvent reconnaissables du fait qu'ils se présentent sous forme de faciès sismiques « *sourds* » dont on ne distingue que les limites sommitale et basale. Par conséquent, la caractérisation des propriétés élastiques sur des échantillons à l'échelle du laboratoire est souvent le seul moyen pour accéder aux propriétés pétrophysiques du réservoir (Huuse and Feary 2005). Cependant, les carbonates sont réputés hétérogènes, la diagenèse et la grande diversité de faciès rendent l'analyse des propriétés d'autant plus complexe, tout en empêchant tout systématisme dans l'interprétation. La taille des échantillons en laboratoire ne permet pas d'appréhender correctement les variations de propriétés dans les carbonates hétérogènes. En effet, certaines hétérogénéités ont une dimension supérieure à celle des échantillons étudiés. Par exemple, un échantillon typique de laboratoire mesure quelques centimètres or certaines structures sédimentaires (rides, lentilles, litages, bio-constructions coralliennes etc.) qui traduisent des changements de faciès, de granulométrie, des horizons diagénétiques, etc., peuvent mesurer jusqu'à plusieurs mètres. Une solution face à ce

problème de représentativité de l'échantillon consiste à étudier des échantillons plus gros et donc plus représentatifs dans le cas des carbonates hétérogènes. Reste-t-il, encore, à déterminer quelles sont les échelles de caractérisation critiques en ce qui concerne les réservoirs carbonatés. Borgomano et al. (2013) ont étudié la représentativité en termes de propriétés pétrophysiques des plugs prélevés sur des affleurements de calcaires Urgoniens de Provence, suivant des tracés linéaires verticaux et horizontaux (analogues de données de puits). Ils ont montré que les données pétrophysiques mesurées sur plugs n'étaient, dans les faits, représentatives de l'ensemble du réservoir que dans de très rares cas. La principale condition pour qu'elles le soient est que les faciès constituant le réservoir soient fins, très homogènes avec des types poreux relativement monotones (ex. exclusivement de la microporosité), autrement les mesures souffrent d'un « effet de support ». De plus ces auteurs, ont montré qu'il était également peu probable de réussir à détecter des lentilles diagénétiques présentes dans ces formations car leurs extensions verticales sont souvent inférieures au pas d'échantillonnage tandis que leurs extensions latérales sont de quelques mètres seulement, contre plusieurs kilomètres pour l'espacement standard de puits.

2.3 Méthodes employées

2.3.1 Philosophie de l'approche

Nous avons vu précédemment que la plupart des mesures pétrophysiques et élastiques faites en laboratoire visent à calibrer et comprendre les données obtenues à l'échelle de la sismique. L'*up-scaling* des propriétés (c'est-à-dire la transposition des observations faites en laboratoire à l'échelle de la sismique) repose sur une hypothèse de base que les données obtenues en laboratoire sont représentatives des propriétés réelles indépendamment de l'échelle. La ligne directrice de ces travaux de thèse est de vérifier la validité de cette hypothèse. Pour ce faire l'accent a été mis sur la caractérisation d'une formation carbonatée qui, premièrement, est relativement simple en termes

de géologie et de propriétés pétrophysiques, et qui deuxièmement, offre l'accès à plusieurs échelles où les caractéristiques géologiques ayant un impact sur les propriétés élastiques peuvent encore être maîtrisées.

L'approche proposée, ici, consiste à étudier les propriétés élastiques d'un réservoir à différentes échelles allant de l'échantillon de laboratoire classique (*plug*), à des mesures inter-puits (*crosshole*), en passant par des carottes d'une dizaine de centimètres de diamètre par 25 à 80 cm de long. Dans ces travaux, nous parlerons d'« échantillonnage imbriqué » ou de « *sub-sampling* » car tous les échantillons présentent un lien direct avec leurs analogues des échelles inférieures/supérieures, c'est-à-dire les plugs sont issus des carottes qui sont-elles mêmes issues des forages utilisés pour les mesures inter-puits. Les valeurs de vitesse d'ondes P et S et d'anisotropies obtenues sont comparées entre elles, puis sont confrontées à la réalité géologique. Cette approche peut se décomposer en deux volets : (1) les analyses en laboratoire qui couvrent l'échelle centimétrique à pluri décimétrique, et (2) les analyses de terrain qui couvrent l'échelle métrique à décamétrique.

2.3.2 Investigation multi-échelle en laboratoire

Les points clés de l'approche en laboratoire sont donnés dans la **Figure 2.1**.

En laboratoire nous avons étudié six carottes ($\varnothing = 12.5$ cm, $L = [25-80]$ cm), ainsi que trois ensembles de plugs de tailles différentes. Le premier ensemble ($n=46$, $\varnothing = 2.54$ cm, $L=3.81$ cm) offre un échantillonnage discret des vitesses d'ondes P et S sur l'ensemble du forage P₂ (forage contenant la sonde de réception, **Figure 4.1**). Il a également été utilisé pour déterminer des valeurs de porosité et de perméabilité (cf. §4.5.1, et travaux de J. Cochard). Le second ($n=21$, $\varnothing = 3.81$ cm, $L=3.81$ cm) a été utilisé pour des mesures de vitesse mais aussi pour déterminer l'anisotropie suivant la méthode dite des « trois-plugs » (cf. Section 5:). Enfin le troisième ($n=7$, $\varnothing = 2.54$ cm,

L=2.54 cm) a été utilisé pour des mesures de porosité et de vitesse en conditions saturée ou non-saturée (Travaux de C. Gilbert, stagiaire).

Les mesures de vitesse sur plugs ont été relativement simples à réaliser et la méthode peut être résumée en quatre étapes : (1) l'échantillon est placé entre deux transducteurs acoustiques (d'ondes P ou S), l'un étant la source et l'autre le récepteur, (2) une force (uni axiale) est exercée sur les capteurs et l'échantillon afin d'assurer un couplage optimal (selon le cas, un gel couplant ou une fine feuille de plomb été utilisée pour renforcer la qualité du couplage aux interfaces capteur-roche), (3) une impulsion électrique est envoyée par un générateur puis est converti successivement par les transducteurs en signal acoustique puis électrique, qui est ensuite enregistré par un oscilloscope, et (4) les temps de trajet sont pointés sur le signal au début de la perturbation provoquée par l'onde (« *onset* »), la vitesse peut ensuite être calculée en fonction de la longueur de l'échantillon et du temps de trajet.

Les mesures acoustiques sur carottes ont représenté un défi plus important, notamment pour tenir compte des contraintes imposées par l'analyse d'échantillons de cette dimension. La première difficulté était de définir une méthodologie permettant de mesurer les propriétés acoustiques sur l'ensemble de la carotte et donc en trois dimensions (3D). La seconde était d'acquérir ces mesures en maîtrisant le positionnement exact des transducteurs (et donc la distance qui les sépare). Ces deux premiers points ne sont réalisables qu'en faisant appel à un système automatisé. Le troisième point était le couplage, à cette échelle l'utilisation d'un gel couplant sur les échantillons nuit gravement à la reproductibilité des mesures. En effet ce dernier est rapidement absorbé par la roche, et les propriétés élastiques évoluent avec cette saturation progressive. De plus, l'emploi de transducteurs (de contact) sans couplant et sans optimisation de la surface de contact avec la roche est synonyme de signaux de qualité médiocre. Nous avons choisi de répondre à ce problème en

effectuant les mesures en milieu saturé. Enfin, la dernière difficulté (qui s'applique aussi aux mesures sur plugs) était d'adapter la fréquence du signal acoustique utilisée pour tenir compte de la dissipation de l'énergie dans un milieu poreux, tout en gardant un seuil de détection adéquat pour étudier les caractéristiques géologiques.

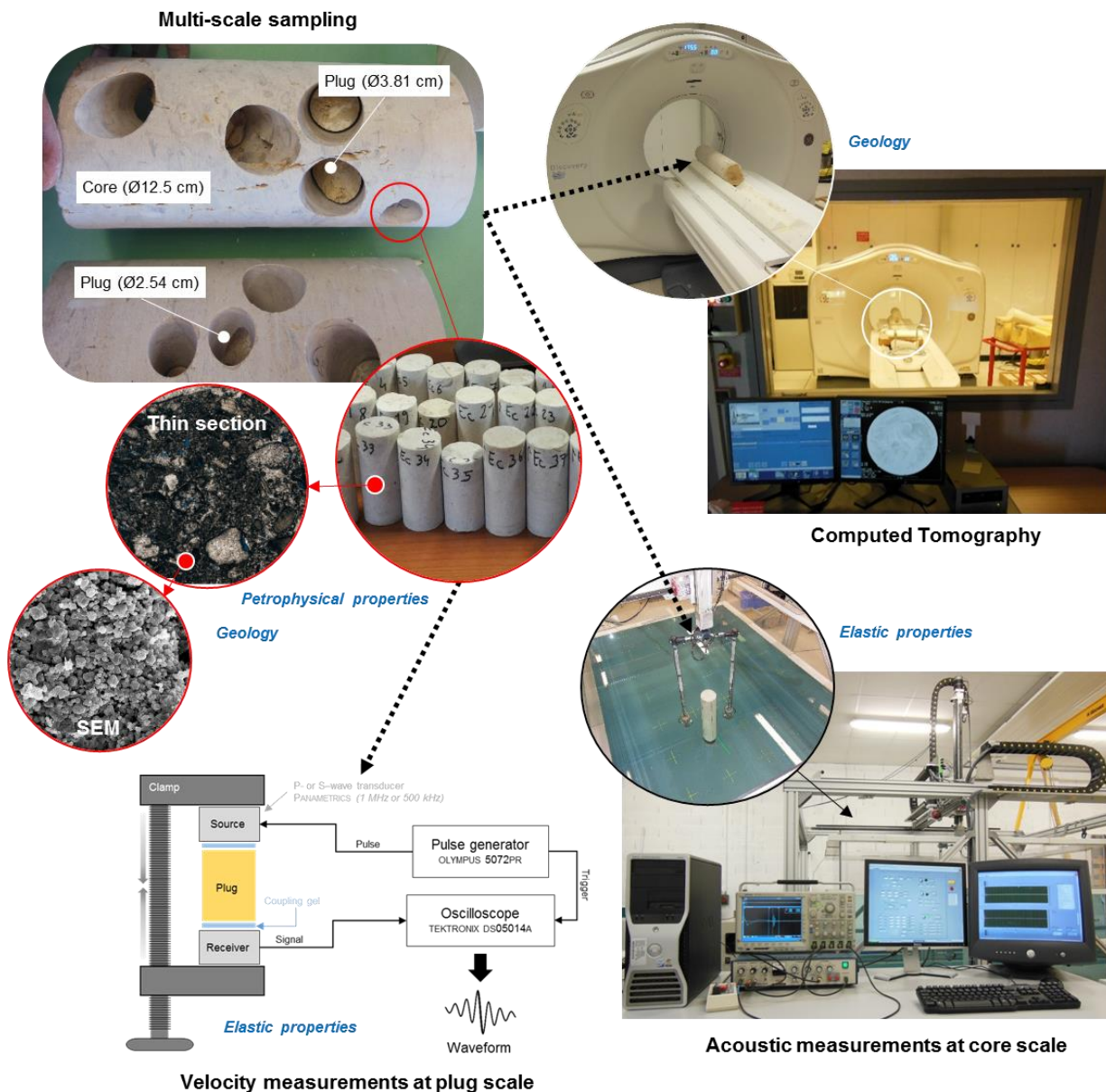


Figure 2.1. Analyse multi-échelle des propriétés pétrophysiques et élastiques en laboratoire. Chronologiquement, les caractérisations non-destructives (mesures des propriétés élastiques, tomographie) ont été réalisées avant les opérations destructives (carottages, lames minces, etc.).

La caractérisation des carottes a nécessité une solution innovante prenant en compte l'ensemble des contraintes évoquées ci-dessus. Nous avons utilisé une cuve acoustique, instrumentée pour permettre l'acquisition de signaux avec une fréquence centrale de 250 kHz. Cette fréquence nous est apparue comme étant un bon compromis permettant à la fois une caractérisation fine des structures géologiques à l'échelle des carottes et avec des transducteurs suffisamment énergétiques pour en permettre l'enregistrement. Les transducteurs sont montés sur un support en forme de U et leur déplacement, ainsi que l'acquisition des signaux sont entièrement contrôlés par ordinateur.

Tout comme les propriétés élastiques, les caractéristiques géologiques ont été étudiées à différentes échelles. L'analyse de la géologie à l'échelle des carottes comprend d'une part, des descriptions macroscopiques des faciès et de la fracturation. Et d'autre part, l'analyse des données de tomodensitométrie (CT scan) qui met en évidence les contrastes de porosité susceptibles d'affecter le signal. À l'échelle du plug ce sont les propriétés à l'échelle microscopique qui suscitent l'intérêt. Les lames minces et la caractérisation à l'aide d'images de microscopie électronique à balayage (MEB) ont permis de couvrir l'échelle centimétrique à micrométrique.

2.3.3 Investigation multi-échelle sur le terrain

Les points clés de l'approche sur le terrain sont donnés dans la **Figure 2.2**

L'approche crosshole a été motivée par un simple constat, à savoir : les carottes issues des zones les plus fracturées du réservoir sont morcelées et donc les propriétés originelles des fractures ne peuvent être que partiellement caractérisées en laboratoire. L'implantation des forages (très proches les uns des autres) de la galerie GAS du Laboratoire Souterrain à Bas Bruit, en font une configuration idéale pour caractériser les propriétés élastiques tout en incluant l'effet des fractures.

Pour ce faire il a été nécessaire de développer un outil permettant l'acquisition des données acoustiques aux fréquences ultrasonores et ce entre deux puits distants de deux mètres. Ainsi la

première difficulté à laquelle nous avons été confrontés était l'adaptation des outils d'acquisition aux caractéristiques techniques du site d'étude. Ces dernières peuvent être classées par ordre d'importance comme suit : (1) l'écart minimal des forages étant de 2 m, la source devait être suffisamment puissante pour permettre au signal de couvrir cette distance ; (2) le réservoir n'étant pas saturé, le couplage devait être mécanique ; (3) l'orientation des capteurs et donc la distance parcourue par l'onde devait être maîtrisée ; et (4) les forages ayant une valeur patrimoniale, leur intégrité devait être préservée.

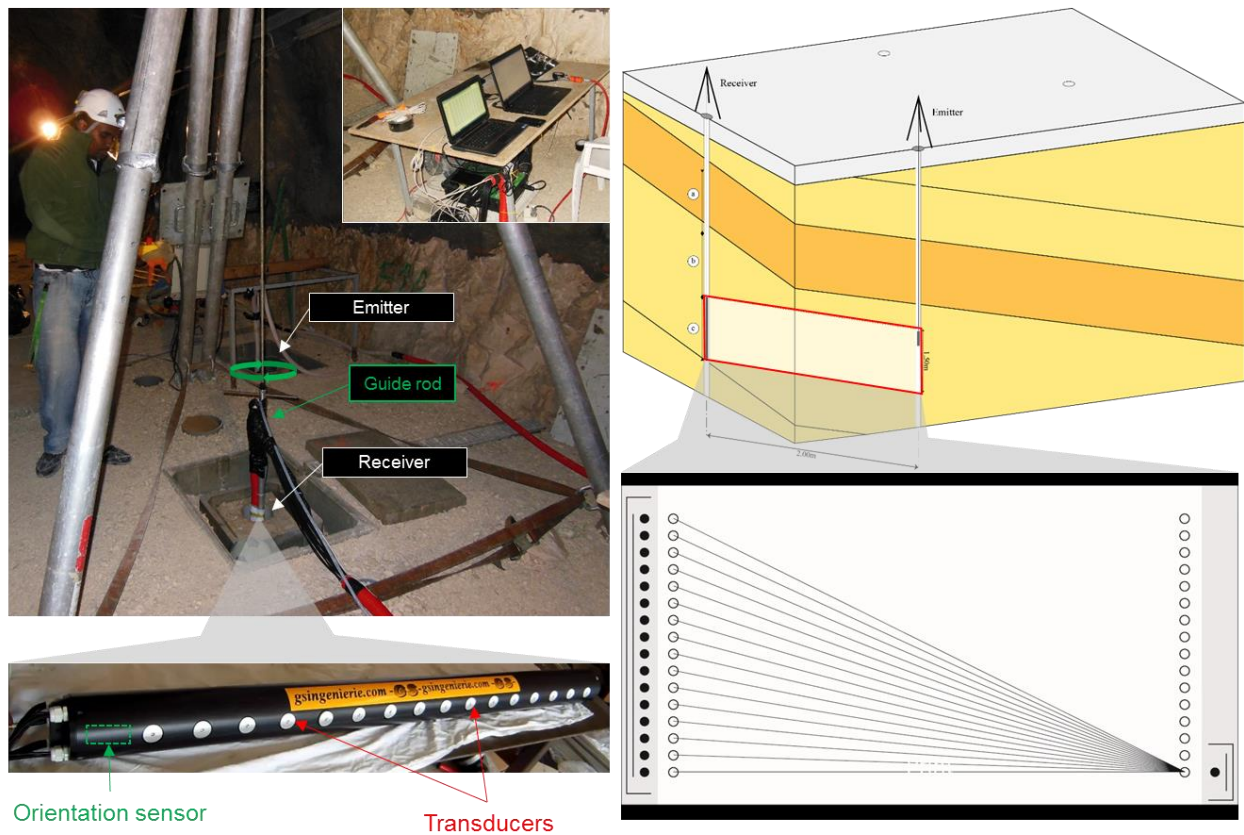


Figure 2.2. Acquisition des données acoustiques sur le terrain. Les sondes émettrice (émetteur unique) et réceptrice (16 récepteurs) sont placées dans leurs forages respectifs, orientées et bloquées. Après chaque tir, la sonde émettrice est déplacée verticalement d'un pas de 10 cm jusqu'à couvrir la totalité d'une section (15 à 16 tirs). L'acquisition des signaux, l'orientation des sondes et la pression exercée pour le couplage des capteurs sont monitorés en direct.

Pour faire face à ces problèmes nous avons développé une paire de sondes acoustiques permettant la réception et l'envoi de signaux acoustiques avec une fréquence centrale autour de 50-55 kHz. Ces sondes sont innovantes car conçues pour être employées en configuration crosshole et sans fluide assurant le couplage. De plus, elles sont équipées de transducteurs directionnels conçus pour s'adapter précisément aux dimensions des forages. Elles possèdent également des capteurs d'orientation et un dispositif de guidage permettant de contrôler en temps réel leurs positions. Ces sondes ont permis de caractériser avec succès le réservoir sur une profondeur d'environ 14.5 m. Bien que les conditions expérimentales n'ont pas permis d'avoir une couverture angulaire (cumulée) supérieure à 74° , cela était cependant suffisant pour mettre en évidence de l'anisotropie dans certains cas et l'influence conjointe des fractures et des strates sur le signal.

2.4 Principaux résultats

Les résultats de ces travaux montrent que les vitesses moyennes d'ondes P et S sont dictées par la porosité matricielle qui est indépendante de l'échelle. En revanche, la variabilité des vitesses autour de ces valeurs moyennes peut varier. On constate que l'augmentation du volume de roche étudié entraîne une augmentation de la variabilité notamment à cause d'une meilleure prise en compte des hétérogénéités sédimentaires ou structurales qui sont des facteurs potentiels d'anisotropie.

À l'échelle du plug, les propriétés élastiques mesurées correspondent à celles de la matrice (**Figure 2.3**). Les échantillons peu poreux ont des valeurs de vitesse qui tendent vers celles de la calcite. Ces valeurs varient peu entre les plugs extraits d'un même faciès, par contre on observe l'inverse dans le cas des faciès les plus poreux.

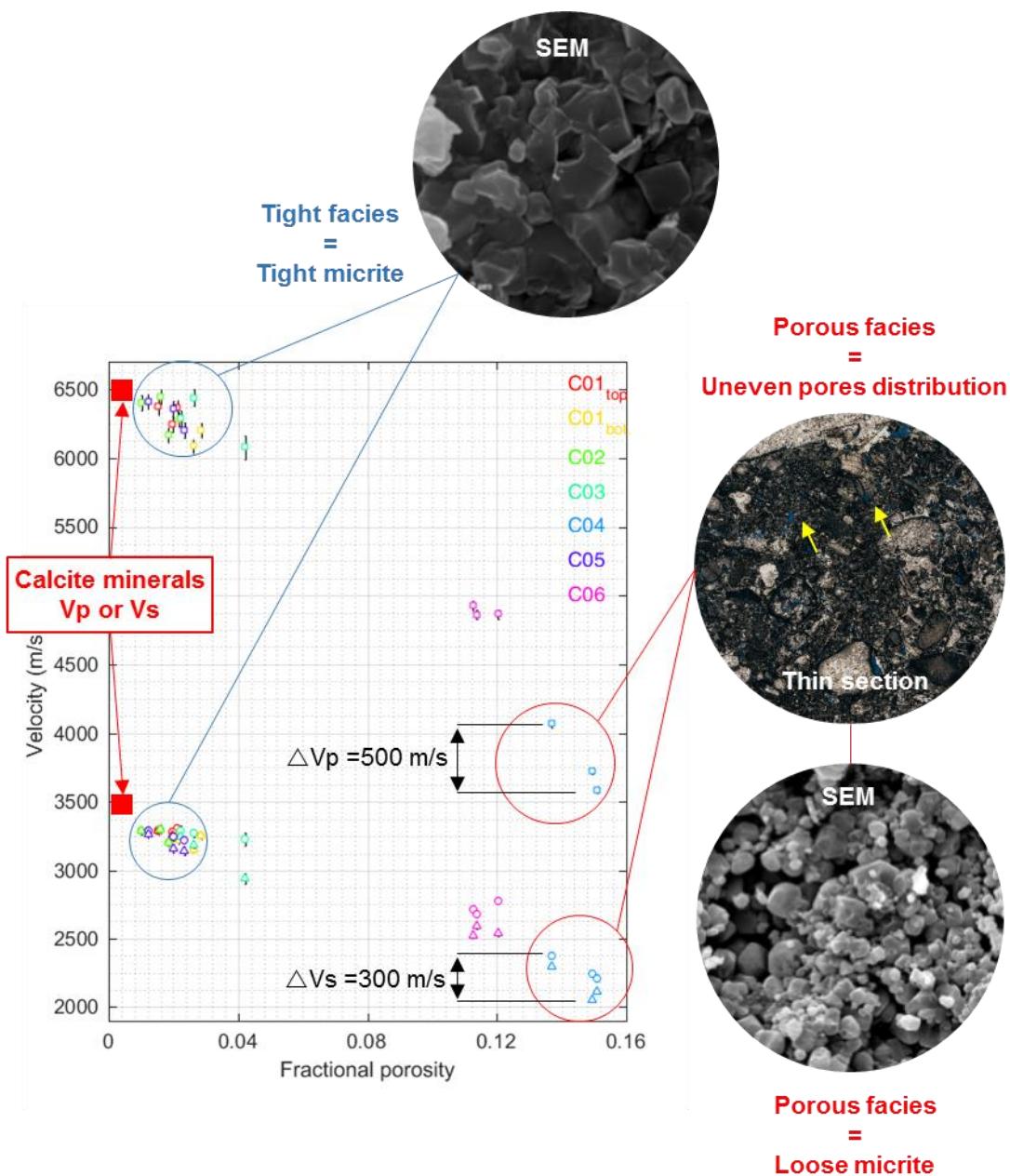


Figure 2.3. Propriétés élastiques et pétrophysiques à l'échelle de la matrice. Les vitesses d'ondes P et S sont corrélées à la porosité mais on note des écarts significatifs entre des échantillons poreux venant du même faciès. Cela montre l'impact de l'hétérogénéité des carbonates de plateforme.

Les modules élastiques et l'anisotropie estimés pour les faciès peu poreux sont isotropes, ce qui s'explique par l'homogénéité de ces faciès à l'échelle du plug. L'analyse des valeurs obtenues dans le cas des faciès poreux hétérogènes est plus difficile. Clairement, le plug n'est pas un volume

représentatif des propriétés pétrophysiques des matrices hétérogènes, par conséquent la détermination de l'anisotropie nécessite de passer à une échelle supérieure telle que celle des carottes (**Figure 2.4**)

À l'échelle de la carotte il faut tenir compte à la fois des propriétés matricielles et macroscopiques. Un faciès peut être homogène du point de vue matriciel (~réseau poreux monotone) et présenter des fractures à l'échelle de la carotte, ce qui entraîne une distribution anisotrope des propriétés. D'autre part un faciès hétérogène (~plusieurs types de pores, avec différentes dimensions) peut le devenir encore plus à grande échelle à cause des inclusions (fossiles). Trois cas de figure se présentent dans notre étude :

- Le faciès est homogène et/ou non-poreux. Les vitesses d'ondes P ou S mesurées sont les mêmes qu'en laboratoire.
- Le faciès est fracturé homogène et/ou non-poreux. Le signal acoustique est très affecté par la fracturation. L'anisotropie de la vitesse d'onde P peut atteindre 10-15%. Ce type d'anisotropie est très fréquemment commenté dans la littérature. Néanmoins l'approche employée ici montre que l'anisotropie peut varier spatialement, en fonction de la répartition et de la densité des fractures. Ce constat pose la question de la validité ou de l'applicabilité d'un modèle unique d'anisotropie à l'ensemble d'un réservoir.

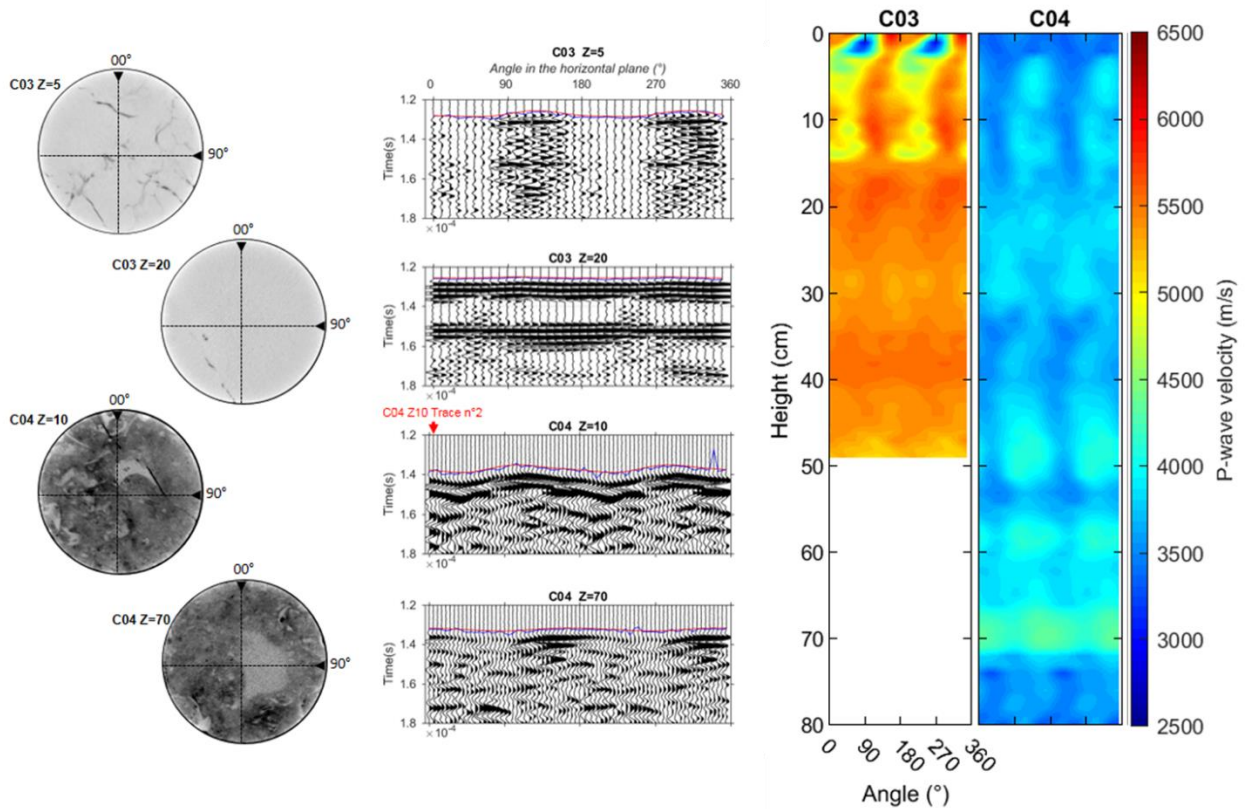


Figure 2.4. Exemples d'hétérogénéités et leurs conséquences sur le signal acoustique. Deux coupes transversales (CT scan) d'une carotte non-poreuse, homogène, et fracturée (C03), sont comparées à deux autres provenant d'une carotte poreuse, hétérogène et faiblement fracturée (C04). Les traces enregistrées aux mêmes côtes que ces coupes permettent d'illustrer les caractéristiques géologiques influençant le signal acoustique. Dans les trois premières coupes les fractures provoquent une atténuation du signal et de l'anisotropie, tandis que dans le dernier exemple c'est un corail qui provoque l'anisotropie. Les cartes de vitesse montrent qu'à l'échelle des carottes on note une grande variabilité des vitesses en particulier dans les zones fracturées ou hétérogènes.

- Le faciès est hétérogène. Contrairement aux deux premiers, ce dernier cas est peu ou pas documenté dans la littérature. L'étude de carottes pluri-décimétriques permet de mesurer l'impact des hétérogénéités sédimentaires et diagénétiques sur la propagation des ondes P. Des variations locales de la porosité au sein d'une matrice poreuse ont été mises en évidence. Ainsi, la présence des macro-fossiles non-poreux provoque une anisotropie pouvant atteindre 5%. Bien qu'inférieure à celle liée aux fractures, cette anisotropie

apparente est non négligeable et ne pourrait pas être mesurée sur des échantillons standards. Cependant, cette anisotropie apparente liée aux fossiles reste très localisée à l'échelle de la carotte et ne peut donc pas être interprétée comme de l'anisotropie au sens strict. Compte tenu de la nature des éléments qui la produisent, c'est-à-dire coraux en position de vie, accumulation de fragments de rudistes, on peut penser qu'à l'échelle du réservoir ce type d'arrangement préférentiel de fossiles puisse causer une certaine forme d'anisotropie.

À l'échelle inter-puits les vitesses moyennes des ondes P et S sont dictées au premier ordre par la porosité. Au second ordre intervient la fracturation qui va conditionner l'anisotropie et donc les variations autour de la vitesse moyenne. À cette échelle la réponse acoustique varie spatialement en fonction de la distribution des fractures, et de la porosité. Dans les zones fracturées, l'anisotropie est du même ordre de grandeur que pour les carottes fracturées ~10-15%, tandis qu'elle est quasiment nulle dans les zones non-fracturées (**Figure 2.5**). L'anisotropie mesurée peut être influencée par la position relative de la source sismique, par exemple la position de la source par rapport à une couche présentant un fort contraste de porosité avec les couches adjacentes. Ce constat interpelle sur l'interprétation des données crosshole acquises au sein de réservoirs carbonatés hétérogènes, avec des tirs relativement limités ou dispersés et se trouvant potentiellement dans des couches ayant des propriétés différentes.

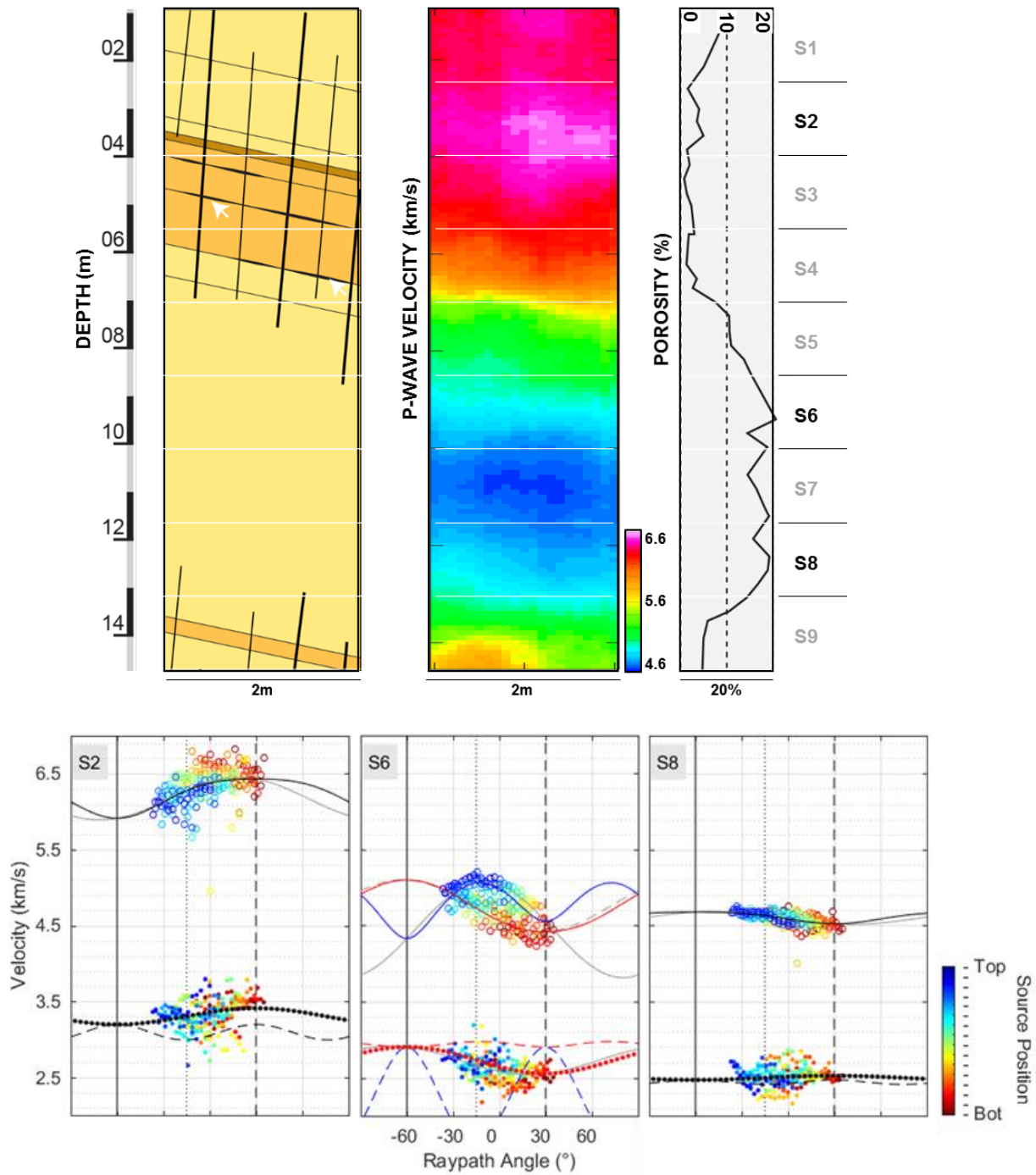


Figure 2.5. Considération des hypothèses d'isotropie et d'anisotropie. La tomographie isotrope de l'espace inter-puits est comparée au relevé de la porosité et à une représentation schématique de la géologie. Les lignes représentent les différents modèles obtenus en utilisant les équations exactes de propagation des ondes P (cercles) et S (points) en milieu poreux..

2.5 Conclusion et perspectives

Les résultats obtenus à l'issue de ces travaux de thèse montrent que tout comme pour leurs propriétés pétrographiques, il n'existe aucun systématisme dans l'interprétation des propriétés élastiques des réservoirs carbonatés. Le recours usuel à l'échelle du plug (en laboratoire) et de la sismique (plusieurs kilomètres), soit deux échelles où les carbonates peuvent être perçus comme homogènes ou isotropes, a contribué à la croyance générale concernant l'isotropie des carbonates. L'approche présentée ici montre la nécessité de déployer des mesures et des protocoles couvrant les échelles métrique à pluri-métrique (décamètre) qui semblent être primordiales pour caractériser les propriétés élastiques des formations carbonatées poreuses. Ce travail montre que dans certains cas, il peut apparaître deux niveaux d'anisotropie liés respectivement à l'hétérogénéité des faciès et aux fractures.

Section 3: Experimental settings

3.1 Abstract

This section describes the experimental set-ups designed and developed especially for this study. The two main technological developments are discussed i.e.: (1) the crosshole acoustic survey that required specifically tailored probes to adapt to the experimental settings; and (2) the core-scale characterization in the acoustic tank, which is an innovative way to image elastic properties of decimeter-scaled cores. Other “routinely-employed” methods are not presented here, but they are instead detailed in the “*Material and Methods*” part of the results sections.

3.2 A new crosshole acoustic survey to explore carbonates at the multi-meter scale

3.2.1 Introduction

Larger wavelengths (low frequencies) are synonym of larger investigated area, unfortunately it also means a loss in the resolution of seismic data. The main challenge when using acoustic signals to image earth material is to find the right balance between the desired range of investigation and the resolution. The objective of the crosshole survey was to carry out acoustic measurements using ultrasonic frequencies onto large volume of rocks that cannot be handled in laboratory. The main motivation was that ultrasonic frequencies around 50 kHz (i.e. wavelengths ~10 cm in carbonates) give sufficient resolution to characterize macroscopic features within a carbonate reservoir. Knowing that the elastic properties of carbonates are tightly related to their petrophysical

properties, carrying out acoustic measurements with such a fine resolution potentially enables to characterize accurately the petrophysical properties over relatively large areas. However, ultrasonic frequencies are best suited for laboratory conditions, where the experimental conditions can be mastered properly. Our ambitious objective of conducting such experiments on the field required technological developments to address the constraints related to the experimental settings. For example, the experimental conditions needed to be as much controlled as possible to guarantee the reproducibility of the data. The geological context had to be simple to enable interpretation of the data without strong (non-verifiable) assumptions about the geology. The survey was meant to be a full-scale test for ultrasonic wave propagation in a porous and fractured carbonate reservoir.

3.2.2 Guidelines and specifications

Most of the constraints cited above were addressed by the probes design. In fact, two acoustic probes named PETROACII, have been designed as a part of this PhD work. They were meant to carry out a crosshole acoustic logging over a fractured and porous carbonate formation, using ultrasonic frequencies. The probes were designed especially to address several challenging technical constraints related either to the experimental conditions (e.g. dry boreholes) or to the purpose of the study. The probes needed to fulfill four main tasks to be suitable for the survey, and the latter served as guidelines during the probes design. These tasks are listed below:

- Measuring ultrasonic waves in a porous media at distances larger than 2 m,
- Performing the measurements between two dry boreholes,
- Ensuring optimal coupling between the transducers and the rock,
- Real time monitoring of the transducers position and orientation.

The experimental set-up developed during this PhD works can be divided in three subsets dedicated to: (1) acquisition and monitoring, (2) displacement and orientation, and (3) mechanical coupling (**Figure 3.1**).

The acquisition chain includes: (1) the computer-controlled acoustic acquisition system, the TDAS16, and (2) the acoustic probes. The TDAS16, manufactured by BOVIAR (www.boviar.com), is a computer-controlled acquisition system that includes, a built-in signal generator and receiver; and 17 piezoelectric-transducers (sixteen receivers and one emitter). The TDAS16 was intended to carry-out non-destructive investigations, mainly in the field of civil engineering. Its relatively highly-energetic emitter (0.05J) and the wide working range of its transducers (10Hz to ~80kHz) make this device suitable for measuring acoustic waves over multi-metric distances, depending on the material properties. The probes are fine-designed casings intended to hold the TDAS16 transducers, and ensure optimum coupling against the borehole-wall. The first probe, PETROACII-R is dedicated to the reception of acoustic waves; while the second probe PETROACII-E is the source. These two probes will be referred in the text as the reception-probe, and the emission-probe. Both probes are cylindrical, and have a diameter of 0.125m. The reception-probe is 1.75m long, has sixteen receivers lined-up vertically. The distance between the axes of two receivers is 0.01m, so that the distance between the first and the last receiver is 1.50m. The emission-probe is 0.25m long, and has only one transmitter.

The accurate positioning of the probes, ideally with an accuracy $\geq 2\text{cm}$, ensures the reliability of the sensors-array geometry, enabling accurate indexing of borehole wall imagery. The displacement and orientation subset was composed of four elements for each probe: (1) a rig, (2) an electric winch, (3) a guide rod, and (4) an orientation sensor.

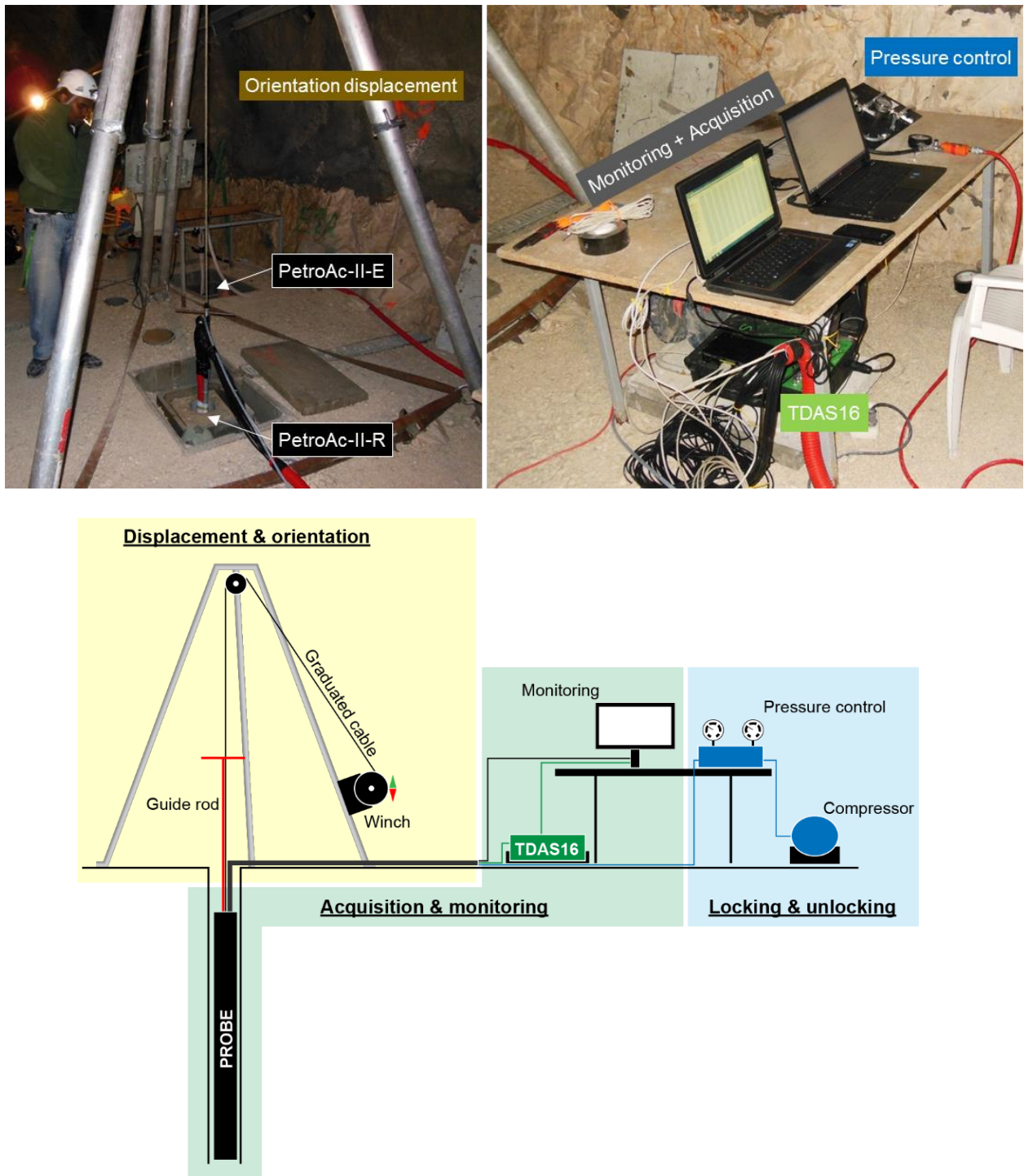


Figure 3.1. Photographs, and schematic overview of the experimental set up. Three subsets related to the logging process are figured, i.e. the elements enabling any motion of the probes (yellow, and blue), and acquisition and monitoring system (green).

The cables and guide rods were marked with graduations, so that the probe depth which was indexed on the uppermost sensor depth could be read from the borehole top and from the winch. The motion along the vertical axis was provided by an electric winch that lifts or lowers the probe, meanwhile the rotation around the vertical axis was enabled by the guide rod. The multi-function orientation sensors YOCTO-3D (manufactured by YOCTOPUCE, www.yoctopuce.com) were supplied with their programming libraries, enabling hardware control. The YOCTO-3D features a 3D accelerometer, a 3D gyroscope and a 3D magnetometer. It enables real time monitoring of the 2D inclination, the magnetic orientation, and provides a 3D orientation based on inertial measurements. The azimuth was measured according to the transducers orientation, and the guide-rod allowed to adjust the orientation according to the live-monitored position (**Figure 3.4**).

Finally, the coupling between the probes and the borehole-walls was mechanic because the experiment was carried-out between two dry boreholes. The coupling required some technical adaptations in the probes design. For example, the transducers were equipped with adapters designed for fitting the borehole curvature and maximizing the contact area ($\sim 12\text{cm}^2$) and all the transducers were mounted on independent retractable chassis (one per transducer). The chassis enabled the probes to accommodate potential irregularity of the borehole-wall, by allowing a transducer to move out few centimeters further than another if needed (**Figure 3.2**). The mechanism was powered by a pneumatic system which could be divided in three parts: (1) a compressor, (2) a pressure-control desk, and (3) pneumatic chambers located inside the probes. The air supply from the compressor was distributed into two independent circuits, towards either the emission or the reception probes. Both circuits are managed from the pressure-control desk, which is equipped with pressure gauges, and valves enabling either inflation or deflation of the pneumatic chambers.

When the probes are at rest, their transducers are retracted inside the probes bodies/shells. When the probes are oriented and ready to operate, the pneumatic chamber located behind the transducers inflates and pushes the transducers out of the shells. The pressure exerted by the chamber (1.5 bar) pushes the back of the probes, which allows to maintain the transducers against the borehole-wall (**Figure 3.2**).

3.2.3 Acquisition workflow

The acoustic logging has been carried-out between two boreholes located two meters apart, along the azimuth N20°. The boreholes were both ~22 m deep, but the study has been conducted from 1 to 14.5 m depth. The size of the investigated area was 2 m × 13.50 m.

Prior to operation, the probes were lowered to the bottom of the investigated area, while the sections (1.5m each) of the guide rods were assembled up to the required length. Once the probes reached the bottom of the investigated area, their orientations were monitored and adjusted (**Figure 3.4**) in order that the probes face each other. For technical reasons related to the probes dimensions and the signal attenuation through the rock, the acquisition was divided into different sections (i.e., vertical intervals with limited height). Each section was 1.5 m high, and was delimited by the positions of the first and the last receiver of the reception-probe.

The acquisition process is detailed in **Figure 3.3**. The acquisition for a section started with the emitter placed face to face with the bottom receiver. Sixteen full-waveforms acoustic signals were recorded per shot. After each shot, the emission-probe was moved 10 cm up. After completion of a section the reception-probe was moved 1.5 m up, and another section was processed. Consequently the two successive sections overlapped each other, since the position of the top receiver becomes that of the bottom receiver in the next section.

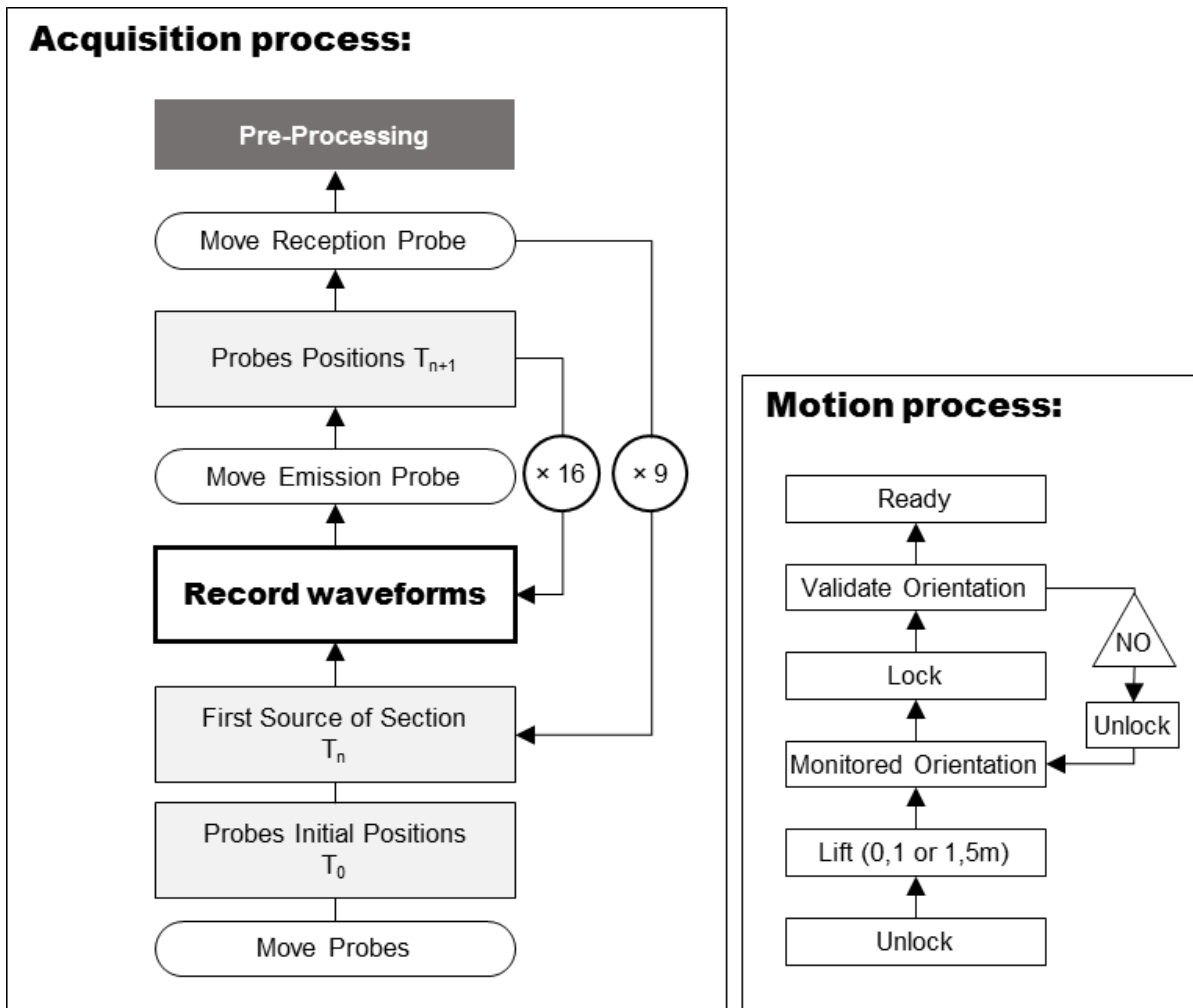


Figure 3.3. Simplified flow chart of the acoustic logging. The main acquisition steps are summarized (left), while the probes motion process, cf. “move” on the main chart, is detailed (right).*

Different steps of the process were not optimum because we relied on some preexisting apparatus with the following limitations. The TDAS16 enabled processing (i.e. display, stack, and record) only four channels at a time. The probes displacement and orientation were manually executed, and required at least two operators. Consequently, it was mandatory to keep tracks of all the subsidiary steps of the acquisition process. For example we kept logs of the start/end pressures of the pneumatic chambers, the start/end times for the section processing, the depths, and the files

recorded. These logs prevented any mistakes during operations, and enabled verifying the data during pre-processing.

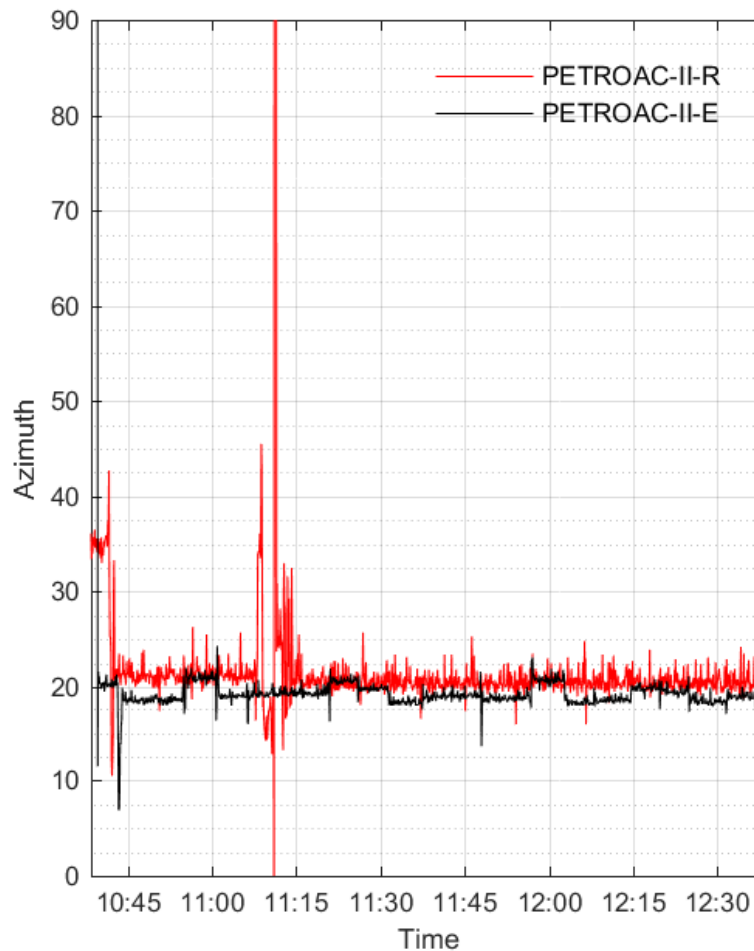


Figure 3.4. Extract of the probes orientation logs.

The Emission (PETROAC-II-E), and Reception (PETROAC-II-R) probes positions are live-monitored during an acquisition session. One can see both curves were centered on azimuth N20 despite a standard deviation of $\pm 2^\circ$. The high perturbation in the red curve, and the lower but sharp perturbations of the black ones denote the probes displacements. The increased level of noise on the red curve may be related to the increased number of transducers cables. The process required about six minutes to complete the acquisition for one source position, and this is visible on the logs (cf. duration between two perturbations in the black curve). This figure shows the consistency of the orientation during the acoustic logging.

3.2.4 Calibration

A signal recorded by any measuring instrument can be expressed using (1):

$$O(u) = (F_i \times I)(u) \quad (1)$$

Where F_i is signature of the experimental apparatus, I is the input signal sent to the generator, O is the output signal recorded at the end of the acquisition chain.

The TDAS16 being a turnkey acquisition-system, only few details are available on its internal design. Some elementary information such as the original source signal $I(u)$ were not available, and only $O(u)$ could be retrieved experimentally. Since, the field works were focused neither on frequency domain nor the amplitudes, consequently we did not process the signal as far as the deconvolution stage. Instead, we carried out different calibration tests to characterize the output signal in homogeneous media. For example, we needed to evaluate the time delay introduced by the acquisition chain, the radiation pattern of the directional transducers, and the frequency spectrum of the emitted signal.

3.2.4.1 The source signal

The tests series were conducted though air at 20°C, in that conditions the velocity of the compressional waves is 340m/s. The receiver was fixed onto a rigid framework, and the emitter was mounted onto a computer-controlled Axis Positioning System, which enabled translation in 3D (axis XYZ), and rotation on the vertical axis (Z).

The first test was meant to record the output signal. The emitter was placed face to face with the receiver, and acoustic signals were measured for incremental distances between the two transducers (i.e. 2, 5, 10, and 20cm), see **Figure 3.5**.

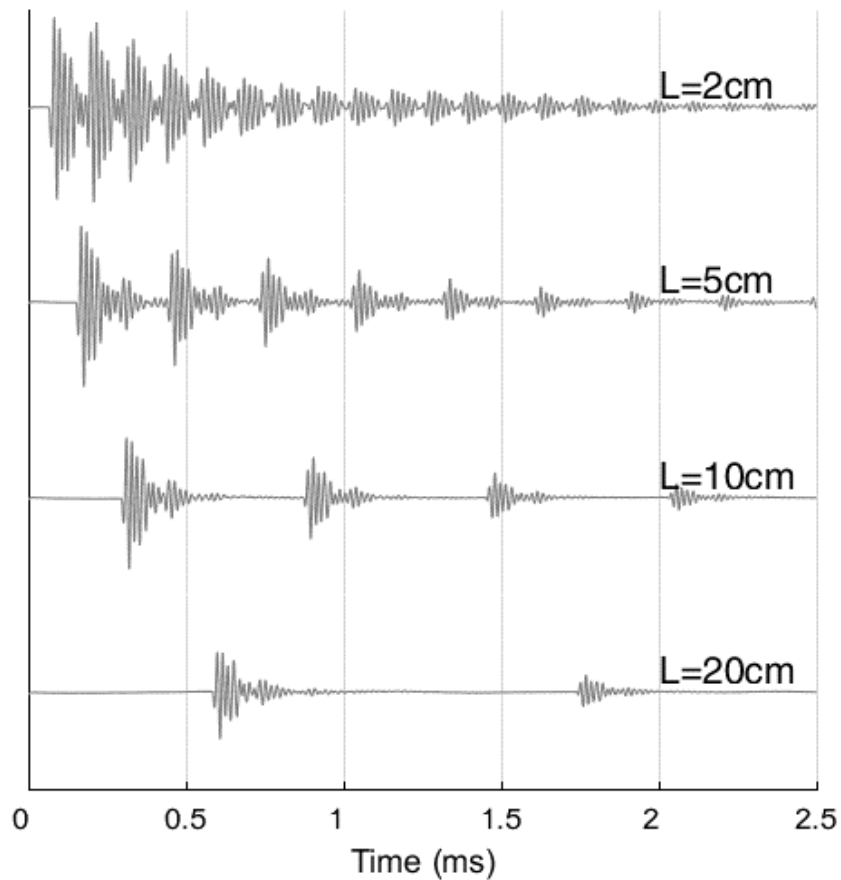


Figure 3.5. The output signal through air at 20°C. Multiple signals are measured as a function of an incremental emitter-receiver distance (L).

We performed a wavelet transform to characterize the source signal in the time-frequency domain (**Figure 3.6**). This analysis showed that the signal contained one main wave train and two echoes (with lower amplitudes) of the latter. One explanation for that could be the design of the source or the reverberation inside the receiver casing. However, this effect could be removed using filters, and other analytical methods in future studies.

As claimed by the manufacturer, the frequency spectrum ranged from 10 to 80 kHz, but the spectrum did not form a regular Gaussian distribution. Indeed, one can see on the modulus plot (**Figure 3.6**) a relatively low frequency component (~ 37 kHz), detached from the main component range, .i.e. 45 to 85 kHz.

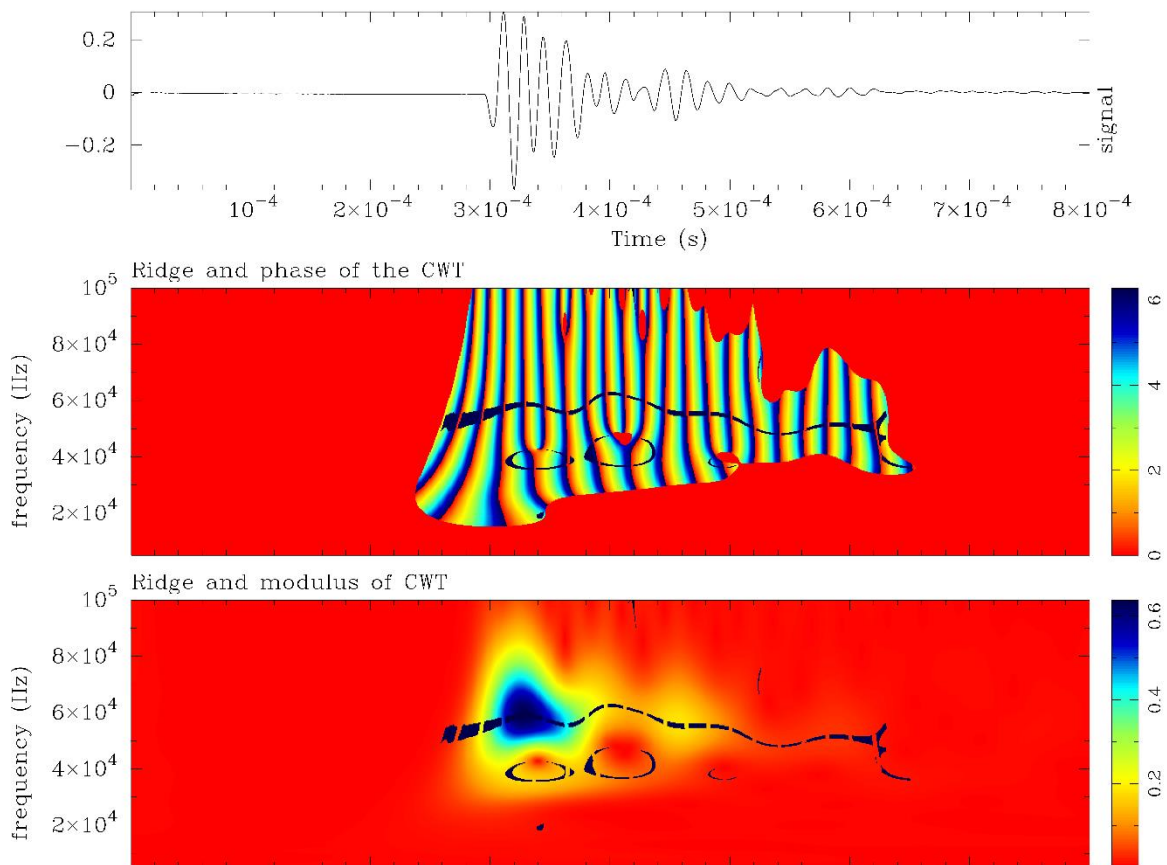


Figure 3.6. Results of a wavelet transform onto the source signal.

Phase and modulus of the wavelet transform (using Morlet wavelets) of the TDAS16 source signal through air at 20°C, with an emitter-receiver distance of 10cm. The time of first arrival is 295.2 μ s, that's to say the velocity was 339m/s.

3.2.4.2 Directionality of the transducers

Since we used directional transducers, we needed to test the directionality of the transducers, and to do so, we implemented a simple experiment. As in the previous example, the receiver was fixed and the emitter motion was controlled by the APS. For a given emitter-receiver distance, the emitter rotated on the vertical axis over 180°, while every 15° the signals were recorded. The results are given in **Figure 3.7**. One can see that the maximum amplitudes were recorded for the

transducers placed face to face, and the signal was almost entirely attenuated 30° off the transducers axes.

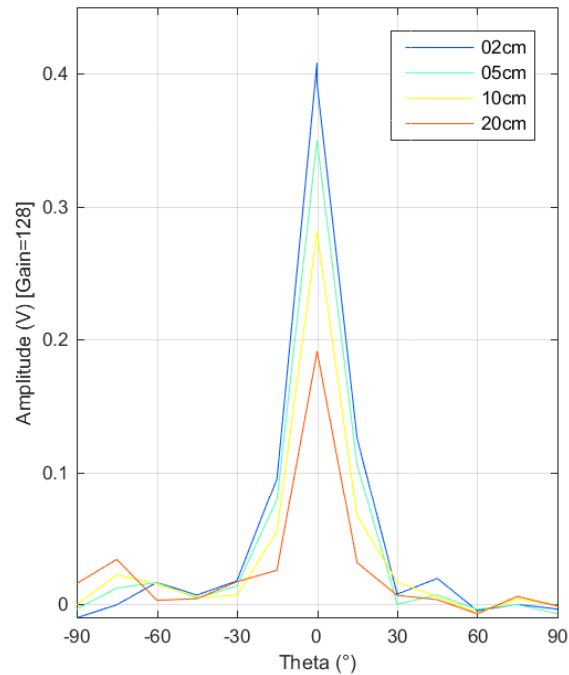


Figure 3.7. Radiation pattern of the couple emitter-receiver through air at 20°C.

The receiver is fixed, and the emitter rotates on its own vertical axis. The amplitude of the second positive peak (=the maximum amplitude) was picked from the waveforms. At Theta=0° the transducers are face-to-face. The experiment was repeated with different spacing of the transducers.

3.2.4.3 Instrumental delay, and modification of the source-signal

The last thing we needed to test was the delay introduced by the instrumentation. We placed the emitter directly on the receiver. In that configuration the emitter-receiver distance was assumed to be zero, so that the delay of the first arrival was expected to be the instrumental delay. In this first configuration we observed an average delay of 4.8 μ s. Then, we equipped the emitter and the transducers with the borehole-wall adapters, and we repeated the experiment. In this second

configuration we obtained an average delay of $18\mu\text{s}$, which meant the adapters added an additional $13.2\mu\text{s}$ to the initial instrumental delay. The time values obtained from the field measurements were systematically corrected from this $18\mu\text{s}$ instrumental delay.

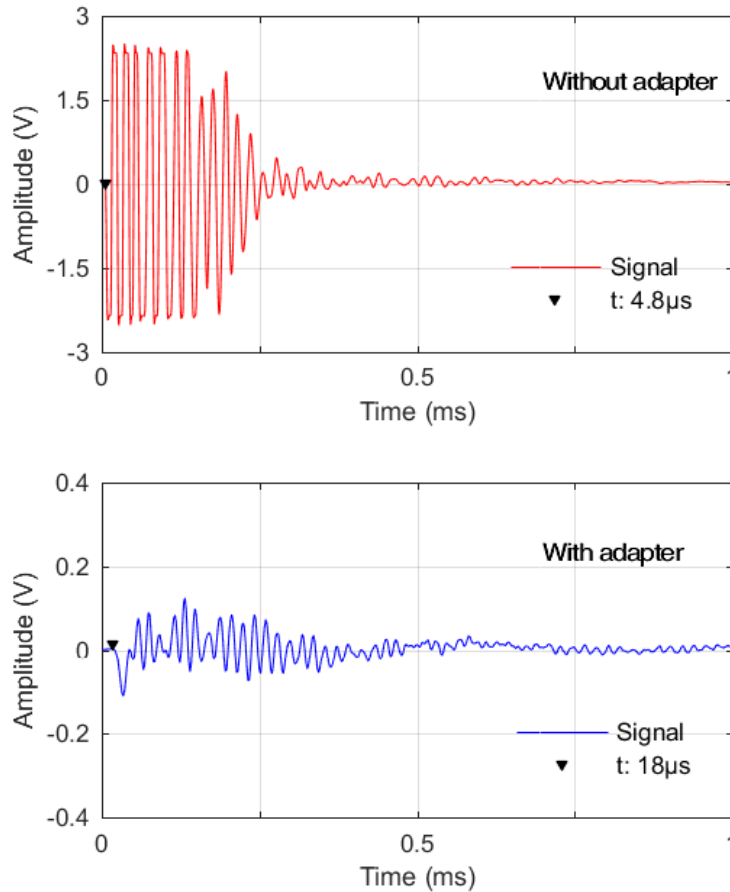


Figure 3.8. Time delay introduced by the probes design.

One can see the amplitude was significantly lower when the adapters were used. This was caused by the coupling. Indeed, the contact area between two adapters was significantly lower because of their convex shapes, whereas the flat face of the transducers enable better coupling. Since, the adapters fit the shape of the boreholes this loss of amplitude related to the contact surface

was lower during the operation in situ. Moreover, the field measurements were made with a gain (1024) that enabled measuring the signals with amplitudes large enough to be interpreted.

3.3 Acoustic characterization of 5” diameter water-saturated cores

The laboratory approach focused on six cores extracted from the emission borehole (cf. GAS gallery, LSBB). The aim was to characterize these fractured porous or non-porous cores in saturated conditions using ultrasounds. The cores were quite large (\varnothing : 12.5cm). Moreover, some of them were one meter long. Thanks to their dimensions, these cores gave us the opportunity for characterizing both the matrix and the fractures at an unusually large laboratory scale.

3.3.1 Overview of the semi-automatized acquisition system

The experimental set-up is quite straightforward, the core to be characterized was placed into an acoustic tank filled with tap water. Two transducers were mounted face to face onto a U-shaped holder, so that they could rotate around the core. The holder was itself mounted onto an automated positioning system, and the transducers were connected to the acquisition system (**Figure 3.9**). The tank dimensions were $2 \times 1.5 \times 1.5$ m, that's to say a maximum capacity of 4.5m^3 , but we used about 3 m^3 of water during the experiment. The automated positioning system enabled tridimensional XYZ translations and rotations around the Z axis. The APS named RHONAX-CA16I was designed for industrial applications requiring accurate 2D or 3D movements. The motors step accuracy was 0.01 mm in translation and 0.009 degrees in rotation.

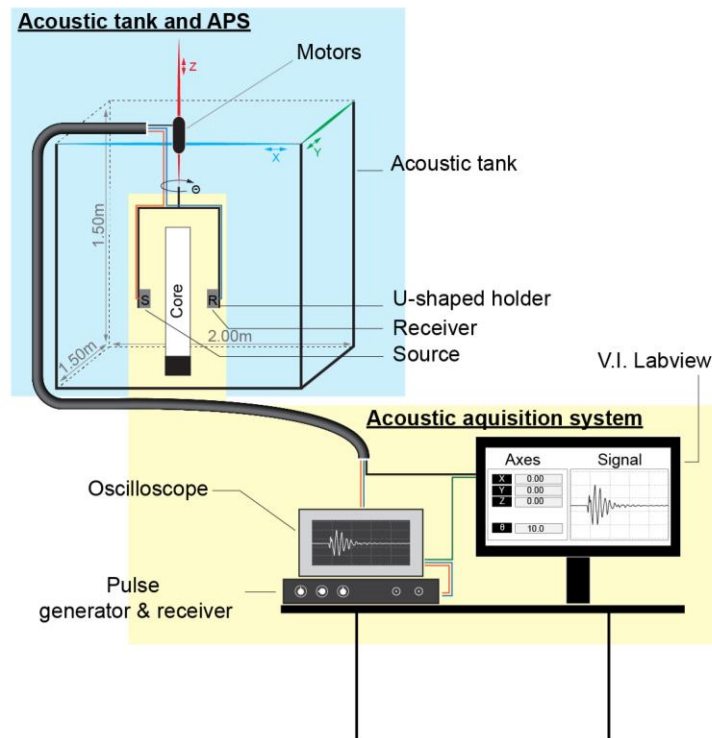
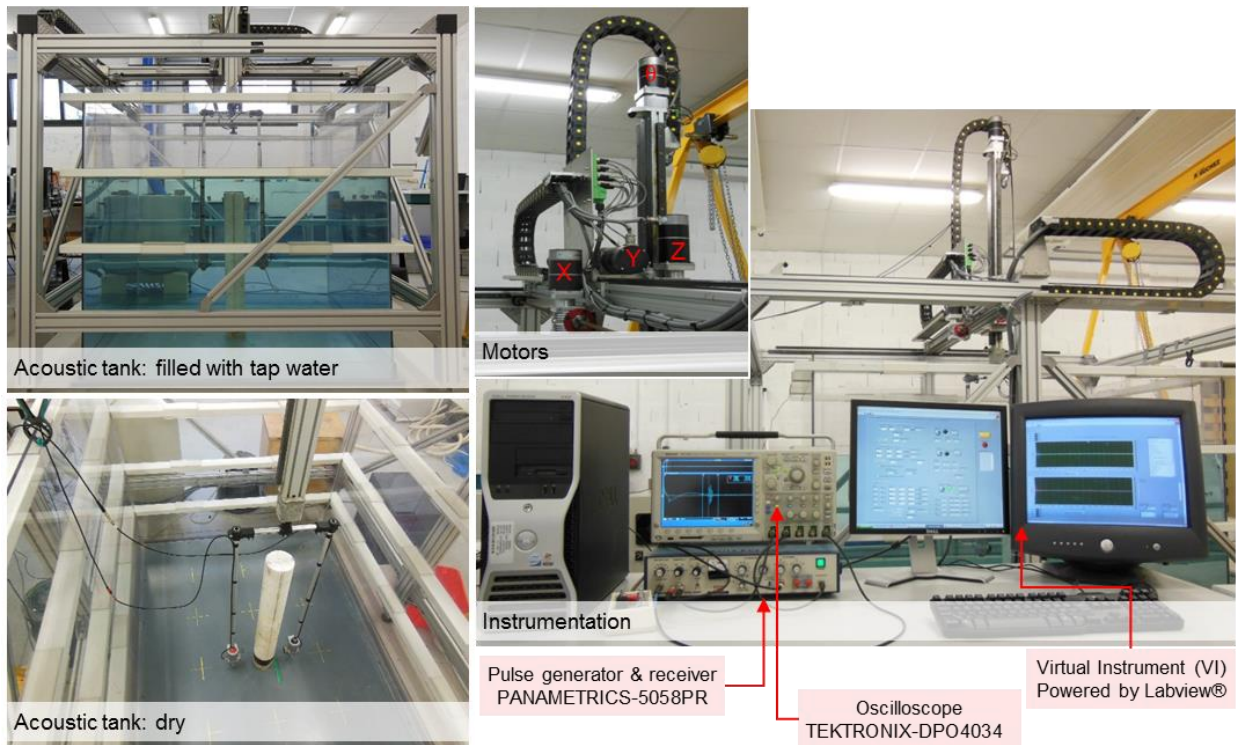


Figure 3.9. Photographs and schematic view of the laboratory experimental set. [Core-scale] In details, the experimental set-up can be divided in two main parts: the acoustic tank with the automated positioning system (APS) and the acoustic acquisition system (AAS).

The acoustic acquisition system itself was composed of three elements: (1) a pair of immersion transducers manufactured by IMASONIC with a nominal frequency of 250 kHz; (2) the integrated pulse generator and receiver, PANAMETRICS-5058PR; and (3) the oscilloscope, TEKTRONIX-DPO4034, which sampled the signals at 2.5MHz. The AAS and the APS were both controlled by PC using a Virtual Instrument powered by LabVIEW (**Figure 3.9**).

The cores were selected according to different criteria such as shape, integrity, length, and geological interest. We preferred cores with regular cylindrical shapes to avoid complex geometrical considerations in the analyses. Also, the cores with large fractures which may have completely attenuated the signal were not considered. The lengths of the selected cores ranged from 15 cm to 80 cm. After selection, the bottom of the cores were cut, which enabled them to “stand” vertically. Finally, they were saturated in a vacuum chamber two weeks prior to the experiments, then flooded in the acoustic tank.

3.3.2 Acquisition workflow

The U-shaped holder which completed the APS was designed to enable transmission mode (i.e. transducers placed face to face) ultrasonic measurements throughout the samples. The emitter-receiver distance was 26.5 cm. According to the manufacturer, the focal distance was 7 cm for a beam width of 10.26 mm. Therefore, we designed the acquisition protocol accordingly, and the sampling grid was calculated to allow a 50% of overlap between two neighboring measurements.

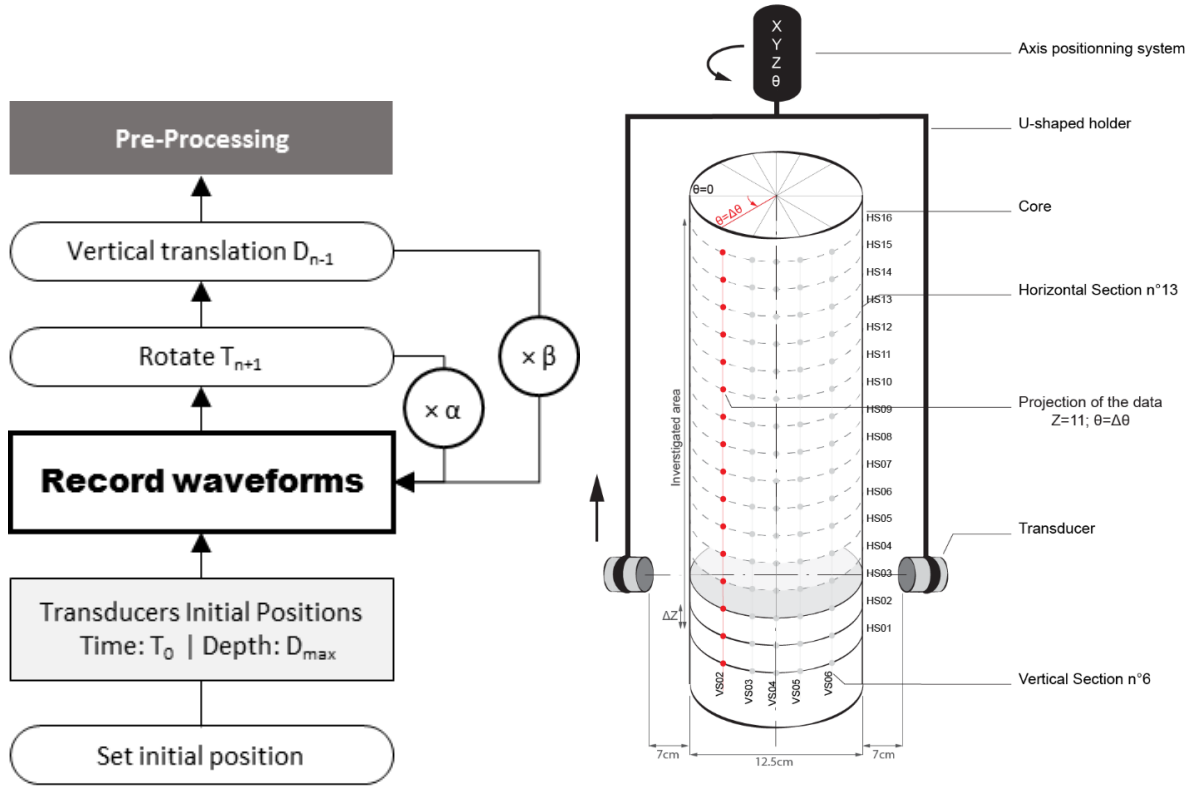


Figure 3.10. Simplified flow chart and schematic view of the acquisition in the acoustic tank. “ α ” depended on the rotation step which can be either 5° ($\alpha=72$) or 10° ($\alpha=36$). “ β ” is the height of the sample.

During the acquisition the transducers rotated around the core (**Figure 3.10**), the rotation step ($\Delta\theta$), was either 5° or 10° , so that for a given depth (i.e. horizontal section), 36 or 72 waveforms were recorded. After each horizontal section the transducers were moved 1 cm up ($\Delta Z=1$ cm) and the process was repeated. Each waveform was stacked sixty four times to improve the signal/noise ratio. Then the signals were corrected from both time delay, and DC offset.

3.3.3 Calibration

3.3.3.1 Source signal and recorded signal

In theory, the source signal created by the PANAMETRICS-5058PR, was intended to be a Dirac function, i.e. a signal with finite energy, duration equal to zero, and where each frequencies

are included with an equal intensity. In practice, the signal generated included a main pulse, that last less than 10 ns (after the manufacturer), and a coda, which was the response of generator going back to its initial state. So the signal generated with the coda, gave a pulse signal with a duration of $30\mu\text{s}$ (**Figure 3.12**). Nevertheless, the frequency content of the recorded signal, i.e. after the source signal passed through the acquisition chain was conditioned by the transducers. The bandwidth of the recorded signal ranged from 220 to 500 kHz, and the central frequency was ~ 320 kHz (**Figure 3.11**).

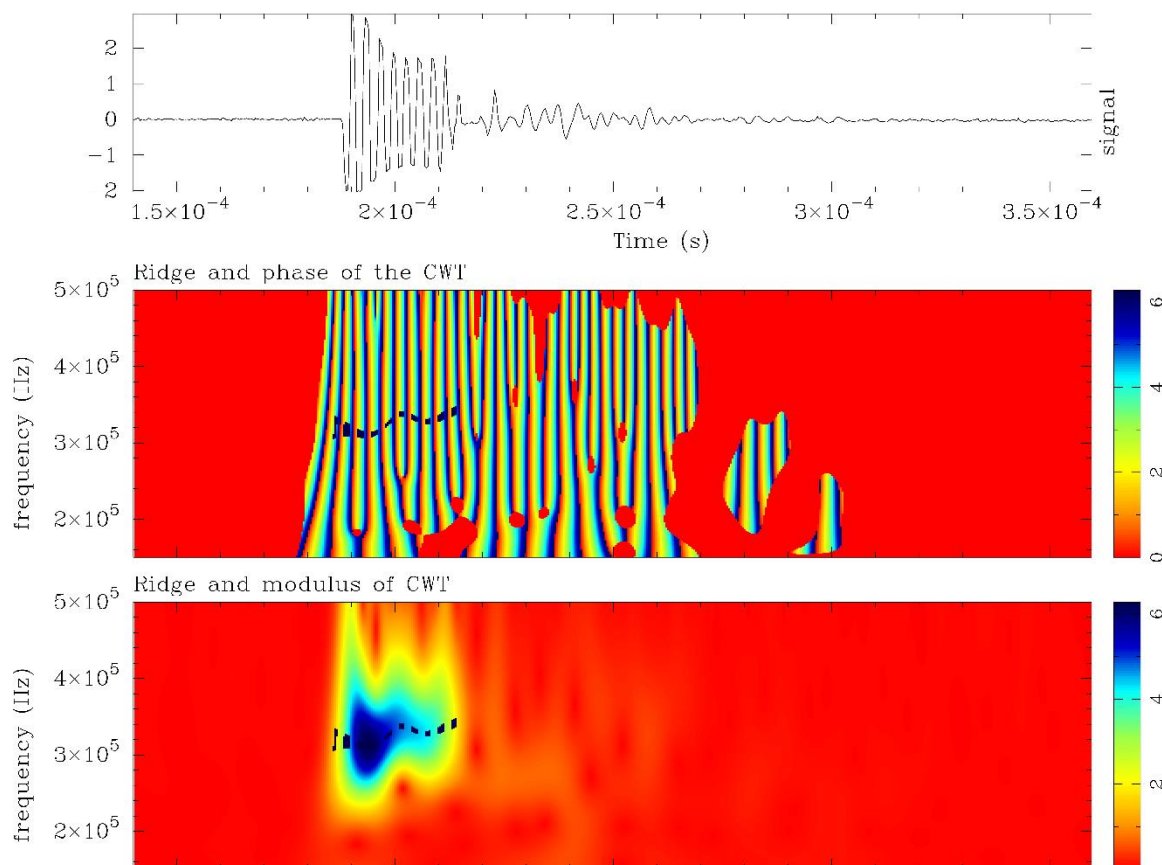


Figure 3.11. Results of a wavelet transform onto a recorded signal.

Phase and modulus of the wavelet transform (using Morlet wavelets) of the recorded signal, with the laboratory acoustic acquisition system, through water at 20°C , and with an emitter-receiver distance of 26.5cm.

3.3.3.2 Instrumental delay

The delay introduced by the apparatus was measured at atmospheric pressure, and with water temperature of 20°C. A signal was recorded and the measured travel-time was compared to the theoretical value (**Figure 3.12**). Indeed, given the experimental conditions the P-wave velocity should be 1480 m/s (Smith and Lawson 1954), corresponding to a travel-time of 179.1 μs between the 26.5-centimeter spaced transducers. Nevertheless, the value measured was 187.6 μs , giving an instrumental delay of about 8.5 μs .

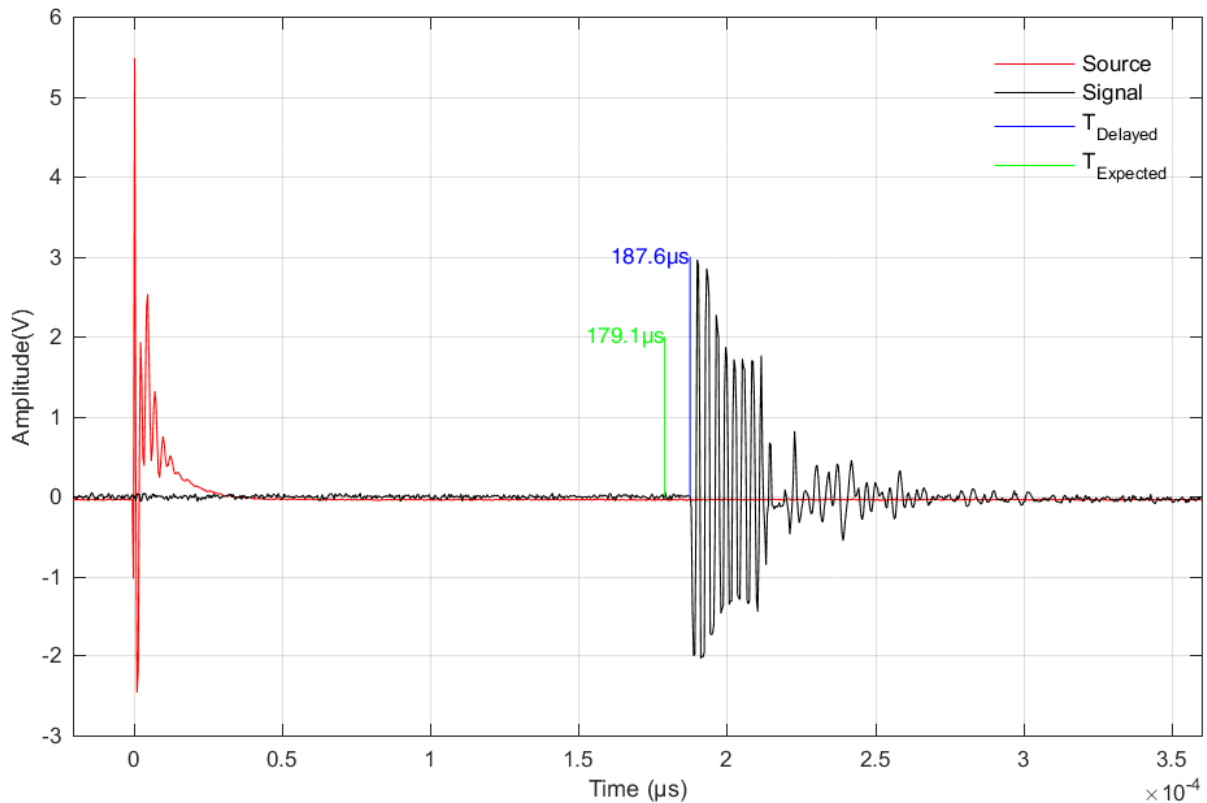


Figure 3.12. Source signal compared to the recorded signal in water at 20°C.

3.4 Other methods used in this work

The works presented in this PhD required using several characterization methods other than acoustics. The multi-disciplinary and multi-scale approach proposed here, mixed both geology and geophysics, and relied on several principle, instrumentation, and methodology, that won't be detailed even if their outputs will be presented and discussed in the manuscript. However, a short list of the methods is given below.

- **Petrographic analyses** using blue-stained thin sections that enabled bioclasts and pores recognition with optical microscope.
- **Scanning Electron Microscope (SEM)** used for characterization of intercrystalline porosity ($<5\mu\text{m}$) located between calcite micro-crystals (micrite).
- **X-ray Computed-Tomography (CT scan)** has been carried out to produce cross-sectional tomographic images, i.e. "virtual slices" of specific areas of the cores.
- **Photogrammetry** was used to produce high resolution models and real-color images of the cores surface.
- **Helium porosity** using dried 1" mini-cores, enabled porosity measurements.

Section 4: Field scale investigation of a carbonate series assuming seismic isotropy

4.1 Abstract

Physical properties of carbonate rocks cannot be fully captured from laboratory-sized samples. Heterogeneous facies distribution and diagenetic transformations lead to significant variations in petrophysical properties within a few meters. Seismic profiles and wells log data are routinely used to characterize petrophysical properties of carbonate reservoirs. However, these methods are less effective below the standard seismic detection limit (≈ 20 m) or in formations with low impedance contrasts. Sonic logs and plug scale velocity measurements are often used to calibrate empirical velocity-porosity transforms used to estimate the porosity at the reservoir scale from seismic data. The basic assumption made during this process is that the plug scale elastic properties are representative of the reservoir scale properties. This assumption is often violated in carbonates. Indeed, their heterogeneity may require multi-decimeter or multi-meter scaled samples to have a representative volume of rock. In these cases, the relevant scale to characterize their elastic properties may lie within the scale gap between laboratory measurements and field scale seismic data. Here we show a crosshole acoustic-survey that has been carried out using ultrasonic frequencies (50 kHz), with a vertical-resolution of 10 cm. The results are compared to plug-scale laboratory measurements (1 MHz and 500 kHz, for the P- and S-wave velocity respectively). The crosshole ultrasonic survey allows estimating the elastic properties of both intact matrix and fractured-matrix. The average P-wave velocities are of the same order as those obtained from plug-

scale measurements, highlighting that the average velocity is dominated by the intact matrix signature. The velocity variation around the average P-wave velocity which is most likely related to fractures.

4.2 Introduction

Seismic imaging is fundamental to the characterization of subsurface structures in 3D. Since the beginning, this technology has constantly improved in terms of acquisition and processing e.g., resolution, correlation with rock properties. However, reliable correlation of acoustic wave velocity with petrophysical parameters such as porosity or density are essential to calculate the impedance models used for synthetic seismic and for the identification of seismic reflectors (Gardner et al. 1974; Christensen and Szymanski 1991; Stafleu et al. 1994; Anselmetti, Salis, et al. 1997; Eberli et al. 2001; Zampetti et al. 2005; Verwer et al. 2008). It is also required for inversion of reservoir properties using seismic data (Huuse and Feary 2005; Xu and Payne 2009).

Unlike siliciclastic rocks, which have been subject to extensive studies to understand their acoustic properties, carbonate rocks have been less studied (Christensen and Szymanski 1991; Knight and Dvorkin 1992; Vernik and Nur 1992; Dvorkin and Nur 1996; Galmudi et al. 1999; Storvoll and Bjørlykke 2004). Indeed, the unstable nature of carbonate minerals makes interpreting their properties difficult. The reason is that the carbonate rocks properties may be significantly modified multiple times during the rock diagenetic history and in very complex different ways, since exposure to meteoric fluids can cause dissolution; whereas marine or subsurface fluid can cause cementation (Eberli et al. 2003; Vandeginste et al. 2013).

During the past decades, significant efforts have been made to bridge knowledge gap between siliciclastic and carbonate rocks. Major rules have been evidenced since pioneering works (Kisslinger 1950; Wyllie et al. 1956; Gardner et al. 1974; Rafavich et al. 1984). It was

demonstrated that the main parameters controlling carbonate-rocks acoustic properties are the porous network attributes (e.g., pores types and shapes), the diagenetic properties (e.g., cementation, dissolution and recrystallization). Finally the impact of mineralogy (in the case of pure carbonates) is commonly coupled with that of pore types, since mineralogy changes correlate with modification of the pores network (Rafavich et al. 1984; Anselmetti and Eberli 1993, 2001; Stafleu et al. 1994; Z. Wang 1997, 2001; Kenter, Fouke, et al. 1997; Kenter, Podladchikov, et al. 1997; Kenter et al. 2002; Assefa et al. 2003; Baechle et al. 2008; Verwer et al. 2008).

However, the studies cited above have been carried out on centimeter-sized samples (<5 cm) at laboratory scale, mainly because of size limits of the laboratory instruments. Despite these methods gave satisfactory results, their limitations can be discussed. The first and the main limitation is the representativeness of the samples. Indeed, these studies commonly assume that the laboratory-sized sample is a representative elementary volume of the studied formation, and is isotropic. These basic assumptions may be true if the formation is not fractured, and relatively homogeneous, but this is rarely the case in natural formations. Moreover, the sample collection is systematically biased depending on the study they are intended to (e.g., preference is given to non-fractured samples when it comes to carry out ultrasonic measurements, etc.).

Few attempts have been made to understand how rock properties measured at laboratory scale vary with the increasing roc volume, principally because of technical-limitations e.g., (C. Matonti et al. 2015).

In this section, we present acoustic velocity measurements between two boreholes (crosshole). We compare our field-scale velocities to laboratory-scale measurements to discuss the limitations of upscaling laboratory-measured values to describe reservoir-scale properties. We also discuss the impact of non-consideration of potential anisotropy onto the final interpretation of the data.

4.3 Geological context

4.3.1 The Urgonian platform in Rustrel area

The study area is located at the southern limit of the Monts de Vaucluse massif 80 km north of Marseille (SE France) in Rustrel. A former military underground facility converted into a scientific laboratory gives an access to the non-saturated and unaltered part of a lower Cretaceous carbonate reservoir. The Low Noise Underground Laboratory (LSBB) presents major interests regarding characterization of carbonate reservoirs in subsurface conditions. Thanks to the GAS gallery (**Figure 4.1**), the reservoir units are accessible from 250 to 500 m underneath the surface topography. More documentation about the LSBB facility is available at <http://www.lsbb.eu/>.

The Provence platform developed on the southern margin of the Vocontian Basin, which represents the western extent of the Alpine basin. Lower Cretaceous sedimentary deposits in Provence mainly consist in carbonates sediments with ages ranging from Berriasian to Aptian (Jean-Pierre Masse 1993; Leonide et al. 2012). From late Hauterivian to early Aptian the platform was the scene of prograding northward shallow-water carbonate environments. Deposits from this period formed the so-called Urgonian platform or formation. The maximum extension of the Urgonian platform occurred during late Barremian to early Aptian and is materialized by one kilometer thick deposits of a shallowing upward sequence, characterized by Barremian hemipelagic facies being gradually replaced by shallow-water bioclastic and rudists limestones. The Urgonian limestones of the Monts de Vaucluse region have been divided in three lithostratigraphic units named U1, U2 and U3, detailed descriptions of these units are available (Jean-Pierre Masse 1976; Leonide et al. 2012).

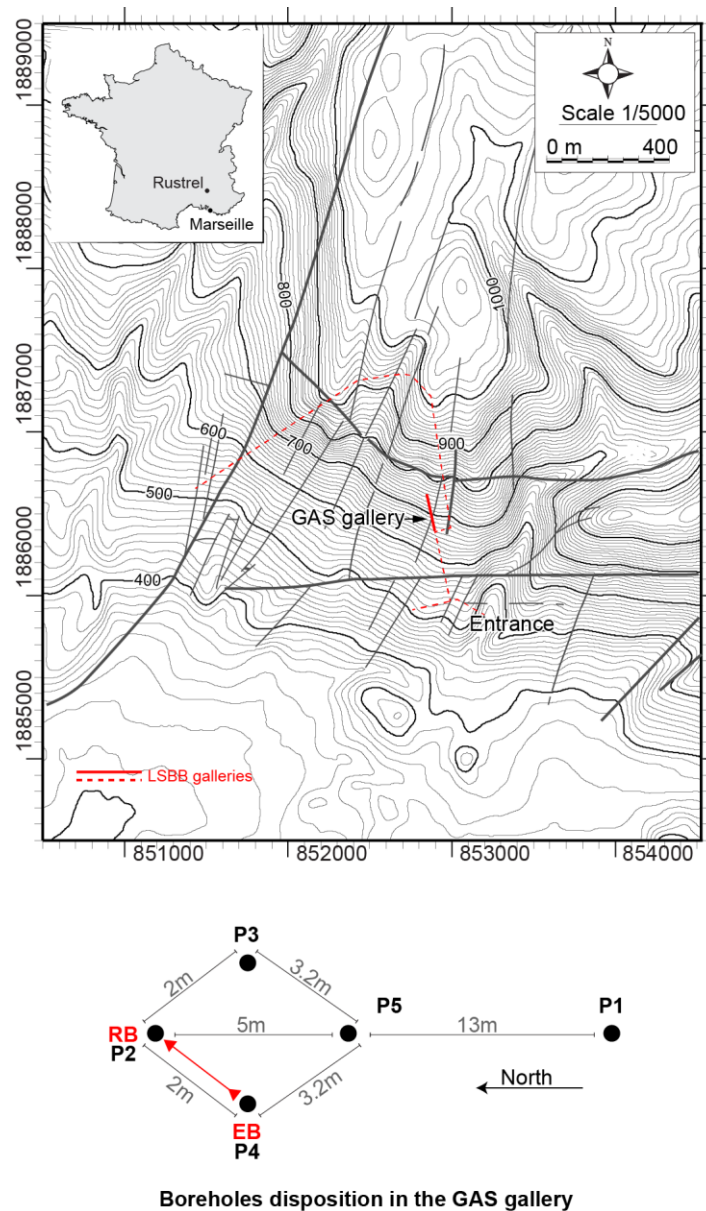


Figure 4.1. Localization GAS-gallery in the LSBB, and disposition of the boreholes.

The U2 member where is located our study site, is characterized by the dominance of rudists-rich limestones and consists of massive beds of “chalky” or “tight” limestones with textures ranging from mudstone to grainstone with a wide range of granulometries typically varying from mud to gravel. In the southeastern part of the Monts de Vaucluse (e.g., Rustrel), biostratigraphic analyses revealed that Barremian–Aptian boundary was close to the U1-U2 boundary, whereas

carbon isotope stratigraphy indicates that the U2–U3 stratigraphic discontinuity corresponds to the Mid-Bedoulian event (Jean-Pierre Masse 1999; Jean-Pierre Masse and Fenerci-Masse 2011; Leonide et al. 2012).

From a structural point of view the studied area is located north of the Cavaillon syncline. This fold affecting the Mesozoic deposits, is oriented E-W and is filled with Oligocene to Miocene formations presenting angular unconformity with the previous formations. The fold flanks are composed of lower Cretaceous carbonates. The northern part of the fold, is a fractured monocline trending N080° and dipping 10°-20° to the South (Jeanne et al. 2013). The Urgonian facies formation is affected by two fractures families: N030 and N120. Two fault sets affect the strata: N120°-trending and 75°N-dipping normal faults and N030°-trending and 85°E-dipping strike-slip faults. The first set is characterized by kilometer size faults whereas the second set is characterized by decameter to hectometer thick faults (Jeanne et al. 2013). Detailed tectonic and structural context about the region is available for review (Lamarche et al. 2012).

4.3.2 Geology of the study site

Five vertical fully-cored boreholes (~21 m deep) named P1 to P5 were drilled in the GAS gallery as part of previous studies (e.g., (Jeanne, Guglielmi, and Cappa 2012), **Figure 4.1**). P2, P5, and P1 are aligned over a distance of 13 m, the P3 and P4 are placed on either side of the P2-P5-P1 axis so that P3–P4 axis is perpendicular to the latter. The boreholes implantation enables to characterize the fracture-networks. P2-P5-P1 axis is oriented N0, which is the same as the stratigraphic dip direction (~30° southward). P1 is the close to a fault zone which is located 5 m apart southward. This fault oriented N30 is associated to the N30 and N120 fractures network. The fractures density is maximum at P1, and decreases towards P2. The intersected formations can be divided in three mechanical units, two are characterized by dense fractures networks (at depths of

0 - 6 m and 14 – 21 m in P2) and one is moderately-to-un fractured (depths of 6 – 14 m in P2). The fractures density is controlled by both porosity and the fault zone nearness (Jeanne, Guglielmi, and Cappa 2012).

The layers intersected by the wells mainly are bioclastic limestones and correspond to inner platform facies i.e. low to moderate energy, muddy or peloidal calcarenites with abundant rudists (Leonide et al. 2012). Cores analysis allowed distinguishing two main facies groups, respectively a grain dominated facies (grained-facies) and a mud dominated facies (muddy-facies). The grained-facies are calcarenites with textures ranging from packestone to grainstone, and large rudists and/or rudists-shell fragments. The bioclasts are dominated by mollusks and miliolids whereas dasyclads, corals and orbitolinids are scarce. Muddy-facies are calcilutites with textures ranging from wackestone to packestone, they contain large miliolids and peloids, orbitolinids can be abundant. At the regional scale, (Léonide et al. 2014) proposed five major carbonate rock types based on depositional facies, diagenetic features, dominant pore types and petrophysical properties.

Only two are of interest in our case: Tight inner platform (TIP) and Porous Inner Platform (PIP) facies. Bioclastic content of TIP facies are the same as described above for muddy-facies. These facies are characterized by the lack of fabric-selective pores (Choquette and Pray 1970), and their porosity range from 0 to 3%. In most cases, this porosity is related to cracks. Some grained-facies may also be classified as TIP, e.g. grainstones that underwent early marine or meteoric diagenesis. The PIP's have the same characteristics as described for grained-facies, the main difference with TIPs being the wide 5 to 25% porosity range recorded in PIP facies. Unlike TIPs, micritic grains in PIPs are porous while intergranular pore-space is partially occluded. In PIPs, the intercrystalline pores (i.e., microporosity within micritic grains) dominates, and moldic pores are frequent. Non-

fabric selective porosity may also occur corresponding to about 2% of the total porosity (Léonide et al. 2014).

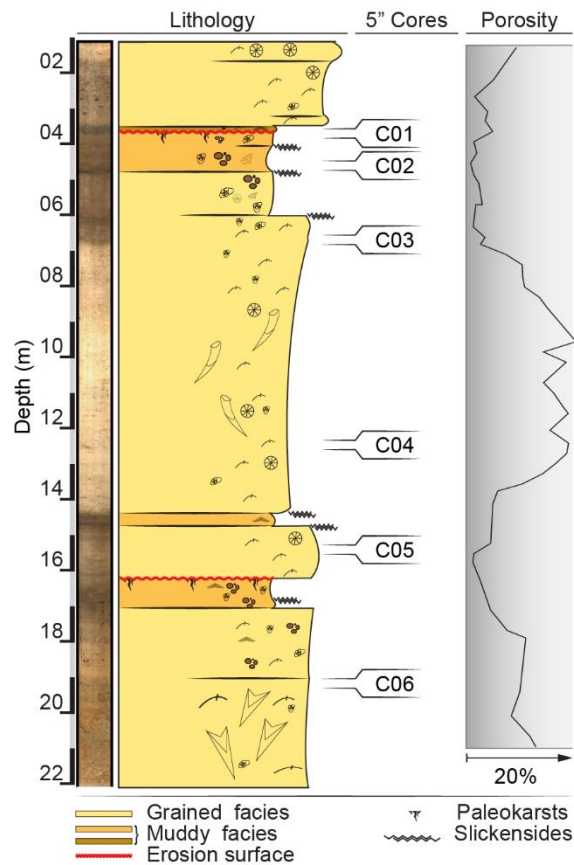


Figure 4.2. Synthetic lithology and porosity logs of studied formations.

Reservoir properties (porosity and permeability) of these formations are more likely related to diagenesis rather than to the environment-of-deposit facies considering the complex diagenetic history of the Urganian platform, characterized by marine and non-marine phases. The composition and distribution of the porous network together with diagenesis over Cretaceous carbonate platforms from SE France have been documented and discussed by many authors (Moss and Tucker 1995; Fournier and Borgomano 2009; Fournier et al. 2011, 2014; Borgomano et al. 2013; Léonide et al. 2014). The latter reported common features for porous formations, i.e. porous

network dominated by secondary porosity, mainly due to dissolution affecting both micritic grains and micritic cements, while moldic and vuggy pores are present in minor proportion. Primary porosity such as inter or intragranular pores exists but has a negligible contribution to the overall porosity. Particular attention was thus paid to grain and matrix micrite microfabrics, i.e. micrite crystals morphology and contacts (**Figure 4.3**). In our case four microfabrics noted from MF1 to MF4 are commonly reported in literature respectively (Fournier et al. 2011; Léonide et al. 2014):

- MF1: subhedral mosaic micrite
- MF2: serrate subhedral/euhedral micrite;
- MF3: punctate to serrate subhedral/euhedral micrite
- MF4: punctate, loosely packed and locally coalescent subrounded micrite

(Léonide et al. 2014) proposed diagenetic chart emphasizing different stages in the diagenetic history of the Urgonian platform that lead to the development or the occlusion of the initial intercrystalline microporous network. A five-staged diagenetic sequence was established. The first stage took place in marine and/or meteoric environment and consisted in early diagenetic processes such as grains micritization, recrystallization and precipitation of early cements in the pore space. Marine and/or meteoric early cements showed the same isotopic (carbon and oxygen isotopes) values as TIPs microfabric MF1, allowing the authors to postulate that early marine and/or meteoric cements precipitated within TIPs intercrystalline microporous network while inter and intragranular pore space of TIPs were also entirely sealed by marine and/or meteoric cements. After that, diagenetic evolution of TIPs was almost completed. Only deeper burial and telogenetic features such as stylolites, fractures and karstification altered these rocks in later stages.

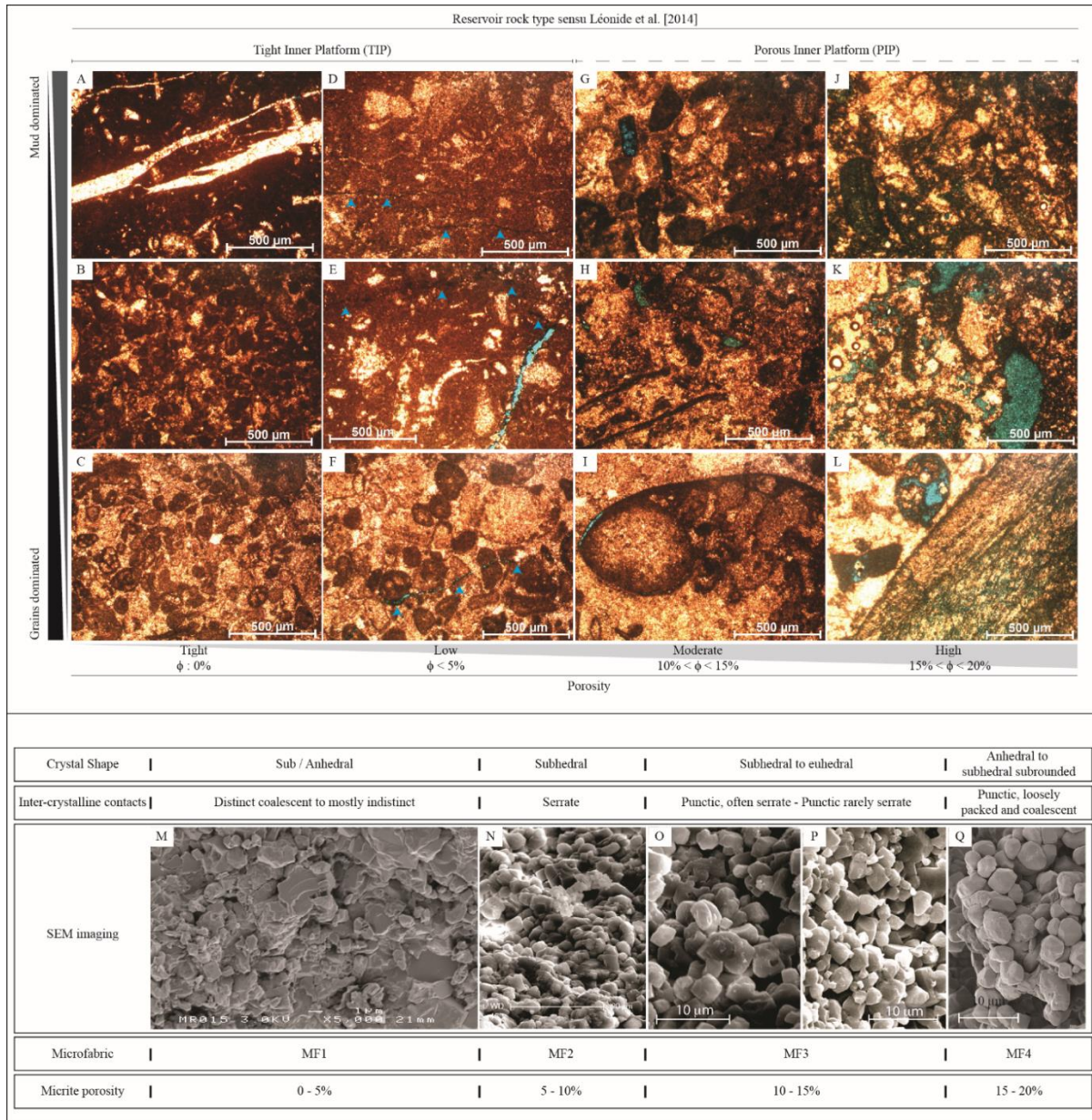


Figure 4.3. Microscopic images of studied facies.

Upper part (a)-to-(l) stained thin sections analyzed with optical microscope; Bottom part (m)-to-(q) a synthetic table of relationships between micrite crystals morphology, contacts and porosity. (a) Sealed fractures in tight peloidal wackestone; (b) Tight bioclastic packstone; (c) Tight miliolids rich grainstone, (d) Tight peloidal wackestone with open micro-cracks (pointed out by blue arrows); (e) Tight peloidal wackestone with micro-karstified stylolithes (see blue arrows); (f) Tight bioclastic grainstone with open crack; (g), (h) and (i) Moderately porous bioclastic packstone to grainstone with porosity located in partially dissolved micritic grains and some of the micritic cements; (j), (k) and (l) Porous bioclastic packstone to grainstone with porosity located in micritic grains and other entirely dissolved grains, but mainly in the micritic cements. (m), (n), (o), (p) and (q) are SEM images of the micrite microfabrics modified from Léonide et al. (2014).

Unlike TIPs, early diagenesis phase of PIPs did not lead to complete occlusion of the intergranular pore space, allowing by the way further diagenetic processes. PIPs went through the second stage of the diagenetic sequence proposed by the authors, and which was associated to a meteoric environment that was evidenced by negative isotopic values. During this meteoric / shallow burial episode, grains microfabrics experienced recrystallization that enhanced their porosity. MF2 and MF3 in PIPs are representative of such diagenetic processes. Further cementation took place during this phase occluding some more of the intergranular pore space. Diagenesis under burial environment was the third stage of the diagenetic sequence. Pores water presented almost the same isotopic characteristics than marine water, and cements precipitated to almost fulfill the intergranular pore space, only a few residual intergranular porosity remained whereas microporosity was preserved. Porous units such as PIPs show no evidence of mechanical compaction at all (e.g. grain breakage or plastic deformation, stylolithes), whereas tight units such as TIPs display stylolithes but no grain deformation either. The authors interpreted the lack of grain deformation as an evidence that cementation and recrystallization events took place in a shallow burial environment prior to stylolithes development in a burial environment. In a later phase circulation of telogenetic meteoric fluids within PIPs probably enhanced the intercrystalline microporosity of the grains by further dissolution or leaching processes leading to microfabric MF4.

4.4 Material and method

4.4.1 Plug-scale velocity measurements

For this experiment, we used a set of plugs ($\varnothing=2.54$ cm, $L=5.08$ cm) extracted from the Reception-Borehole (P2, **Figure 4.1**). The spacing between two plugs along the borehole was approximately 50 cm. The plugs were first oven-dried, then stored at room conditions during

several days. The acquisition set-up included a pulse generator OLYMPUS-5072PR, an oscilloscope TEKTRONIX-DS05014A, and two pairs of contact-transducers PANAMETRICS (**Figure 4.4**). The P- and S-wave contact-transducers have central frequency of 1 MHz and 500 kHz, respectively. Good surface contact was ensured by using a coupling gel, and by applying surface contact force using a vise.

Finally, the travel times were pointed onto the oscilloscope screen, then the P- or S-wave velocity was computed using the relation $v = L/t$, where L and t are the plug's length and the travel-time, respectively.

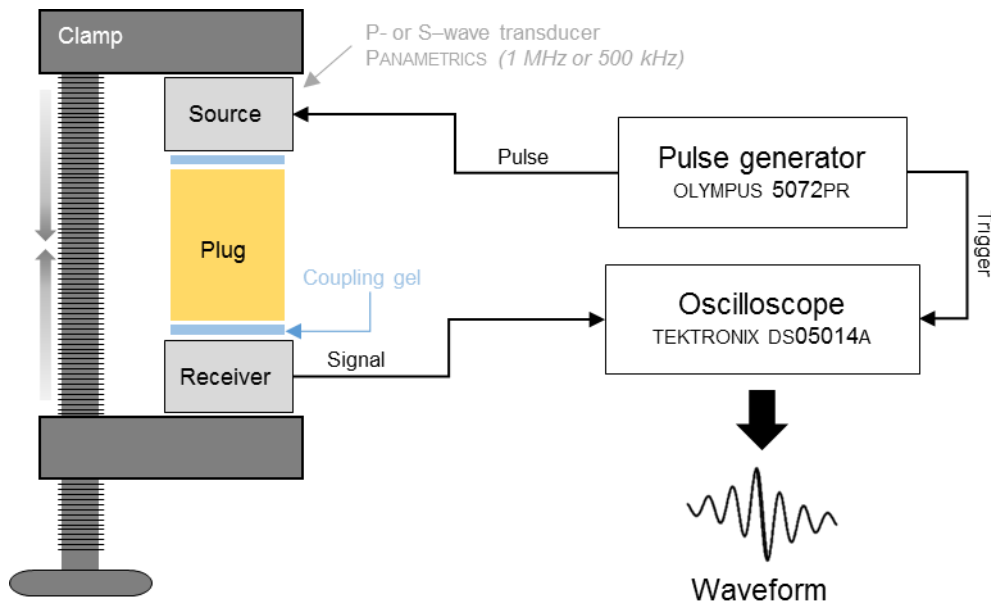


Figure 4.4. Schematic view of the experimental set-up. [Plug-scale measurements]

4.4.2 Field-scale velocity measurements

The acoustic logging has been carried out between P4 (Emission Borehole), and P2 (Reception Borehole) located two meters apart, along azimuth N20° (**Figure 4.1**). They are both ~22m deep. The study was conducted from 1 to 14.5 m depth, consequently, the size of the investigated area is 2×13.5 m. The receiver probe which contains sixteen receivers lined up and spaced of 10 cm

from each other (**Figure 4.5**), was placed in the P2. The reception probe which has only one emitter was placed in P4. For technical reasons, the acquisition was divided into nine sections. Each section is 1.5 m high (i.e. the length of the receivers array), and is delimited by the positions of the first and the last receiver of the reception-probe. The acquisition for a section starts with the emitter placed face to face with the bottom receiver. Sixteen full-waveforms acoustic signals are recorded per shot, in other words a Common Shot Gather (CSG) contains 16 traces. After each shot, the EP is moved 10cm up. After completion of a section the RP is moved 1.5m up. Consequently the next section overlaps the previous one (the position of the top receiver becomes the one of the bottom receiver in the next section). The limited number of receivers and the low offset reduced the angular range of the ray coverage. However, a maximum polar ray-coverage of 37° was obtained for common shot gather with sources located either at the top or bottom of the sections (i.e., 1st and last shot).

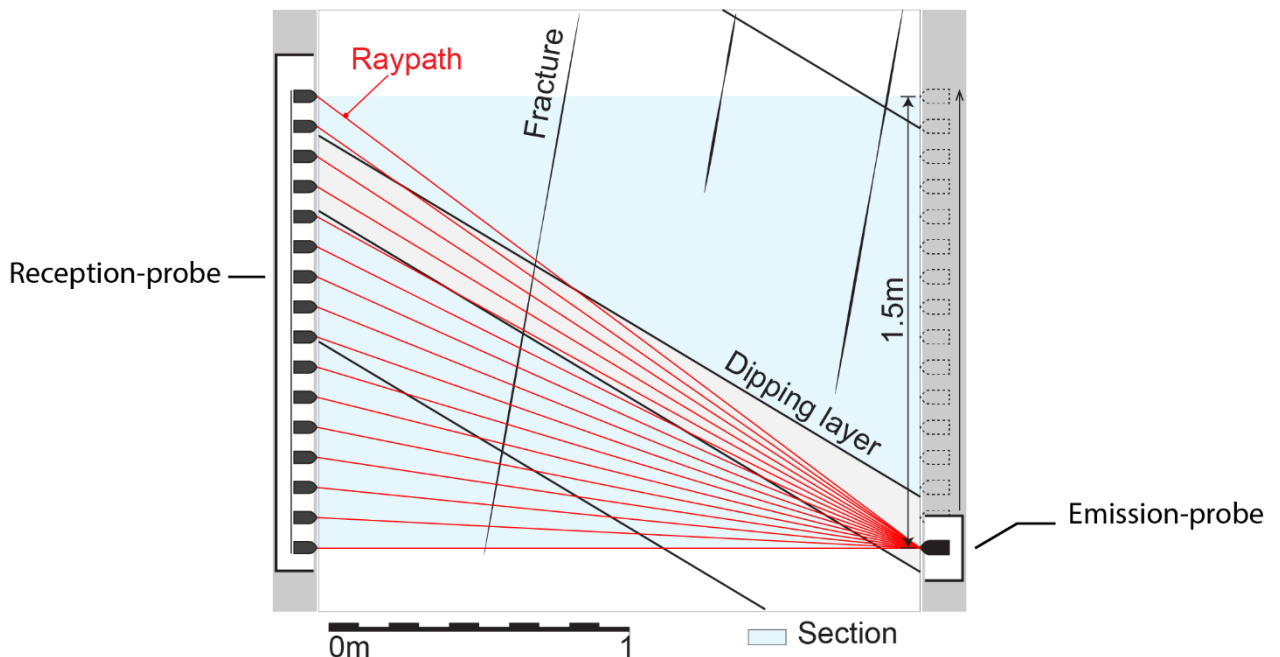


Figure 4.5. Schematic view of one section logging. [Field-scale measurements]

The waveforms were corrected from DC-offset i.e., the mean value was subtracted to the waveform, which is then centered at zero. DC-offset is due to the physical properties of the electronic components and causes the signal to no longer oscillate around zero. The DC offset correction does not alter the interpretation of the signal in the time domain but as the waveform where corrected individually, amplitude variations should not be interpreted in terms of absolute values but as relative values. Finally, we assumed that the wave propagate through a straight line between the emitter and the receiver, so that the length of the raypath can be derived from the sensors coordinates. The waveforms were processed individually using a standardized procedure (e.g., standardized axes unit, and dimension). The P-wave travel times were manually picked assuming they correspond to the onset of the P-wave. Finally the P-wave velocities were calculated as the ratio of the traveled distance over the travel-time.

4.4.3 Tomographic reconstruction using SIPPI

The P-wave travel-times were processed using SIPPI, in order to produce a tomographic image of the velocity field between the two boreholes. SIPPI is a Matlab toolbox designed to solve inverse problems using a probabilistic-approach (as opposed to deterministic-approach). In a probabilistic formulation the inverse problem can be seen as a way of combining information such as: a physical law, e.g. propagation of elastic-waves in a porous media; a set of observations, e.g. P-wave travel-times; and some prior expectations about the parameter, e.g. distribution of the P-wave velocities. The goal is to quantify the probability for different scenarios, to explain both the observations and the prior information. In principle, a successful probabilistic inversion will locate all solutions to the problem and assign a probability to each scenario according to the information provided. An extensive documentation about SIPPI and the probabilistic inverse problem theory, is documented in different papers e.g. (Knud S. Cordua et al. 2009; Looms et al. 2010; Hansen et al. 2012; Knud

Skou Cordua et al. 2012; Hansen, Cordua, et al. 2013; Hansen, Skou Cordua, et al. 2013; Hansen, Cordua, and Mosegaard 2014; Hansen, Cordua, Jacobsen, et al. 2014), and therein references.

In order to solve a probabilistic framed inverse problem with SIPPI, three elements must be provided: (1) a choice of an a priori model; (2) a choice of how to solve the forward problem; and (3) a choice of the noise model that describes the uncertainty of both the observed data and the modeling error.

We used the Fast Fourier Moving Average (FFTMA) a priori model (cf. Hansen et al., [2013a]), which enables to define a spatially correlated multivariate Gaussian a priori probability density function, based on the a priori mean and a covariance model. We set the a priori model with a spherical covariance model (range=8m; sill= σ^2). The mean and the variance (σ^2) were obtained from velocities calculated assuming straight-rays; while the range was deduced from the experimental variograms (cf. supporting information). We further constrained the model by also providing a target distribution that describes the a priori distribution, in our case, it was a bimodal distribution. Once the a priori model is set, the forward problem is the travel-time computation.

In order to solve the forward problem we opted for the eikonal equation, which is a high frequency approximation to the wave equation. It describes the arrival time along a closed curve $u(x)$, traveling with the speed defined by the velocity field $m(x)$.

$$|\nabla(u(x))| m(x) = 1 \quad (1)$$

This forward model is non-linear, and is often referred to as the high frequency ray approximation (Hansen, Skou Cordua, et al. 2013).

4.5 Results

4.5.1 Porosity-Velocity relationship at the plugs scale

Different petrophysical data including porosity and permeability have been carried out on the same plugs used for the P- and S-wave velocity measurements. According to the plugs data, the study site can be subdivided into four main porosity intervals (**Figure 4.6**). The first [0–6 m] has a low porosity (<5%) and P-wave velocity ranging from 5000 to 6250 m/s, and average S-wave velocity ~3000 m/s. The second [6–14 m] has the highest porosity (~15%) values, the lowest P- and S-wave velocity ranges 4500–3000 m/s and 2750–2000 m/s respectively. Then, the porosity drops again around 5% between [14–16.5 m] giving P- and S-wave velocity around ~5500 m/s and ~3000 m/s respectively. The fourth interval is also less porous (~9%) than the second one, the P-wave velocity is about 5000 m/s while it is 3000 m/s for the S-wave. This subdivision into porosity intervals was discussed before in the literature (Jeanne et al. 2012).

However, our dataset gives new insights of the poroelastic properties within the reservoir. We observe that the log of P-wave velocity shows more variability, for example the subdivision due to the four porosity intervals is smoother according to the S-wave log. The latter is bimodal, in our case i.e., only the most porous interval has a distinctive signature (3000→2000 m/s). This indicates that the shear modulus is relatively constant (or shows low variations) for porosity values below ~10%. Moreover, the porosity is linearly correlated to the density in our samples. Our empirical porosity–density relationship is close to the theoretical value for calcite i.e., $\rho_{\text{sample}} = -\rho_{\text{calcite}} \times \phi + \rho_{\text{calcite}}$ where $\rho_{\text{calcite}}=2700 \text{ kg/m}^3$ and ϕ is the porosity (**Table 4.2**). This good correlation ($r^2=0.99$) means that most of the pores are connected, considering the method used (gas porosimetry), and confirms that the rock is made of pure calcite.

We also plotted the P- and S- wave velocity against the porosity (**Figure 4.6**), we approximated the porosity-velocity and the Vp-Vs relationships using linear relations, and quadratic functions of the form of equation (2).

$$f(x) = ax^2 + bx + c \quad (2)$$

Despite the fact that the porosity-velocity is not linear in porous media, our linear fits describe our data with a relatively good accuracy. The coefficients of determination are ~ 0.8 for both the P- and S-wave velocity (**Table 4.2**). However better results are achieved using the quadratic relations, we obtained r^2 of 0.84 and 0.90 the P- and S-wave velocity respectively. The pseudo-linear relationships that we obtain in our samples, may be explained by the facies considered here. Indeed, the studied intervals are also bimodal in terms of petrographic properties. The matrix can be either porous, in that case the gradient of porosity is always related to the dominant pores type (microporosity); or low-porous with stylolites and cracks related porosity. Hence it is not surprising to have \sim bimodal acoustic response for these bimodal facies. Finally, we observe a good linear relationship ($r^2=0.95$) between our P- and S-wave velocity. Fournier et al. (2011) observed this linear trend and the porosity dependency of the Vp/Vs ratio in the Urganian Limestones.

All these elements show that at the plug scale the elastic properties are extremely dependent of the matrix porosity. In our monotonous facies we observe two poles of elastic properties. The first pole corresponds to the tight facies which have P- and S-wave velocity close to calcite minerals velocity (i.e., 6500 m/s for the P-wave, and 3400 m/s for the s/wave). The second pole corresponds to the porous facies, which have lower P- and S-wave velocity. Both poles are linked by a linear correlation caused by the porosity gradient existing between the facies.

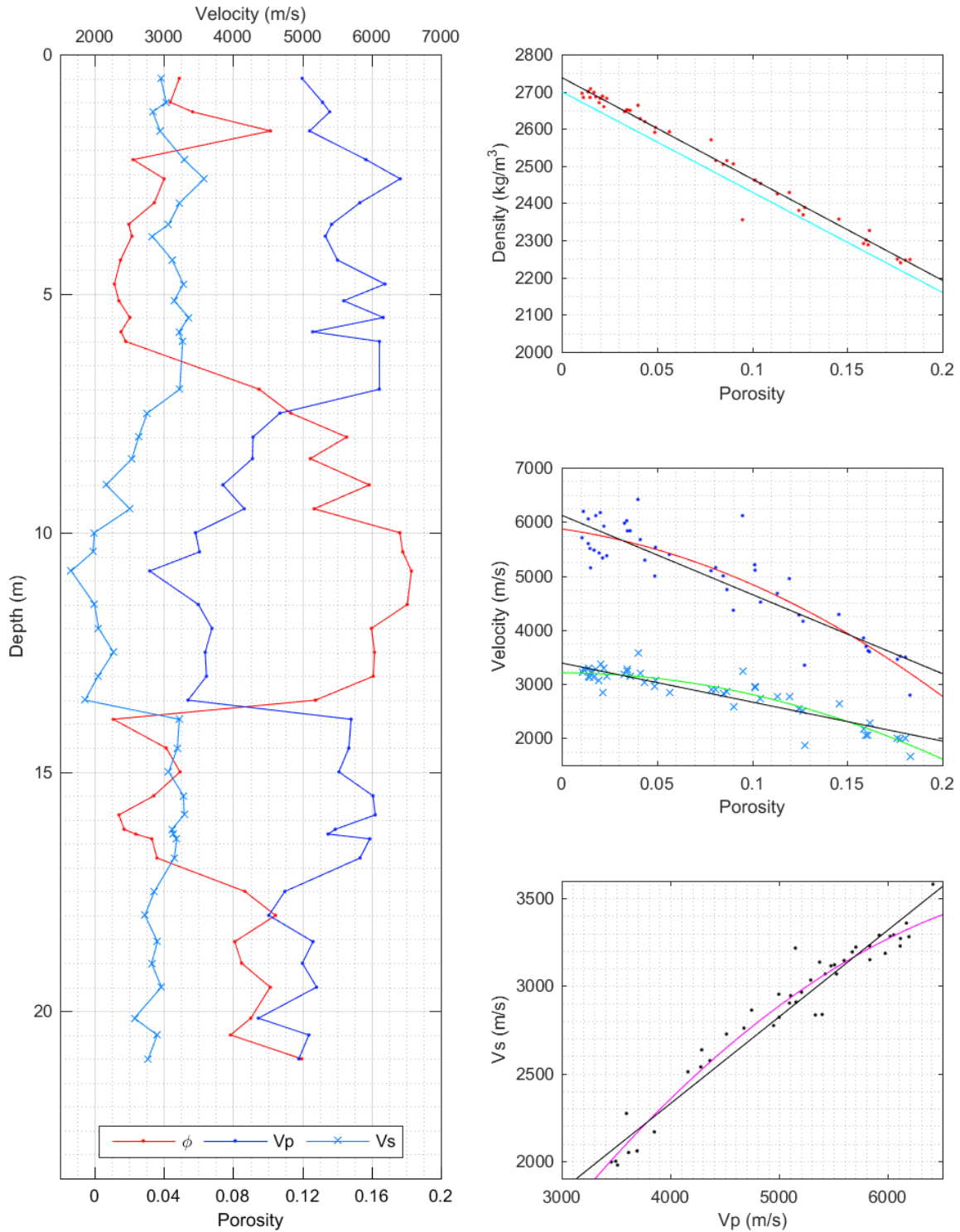


Figure 4.6. Poroelastic data measured on plugs. Note that on the right hand panel the porosity-velocity, and V_p - V_s relationships are approximated with 2nd order polynomials (colored lines), and linear fit (back line). The theoretical (linear) density-porosity relationship for calcite (cyan) is given for comparison with the empirical linear relation.

Table 4.1. Summary of the plugs petrophysical data.

n°	Depth (m)	L (mm)	Density (kg/m ³)	Porosity (%)	Perm. (mD)	Time P (μ s)	Time S (μ s)	Vp (m/s)	Vs (m/s)
1	0,50	50,4	2591	4,89	0,00	9,60	16,59	5253	3040
2	1,00	50,3	2619	4,37	0,00	9,02	16,10	5580	3126
3	1,20	50,5	2592	5,66	0,00	8,86	17,30	5698	2918
4	1,60	50,6	2462	10,16	0,05	9,42	16,70	5368	3028
5	2,20	50,6	2659	2,22	0,01	8,06	14,90	6280	3397
6	2,60	37,9	2355	4,01	0,00	5,42	10,10		3756
7	3,10	50,4	2651	3,45	0,00	8,14	15,10	6188	3336
8	3,55	50,3	2670	1,97	0,00	8,78	15,90	5731	3165
9	3,80	50,3	2688	2,15	0,00	8,94	17,26	5628	2915
10	4,30	50,4	2684	1,49	0,00	8,65	15,65	5825	3219
11	4,80	50,5	2684	1,14	0,00	7,66	14,90	6595	3390
12	5,15	50,4	2700	1,40	0,00	8,52	15,55	5917	3242
13	5,50	40,0	2682	2,03	0,00	5,98	11,40	6681	3504
14	5,80	46,9	2708	1,52	0,00	8,62	14,10	5443	3327
15	6,00	50,4	2686	1,79	0,00	7,74	14,90	6505	3379
16	7,00	50,3	2663	9,50	0,00	7,74	15,10	6503	3333
17	7,50	50,5	2425	11,33	0,22	10,30	17,80	4898	2834
18	8,00	50,5	2357	14,56	1,41	11,30	18,70	4472	2702
19	8,45	50,5	2381	12,46	0,84	11,30	19,40	4466	2601
20	9,00	50,4	2291	15,86	2,27	12,60	22,80	4003	2212
21	9,50	49,9	2369	12,68	0,82	11,50	19,40	4338	2571
22	10,00	50,4	2249	17,63	2,41	14,10	24,80	3577	2034
23	10,40	50,5	2240	17,80	3,54	13,90	25,10	3635	2013
24	10,80	50,8	2249	18,30	3,25	17,67	30,08	2873	1688
25	11,50	50,3	2247	18,06	2,82	13,90	24,70	3616	2035
26	12,00	50,6	2301	15,99	2,06	13,20	24,10	3831	2098
27	12,50	41,3	2326	16,17	2,12	11,00	17,70	3758	2335
28	13,00	47,7	2288	16,10	1,89	12,70	22,80	3755	2091
29	13,50	50,5	2389	12,76	0,69	14,60	26,69	3461	1893
30	13,90	50,4	2695	1,07	0,00	8,34	15,15	6041	3326
31	14,50	50,5	2627	4,13	0,00	8,40	15,30	6006	3297
32	15,00	41,1	2604	4,93	0,00	6,94	12,90	5920	3185
33	15,50	50,5	2651	3,42	0,00	7,90	14,90	6397	3391
34	15,90	50,3	2700	1,40	0,00	7,82	14,80	6434	3400
35	16,20	50,4	2698	1,70	0,00	8,71	15,69	5788	3213
36	16,30	50,4	2682	2,37	0,00	8,90	15,60	5667	3233
37	16,40	50,6	2646	3,30	0,00	7,98	15,40	6345	3288
38	16,80	50,4	2649	3,60	0,04	8,14	15,50	6190	3251
39	17,50	47,8	2514	8,68	0,00	9,57	16,20	4990	2948
40	18,00	50,2	2453	10,45	0,08	10,63	17,94	4722	2798
41	18,55	50,3	2515	8,09	0,07	9,26	16,80	5432	2994
42	19,00	50,5	2504	8,49	0,07	9,60	17,40	5259	2901
43	19,50	50,3	2462	10,14	0,10	9,18	16,50	5483	3051
44	20,15	50,6	2506	9,02	0,00	11,11	19,19	4557	2639
45	20,50	40,3	2570	7,85	0,04	7,42	13,40	5434	3009
46	21,00	50,5	2429	11,96	0,45	9,70	17,70	5201	2850

* Permeability and porosity adapted from Cochard et al., unpublished work

Table 4.2. Empirical poroelastic relationships

	$f(x)=ax^2+bx+c$			r^2	rmse
	a	b	c		
$V_p = f(\varphi)$	-5,227E+04	-5016	5867	0,84	382,1
	–	-14645	6121	0,82	399,0
$V_s = f(\varphi)$	-3,968E+04	-32	3207	0,90	156,4
	–	-7217	3389	0,84	189,6
$V_s = f(V_p)$	-7,394E-05	1	-1252	0,97	87,5
	–	0	344	0,95	111,0
$\rho = f(\varphi)$	–	-2727	2738	0,99	14,4

4.5.2 Crosshole velocity logging

P-wave velocity recorded during the crosshole experiment is consistent with values commonly reported for sonic wave propagation through carbonate rocks, the most part of our values range between 4000 and 6500 m/s. The acoustic P-wave velocity log shows varying trends with depth.

The curve can be divided into four parts (**Figure 4.7**):

- 1) From 1 to 7 m, over 86% of P-wave velocities range between 5500 and 6800 m/s, with a maximum dispersion amplitude of 4200 m/s. Despite the main trend (i.e. mean value $\approx 6250 \pm 250$ m/s), we note sub-trends in this interval corresponding to a high density of points with neighboring values $\Delta V_p < 100$ m/s (e.g., $z_1 \approx [1.5 - 2.5$ m] and $z_3 \approx [4.5 - 5.5$ m]), or conversely a higher dispersion $\Delta V_p > 100$ m/s (e.g., $z_2 \approx [2.5 - 4.0$ m], $z_4 \approx [7.0 - 8.5$ m]).
- 2) From 7 to 10 m, most of the values (85%) range between 4300 and 5300 m/s. This interval is characterized by a high dispersion of the values but with moderate dispersion amplitude roughly of 3000 m/s.
- 3) From 10 to 13 m, values range from 4200 to 4700m/s with the lowest dispersion of all intervals characterized by a dispersion amplitude under 656 m/s. It is noticeable that interval I.3 shows a slightly increasing P-wave velocities trend with deepening.

- 4) From 13 to 14.5 m there is a clear trend of increasing P-wave velocities with depth, and a low amplitude dispersion roughly of 500 m/s. Over 90% of the recorded values range from 4500 to 5500 m/s.

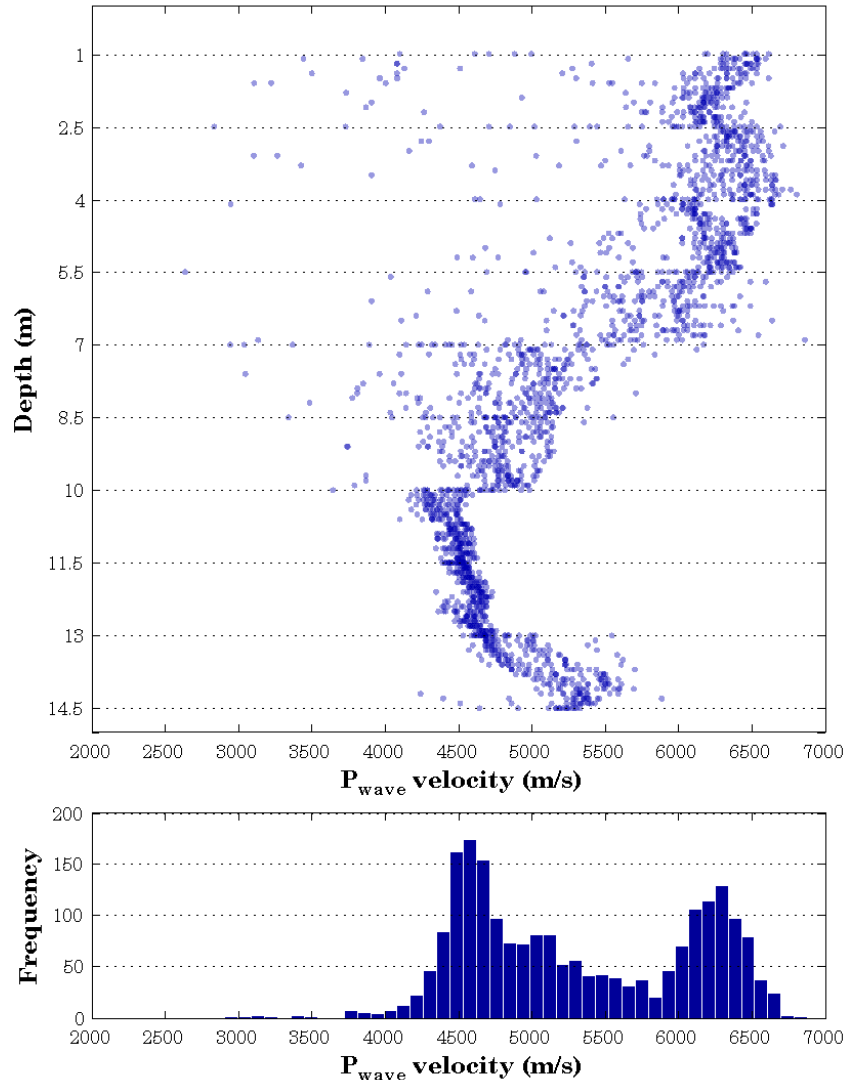


Figure 4.7. Log and histogram of the crosshole P-wave velocities.

The comparison of P-wave velocity log and velocity histograms allowed to conclude that three main velocities classes were recorded. The first one follows a normal distribution centered on 4550 ± 200 m/s which is given mainly by values from interval (3) and a minor contribution from (2).

The second class follows a normal distribution centered on 6250 ± 300 m/s and exclusively corresponds to interval (1) values. The third class follows a normal distribution centered on 5200 ± 500 m/s mainly given by intervals (2) and (4) values.

4.5.3 Tomography

We present in **Figure 4.8**, the a posteriori probability density function (pdf) which describes the distribution of models consistent with the combined states of information given by the a priori model and the data. This pdf was obtained after 10000 iterations of the extended Metropolis algorithm (for more details about the algorithms see: (Hansen, Cordua, et al. 2013; Hansen, Skou Cordua, et al. 2013)). For simplification, we will refer to the a posteriori pdf in the next paragraph as: the velocity-model (VM).

As seen on **Figure 4.8**, the P-wave velocity's distribution is consistent with porosity variations along the studied area. The highest velocities [$\sim 6.5 - 6.3$ km/s] are between 1 and 5.5m depth, and correspond to the low porous interval. The lowest velocities [$\sim 4.6 - 4.8$ km/s] are from 9 to 13m, where the porosity reaches up to 20%. There are two intervals with intermediate velocities (~ 5.2 km/s), located between ~ 7 and 8m and from 13 to 14.5m, they correspond to porosity transition intervals.

However, the tomography does not show at all the impact of the raypaths with significant velocity drops. This is not surprising regarding the method used to compute this tomography. Indeed, it is based on a statistical distribution of the data (cf., initial input), then the solver tries to find statistically the best solution for the eikonal equation. As a result, all the velocities are somewhat averaged, and since the average velocities show good correlation with the porosity.

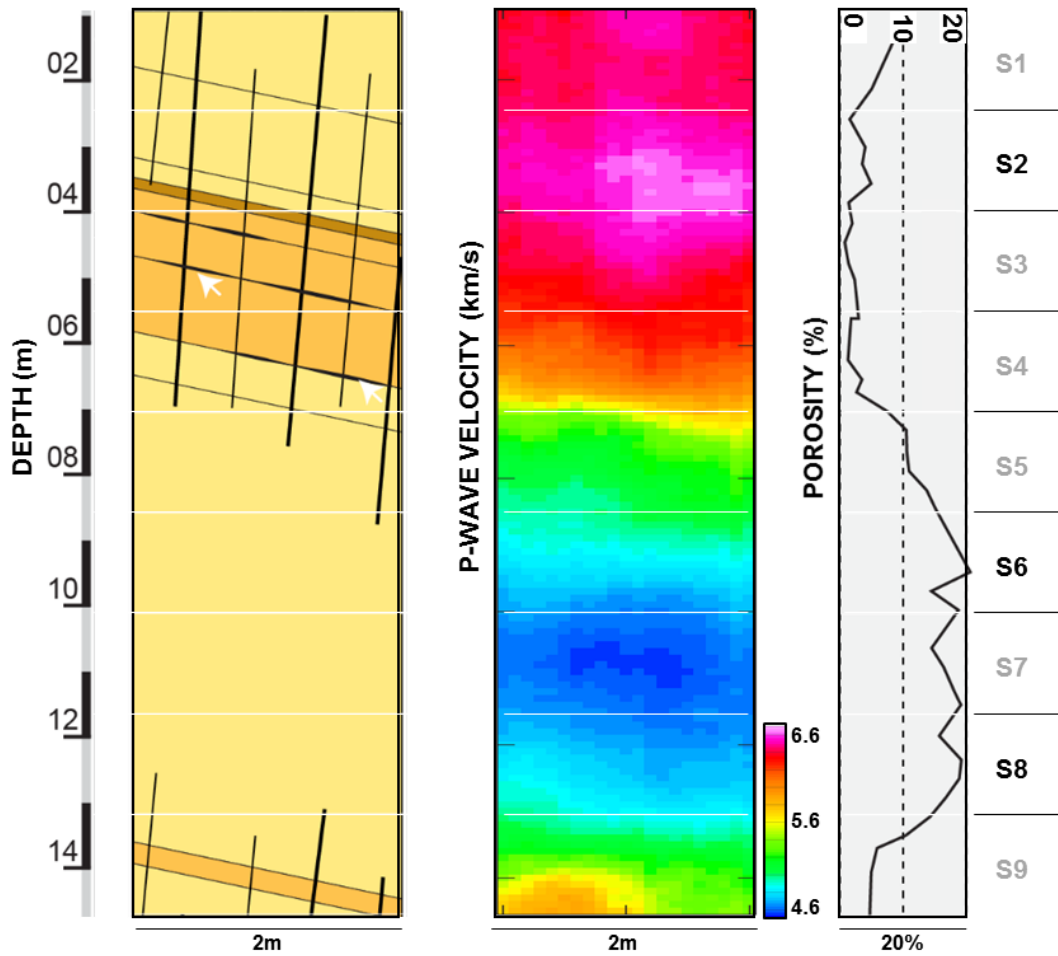


Figure 4.8. Tomography of inter-borehole space. The map of the velocity field is set in perspective with a schematic view of the geology, and the porosity. The tomography of P-wave velocity was computed using the eikonal equation.

One can see from the **Figure 4.9** that the different solutions proposed by SIPPI solver often underestimate the travel time. This is explained by the fact that the solver tends to ignore the values which are too far from the main trend. For example, the scattered travel-times recorded in the most fractured sections (S4-S5) and which correspond to data points from 1000 to 1500 in **Figure 4.9**, are simply ignored. Nevertheless, we have seen above that the main velocity trend was governed by the average matrix porosity. As a result, this tomography may be interpreted as the 2D representation of the average velocity field and/or a reasonable spatial distribution of the intact matrix porosity.

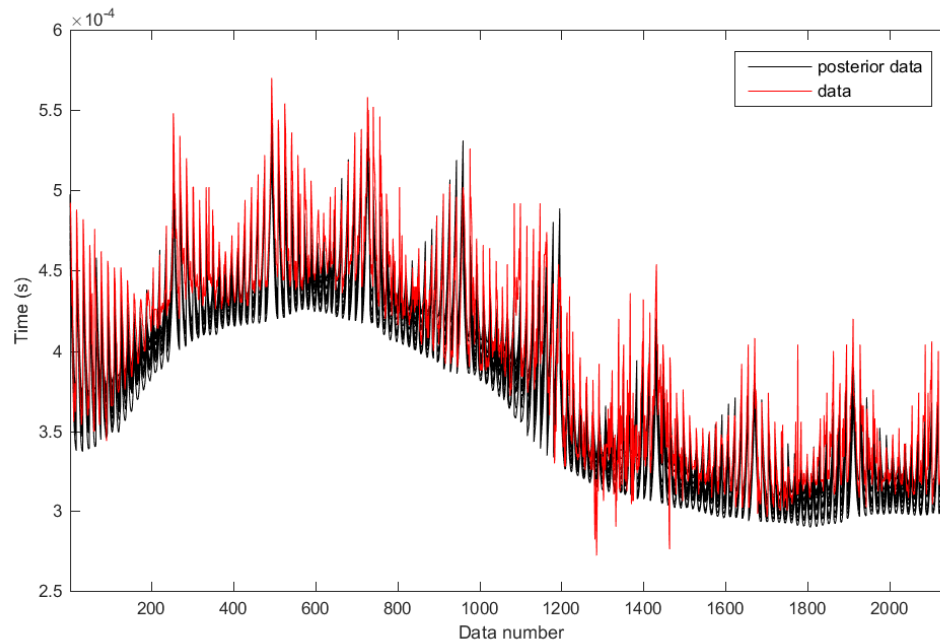


Figure 4.9. Modeling the P-wave travel times using SIPPI. Picked travel-times (red) vs. modeled travel-times ($\times 250$ black lines). The black lines represent a sample of 250 (out of 10000) iterations of the a posteriori probability density function.

4.5.4 Fractures set vs. crosshole velocities

The comparison between the raypaths showing velocity-drops, and the location of the fracture-sets visible on the boreholes walls emphasizes the implication of fractures in lowering the velocities. Indeed, for the investigated area [1.0–14.5 m], the fractures sets are concentrated within the first nine meters which is the interval presenting the largest scattering of P-wave velocity. The [4.0–9.0 m] interval has the highest fractures density.

In **Figure 4.10**, we show schematically the raypaths with velocity drop 5% lower than the average onto a simplified geological model figuring the main stratigraphic layers. One can see that the affected raypaths are concentrated within three intervals respectively [1.20–3.50 m], [5.0–8.5 m], and [9.0–10.5 m]. The borehole imagery shows that the anomalous raypaths of the [1.20–3.50 m], and [9.0–10.5 m] intervals are related to sub-vertical N25°-N30° fractures surrounded by

cracks with centimeter scale open karst conduits; whereas the raypaths of the upper part of the [5–8.5 m] interval (\approx [5–6.5 m] in P4) are affected by open stratigraphic contacts, and sub-vertical fractures alter those from bottom part (\approx [6.5–8.5 m] in P4). Hence, the occurrence of open-fractures on the boreholes walls is well correlated to velocity-drops $\geq 5\%$. But, only 8% of the recorded waveforms show this feature, and most of them are within the 1-to-9 m interval. The relatively low proportion of these “significant” velocity-drops implies that the impact of the discontinuities on velocities measured at the borehole wall is not systematic. For example, [4.0–6.5 m] interval has up to four slickensided/open stratigraphic contacts suggesting inter-layer slip, characterized by anisopachous calcareous-clays filled apertures associated to karstification. These reactivated bedding surfaces are most likely responsible of velocity decrease recorded in the interval. Although, only 11% of the waveforms recorded for this interval showed velocity-drops $\geq 5\%$ (i.e., 45 out of ≈ 400). This can be partly explained by the fact that raypaths were almost parallel to the dip direction of the stratigraphic plans, and only a few had the emitter and receiver from either side of an open stratigraphic contact. For most of the raypaths, the discontinuities did not alter significantly the velocities because of their low aperture (cf., irregular thickness of open stratigraphic contacts). The fact that the discontinuities seen on the boreholes walls do not systematically affect all measurements passing through them is consistent with a differential impact of joints on the P-wave velocity.

In spite of the above example, the discontinuities visible on boreholes walls do not explain properly the $\leq 5\%$ of variability around the average velocity trend. In fact, this variability of about 5% between the two first intervals (i.e., [1–10 m]) is high in comparison to that of the third interval (i.e., [10–13 m] where it is $\pm 1\%$ (**Figure 4.7**)).

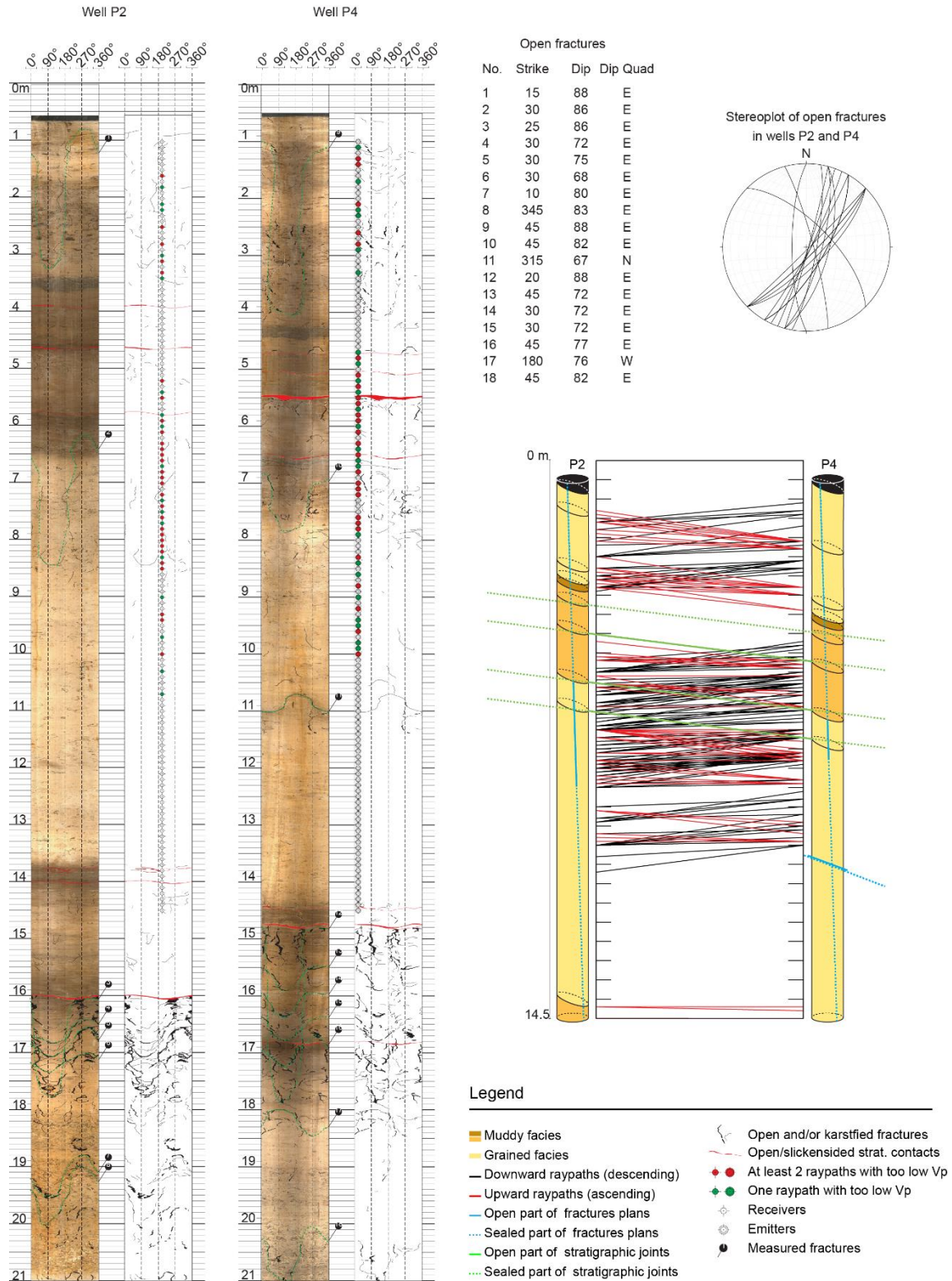


Figure 4.10. Summary of the structural analysis based on the borehole imagery (OPTV). Including: the commented borehole images, stereoplot of the open fractures, and a schematic view of the raypaths affected by fractures.

Because the assumption that fracture-sets may be intercalated is likely, this variability may be related to the occurrence of N25° and N30° sub-vertical fractures, and either smaller fractures or cracks intercalated (but not intersecting) between the boreholes.

4.6 Discussion

4.6.1 Crosshole acoustics vs. existing methods

At seismic scale different methods such as vertical and down-hole seismic profiling (VSP and DSP respectively) were developed and used routinely in industry to characterize and image interwells space. Principal limitation of these methods is that the resolution which is too low to characterize fine-scaled features. Other tools working from sonic to ultrasonic frequencies such as borehole compensated sonic log and borehole televiewer (BHC and BHTV, respectively) allow better resolutions but characterize only the environment close to the tested borehole, as the investigated area is less than 1 m or 30 cm for BHC and BHTV respectively (Serra 1984). Crosshole measurements from sonic to ultrasonic frequencies are the best way to address resolution issues encountered by classical seismic methods. Several crosshole experiments have been documented over the past years and some references about these works can be found in (King et al. 1986). Frequencies commonly used for these experiments generally range from 2 to 200 kHz while investigated distances were lower than 8 m (McCann et al. 1975; Paulsson et al. 1985; King et al. 1986; Lubbe and Worthington 2006). Documented crosshole experiments generally focus on the impact of fractures on elastic wave as many of these study cases were performed over igneous rocks. Nevertheless few examples focus on sedimentary rocks where both rock properties (i.e. porosity) and fracturing affect elastic wave velocities (McCann et al. 1975; Lubbe and Worthington 2006).

In this section we discussed a case study of crosshole measurements performed on fractured sedimentary (carbonate) rocks, with a finer resolution (≈ 10 cm) compared to previously published case studies (≈ 1 m). Our transducers had a central frequency of 50-55 kHz allowing detection of heterogeneities greater than 2 cm. Besides its finer resolution, our experiment shows different advantages over some published examples (McCann et al. 1975; Lubbe and Worthington 2006) (McCann et al. 1975) and (Lubbe and Worthington 2006). Our transducers were mechanically coupled to borehole walls which unlike mud or water coupling allow to avoid borehole related “artifacts” such as tube and Stoneley waves. It also allows “direct” transmission of the wave with a maximum energy to the rock mass by limiting reflection at the interface (i.e. water-rock). Finally, the experimental set-up enables acoustic full-waveform logging that can be interpreted in terms of P- and S-waves travel times and also in terms of amplitude versus offset (AVO).

4.6.2 Impact of diagenesis and pores geometry

The porosity and the pores geometry control the elastic properties in carbonate rocks (Anselmetti and Eberli 1993, 1999; Anselmetti, Salis, et al. 1997; Verwer et al. 2008; Baechle et al. 2009). This general rule was verified in extensive works on the petrophysical and elastic properties of microporous Urgonian limestones (Fournier and Borgomano 2009; Fournier et al. 2011, 2014).

The P- and S-wave velocity presented in this study are consistent with velocity ranges described in Fournier et al., (2014). For example, the field measurements which were performed at 5 ± 2 MPa mean stress (Guglielmi et al. 2015) show high P-wave velocity ranging from 6000 to 6500 m/s in low porosity facies, which are common values reported for calcite minerals (C.-Y. Wang 1966). In the porous interval the porosity ranges from $<5\%$ to $\sim 18\%$, and the P-wave velocities range from 4300 to 5500 m/s. These data are similar to Fournier et al. (2014) values measured in

laboratory conditions upon similar dry facies at 10 MPa effective pressure. The strong consistency between our data and the works of these authors allows us to interpret that at both field (average velocity) and laboratory (plugs velocity) scales, the velocity corresponds to the acoustic response of the intact matrix.

At the plugs scale, cracks (if any) related to stress relief or to the plugs extraction seem to have low impact on our plug scale velocities, since our values are consistent with the literature. The normal force applied during our experiments (by a clamp) may have mitigated the effects of cracks, however, this is only a partial explanation regarding the relatively low pressure exerted on the plugs. Moreover, this low influence was expected because Fournier et al., (2011, 2014) showed that plug extracted from these facies are not systematically affected by cracks, and if any, they were closed at relatively low confining the pressure (~ 2.5 MPa for most of their samples, and < 10 MPa for the others). These authors also noticed that cracks were not the only factor lowering the velocities at low confining pressure. In fact, their most porous samples which have velocities ranging from 3000–4000 m/s at low confining pressure showed pressure dependency of the velocities. While this dependency is low-dip linear relation for the non-porous samples, it is not linear (\sim logarithmic growth) in the porous samples. This indicates that the matrix compliance increases with the overall porosity, and this behavior may be opposed to some porous oolitic rocks which remain stiff thanks to their intergranular cements and despite a relatively high porosity (Assefa et al. 2003). Our data point towards the same conclusions as Fournier et al., (2011, 2014) i.e., the velocity values measured on the porous interval are related to the micrite microfabrics (MF2: *serrate subhedral/euhedral micrite*, and MF3: *punctic to serrate subhedral/euhedral micrite, showing subrounded crystals with subhedral/euhedral overgrowths*), see also **Figure 4.3** and **Figure 5.2**. These authors demonstrated that low velocities in microporous

limestones resulted from the high compliance of intercrystalline micropores and/or from the softness of grain contacts between micrite particles in relatively loose micritic media.

4.6.3 Effects of fractures on the P-wave velocity

In our two-scale dataset, the impact of fractures cannot be characterized from the plug data, since the plugs extraction requires to carefully avoid the fractured areas. Hence, the fractures influence can be characterized only from the field data

At the scale of the carbonate series, the elastic moduli depend on: (1) the elastic properties of the intact rock; and (2) the compliance of the potentials fracture-sets (Brown and Scholz 1985, 1986; Yoshioka and Scholz 1989; Lubbe and Worthington 2006; Worthington and Lubbe 2007). The role of fractures in lowering velocities recorded in-situ has been documented in several studies. For example, (Stierman and Kovach 1979) reported in-situ P-wave velocities 2 km/s lower than those measured in laboratory under equivalent confining pressure. They attributed this discrepancy to macroscopic fractures observable in the wells but not on the tested specimens. (Moos and Zoback 1983) came out with similar conclusions for granitic rocks. They showed that velocity measured in-lab at ultrasonic frequency were roughly 1.5 km/s higher than in-situ velocities obtained by different methods i.e. sonic log, vertical seismic profile and seismic refraction. The authors went further by demonstrating that velocity decrease induced by fractures in most fractured levels could lead to significant acoustic impedance contrasts able to make distinguishable reflectors on whatever synthetic or real seismic profiles (Moos and Zoback 1983).

In our dataset, we observed that the average P-wave velocity measured at the field-scale is equal to the plugs scale velocities, and this was interpreted as the elastic response of the intact matrix. We observed two orders of variations around the average velocity. The first (and the most noticeable) is the velocity variation $\gg 1000$ m/s, these data points may be interpreted as outliers,

but the analysis of the boreholes images showed that they were correlated to the fractured areas visible from the boreholes walls. Our explanation is that the fractures being too close from the source or receivers, the acoustic wave had no choice but to cross the discontinuities, which causes a delay because of the lower velocity in air (dry fracture). In contrast, if the fracture is far enough, the wave may find an alternative path through the rock, the first arrival (cf. P-wave) would still be delayed but in a lower extent. This second case gives the second order of variation around the average values, and is responsible for seismic anisotropy (Hudson 1980; Bakulin et al. 2000b; Grechka and Kachanov 2006).

4.7 Conclusion

In this section we characterized a Barremian microporous and fractured carbonate reservoir in terms of petrophysical and elastic properties. The P- and S-wave velocity measured at two-different scales (i.e., the plugs and the field scales) were interpreted on the basis of the geology, and regarding the literature. The field (crosshole) measurements have been carried out at an intermediate scale between conventional seismic surveys and laboratory measurements. These data give new insight on the elastic properties of carbonate reservoirs. Our data emphasized the strong dependency between our P- and S-wave velocities and the overall porosity. However, the elastic response is not limited to the simple matrix properties. Indeed, as soon as the scale increases the effect of fractures is more and more noticeable. Despite the fact that the data are too sparse to interpret the strongest velocity variations, they consistently pointed toward a ~500 m/s variability which is most likely related to the fractures. In this part of the PhD works we did not consider the velocity variations as a function of the propagation direction, but this variability may be explained by fracture-related anisotropy.

Section 5: Scale dependency of velocity anisotropy in heterogeneous carbonates

5.1 Abstract

The anisotropy of elastic waves in carbonates is investigated at two different scales, to understand the impact of natural fractures, and sedimentary-driven heterogeneity on seismic data. Ultrasonic measurements have been carried-out on saturated cores ($\varnothing=12.5$ cm; 250 kHz), and on dry plug-triplets ($\varnothing=3.81$ cm; 1 MHz), which were sub-sampled from the cores following the “three-plug” procedure. The P- and S-wave velocities are measured at both scales and are interpreted regarding porosity and geological features observed on computed tomography (CT), thin-sections, and scanning electron micrograph (SEM). We observed an azimuthal-anisotropy of maximum 5% caused by the inclusion of large and non-porous fossils (>5 cm) within the porous matrix. In comparison, the azimuthal-anisotropy caused by non-uniform fracture-sets affecting the same facies reaches up to 10–15%. These results show that laboratory-sized samples are not sufficient to characterize whether platform carbonates are heterogeneous or anisotropic. Indeed the size of some heterogeneities may exceed that of laboratory-sized samples, causing laboratory-measured velocity anisotropy to be scale-related or scale-influenced.

5.2 Introduction

Laboratory-scale studies show that P- and S-wave velocity in limestone is mainly controlled by porosity and pores geometry (Fournier et al. 2014). However, upscaling carbonate-rocks properties from the usual plug-sized samples is difficult because of the intrinsically complex facies (e.g.,

mixed grain / pore sizes, pores types), which are further modified by diagenesis (e.g., dissolution, cementation). This is particularly true in platform-carbonates, where facies variation and diagenetic patterns lead to significant properties variations within a few meters. Wang (2002b) investigated anisotropy in tight –thus presumably homogeneous– carbonates and concluded that anisotropy in carbonates was insignificant, or should be related to fracturing only. This conclusion may be valid for tight or fine-grained basin-type carbonates, but it may fail when considering porous platform facies, where alternating zones with significant porosity-contrasts may contribute to elastic-anisotropy. Baud et al. (2016) for example, showed that stylolites –which are frequent in tight-carbonates– produce mechanical-anisotropy; and Adam et al. (2009) noticed sharp P- and S-wave velocity variation for carbonates with band-like pattern of different porosity.

The above examples indicate that in some cases, one may expect heterogeneity at sample scale to result in P- and S-wave velocity anisotropy in platform-carbonates. Nevertheless, it remains difficult to determine from velocity measurements on small centimeter-sized plugs whether sedimentary figures and diagenetic patterns, typically larger than a few centimeters, will cause noticeable anisotropy in larger-scale velocity data. In this study we determine azimuthal variations of velocity in platform-carbonates at the core scale, and compare with measurements carried on plug-sized samples. We also emphasize the scale-dependency of isotropy/anisotropy, and the impact of heterogeneities/discontinuities at the larger scale.

5.3 Material and methods

5.3.1 Rock material

This study focuses on Barremian limestone (Urgonian facies) crossed by the galleries of the Low Noise Underground Laboratory (LSBB) of Rustrel (south-east of France), described in more details in Jeanne et al. (2012). There, 5 fully-cored 20 m deep boreholes located in the GAS-

gallery, sample an alternating series of porous/tight reservoir-units made of low-to-moderate energy facies of the former Urganian-platform. In these monotonous “internal-platform” facies, the footprint of diagenesis dictates the petrophysical properties. The conservation of the porosity was conditioned by exposure of the sediments to meteoric-fluids during early-diagenesis. The pores are located within the micrite intercrystalline-space, and resulted from recrystallization of metastable carbonate-minerals (i.e. aragonite, Mg-rich calcite) during early-diagenesis (Léonide et al. 2014). The resulting porosity-layering leads to unequal repartition of the fracture-sets and stylolites, which are both concentrated in the tight layers (Jeanne et al. 2012).

The samples selection was motivated by the fact that fractured tight-facies and heterogeneous porous-facies are very typical rock types in Urganian limestones. We were interested in exploring if the layering of the porosity observed at field scale could be observed at core scale, which is in general the only observable scale for deep reservoirs. Six cores named C01 to C06 were selected either because of their matrix-properties or because of the presence of macroscopic cracks. The selected cores are representative of the twenty-meter thick carbonate series intersected by the boreholes within the GAS-gallery. Their diameter is 12.5 cm and their lengths range from 20 to 80 cm. Details about the cores geology are summarized in **Table 5.1**, and additional information about their petrophysical properties can be found in **Table 5.2**.

5.3.2 Experimental settings

The study is focused on three main properties: (1) porosity, which is the main factor controlling the rock material elastic moduli; (2) compressional (P-) wave velocity; and (3) shear (S-) wave velocities. The selected cores have undergone a series of measurements. First, the P-wave velocity through the water-saturated cores have been characterized using an automated acoustic acquisition system. Afterwards, they have undergone X-ray Computed Tomography (CT) using a medical

scanner. Finally, two sets of plugs have been extracted from the cores. The first set included three plugs per core ($L=\varnothing=3.81 \pm 0.01$ cm, 1.5 inch) referred to as plug-triplets. Each triplet includes one plug taken in the directions normal, parallel and 45° to the bedding (Z. Wang 2002a; Louis et al. 2005). The triplets were used for P- and S-wave velocity measurements. Porosity was estimated on the dry plug-triplets, assuming that the rock was made of pure calcite with a density of 2700 kg/m^3 . The accuracy of this assumption was assessed on another plug-set, which comprised one plug per core ($L=\varnothing=2.54 \pm 0.01$ cm, 1 inch).

5.3.2.1 Porosity and density measurements and estimation

The porosity measurements have been carried out according to the API recommendation (American Petroleum Institute, 1998). We use the formula $\phi = 1 - (V_{\text{grains}}/V_{\text{bulk}})$ involving the bulk (V_{bulk}), and the grains (V_{grains}) volumes. The bulk volume was determined using two different methods. The simplest was achieved by measuring the external dimensions of the plugs with a digital caliper. The second method is based on Archimedes principle, and the formula $V_{\text{bulk}} = m_{\text{im}}/\rho_w$, where m_{im} is the mass of water displaced by the immersion of the sample in a beaker, and ρ_w is density of water at 20°C . The sample is water saturated before immersion. We found that, the two methods gave the same values with a $\pm 0.05 \text{ cm}^3$ error for samples with low porosity, but the difference reached up to 1 cm^3 for the most porous one. This increased error is due to large moldic pores that do not remain saturated when the sample is in the air, and consequently reduce the estimation of bulk volume by immersion. The grain volume is determined in an apparatus based on Boyle's Law Double-Cell Method. The "porosimeter" is first calibrated, yielding the reference chamber volume (V_{ref}) and the sample chamber volume (V_{cell}). In isothermal conditions (20°C), Helium is admitted into the reference cell at a predetermined reference pressure (P_{ref}), then is vented into the sample chamber. This results in a lower equilibrium pressure (P_{meas}),

then the grain volume can be calculated as follow $V_{\text{grain}} = V_{\text{cell}} - V_{\text{ref}} (P_{\text{ref}} / P_{\text{meas.}} - 1)$. So that, we were able to compute the grain density $\rho_{\text{grain}} = m_{\text{dry}} / V_{\text{grain}}$, where m_{dry} is the dry-plug weight. The average grain density calculated for the porosity plug-set was $\rho_{\text{grain}} = 2646 \pm 50 \text{ kg/m}^3$, which is consistent with the mineral density of calcite i.e., $\rho_{\text{calcite}} = 2700 \text{ kg/m}^3$. Since the volume determined with the plugs dimensions is accurate, and $\rho_{\text{grain}} = \rho_{\text{calcite}}$, we derive the porosity for the triplet plug-sets used for the velocity measurements, using the relation $\phi = ((\rho_{\text{calcite}} - \rho_{\text{bulk}}) / \rho_{\text{calcite}})$, where the bulk density (ρ_{bulk}) is given by $\rho_{\text{bulk}} = m_{\text{dry}} / V_{\text{bulk}}$.

5.3.2.2 Core-scale velocity measurements

First, the core were immersed in a water-filled tank placed in a vacuum chamber one week prior to the experiment, then transferred to an acoustic tank (i.e., 4.5 m³ water-container designed and instrumented to carry out acoustic measurements) filled with 20°C tap-water. The experimental set-up is schematized in (Figure 5.1). The instrumentation included: 250-kHz IMASONIC immersion-transducers, oscilloscope TEKTRONIX-DPO4034, pulse generator–receiver PANAMETRICS-5058PR. The acquisition and displacement systems are both computer-controlled, using a user interface or virtual instrument, designed with LabVIEW.

Two immersion-transducers rotate around the vertical axis (z-axis). The cores true orientation is known by correlation of structures observed on the core surface and on the borehole walls using georeferenced borehole optical imagery (OPTV) and the measurements started at azimuth N0°, so that the rotation angles (θ) are the azimuth with respect to the true north. The vertical step was 1 cm, but we used two different rotation steps $\Delta\theta = 5^\circ$ or 10° (i.e., 5° for C01-C04-C06, and 10° for C02-C03-C05), in order to document impact of downsampling on the apparent anisotropy. At each position $P(\theta, z)$, 64 “raw” traces are stacked and averaged to improve the signal-to-noise ratio,

giving one “pre-processed” trace. Depending on $\Delta\theta$, 36 or 72 pre-processed traces are recorded per horizontal-section (i.e., fixed z).

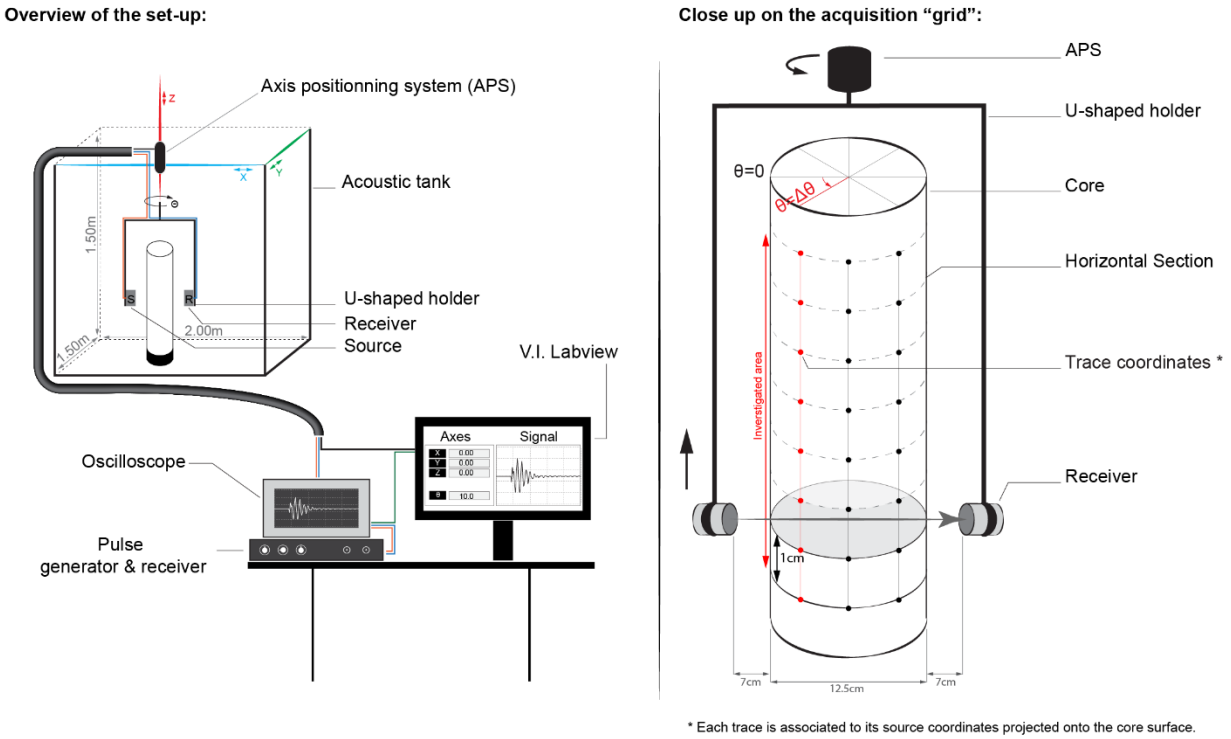


Figure 5.1. Experimental set-up used for the cores characterization.

5.3.2.3 Plug-scale velocity measurements

The oven-dried plug-triplets were stored at room conditions during several days. Then, ~ 400 V pulses were applied by PANAMETRICS 5058PR pulser to pairs of 1MHz (central frequency) contact ultrasonic transducers (PANAMETRICS, Accuscan A103R-RB (P-wave) and Vibrosan V153-RB (S-wave)). The contact was established by applying mechanical force onto the sample-transducer assemblage using a hand clamp, and the rock-transducer interfaces were mediated by 15-micron thick lead foils. The waves transmitted through the samples were recorded by a digital oscilloscope (LeCroy LC334AM). The average error is estimated ± 0.05 and ± 0.1 μ s for the P- and S-wave travel-times, respectively. Three travel-times values were measured across each plug i.e.,

(1) the P-wave, and two orthogonal S-waves travel-times (t_{s1} and t_{s2}) standing for the fast and the slow polarization. Finally, the velocity was computed using the relation $v = L/t$, where L and t are the core's length and the travel-time, respectively.

5.3.2.4 CT-Imagery: characteristics and objectives

The CT imagery was performed at TOTAL E&P France (TOTAL CSTJF's facility), using the medical scanner Discovery CT750 HD. The cores were referenced with respect to their depth in the borehole and re-orientated using OPTV. The scanning starts from the core top (i.e., minimum depth) towards the bottom, at azimuth $N0^\circ$. Hence, the coronal and the sagittal (i.e., dedicated terms in medical imagery) planes correspond to the North–South and East–West sections, respectively. The dataset produced during this process is a referenced image-sequence that can be further processed to obtain a 3D reconstruction of the core. The size of a CT-image is 512×512 pixels (or 140×140 mm), hence the size of the pixel is $273.4 \mu\text{m}$. Each image represents a 0.625 mm thick transversal-section (or slice).

Here, we only make a qualitative interpretation on the CT-data. The resolution of the CT-volumes is insufficient to image the intercrystalline porosity (i.e., the dominant pore-type), which is $\leq 10 \mu\text{m}$. Thus, only moldic porosity and fracture porosity are seen in the images. Micro or Nano-CT scanners (Bera et al. 2011; Mayo et al. 2015) would have been more suitable to characterize the geometry of the porous network. However, the voxels values in a CT-image correspond to a relative absorbance expressed with the Hounsfield scale (air: -1000 , water: 0). Hence, for a given rock type and composition the CT value is correlated to the average density and porosity of the voxel (e.g., Conin et al. 2014). For the nearly pure carbonates cores in this study, we thus consider the variations of pixels gray-depth (16-bit) of the final images as an indicator of density and

porosity variations. Finally, we performed only minor processing of the images such as brightness or contrast adjustments, resizing, and cropping.

5.3.3 Processing the cores data

5.3.3.1 Time-velocity inversion for the cores

The P-wave travel-time was manually picked on the waveforms. In order to calculate the P-wave velocity, we assume that the raypath between the transducers is a straight line. The transducers being face-to-face, and their axis being normal to the core's axis, the ray is not deviated at the rock–water interfaces for weakly anisotropic cores. Moreover, the velocity through water being lower than that of the rock, the first P-wave arrival should always correspond to the straight raypath (**Figure 5.6**). Several parameters such as water temperature, emitter-receiver distance, and core diameter (D_{core}) were constant. Consequently, the distance and the travel-time through water (D_{water} and t_{water} , respectively) are also constant. The t_{water} is given by the ratio of D_{water} and the P-wave velocity in a 20°C water ($V_{\text{pwater}} = 1480$ m/s). As a result, the core “bulk” velocity (V_{pcore}) that we calculate using equation (2), is the P-wave velocity through the saturated core.

$$V_{\text{Pcore}} = D_{\text{core}} / (t - t_{\text{water}} - t_{\text{delay}}), \quad (1)$$

Where t and t_{delay} are the picked travel-time, and the instrumental delay, respectively.

The velocity data acquired on cores for each horizontal-section were fitted with Fourier series. Since the acquisition was carried out over 360°, there must be a 180°-periodicity in the data because of raypath reversibility. Only the two first harmonics are retained, (equation 2).

$$V_{\text{Pfit}}(\theta) = A_1 \cos(2(\theta - C_1)) + A_2 \cos(4(\theta - C_2)) + V_{\text{P0}}, \quad (2)$$

where θ is the angle in the horizontal plane, A_i is the amplitude of the harmonic, C_i is a constant, and V_{p0} is the average velocity.

We recalculated the travel-times from the fitted-velocities, and these new values were compared to the picked travel-time (**Figure 5.6**). We found that the fit error was $\leq 4\%$, and that the outliers were removed efficiently. Consequently, we consider only the fitted-velocities in the following.

Finally, we assumed that the cores anisotropy is captured by the amplitude of the first harmonic (cf. A_1), so that we can approximate the strength of this anisotropy (ε') using the best-fit parameters of the equation (2); and the relation $\varepsilon' = A_1 / (A_1 + V_{p0})$.

5.3.3.2 Plug-scale anisotropy

We here show how plug-scale velocity measurements may be interpreted in term of anisotropy, assuming the three plugs taken with orientation 0° , 45° and 90° from core axis do have exactly the same properties. We will show later that, in our case, this assumption is probably wrong. For simplicity, we calculate the anisotropic stiffness tensor assuming transverse isotropy (TI), presumably representative of sedimentary layering or of the effect of a set of parallel cracks. Note that we here consider only a vertical symmetry axis (VTI), but the same calculation would have been possible for the horizontal case (HTI), the main difference being a ninety-degree rotation of the stiffness tensor in the second case (cf. Rüger (1997) for detailed explanation). We do not discuss the orthorhombic case neither, because plug-scale is lower than that of the fracture sets. At plug-scale, any anisotropy is related either to matrix, or micro-cracks, but not to macroscopic fractures.

For TI materials, the stiffness tensor (C_{ij}) written in Voigt's notation, requires only five independent components to fully describe the elasticity, cf. equation (3).

$$C_{II} = \begin{pmatrix} c_{11} & c_{12} & c_{13} & & & \\ c_{12} & c_{11} & c_{13} & & & \\ c_{13} & c_{13} & c_{33} & & & \\ & & & c_{44} & & \\ & & & & c_{44} & \\ & & & & & c_{66} \end{pmatrix}, \quad c_{66} = \frac{c_{11} - c_{12}}{2} \quad (3)$$

After equation (4), components of C_{II} can be obtained from the density (ρ), and five velocity measurements including both quasi-longitudinal (V_p), and pure-shear (V_{sh}) phase-velocities (Mavko et al. 2009).

$$\begin{aligned} c_{11} &= \rho V_{p(90^\circ)}^2 \\ c_{33} &= \rho V_{p(0^\circ)}^2 \\ c_{44} &= \rho V_{sh(0^\circ)}^2 \\ c_{66} &= \rho V_{sh(90^\circ)}^2 \end{aligned} \quad c_{13} = -c_{44} + \left(\begin{aligned} &4\rho^2 V_{p(45^\circ)}^4 - 2\rho V_{p(45^\circ)}^2 \\ &\times (c_{11} + c_{33} + 2c_{44}) \\ &+ (c_{11} + c_{44})(c_{33} + c_{44}) \end{aligned} \right)^{\frac{1}{2}} \quad (4)$$

Thomsen (1986) introduced a convenient notation for TI media which are only weakly anisotropic. Using this notation the five elastic coefficients of VTI media can be replaced by the velocities of the P- and S-wave propagating along the vertical axis, α and β respectively, and three dimensionless anisotropy parameters denoted as ε , δ , and γ , (equation (5)).

$$\begin{aligned} \alpha &= \sqrt{c_{33}/\rho} \\ \beta &= \sqrt{c_{44}/\rho} \\ \varepsilon &\equiv (c_{11} - c_{33})/2c_{33} \\ \gamma &\equiv (c_{66} - c_{44})/2c_{44} \\ \delta &\equiv \left((c_{13} + c_{44})^2 - (c_{33} - c_{44})^2 \right) / (2c_{33} (c_{33} - c_{44})) \end{aligned} \quad (5) \text{One of the}$$

advantages of Thomsen notation is that ε , δ , and γ go to zero for isotropic media, and therefore conveniently characterize the strength of the anisotropy. The parameter ε is close to the fractional

difference between the horizontal and vertical P-wave velocities i.e., the P-wave anisotropy. Likewise, γ represents the same measure for the pure shear wave. For each plug-triplet, the components of C_{II} , and the anisotropic parameters ε , δ , and γ were computed using equations (4) and (5), respectively (**Table 5.4**).

5.4 Results and discussion

5.4.1 General properties of the matrix

5.4.1.1 Petrography

The general description of the Urgonian limestones in Provence area, in terms of constituents, also applies to our samples, e.g. (Fournier et al. 2011, 2014; Borgomano et al. 2013; Léonide et al. 2014). More specifically, the thin-sections analyses (**Figure 5.2**) showed that the samples are exclusively made of carbonate minerals; the primary porosity (i.e., inter- or intra-granular) is completely occluded by calcite with different size ranging from micrite to sparite; the porosity observed within the tight samples are exclusively related to cracks and stylolites Crack or stylolite-related porosity also occur in porous samples, however, the main part of the porosity is located in intercrystalline space within the micritic grains. The observed proportion of this microporosity (~95%) within our thin-section is of the same order as those published on similar facies (Fournier et al. 2014). Moldic and vuggy pores account for most of the 5% left. SEM images show that the overall porosity measured is correlated to the micrite crystals size and shape. Large euhedral micrite crystals are synonym of higher porosity, while anhedral micrite crystals are observed in tight facies.

Table 5.1. Summary of the geological characteristics of the selected cores.

Label Depth	General description	Texture*	Pores* Types	Relative abund.	Grains size		Micrite Size	Shape	Fracturing*	
					Macro.	Micro.*			Cracks	Stylolites
C01 04.20 – 04.70 m	Contact between two non-porous facies macroscopic bioclasts are large rudists fragments fractures filled with < 2 mm thick calcite cement presence of stylolites	rudstone - grainstone	n/a <i>(if any = cracks or stylolites)</i>	n/a <i>(if any = rare)</i>	≥ 2 mm ≤ 5 cm	< 300 μm	≤ 2 μm	anhedral - subhedral	yes	yes
C02 04.70 – 04.95 m	Our most homogeneous facies fine-grained peloidal and foraminifera rich facies marginal pores within cemented fractures	grainstone - packestone	n/a <i>(if any = cracks)</i>	n/a <i>(if any = rare)</i>	n/a	≥ 100 μm ≤ 300 μm	≤ 2 μm	anhedral - subhedral	no	no
C03 06.50 – 07.10 m	Fractured, non-porous, and coarse facies abundant centimeter-scaled rudists open fractures	grainstone - rudstone	n/a <i>(if any = cracks)</i>	n/a <i>(if any = rare)</i>	≥ 2 mm ≤ 5 cm	< 300 μm	≥ 2 μm ≤ 5 μm	anhedral - subhedral	yes	yes
C04 12.90 – 13.70 m	Our most homogeneous facies (fine grained) peloidal and foraminifera rich facies marginal pores within cemented fractures	grainstone - rudstone	Micro-porosity moldic vuggy	micr.: dominate mold.: present vug.: present	≥ 2 mm ≤ 10 cm	≥ 200 μm ≤ 2 mm	≥ 1 μm ≤ 5 μm	euهدral - subhedral	yes	no
C05 15.50 – 16.20 m	Fractured, non-porous, and fine-grained facies several fractures with different orientations open fractures	grainstone	n/a <i>(if any = cracks)</i>	n/a <i>(if any = rare)</i>	≥ 2 mm	≤ 100 μm	≥ 2 μm ≤ 5 μm	anhedral - subhedral	yes	yes
C06 18.90 – 19.44 m	Coarse and porous facies high concentration of large rudists high porosity contrast	grainstone - rudstone	Micro-porosity moldic vuggy	micr.: dominate mold.: present vug.: present	≥ 2 mm ≤ 10 cm	≤ 100 μm	≥ 1 μm ≤ 5 μm	euهدral - subhedral	yes	no

* These observations are from thin-sections analyses and are valid at the matrix scale, but at larger scale fracture-porosity dominates (cf. fractured reservoir).

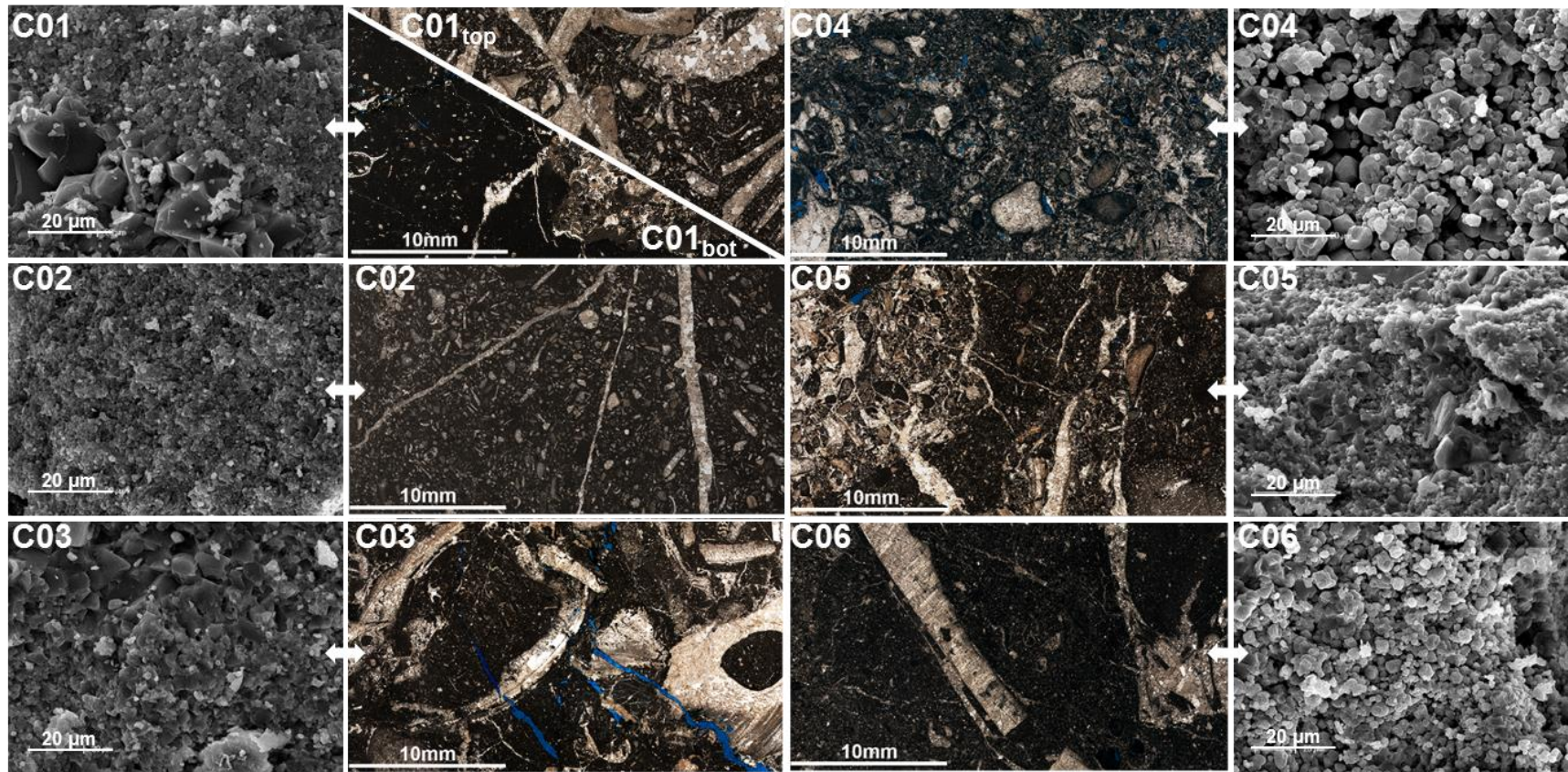


Figure 5.2. Stained thin-sections and SEM-images of cores. Notice the contrast in micrite crystals shape and inter-crystalline pores between the non-porous C01/C02/C03/C05 and the porous C04/C06.

The matrix-properties of C01, C02, C03, and C05 are similar, i.e., they have low-porosity <1%, and low-permeability $<9.87 \times 10^{-16} \text{ m}^2$. (Figure 5.2, Table 5.1). C04 and C06 have porosity ranging from 10 to 15 %, and permeability up to $\sim 3.46 \times 10^{-15} \text{ m}^2$. However, these porosity are matrix-scale values because, some additional fracture-related porosity exists at larger scale.

5.4.1.2 Porosity analysis using computed tomography

CT-images (Figure 5.3) show uneven distribution of the porosity within the porous samples, which have spatial extension large enough to make the sample heterogeneous in terms of petrophysical properties.

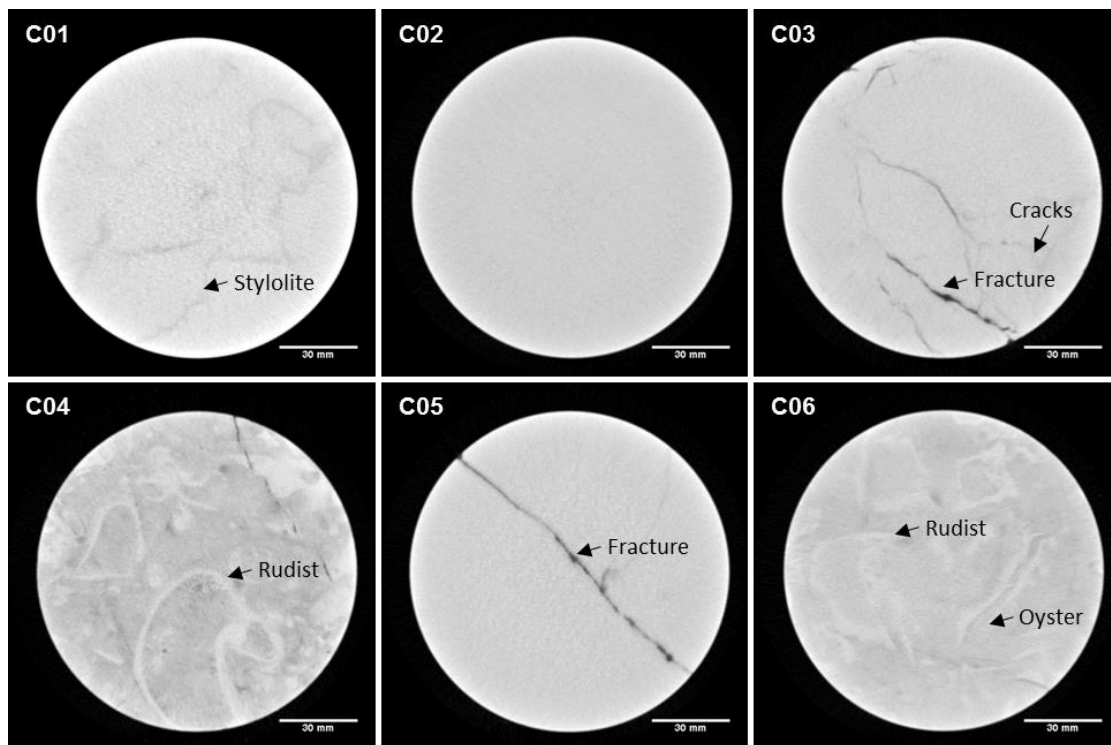


Figure 5.3. A selection of slices from the cores CT-scan. Note the density contrast caused by the fossils (C04/C06), fractures (C03/C04/C05/C06), or stylolites (C01); also note the scale of these heterogeneities in regards of that of the plug-triplets (38 mm)

The tight matrix are homogeneous regardless of their constituents whereas the porous matrix can be either homogeneous or heterogeneous. Locally, a porous facies may be homogeneous only if there are not any fossils included (cf. C04/C06). Large fossils embedded in a porous matrix

introduce high porosity-contrasts, which likely influence acoustic wave propagation. Similarly, fractures and stylolites are a factor of heterogeneity as in the case of C01/C03/C05. The size, orientation, and frequency of the fracture-sets is variable even at core scale, and may produce some apparent anisotropy.

5.4.1.3 Porosity-velocity correlation

There porosity shows a good correlation with the P-/S-wave velocities (**Figure 5.4, Table 5.2**). As expected, C04 and C06 have the lowest P- and S-waves velocities, while all the others have well grouped and higher P- and S-wave velocity. However, P- and S-waves velocity values for a given core may show some variability.

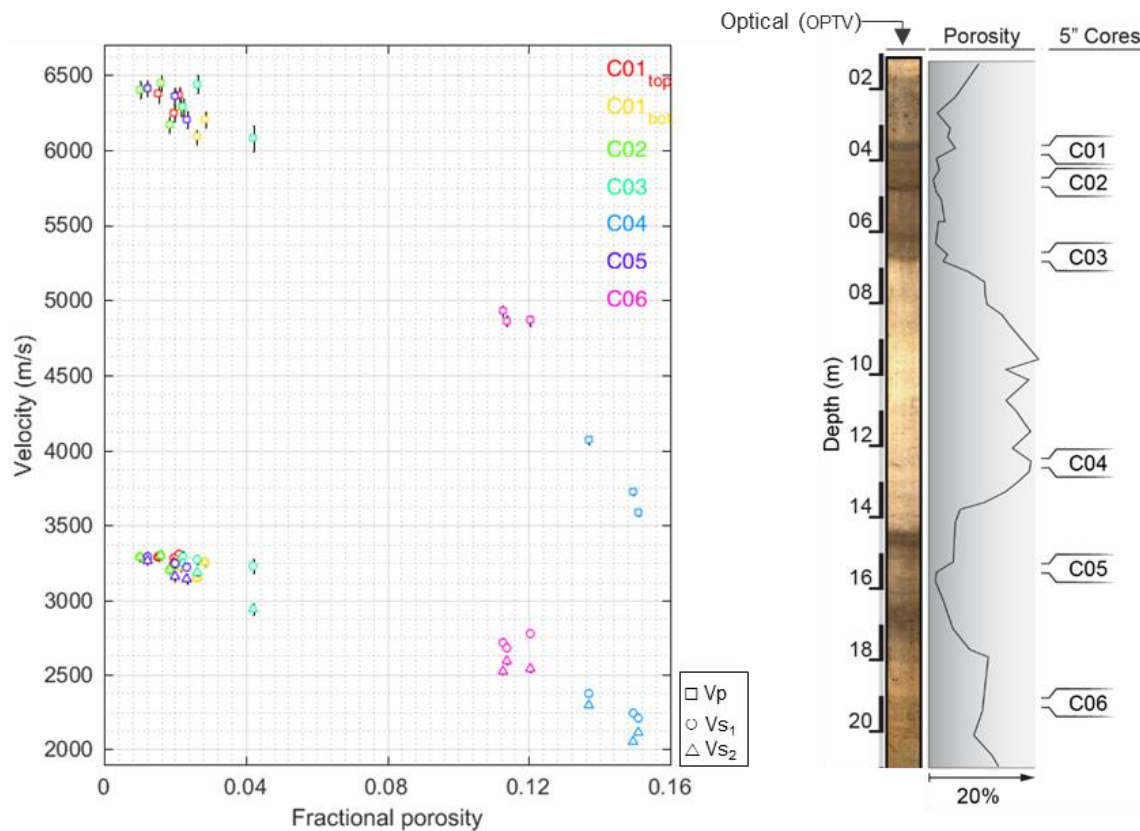


Figure 5.4. Cross-plot of the P and S-wave velocity against porosity at plug scale. This figure shows the porosity and velocity data of the plug-triplets, and optical/porosity logs of the carbonate series. Error bars are figured for the velocity values, while the error on the porosity derived from the density value was not significant ($\ll 1\%$).

Except C06, which shows nearly constant P-wave velocity regardless of plug orientation, all other plug-triplets have P-wave velocity variations ranging from 50 to 500 m/s. The direction of maximum P-wave velocity is variable (**Table 5.2**). For example, it is parallel to bedding in C02 and C03, whereas it is normal in C01 and C04. The velocity differences between the fast and slow polarization of the shear wave (i.e., V_{S1} and V_{S2} respectively) is significant only in: C03 at direction 45°; C04 at directions 0° and 45°; and at C06 at directions 45° and 90°. The velocity variations of ~12% observed between plugs from C04 appears to correlate with (relative) porosity variations of ~2%. This suggests that the variation of velocity between these plugs could be a consequence of heterogeneity rather than plug scale anisotropy.

5.4.2 Comparison of the elastic properties at two scales

5.4.2.1 The P-wave velocity

The velocity variations of ~12% observed between plugs from C04 appears to correlate with (relative) porosity variations of ~10%. This suggests that the variation of velocity between these plugs could be a consequence of heterogeneity rather than plug scale anisotropy (**Table 5.2**, **Table 5.3**, **Figure 5.5**). For the porous samples, the average velocity measured on the dry plugs is lower than that measured on the saturated cores. Since the bulk modulus of water is higher than that of air, higher P-wave velocity is expected for the saturated-cores. For tight samples the plugs average-velocity is equal or slightly higher than the core average-velocity. For C02, velocities display little variability at both core-scale and plug scale and the difference between the measurement scales is not significant. The fractured-cores C03/C05 display a relatively high standard deviation and have $V_{p_{avg}}$ significantly lower than the plug-scale velocities (**Table 5.3**). Unlike for the porous cores (C04/C06), this cannot be explained by pore-fluid substitution.

Table 5.2. Summary of the petrophysical data from the plug-sets.

Label	Depth (m)	... to bedding	Density (kg/m ³)	Porosity (%)		Permeability* (mD)	Vp	Vs ₁	Vs ₂	Vs _{avg}
				Meas.	Estim.					
C01 (top)	04.20 – 04.70	Normal	2643		2,12		6367	3307	3247	3277
		45°	2647	0,0	1,97	< 0,1	6242	3286	3252	3269
		Parallel	2658		1,54		6371	3288	3288	3288
C01 (bot.)		Normal	2641		2,17		6283	3286	3225	3255
		45°	2623	0,0	2,87	< 0,1	6205	3256	3256	3256
		Parallel	2629		2,61		6086	3156	3156	3156
C02	04.70 – 04.95	Normal	2650		1,85		6165	3205	3205	3205
		45°	2672	2,5	1,02	< 0,1	6401	3288	3288	3288
		Parallel	2657		1,61		6445	3304	3304	3304
C03	06.50 – 07.10	Normal	2640		2,24		6287	3294	3246	3270
		45°	2586	0,0	4,22	< 0,1	6077	3233	2940	3087
		Parallel	2629		2,63		6440	3273	3190	3231
C04	12.90 – 13.70	Normal	2330		13,69		4069	2370	2297	2333
		45°	2297	15,0	14,94	3,54	3727	2241	2055	2148
		Parallel	2292		15,11		3585	2210	2109	2160
C05	15.50 – 16.20	Normal	2646		2,00		6354	3251	3157	3204
		45°	2667	1,2	1,22	< 0,1	6410	3295	3264	3279
		Parallel	2637		2,34		6205	3226	3143	3184
C06	18.90 – 19.4	Normal	2396		11,26		4928	2709	2517	2613
		45°	2375	9,0	12,04	0,40	4864	2770	2535	2653
		Parallel	2393		11,38		4862	2674	2589	2632

* Values from J. Cochard et al., unpublished work. Measured with a steady state gas permeameter (Poroperm, by Vinci Technologies).

Instead, this low $V_{p_{avg}}$ seems to be related to local velocity drops caused by the fractures. Most of the local velocity variations observed on the cores are related to fractures, but some of the positive velocity anomalies observed in the porous cores (e.g., bottom of C04) correlate with dense/non-porous fossils embedded in the porous matrix, (**Figure 5.3, Figure 5.6**).

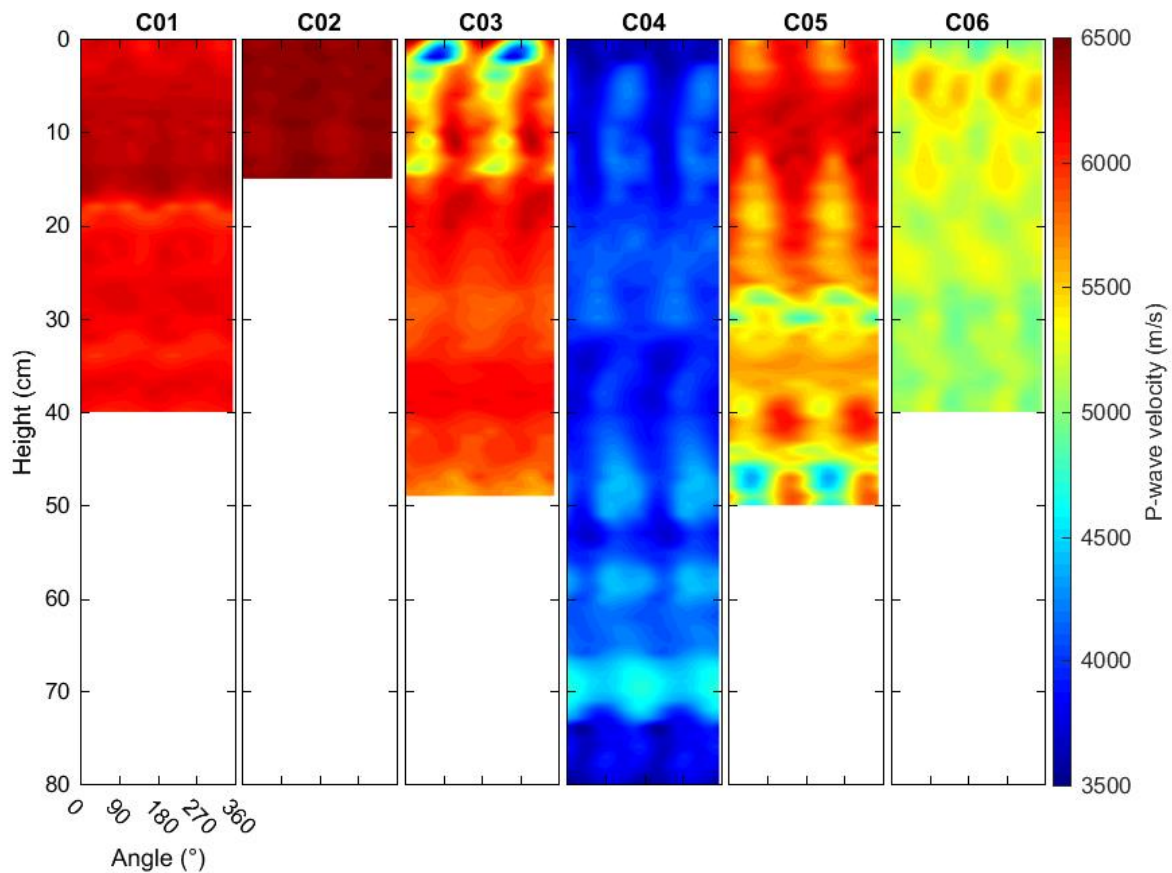


Figure 5.5. Maps of modeled P-wave velocity. Refer to Figure 5.6 which relates the velocity-anomalies to geological features.

Table 5.3. Average P-wave velocity.

Label	Porosity*	Average P-wave velocity (m/s)	
		Triplet	Core
C01	0,02 ± 0	6327 ± 74	6171 ± 108
	0,03 ± 0	6191 ± 99	
C02	0,01 ± 0	6337 ± 151	6423 ± 37
C03	0,03 ± 0,01	6268 ± 182	5863 ± 354
C04	0,15 ± 0,01	3794 ± 249	4034 ± 230
C05	0,02 ± 0,01	6323 ± 106	5707 ± 390
C06	0,12 ± 0	4885 ± 38	5199 ± 147

5.4.2.2 The anisotropy

The anisotropy determined using the plug-velocities appears negligible in most of the cases (**Table 5.4**). For all the samples the shear wave anisotropy expressed through the Thomsen parameter is $\gamma \ll 1\%$. The same observation is made for the P-wave anisotropy except for C04 ($\epsilon = 12\%$), but it is strongly suspected that the apparent anisotropy determined from this plug-set is in fact a consequence of porosity variations between plugs.

Table 5.4. Plugs-scale coefficients C_{ij} , and derived anisotropy parameters.

	C01	C02	C03	C04	C05	C06
C₁₁	107,9	110,3	109,0	29,5	101,5	56,6
C₁₃	41,6	55,5	29,1	7,5	61,3	21,8
C₃₃	107,1	100,7	104,3	38,6	106,8	58,2
C₄₄	28,6	28,9	27,6	10,9	26,8	16,6
C₆₆	28,7	29,0	27,5	10,7	26,7	16,6
ρ_{avg}	2649	2660	2618	2306	2650	2388
Anisotropy parameters						
ϵ	0,004	0,048	0,023	-0,118	-0,025	-0,014
γ	0,003	0,001	-0,002	-0,008	-0,002	-0,001
δ	-0,074	0,137	-0,167	-0,201	0,080	-0,053

$C_{ij} \times 10^9$; ρ (kg/m³)

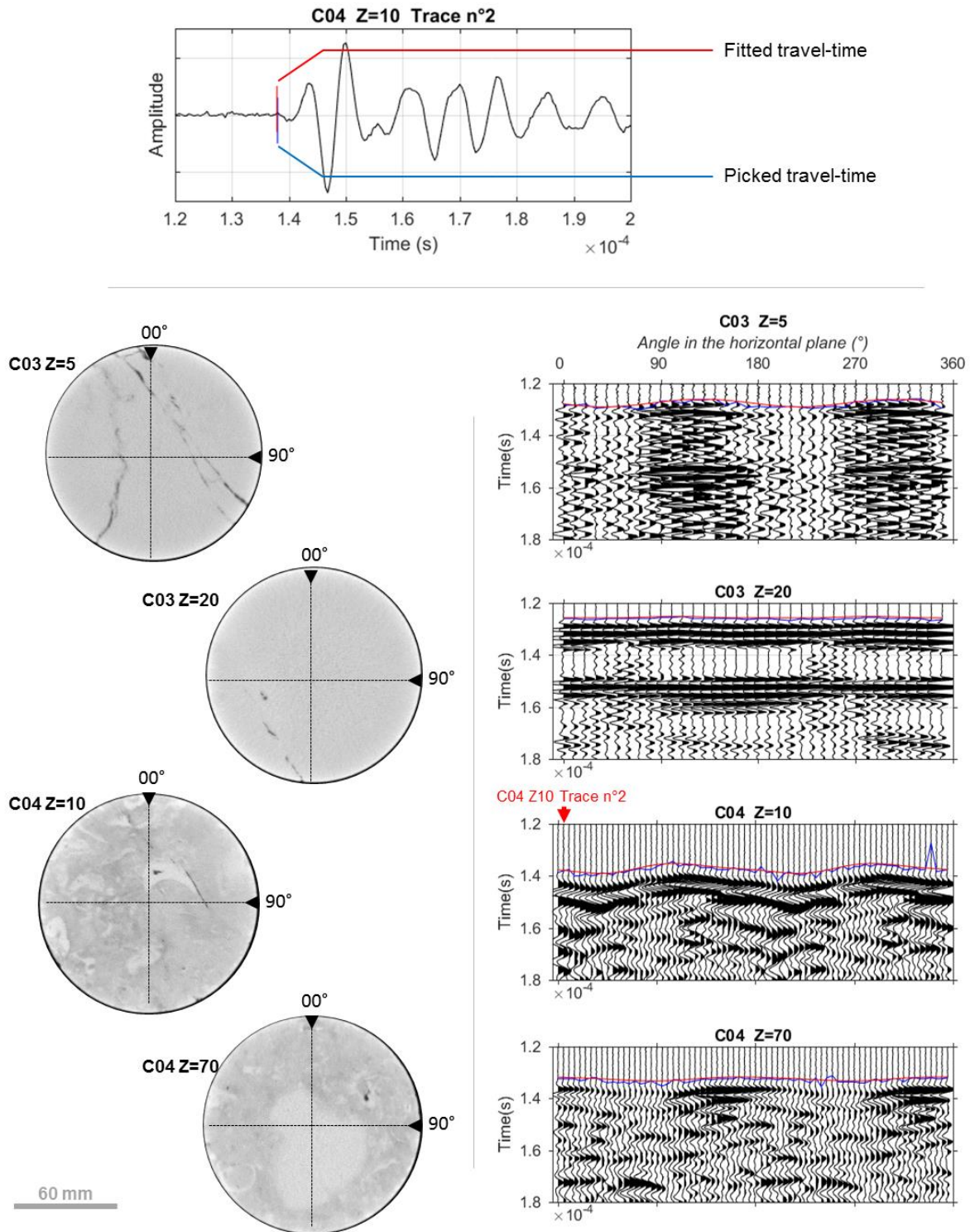


Figure 5.6. Comparison between waveforms and CT-images
 This figure illustrates the impact of both fracture-sets and/or non-porous fossils within the tight or porous matrix.

The core-scale anisotropy ϵ' is at most 2% for C01/C02, which means that for these homogeneous and low/non-fractured samples, the P-wave anisotropy is almost negligible (**Figure 5.7**). C04 and C06 show anisotropy up to 3 or 5%, these higher values are correlated to the presence of dense fossils either corals or rudists embedded in the porous matrix. In the fractured-samples C03/C05, ϵ' locally exceed 10%, meaning that comparatively to the matrix-related anisotropy, the fracture-related anisotropy is dominant. **Figure 5.6** shows that fracture-bearing parts of the cores show velocity anisotropy, and that fractures also attenuate the waveforms. Finally, the fast-velocity axis correlates with the orientation of the dominant N120 fracture-set visible in the cores, and described by Jeanne et al. (2012).

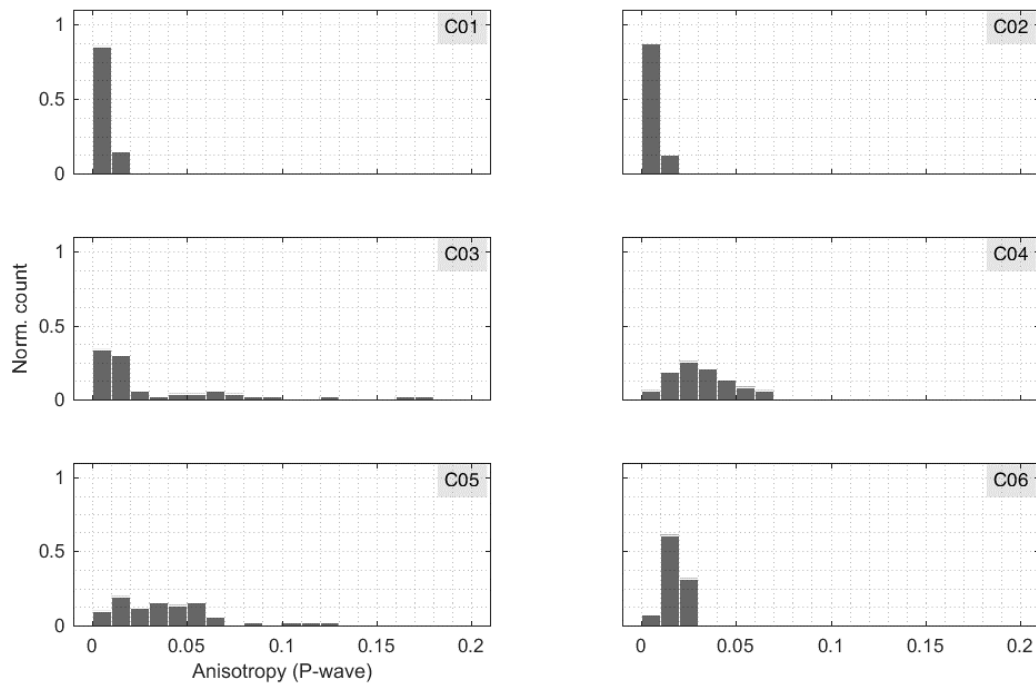


Figure 5.7. P-wave anisotropy (ϵ') at the cores scale.

5.4.3 Lessons from this two-scale approach

5.4.3.1 About the methodology

In this study we used different ultrasonic frequencies (1 MHz, and 250 kHz), thus the wavelengths (λ) and the detection limit were also different. For the plug-sets $\lambda=4.0\text{--}6.5$ mm, which is much larger than the size of the pores in the matrix, which will appear as largely homogeneous. However, this is also the scale of the large moldic/vuggy pores and of the non-porous rudist-fragments, which play as heterogeneities when present. For the cores $\lambda=1.5\text{--}3.0$ cm, which makes it of a scale comparable to heterogeneities and discontinuities observed on the CT-images. At this scale the signal related to the matrix is also averaged, and the main heterogeneities are the fracture-sets or the large fossils embedded in the porous matrix. Although the wavelengths were not the same this approach emphasized consistently and at two different scales the impact of fracturing and porosity-contrasts on the apparent anisotropy.

One may wonder about the impact of the pores fluids on our results, since the measurements were performed on the dry plugs, whereas the core were saturated with water. As discussed above only two out of the six cores were porous and may be impacted by pore-fluids substitution. And as expected, the P-wave velocity was higher in the water-saturated cores than in the dry plugs. Since, the fluids air/water have shear moduli equal to zero, the only incidence of the water saturation is on the rock bulk modulus which increases.

5.4.3.2 Anisotropy in homo- and heterogeneous facies

For low porosity facies, the porosity contrast between matrix and fossils is not significant, and the low porosity can be seen as a “homogenization” factor. Observations made on these facies whether intact (C01, C02), or fractured (C03, C05) agree with the conclusion in Wang (2002b) i.e., without fracturing these carbonates are isotropic. Hence, the effect of fracturing on these

isotropic backgrounds may in principle be handled at the larger scale using anisotropic symmetries (e.g., orthorhombic, VTI, or HTI), to calculate stiffness coefficients.

However, defining whether azimuthal velocity variations may be interpreted in terms of Thomsen anisotropic parameters is subject to caution when considering porous platform-carbonates with large and non-porous inclusions (C04, C06). In C04 porosity variations between adjacent samples make the determination of anisotropy using the three-plug procedure difficult because the assumption that plug samples are representative is no longer satisfied. Moreover, we assumed a vertical transverse isotropy symmetry to determine the anisotropy at the plug-scale but TI symmetry may not be verified in carbonate rocks at that scale (Z. Wang 2002b). Even if anisotropy could be measured reliably at the sample scale (for instance using methods in Cheadle et al. (1991); Wang (2002a); Louis et al. (2004, 2012), the parameters obtained may not be representative of the properties of the facies. Since the P- or S-wave velocities varied as a function of the porosity, it is likely that the velocity variations for this plug-set (e.g., C04) are related to porosity change rather than anisotropy. Wang (2002b) faced this issue with his most-porous sample ($\phi=16\%$), and this is probably the reason why he ignored the 10–20% anisotropy measured on this particular sample. In order to characterize accurately the anisotropy on such porous formations, one would need to determine the size of representative elementary volume, which is obviously bigger than plug-scale and carry-out the velocity measurements at this scale.

5.4.3.3 Implications for exploration seismology

Plug-scale estimation of the elastic moduli may be valid when the samples are homogeneous and have low porosity. However, our results show that for porous and heterogeneous facies the assumption that individual plugs are representative may be wrong. We showed that interpretation in terms of elastic anisotropy based only on plug-scale velocity data leads to erroneous estimation

of anisotropy, whereas more accurate values could be obtained if the measurements were carried on bigger samples. For instance, our data showed that one would estimate a P-wave anisotropy of about 10% based on the plug-velocities, whereas it barely reached 5% at the core-scale. On the other hand, the anisotropy caused by macroscopic fractures cannot be estimated from measurements on plug data but appears to reach 10% at core scale (12.5 cm), and could be even larger at the seismic scale as bigger fractures are present in the formation. Knowing that plug-velocity data are basic data that geophysicist may use to calibrate and interpret seismic reflection surveys, a five-percent error on the anisotropy can have critical influence on the basic steps of processing and interpretation of seismic data e.g., normal moveout, velocity analysis, deep moveout removal etc. (Tsvankin and Thomsen 1994).

Carbonate rocks' heterogeneity is often neglected in exploration seismic surveys even though it may have significantly impact the meaning of the data e.g., seismic reflectors, velocity values (Fournier and Borgomano 2007; Agar S. 2015) . In this study, we showed that fossils embedded in a porous matrix may increase or alter the anisotropic velocity-field at the core scale. We estimated that the contribution of the inclusions could reach up to 5%. Considering the nature of the emphasized heterogeneities (e.g., sorted-bioclasts, corals in life position), they may be organized spatially (e.g., alignment, clustering) and thus potentially induce anisotropy at even larger scales. Such effects related to grain size/sorting, and pores orientation have been observed in several studies on sandstones. For instance, Louis et al. (2005) reported that porosity contrasts and grain sorting due to sedimentary figures induce elastic anisotropy.

5.5 Conclusion

The approach developed in this paper is to compare the elastic properties on centimeter-sized (plugs) and decimeter-sized (cores) samples. We show that some characteristics of the fractures

sets (i.e. orientation, intensity) may be captured by automated acoustic measurements on cores. This method appears a promising way to confront theoretical models of wave propagation in fractured-media to data. In this study, we showed that tight carbonate facies must be handled differently from the porous ones, which are more prone to heterogeneity of porosity and of P and S-wave velocities. Working at both scales, we showed that the plugs can be considered as representative volumes for tight samples, but not for heterogeneous facies. In the latter case, the plug-sized sample do not allow an accurate estimation of the elastic anisotropy of the matrix. However, it is unclear whether the observed azimuthal-anisotropy could be correctly interpreted in terms of anisotropic elastic properties both at plug and core scales in porous platform-carbonates. Upscaling to the seismic scale (1-50 m wavelength) may be further complicated, unless attention is paid to the geometry of the observed velocity variations and their relationships with geological structures.

Section 6: Anisotropy in porous and fractured carbonates at field-scale

6.1 Abstract

Carbonate rocks have a great ability to undergo diagenetic, and tectonic alterations due to their unstable nature. Their petrophysical properties are not fully apprehended with laboratory-scaled samples, since diagenesis is the result of microscopic changes that affect centimeter to decameter-scaled areas. In this study, a multi-meter-scale crosshole acoustic-survey has been carried-out in situ, using ultrasounds with a frequency-range centered on 50 kHz, and a vertical-resolution of 10cm. The main conclusions of the study are: (I) the multi-meter scale enables measuring the elastic properties of both the matrix, and the fractured-matrix. The elastic wave velocities are of the same order as the laboratory-scale ones, mainly because of the limited number of fractures encountered. (II) A weak anisotropy, is detected, varying between + 10 % (slow axis perpendicular to strata) and -2 % (slow axis parallel to strata) and likely results from a combination of matrix heterogeneity and fractures effects. (III) In heterogeneous layered formations, variation of mean velocity with source and receivers locations significantly impact anisotropy parameter estimated by curve fitting. One should be aware of this potential bias while interpreting crosshole surveys with sparse data, especially in carbonate formations.

6.2 Introduction

The petrophysical properties of carbonate formations change as a result of diagenetic processes, and their elastic properties vary accordingly. However, a good understanding of the relations

between elastic and petrophysical properties is essential for both modeling, and inversion of seismic data e.g. (Gardner et al. 1974; Christensen and Szymanski 1991; Stafleu et al. 1994; Anselmetti, Eberli, et al. 1997; Eberli et al. 2001; Huuse and Feary 2005; Zampetti et al. 2005; Verwer et al. 2008; Xu and Payne 2009). Since the works of *Wyllie et al.*, [1956], it is admitted that the porosity is the main control on the elastic waves velocities, and this relation is known as Wyllie's time average equation (WTA). Several authors showed that the WTA partly explains the velocities in carbonates, and they argued that some of the variations are rather related to both pores' types and geometry e.g. (Anselmetti and Eberli 1993, 1999; Anselmetti, Salis, et al. 1997; Verwer et al. 2008; Baechle et al. 2009; Fournier and Borgomano 2009; Fournier et al. 2011, 2014). Nevertheless, these studies were carried-out at laboratory scale, using assumed homogeneous samples; and the elastic moduli were computed assuming isotropic media. Moreover, the velocity variations in a given sample were often interpreted as the result of either preferential alignment of both minerals and pores, or to micro-cracks resulting from the extraction (Nur and Simmons 1969; Todd and Simmons 1972). So that, the anisotropy is often neglected in laboratory-scale studies on carbonates. Meanwhile, anisotropy has often been observed at larger scale in seismic data, and *Helbig and Thomsen*, [2005] proposed a historical review about the topic. Many authors have related seismic-scale anisotropy either to the matrix, or to the fracturing of the considered formations e.g.(Backus 1962; Crampin 1981; Berryman et al. 1999; Bakulin et al. 2000a; Grechka and Kachanov 2006). In the first case, the anisotropy can be calibrated with laboratory measurements, but when the anisotropy is related to fracturing the calibration is trickier, since the scale of the fracturing is greater than laboratory samples. Indeed, some authors showed that velocities from sonic logs were significantly lower than laboratory ones, when fractures were involved (Stierman and Kovach 1979; Moos and Zoback 1983). So for fractured media, modeling

has been preferred to improve the understanding of the impacts of fracturing on the elastic properties. Nevertheless, the models are based on assumptions (e.g. number of fractures set, orientation, shape, etc.) that may have significant implications on the final results e.g. (Hudson 1981; Bakulin et al. 2000a, 2000b; Grechka and Kachanov 2006; Berryman 2008). However, despite the fact that modeling gives valuable approximations of the anisotropy, it is still difficult to decide what part is related either to matrix, or to fracturing. This issue may be addressed by studying the elastic properties of carbonate formations, from meter to multi-meter scale, since these scales enable evaluating quantitatively the signatures of both matrix, and fracturing (McCann et al. 1975; Lubbe and Worthington 2006; Worthington and Lubbe 2007; Bereš et al. 2013; C. Matonti et al. 2015).

This section aims at (i) characterizing the anisotropy of a carbonate formation at (multi-) meter-scale, and under effective-stress conditions; (ii) discussing the hypotheses about the origins of the anisotropy, and how it is transposed to the data. (iii) Studying the anisotropy as a function of the scale investigated, and its impact on the elastic properties which may be deduced therefrom.

We present the results from a crosshole acoustic-survey, which has been performed in a thick series of fractured, porous, and layered carbonates. Two probes with lined piezoelectric-transducers, were specifically designed for this study, enabling the investigation of dry-boreholes, and a good control on the raypaths. The originality of the approach lies into the scale and the resolution of the experiment; the inter-borehole distance of 2m was short enough for using ultrasounds to explore the elastic properties, from pores to fractures scales. We first give a description of the studied carbonates, and of the experimental-setting. Then, we apply various acoustic-wave formulations from simple cosine approximation to more accurate formulas, such as wave equations for transversely-isotropic media. Finally, we discuss the mechanisms behind the

measured anisotropy, and their implication on multi-scaled characterization of the carbonate formations.

6.3 Geological setting

This study took place in the south-east of France, in a former military underground-facility converted into a scientific laboratory: the LSBB of Rustrel (Low Noise Underground Lab; www.lsbbeu), where a gallery (GAS-gallery) gives a direct access to the vadose zone of a fractured-porous carbonate reservoir. The GAS-gallery floor is ~250m below the surface topography. Five vertical fully-cored boreholes named P1 to P5 were drilled in 2009 (**Figure 6.1**), and were studied as part of previous works (Jeanne 2012; Jeanne, Guglielmi, Lamarche, et al. 2012; Jeanne, Guglielmi, and Cappa 2012; Jeanne et al. 2013).

The limestones intersected by the LSBB's galleries and by the boreholes date from the Barremian and correspond to the Urgonian facies. These rudists-rich bioclastic formations were deposited within a widely extended carbonate platform during early Cretaceous. Extensive documentation and references describing the characteristics of this platform in terms of biostratigraphy, and petrophysical properties are available e.g. (J.-P. Masse and Philip 1976; Jean-Pierre Masse 1976; Jean-Pierre Masse and Allemann 1982; Jean-Pierre Masse and Fenerci-Masse 2006, 2011, 2013a, 2013b, Fournier et al. 2011, 2014; Leonide et al. 2012; Léonide et al. 2014). For the sake of this study, we will only describe the formations explored by the acoustic logging.

The **Figure 6.1** summarizes the geological background over the studied interval. The south-dipping layers intersected by the boreholes are inner-platform facies i.e. low to moderate energy, muddy or peloidal carbonate sands with abundant rudists (Leonide et al. 2012). The cores' analysis emphasized two main facies types; both are bioclastic, but their matrixes' granulometry are different (Wentworth 1922; Dunham 1962):

- The grained-facies are calcarenites (packestone to grainstone), their granulometry range from fine to coarse sand. Rudists and/or rudists-shell fragments, are the most abundant bioclasts.
- The fine-grained facies are calcilutites with their textures ranging from wackestone to packestone, they are rich in foraminifera such as miliolids and orbitolinids.

The porosity of these formations is related to diagenesis, as these facies are characterized by the lack of fabric selective porosity. *Léonide et al.*, [2014] reported for other area of the platform porosity values lower than 3% for the fine-grained facies, and between 5 to 25% for the grained-facies. These value are consistent with values published in previous works on the studied boreholes (Jeanne et al. 2013). In the case of the fine-grained facies, the intercrystalline space of their micrite is completely filled with cement. Their porosity is explained by cracks and stylolites. The grained-facies are not always porous. When they are, their porosity is related to a partial occlusion of the intercrystalline pore space during the diagenesis. It mainly is a microporosity of both, the micritic grains and cements. Other pore-types such as: moldic and vuggy pores are present in minor proportions. Inter or intragranular pores have a negligible contribution to the overall porosity (Fournier et al. 2011; Borgomano et al. 2013). From a structural point of view, the studied interval can be divided in three mechanical units: two are densely fractured (from 1 to 6m, and from 14 to 21m), and one is moderately fractured (from 6 to 14m). Despite a multi-phased tectonic history which resulted in a complex fractures network, only two sets of fractures were reactivated at a later stage, and remained open. These fractures planes are sub-vertical (dip $\sim 80^\circ$), and oriented N30 and N120. The fractures density is controlled by both porosity and the fault zone nearness (Jeanne, Guglielmi, and Cappa 2012; Jeanne et al. 2013). The open-fractures sets are located mainly in area with gradual porosity changes close to the fine-grained facies. It was interpreted that these fractures

sets were likely open or reactivated during the Pyreneo-Provençal tectonic inversion (Eocene) (Lamarche et al. 2012; Lavenu 2013). Under pressure-solution conditions, the fine-grained facies may have produced carbonate rich fluids (cf. stylolites) that migrated and precipitated nearby, occluding some of the fractures and decreasing locally the overall porosity of the porous layer.

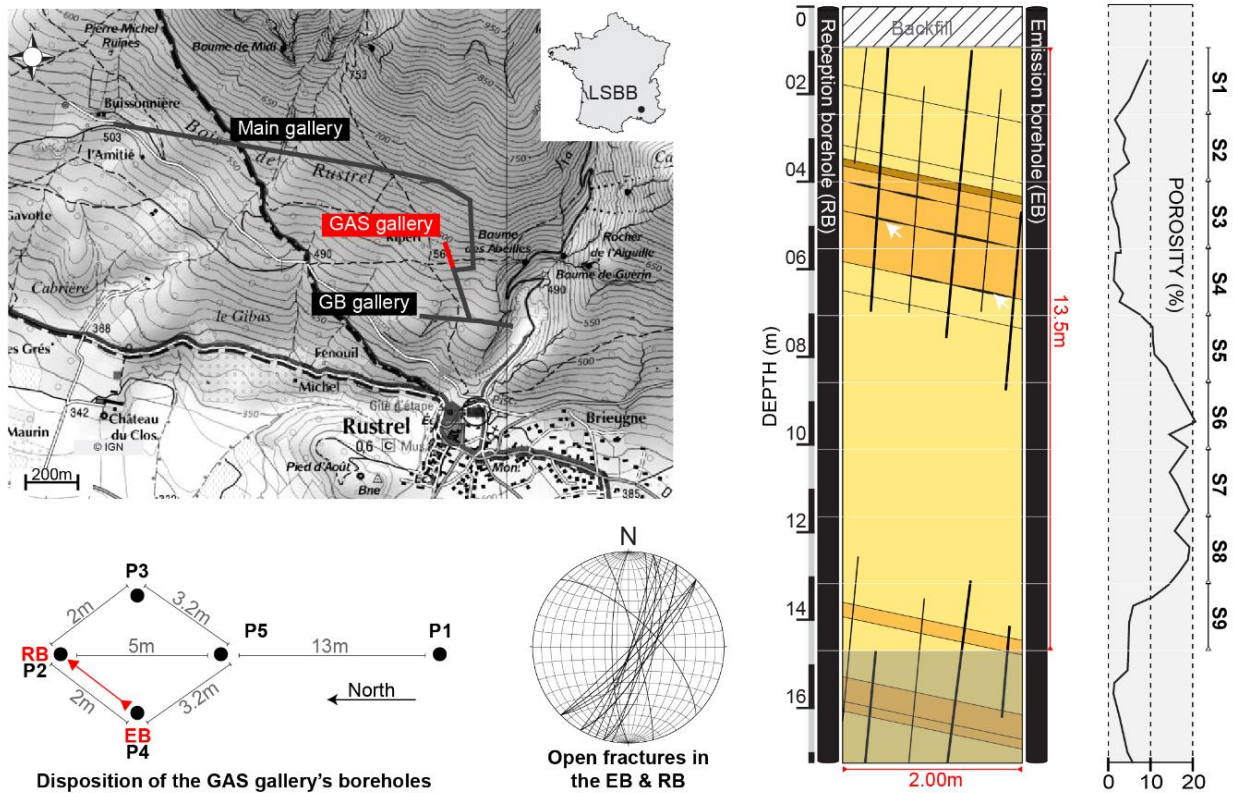


Figure 6.1. Overview of the geological setting.

The cross section shows the geological structures between the emission-borehole (EB) and the reception-borehole (RB) such as: the layers; the sub-vertical fractures, and the slickensided bed-to-bed contacts (white arrows). The light yellow is for grained (bioclastic) facies, and the orange stands for fine-grained (peloidal) facies. The (helium-) porosity log of the RB is modified from (Jeanne et al. 2013). The subdivisions (S1 to S9) delimitate the acoustic-logging section. The apparent-dip of fractures intersecting either the EB or the RB are reported in the stereonet (Schmidt projection, lower hemisphere).

6.4 Material and methods

6.4.1 Probes characteristics

A set of two acoustic probes was designed for this study, in order to perform a crosshole acoustic logging. The first probe, PETROACII-R is dedicated to acoustic waves reception; while the second one PETROACII-E is the source. These two probes will be referred in the text as the reception-probe (RP), and the emission-probe (EP), respectively. Both probes are cylindrical, and have a diameter of 0.125m. The RP is 1.75m long, has sixteen receivers lined-up vertically. The distance between the axes of two receivers is 0.01m, so that the distance between the first and the last receiver is 1.50m. The EP is 0.25m long, and has only one transmitter. The probes were designed to meet different technical criteria related to the purpose of the study, and to the experimental settings:

- Measuring ultrasonic waves in a porous media at some distances greater than 2m,
- Performing the measurements between two dry boreholes,
- Ensuring optimal coupling between the transducers and the rock,
- Real time monitoring of the transducers' position and orientation.

The core of the experimental apparatus is the acoustic acquisition system, the TDAS16, manufactured by BOVIAR (www.boviar.com). The TDAS16 is a computer-controlled acquisition system that can be divided in three parts: (1) the built-in signal generator and receiver; (2) the piezoelectric-transducers (sixteen receivers and one emitter); (3) a computer with the related acquisition-software.

The TDAS16 is intended to carry-out non-destructive investigations, mainly in the field of civil engineering. Thanks to its relatively highly-energetic emitter (0.05J), and to the wide working

range of its transducers (10Hz to ~80 kHz), this device is designed to measure acoustic waves over multi-metric distances, depending on the material properties. The TDAS16 being a turnkey acquisition-system, only few details are available on its internal design. However, the calibration tests that we carried-out, gave a comprehensive characterization of the signal. Our choice to use this tool was motivated by previous PhD works from *Matonti*, [2015], where the TDAS16 was successfully used to characterize fractured-porous limestones over distances greater than 4m.

The transducers are cylindrical. The dimensions of the emitter (\O : 47mm, L: 76mm) are different from those of the receivers (\O : 40mm, L: 43mm). The sensing element is made of piezoceramic material, while the casing of the sensing part is in aluminum. The emitter is activated by an electric pulse from the TDAS16. The transducers are directional, the calibration tests (in air, at 20°C) confirmed that the maximum amplitude is recorded in the axis of the emitter; and is entirely attenuated 30° off the axis. The transducer-to-borehole-wall adapters are made of the same aluminum as the transducers casing, in order to avoid impedance contrasts. However, the transducer-to-adapter interface slightly modify the signal, notably by an increase of the lower frequencies (<25kHz), although the main peak (~53kHz) remains close to its initial value (50kHz). The aim of the adapters will be further discussed in a next paragraph, and additional information on calibration tests are available in the supporting information.

The acquisition software enables to control the TDAS16, and to set the acquisition settings, while live monitoring the recorded signals. In this study, we kept the same settings during the entire process. The signals were recorded during 20ms, with a sampling frequency of 500 kHz. They were amplified with maximum gain available, i.e. 1024 times; and each trace was stacked 100 times.

Since we used directional contact-transducers, orientation and coupling were the most important concerns to ensure both, reliability and reproducibility of the measurements. The two probes were equipped with orientation sensors, YOCTO-3D, manufactured by YOCTOPUCE (www.yoctopuce.com). This multi-function orientation sensor features a 3D accelerometer, a 3D gyroscope and a 3D magnetometer. It enables live monitoring of the 2D inclination, the magnetic orientation, and provides a 3D orientation based on inertial measurements. A guide-rod fixed to each probe permitted to adjust the orientation according to the live-monitored orientation-sensors.

The coupling between the transducers and the borehole-wall is mechanic. When the probes are at rest, their transducers are retracted inside the probes bodies/shells. When the probes are oriented and ready to operate, the pneumatic chamber located behind the transducers, inflate and push the transducers out of the shells. The pressure exerted by the chambers (1.5 bar) push the back of the probes, which allows to maintain the transducers against the borehole-wall (**Figure 6.2**). Some original designs were developed to ensure an optimal coupling:

- Transducer-to-borehole-wall adapters,
- Independent and retractile chassis (one per transducer),
- Pneumatic coupling and locking system.

The adapters are cylindrical, and have the same diameter as the transducers. They have a curved face designed to fit the borehole curvature and maximize the contact area ($\sim 12\text{cm}^2$ per transducer). The retractile chassis enable the probes to accommodate the potential irregularity of the borehole-wall. Indeed, a transducer can move out of a few centimeters further than another if needed, and thus accommodate the roughness of the borehole-wall. The pressure exerted against the borehole-wall was enough to lock the probes, since their weights were less than 30kg. However, it was only a second-order locking because the probes were hanged and lifted by electrical winches.

6.4.2 Acoustic logging and data acquisition

The acoustic logging was conducted between the boreholes P2 and P4 (**Figure 6.1** and **Figure 6.2**). The EP was placed in P4, and the RP was placed in P2. These two boreholes will be referred in the text as the emission-borehole (EB), and the reception-borehole (RB), respectively. The emission and the reception boreholes are two meters apart, along the N20 azimuth. They are both ~22m deep. The measurements were conducted from 1 to 14.5m. Thus, the size of the investigated area is $2\text{m} \times 13.50\text{m}$. For technical reasons, the acquisition was divided into sections. Each section is 1.5m high, and is delimited by the positions of the first and the last receiver of the reception-probe (**Figure 6.2**). The acquisition for a section starts with the emitter placed face to face with the bottom receiver. Sixteen full-waveforms acoustic signals are recorded per shot. After each shot, the EP is moved 10cm up. After completion of a section the RP is moved 1.5m up. Consequently the next section overlaps the previous one (the position of the top receiver becomes the one of the bottom receiver in the next section). At the end we measured 9 sections (referred in the text as S1 to S9), and we recorded ~256 waveforms per section. Our section-based logging resulted in patterns in the rays' coverage (**Figure 6.3**). The center of the sections were better covered (the number of rays $n_{\text{Rays}} \approx 40$) than the top and the bottom borders (the worst coverage was $n_{\text{Rays}} \approx 5$). However, most of the cells were covered by more than 20 rays. In addition, there is less data for the longest emitter-receiver distance ($D_{\text{E.R}}$) than for the shorter ones, this is due to our acquisition process, e.g. the $D_{\text{E.R.}} = 2.5\text{m}$ occurs twice per section, at the top and at the bottom, whereas $D_{\text{E.R.}} = 2\text{m}$ occurs for every single shot.

In an effort to characterize the anisotropy along the studied area, we calculated the raypath-angle (ϕ). ϕ was defined as the angle between the normal to the borehole-wall, and the assumed-

straight raypath (**Figure 6.2**). For each section, the rays-coverage had an azimuthal range of 74° , as the raypath-angles ranged from -37° to 37° .

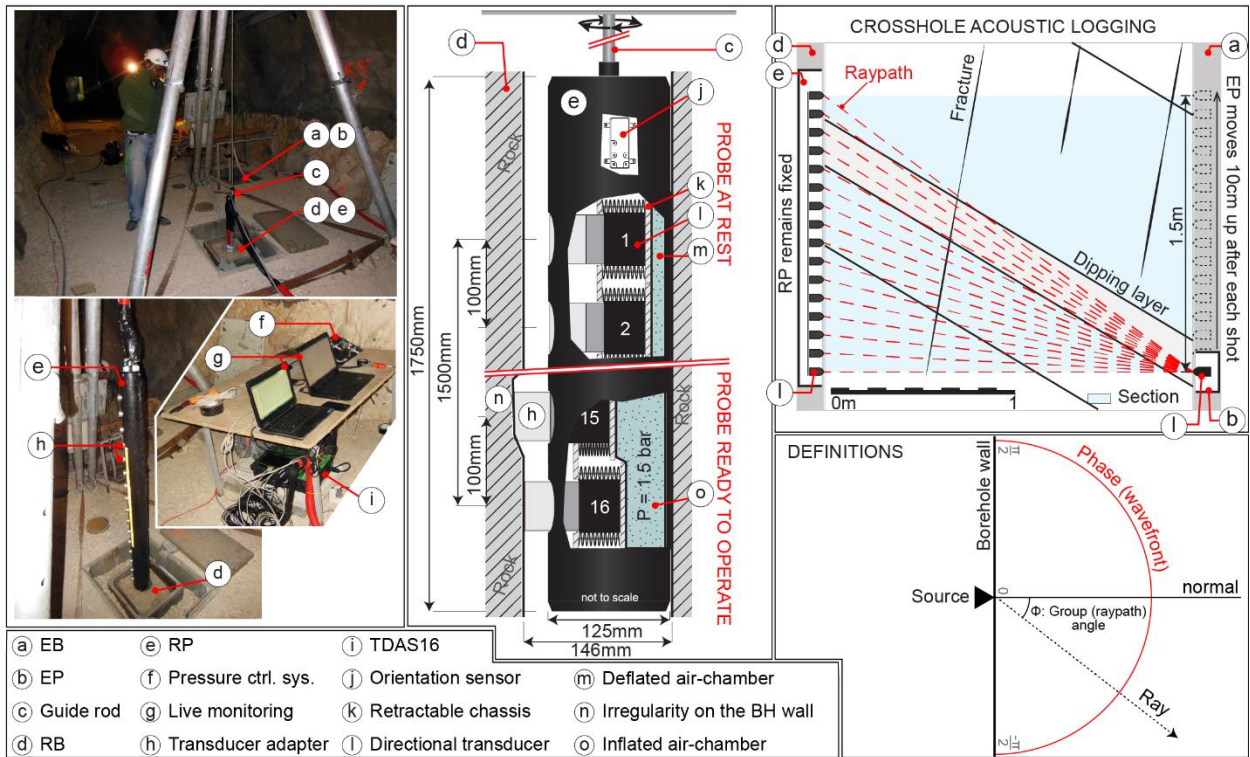


Figure 6.2. Design of the acoustic-probes, and experimental setup during acoustic logging. On the left, three photographs of the experiment showing: (1) the location of the boreholes within the gallery; (2) the monitoring desk; (3) the reception-probe out of the reception-borehole, but in “ready-to-operate” state. In the middle, a schematic view of the reception-probe design, showing both “rest” and “ready-to-operate” states; and how the reception-probe accommodates irregularity of the borehole-wall (e.g. karst). On the right, schematic view of the acoustic logging for one section. Finally, the lower-right corner shows how the raypath-angle was measured, and defines some other terms used in this paper.

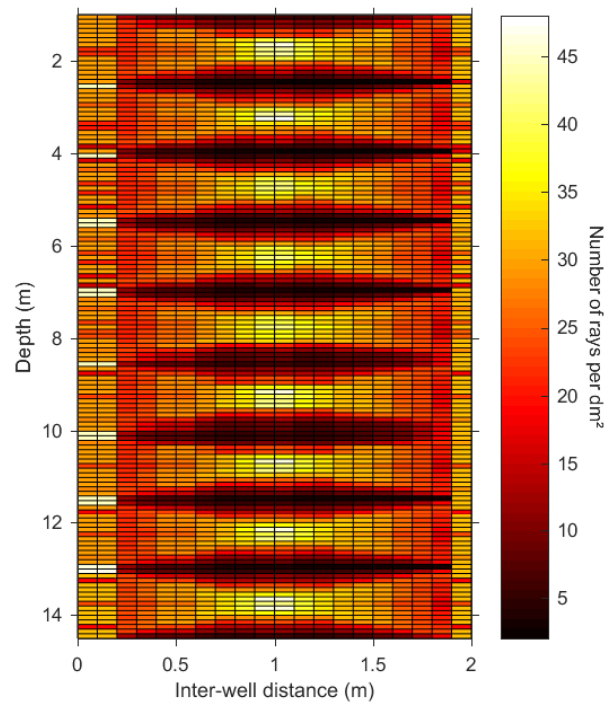


Figure 6.3 Rays' coverage, assuming straight-rays' geometry. This map shows how many times each cell ($10 \times 10 \text{ cm}$) was illuminated ($n_{\text{rays}} \geq 2$).

6.4.3 Data processing

The signal processing was limited to the strict minimum. The data underwent two corrections: (1) the correction of time delay introduced by the probe design; (2) the correction of the DC-bias. The first correction consisted in subtracting the delay ($13.2 \mu\text{s}$, after calibration tests) to the measured time. The DC-bias was corrected by centering the signal on zero, this was achieved by subtracting the signal's average value from the signal itself. We focused on the P- and S-waves travel-times, which are the signal attributes most commonly-used to characterize material properties, because they depend on the elastic moduli. The P-wave travel-time was manually picked on the waveform, by selecting the time value corresponding to the beginning of the P-phase (i.e. the time before the first point with an amplitude ten times greater than the mean noise level; **Figure 6.4**).

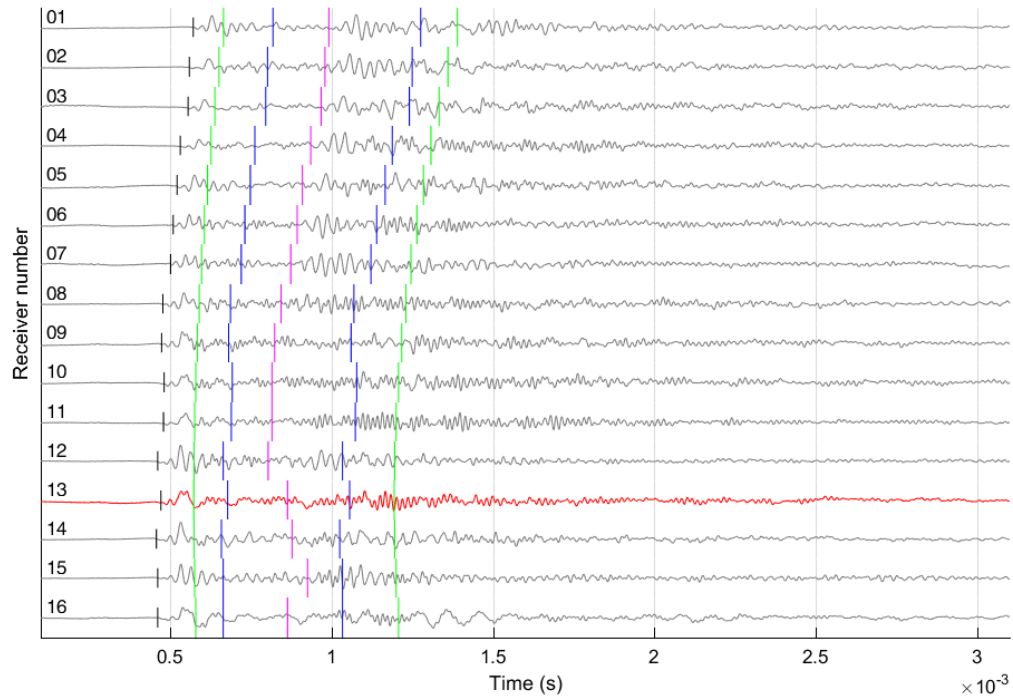


Figure 6.4. Examples of waveforms recorded for one shot. The emitter was at the same depth as the receiver n°13 (red trace). The black and the pink lines are the handpicked P- and S-waves travel-times, respectively. The green lines delimit the S_{window} based on the expected S-wave velocity range, while the blue ones delimit S_{window} based on the expected V_p/V_s ratio.

We also manually-picked the S-wave travel-time. As it is a late-arriving phase, it requires *a priori* knowledge to distinguish it, for example, from the P-wave coda given the “short” distance between emitter and receiver. First, we needed to define a time interval (S_{window}) in which the first-arrival of the S-wave is most likely to be. The bounds of the S_{window} were set according to maximum and minimum S-wave velocity and V_p/V_s ratio (i.e. 1.7 to 3.6km/s; 1.4 to 2.2, respectively) published for the studied limestones (Fournier et al. 2014).

Then the waveforms were processed in 3 steps:

- the overall quality of the waveform is rated from 1 to 4, 4 being the poorest quality,
- the S-phase is picked, then validated or re-picked,

- The quality of the picking is rated from 1 to 4 (1: reliable; 2: good; 3: acceptable uncertainties; 4: strong uncertainties).

The data from the rating were used to perform a quality control on the S-wave travel-times, and to ensure that there was no bias introduced by the picking process. Despite this methodology, the resulting S-wave travel-times have much more uncertainties than the P-wave travel-times, and hence will be interpreted with caution in this paper.

6.5 Results

6.5.1 P-wave travel-times

The relationship between the P-wave travel-times and the raypath-angles (ϕ) is shown in the Figure 6.5. A different view of the problem is given in Figure 6.6, where the P- and S-waves velocities are plotted against ϕ . The time-angle plots show a parabolic distribution of the data centered on 0° . This is consistent with our acquisition settings where 0° corresponds to the raypath normal to the borehole-wall, and is therefore the shortest emitter-receiver distance. The parabolas are more and less well defined, the sections: S1, S2, S3, S7, and S8 have a relatively low dispersion, whereas the values in S4, S5, S6, and S9 are more dispersed. One will notice a gradual time-shift correlated to the shots numbers for both S6 and S9. In S6, the bottom shots (cf. red dots) have higher time values than the top shots (cf. blue dots), whereas it is the exact opposite for the S9. The time-range (excepted outliers) can vary from a section to another, from 0.325 to 0.425ms in S1, S2, S3, and S4; and from 0.45 to 0.575ms in S7 and S8. The isovelocity-lines emphasize the fact that, in some sections, the parabolas described by the data are not symmetric. For example, time values measured for the angular-intervals $[-37^\circ$ to $0^\circ]$ and $[0^\circ$ to $37^\circ]$ can be different from

each other in spite of the raypaths symmetry (e.g.:S3, S9, etc.). The asymmetry of the parabolas is interpreted as an anisotropy of the wavefront propagating from the source towards the receivers.

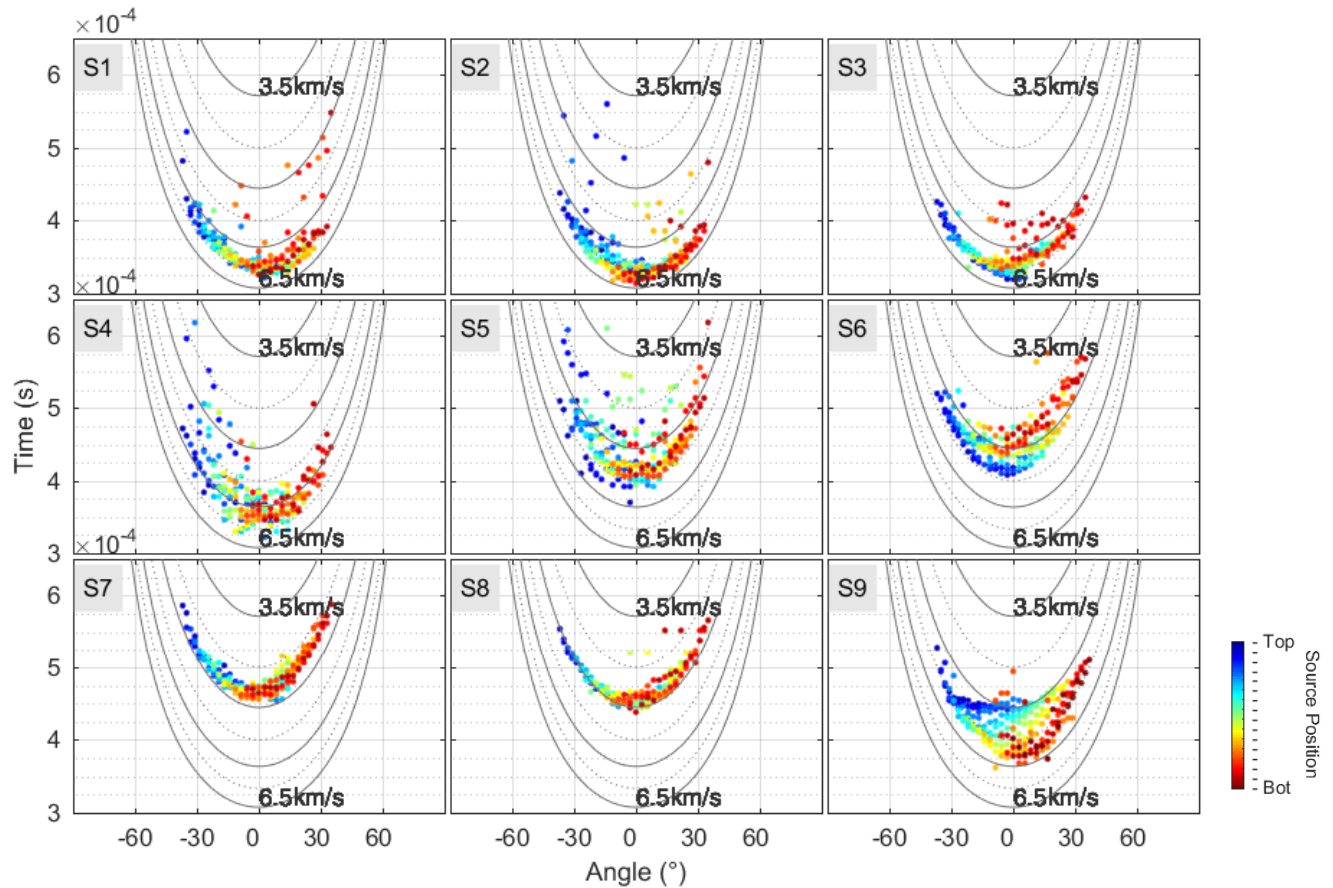


Figure 6.5. P-wave travel-times versus raypath angle. The travel times are plotted as a function of propagation angles and shot-position number. The solid and the dashed lines are theoretical times (i.e. isovelocity, range: [3.5–6.5km/s]), assuming straight-rays and seismically isotropic medium.

6.5.2 P- and S-waves velocity

A cross-plot of the P- and S-waves velocities as a function of both the raypath-angles (ϕ), and the source positions is presented in the **Figure 6.6**. The data show the angular dependency of the velocities, thus the sections are seismically-anisotropic.

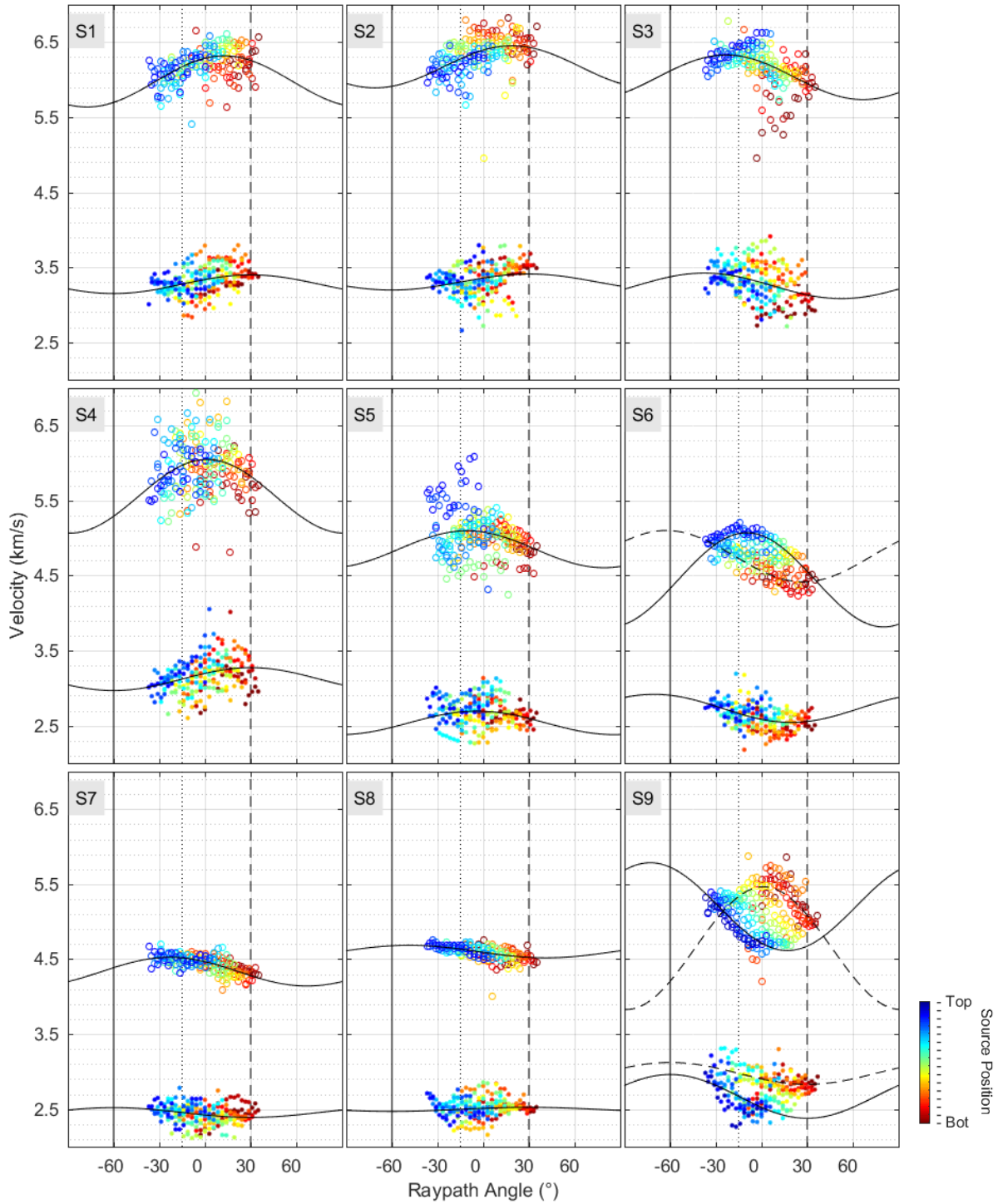


Figure 6.6. P- and S-wave velocity as a function of raypath angle. P- (open-circles) and S-waves (dots) velocity. The solid or dashed sinusoids are cosine models fitted onto the data. The vertical solid (normal), dotted (45°) and dashed (parallel) lines are relative position to bedding.

For all the sections except S4, the P-wave velocities show a good consistency within a section, or at least, for a given source's location (cf. colors). The lack of consistency in S4 P-wave velocities can be explained either by: (1) the error while picking due to fracture-related attenuation of the waveforms; or (2) by the fact that the first-arrival does not correspond to straight-rays. For all the other sections the data have a relatively low dispersion and don't have much outliers. The sections S1, S2, S3, and S4 show the highest velocities i.e. [5700 – 6500m/s], but in spite of this range, the standard deviation for a given ϕ is often less than ± 250 m/s. The standard deviation is even lower for S7 and S8 (i.e. ± 100 m/s), for these two sections the P-wave velocities range [4300 – 4700m/s] is the tightest, and has the lowest values. The last three sections S5, S6, and S9 have a P-wave velocity range of [4500 – 5500m/s]. S6 and S9 show some evident relations between the recorded velocities and the source location. In these two sections the data for each shots do not lie onto a common trend (sinusoid), unlike the others. In S9, we observe different sinusoids of same amplitude, which are shifted towards the upper-left corner as the source depth increases (blue→red). The data for S6 are also shifted, but this time towards the lower-right corner.

In terms of S-wave velocities, the analysis is less straightforward than for the P-waves because of increased uncertainties on the picking of the S-phase. Nevertheless, the main trends can be retrieved statistically, if the average values are accounted and outliers are ignored. The trends are quite remarkable from the data of S1, S2, S6 and S9, and the standard deviation is of the same magnitude as for the P-waves. For S3, S4, S7 and S8, the main trends are still visible despite their higher standard deviation. The data from S5 seem to be the less consistent than the other, since no obvious trend was identified. The S-wave velocity ranges are: [2900 – 3700m/s] for S1, S2, S3, and S4; [2300 – 3100m/s] for S5 S6 and S9; [2300 – 2700m/s] for S7 and S8.

6.5.3 Characterization of the apparent-anisotropy

The “trends” quoted in §6.5.2 can be approximated by periodic functions, where both the directions of maximum and minimum velocities are normal to each other. Since the azimuthal range was 74° during the sections’ logging, we almost covered a quarter of these sinusoids. In order to model the missing P- and S-waves velocities, we fitted a cosine function of the form of equation (1) raypath-angles, we did not account the outliers to stay closer to the main trends.

$$V(\phi) = \Delta V \times \cos(2 \times (\phi - \phi_0)) + V_0 \quad (1)$$

Where $V(\phi)$, ΔV and V_0 are expressed in km/s and correspond to: the velocity along the raypath, the amplitude of the anisotropy, and the average velocity, respectively. The raypath-angle (ϕ) and the direction of maximum velocity (ϕ_0) are expressed in radians.

The cosine-model assumes the ellipticity of the wavefront, although this assumption has some known limitations. In anisotropic media only the wavefront of the pure shear waves (V_{sh}) is an oblate ellipsoid. It is never the case for the quasi-shear waves (V_{sv}), and for the quasi-longitudinal (V_p), it happens only if $(c_{11} - c_{44})(c_{33} - c_{44}) - (c_{13} + c_{44})^2 = 0$ (Helbig 1983). Nevertheless the assumption of an elliptical wavefront is still used for simplification in recent publications (e.g. (Rao et al. 2016)). Here we made this assumption to enable further processing, and because of the short distances involved.

For most of the sections, we fitted a cosine function for all the data, but because of the shift in S6 and S9, we fitted instead two cosine functions: one for the data from the top of the section (i.e.: shot n°1 from S6 and S9, namely S6top and S9top), and another for the bottom (i.e.: shot °14 for S6 and n°16 for S9, namely S6bot and S9bot). The resulting models are plotted in Figure 6.6, and

Table 6.1 summarizes the best-fit parameters. The goodness of the fit of each models, was estimated using the root-mean-square-error (RMSE), computed after equation(2).

$$RMSE = \sqrt{\frac{\sum_{t=1}^n (V_{t_{mod}} - V_{t_{obs}})^2}{n}} \quad (2)$$

Where $V_{t_{mod}}$ and $V_{t_{obs}}$ are the modeled and observed velocities, and n is the number of observations.

The P-wave velocity models accurately reproduce the trends for most of the sections, whereas in terms of S-waves the results are less obvious for S5, S7, and S8. However these first approximations are in good accordance with the geology. The models emphasize the relations between the layering and the direction of maximum velocity, which is parallel to the layering for both S1 and S2 ($\phi_0 \approx 30^\circ$), whereas it tends to be normal to the layering for S3, S7 and S8 ($\phi_0 \approx 60^\circ$).

The amplitude of the sinusoids reflect the magnitude of the apparent-anisotropy. Generally speaking, it is $\leq 15\%$ for the P-waves ($\Delta V_p < 500\text{m/s}$), and $\leq 11\%$ for the S-waves ($\Delta V_s < 200\text{m/s}$). The sections S7 and S8 have the lowest apparent-anisotropy, $\leq 8\%$ for both the P- and S-waves ($\Delta V_p < 192\text{m/s}$, $\Delta V_s < 65\text{m/s}$), whereas it reaches up to 30% for the bottom-shot in S9 ($\Delta V_p = 818\text{m/s}$), see Table 6.1. One, can attributes this unexpectedly high apparent-anisotropy to the fact that the model are less constrained for particular shots (i.e. less data) than for an overall section. However, in these cases the data alignment show a steeper slope than for the other sections, which is consistent with a higher anisotropy.

Table 6.1. Results of the cosine fit per section

		$f(x) = \Delta V \times \cos(2 \times (\phi - \phi_0)) + V_0$			RMSE
		ΔV	ϕ_0^{**}	V_0	
P-wave:	S1	341	13	5976	169
	S2	281	19	6171	205
	S3	297	-23	6031	230
	S4	491	1	5558	347
	S5	246	-11	4852	280
	S6	–	–	–	–
	S7	192	-23	4333	353
	S8	83	-49	4602	171
	S9	–	–	–	–
	S6Top	628	-10	4444	274
	S6Bot	342	-63	4760	234
	S9Top	586	-73	5200	467
	S9Bot	818	1	4647	409
	S-wave:	S1	125	30	3273
S2		107	30	3302	188
S3		170	-38	3251	220
S4		153	30	3121	207
S5		157	-4	2537	178
S6		–	–	–	–
S7		65	-60	2455	233
S8		27	30	2498	152
S9		–	–	–	–
S6Top		187	-71	2730	139
S6Bot		187	-71	2730	139
S9Top		292	-60	2670	325
S9Bot		146	-60	2977	257

6.5.4 Stiffness tensor assuming TI symmetry

By definition a transversely-isotropic material is an orthotropic material which has the same properties in one plane (e.g. the x-y plane) and different properties in the direction normal to this plane (e.g. the z-axis). For such material, the elastic-moduli tensor (C_{ijkl}) requires only five independent components, out of twenty-one originally (general case), to fully describe its

elasticity. Moreover, because of strain symmetry the $3 \times 3 \times 3 \times 3$ tensor C_{ijkl} can be casted in a 6×6 elastic stiffness-tensor (C_{ij}) without any loss of generality, using Voigt's notation (e.g. (Thomsen 1986; Mavko et al. 2009)).

$$C_{ij} = \begin{bmatrix} C_{11} & (C_{11} - 2C_{66}) & C_{13} & 0 & 0 & 0 \\ (C_{11} - 2C_{66}) & C_{11} & C_{13} & 0 & 0 & 0 \\ C_{13} & C_{13} & C_{33} & 0 & 0 & 0 \\ 0 & 0 & 0 & C_{44} & 0 & 0 \\ 0 & 0 & 0 & 0 & C_{44} & 0 \\ 0 & 0 & 0 & 0 & 0 & C_{66} \end{bmatrix} \quad (3)$$

The five components of the stiffness-tensor for a vertical transversely-isotropic (VTI) material are directly related to the phase velocities of the three modes, i.e.: quasi-longitudinal (V_p), quasi-shear (V_{sv}), and pure-shear (V_{sh}), by the relations in equations (4) and (5) (6).

$$V_p(\theta) = \left(c_{11} \sin^2 \theta + c_{33} \cos^2 \theta + c_{44} + \sqrt{M} \right)^{1/2} (2\rho)^{-1/2} \quad (4)$$

$$V_{sv}(\theta) = \left(c_{11} \sin^2 \theta + c_{33} \cos^2 \theta + c_{44} - \sqrt{M} \right)^{1/2} (2\rho)^{-1/2} \quad (5)$$

$$V_{sh}(\theta) = \left(\frac{c_{66} \sin^2 \theta + c_{44} \cos^2 \theta}{\rho} \right)^{1/2} \quad (6)$$

Where $M = [(c_{11} - c_{44}) \sin^2 \theta - (c_{33} - c_{44}) \cos^2 \theta]^2 + (c_{13} + c_{44})^2 \sin^2 2\theta$, ρ is the density, and θ is the phase's angle, i.e. the angle between the wave vector and the unique-axis.

The five components of the stiffness-tensor for a VTI material can be obtained from five velocity measurements: $V_p(0^\circ)$, $V_p(90^\circ)$, $V_p(45^\circ)$, $V_{sh}(90^\circ)$, and $V_{sh}(0^\circ) = V_{sv}(0^\circ)$ (Mavko et al. 2009).

$$c_{11} = \rho V p_{(90^\circ)}^2 \quad (7)$$

$$c_{13} = -c_{44} + \left[4\rho^2 V p_{(45^\circ)}^4 - 2\rho V p_{(45^\circ)}^2 (c_{11} + c_{33} + 2c_{44}) + (c_{11} + c_{44})(c_{33} + c_{44}) \right]^{1/2} \quad (8)$$

$$c_{33} = \rho V p_{(0^\circ)}^2 \quad (9)$$

$$c_{44} = \rho V s h_{(0^\circ)}^2 \quad (10)$$

$$c_{66} = \rho V s h_{(90^\circ)}^2 \quad (11)$$

In this study we assume that the southward-dipping layers are transversely isotropic. This leads to a tilt of the symmetry axis with respect to the earth surface. In this assumption of tilted transverse isotropy (TTI), the stiffness tensor for vertical transverse isotropy corresponding to the equation (3) has to be rotated in accordance with the orientation of the symmetry axis (Tsvankin 2001). To avoid any manipulation of the stiffness tensor, we implicitly make this rotation by defining the unique-axis, as the normal to the stratigraphic-layers. For simplification angles discussed below are defined accordingly, so that 0° is normal to the layers, whereas 90° is parallel.

For each sections we computed the elastic-moduli after equations (7) to (11). The azimuthal range of our rays-coverage was 74° (cumulative) but included two out of the three required directions (i.e. 45° and 90°) for calculation of the stiffness tensor. However, we got around the missing data of the 0° direction by approximating the missing velocities using equation (1) with the appropriate parameter from **Table 6.1**. We also computed the phase velocity using equation (4) to (6). For a direct comparison with the experimental data, we converted the phase-angle (θ) into the equivalent raypath-angle (ϕ) using the relation $\phi = \theta + \phi^*$, where ϕ^* is the raypath-angle normal to the layering (**Figure 6.7, Table 6.2**).

Table 6.2. Summary of the stiffness-tensor components, and anisotropy parameters.

	S1	S2	S3	S4	S5	S6	S7	S8	S9	S6Top	S6Bot	S9Top	S9Bot
Stiffness coefficients:													
C_{11} ($\times 10^9$)	98,5	108,0	94,2	90,0	59,9	–	41,4	46,1	–	50,2	45,1	48,1	66,0
C_{13} ($\times 10^9$)	51,3	52,5	55,0	59,9	40,3	–	21,0	21,5	–	35,2	10,8	6,1	39,1
C_{33} ($\times 10^9$)	81,6	91,3	99,6	74,3	58,1	–	43,4	49,3	–	45,3	60,0	72,2	45,1
C_{44} ($\times 10^9$)	24,9	26,7	30,3	23,4	15,4	–	14,3	13,7	–	20,4	19,5	19,3	24,9
C_{66} ($\times 10^9$)	29,0	30,4	26,1	28,4	16,9	–	12,9	14,3	–	15,8	15,1	12,5	20,4
ρ (kg/m ³)	2516	2612	2663	2652	2505	–	2257	2250	–	2418	2308	2201	2551
Thomsen's parameters:													
ϵ	0,10	0,09	-0,03	0,11	0,02	–	-0,02	-0,03	–	0,05	-0,12	-0,17	0,23
γ	0,08	0,07	-0,07	0,11	0,05	–	-0,05	0,02	–	-0,11	-0,11	-0,18	-0,09
δ	0,28	0,18	0,18	0,57	0,26	–	0,16	-0,01	–	1,10	-0,15	-0,28	2,01

* $\rho = -0.0262 \cdot x + 2706.1$, where x is the percentage of porosity ($r^2=0.9717$), adapted from Jeanne,[2012].

ϵ : P-wave anisotropy; γ : S-wave anisotropy; δ : Thomsen's parameter;

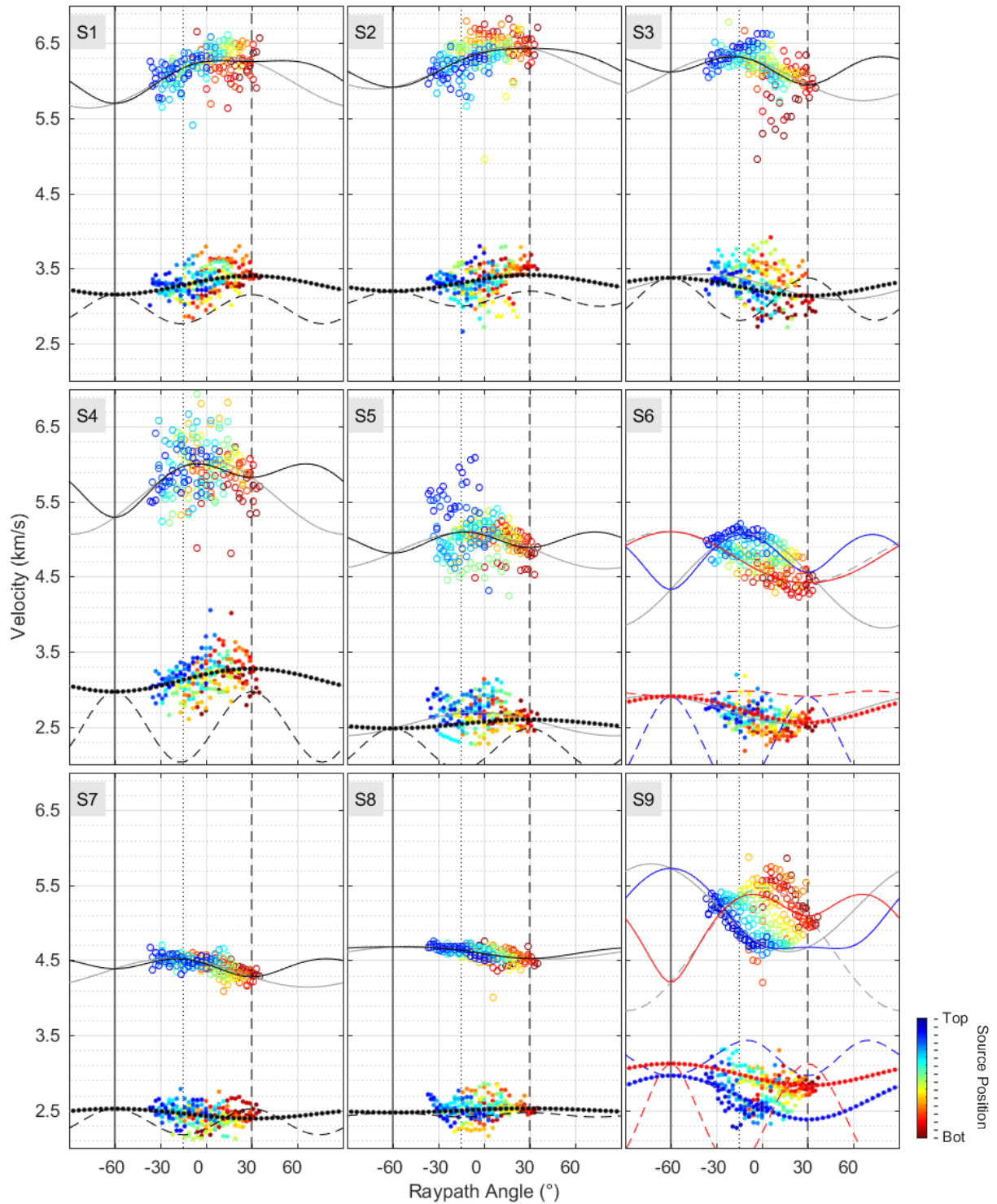


Figure 6.7. Velocity models computed using the stiffness coefficients. The solid, the dotted and the dashed models stand for: $V_p(\phi)$, $V_{sh}(\phi)$, and $V_{sv}(\phi)$, respectively. The cosine models (grey) are also plotted for comparison.

In most cases, the wave-models computed from the stiffness coefficients, reproduce quite accurately the main trend in the data distribution, and this validate the assumptions made previously. Finally, we calculated the three dimensionless quantities ε , γ , and δ that characterize the anisotropy (Thomsen 1986), which are given by the equations below. And one can see from **Table 6.2** that the anisotropy is weak anisotropy for all the sections.

$$\varepsilon \equiv \frac{c_{11} - c_{33}}{2c_{33}} \quad (12)$$

$$\gamma \equiv \frac{c_{66} - c_{44}}{2c_{44}} \quad (13)$$

$$\delta = \frac{(c_{13} + c_{44})^2 - (c_{33} - c_{44})^2}{2c_{33}(c_{33} - c_{44})} \quad (14)$$

6.5.5 Forward modelling

6.5.5.1 Models setting

We discuss the effects of both fractures and layers, using synthetic modeling which emphasize the impact of the settings on the apparent-anisotropy. We used two 2D velocity-models (i.e. “layered” and “faulted”) tested under both assumptions of isotropic and transversely-isotropic backgrounds. This model is not a fitted model but a theoretical case example which purpose is to show the relative effects of intrinsic elastic anisotropy and of heterogeneities associated with sedimentary layering and large scale (i.e. larger than section height) fault or fracture zones on the apparent anisotropy, evaluated from the cross-hole travel time data. An arbitrary value, of 10%, was selected for the anisotropic background, and the orientation of maximum velocity was set to be -60° . The velocity of the layers, also arbitrary, were $V_1=4.7\text{km/s}$, $V_2=5.2\text{km/s}$, and $V_3=5.7\text{km/s}$,

for the layered model; or $V_1=5.7\text{km/s}$, and $V_2=5.2\text{km/s}$, for the faulted model presented in **Figure 6.8**.

- The first model is that of a “layered” medium, where the velocities within each layer are assumed homogeneous and related to the matrix properties. Assuming the same experimental-settings as in S9, i.e. three tilted intervals (or layers) with different thickness, and different average-velocities (V_n) such as $V_1 < V_2 < V_3$.
- The second model is that of a “fault” affecting a homogeneous medium. The fault is assumed to be cutting the entire section, and to tighten towards the bottom of the model. We assumed the fault’s core to have a lower velocity (V_2) than the intact rock (i.e. $V_2 < V_1$)

For both models, we assumed the rays are not deviated at the interfaces, and that the straight-ray’s velocity (V_{ray}) can be calculated using equation (15).

$$V_{ray} = \frac{L_{ray}}{\sum_{n=1} l_n} \times \alpha \quad (15)$$

Where L_{ray} and l_n are respectively the lengths of the ray, and of the segment from that ray which cross the interval n ; and where α is an anisotropic-coefficient ($\alpha=1$, in case of isotropic background) calculated using $\alpha(\phi) = 0.05 \times \cos(2 \times (\phi - \phi_0)) + 1$, with $\phi_0 = -60^\circ$. The results of the simulation upon these synthetic-models are presented in **Figure 6.8**.

For the simulation in the assumption of a homogeneous media ($V_1=V_2 (=V_3)$), both models do not show any velocity variation for an isotropic background. Conversely, if an anisotropic background is assumed, the ray-velocity is the product of the medium velocity with the anisotropic-coefficient ($0 < \alpha \leq 1$), such that $V_{ray} = V_1 \times \alpha$.

For more readability, let ζ designate the function that relates the velocity to the raypath-angle, such as $\zeta \rightarrow V = f(\phi)$. If some velocity contrasts are assumed, even as low as 100m/s, (i.e. $V_1 \neq V_2$ ($\neq V_3$)), then ζ is translated as a function of the source location (cf. shot-related shift). The direction of that shift depends on the location of the “slowest velocity-interval” in regard of the “faster” one(s).

6.5.5.2 Synthetic models

The synthetic layered-model (**Figure 6.8**) shows that the difference of 1km/s between V_1 and V_3 , causes an apparent-anisotropy ranging from ~5 to 10% (i.e. 230–500m/s). Regardless to the background isotropy/anisotropy, the presence of at least two intervals of different average velocities introduces some apparent-anisotropy, and shot-related shift. When the background is isotropic, the shift is horizontal, and the amplitude of apparent-anisotropy only depends on the input velocities and the $V(\Phi)$ curves are strongly shifted as a function of emitter location. For a transversely-isotropic background, the shift comparable in amplitude, but and the background anisotropy increases the overall apparent-anisotropy.

Finally, location of the source is determinant in the amount of apparent-anisotropy. Since the relative distance traveled across an interval depends on both the raypath-angle and the source’s location, the greater is the distance across the faster intervals the higher the velocity. The layers’ thicknesses and the velocity variation between the intervals determine the “shape” of ζ . The interfaces between two intervals (or layers), are materialized by break-points in ζ . Thick intervals imply the predominance of one over the two others at the section’s scale, consequently, there are few velocity-variations, so ζ tends to be linear if the background is isotropic, otherwise it follows the trend given by α .

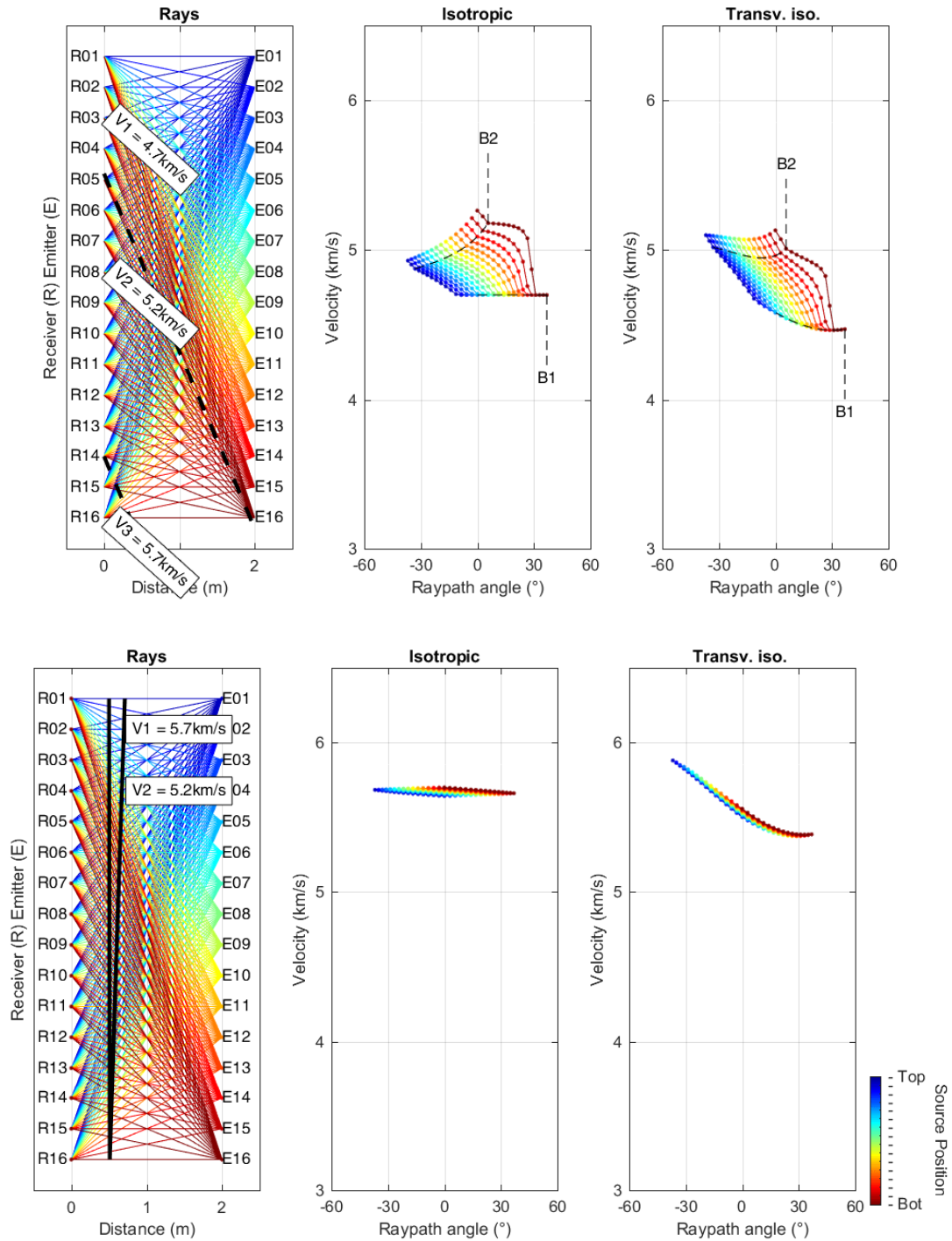


Figure 6.8. Synthetic examples of apparent-anisotropy caused by heterogeneities.

The first row shows the result for a layered-model assuming straight rays, crossing an isotropic or transversely-isotropic background. On the rays plots, the black dashed lines denote the layer boundaries, which are materialized by breaking points in the velocity plots (i.e. B1 and B2). The 2nd row is for the faulted-model, the black solid line delimit the fault core.

In the synthetic faulted-model, where an anisopachous fault with a fault core 500m/s slower than the intact-rock, is considered (**Figure 6.8**). The apparent-anisotropy is <1% for an isotropic-background, whereas it is slightly higher than 10% for the anisotropic-background. Only weak shift of ζ is observable in that conditions. In order to observe a shift similar to that observed in our data (cf. S9), the fault core would need to be 2.7km/s slower than the intact-rock. The core of the fault is a finite area, with a size much lower than rest of the model, consequently, the distance across the fault core is much lower than the length of the raypath. Hence, we can illustrate with this example how a localized heterogeneity can induce some apparent-anisotropy. However, the occurrence of a fault like this within the studied area is unlikely. Since we used equation (15), the model can also represent the impact of a fracture network, where the fracture density decreases from the top to the bottom of the model, such model suits the geological observations; and one can see the thickness of that fault as the cumulative sum of distance across the different fractures encountered by the ray.

Forward modeling of travel-time thus shows that geometrically simple heterogeneities at the scale of the investigated sections will always result in variations of the ζ curves with emitter location. The effect of formation scale heterogeneities is apparent in travel-time data from section S3-to-S6 and S9 and contributes to the apparent anisotropy values in these intervals. However ζ curves are superposed for sections S1-S2 and S7-S8 which indicates that the anisotropy measured in these intervals is in large part related to the intrinsic elastic properties of the rock mass.

6.6 Discussion

It is admitted that one condition to have an anisotropy in layered media, is that the wavelengths must be much greater than the layers' thickness (Backus 1962; Berryman 1979). In our case, the wavelengths used were about 12cm or less, whereas the layers were meter-scaled. The intrinsic

anisotropy we observe should thus be attributed either to fractures or to the matrix anisotropy at a smaller scale (pores or mineral orientation) (Hudson 1980, 1981; Rüger 1997; Tsvankin 1997; Guéguen and Sarout 2009). However, data from several sections (e.g. S4 to S6 and S9) are influenced by velocity gradients, correlated with porosity variations between layers. The synthetic modeling showed in these sections that the layering can explain a large part of the apparent-anisotropy, and that its signature is a shifting related to the source position.

In section S1 and S2 and in section S7 and S8 the effect of layering is minimal. S1 and S2 correspond to a relatively high velocity layer. This layer has about 10% P-wave velocity anisotropy (ϵ) with maximum velocity more or less along the stratification. Sedimentary rocks most often have slow axis perpendicular to stratification. Shales in particular, tend to develop a high anisotropy during compaction from porosity fabric (pore shape and orientation) and clay mineral re-orientation (Thomsen 1986; Johnston and Christensen 1995). Calcite minerals are also highly anisotropic (Chen et al. 2001) but limestone is not thought to develop strong preferred orientations during burial and diagenesis as pelitic rocks do. In the context of LSBB, the cracks are expected to be dry and thus the reduction of elastic modulus will be maximum perpendicular to crack orientation (Hudson 1980, 1981; Rüger 1997; Tsvankin 1997; Guéguen and Sarout 2009). Despite that fractures sets cause orthorhombic symmetry rather than transverse isotropy (Grechka and Kachanov 2006; Berryman 2008), we postulate that the transverse isotropy approximation is still relevant here, seeing that the velocity models are quite consistent with the experimental data (at least for the P-wave velocities, **Figure 6.7**). The anisotropy observed in S1 and S2 could thus be explained (i) by the stress relief normal to the layers causing the opening of stratigraphic-joints, (ii) the presence of open stylolithes (Baud et al. 2016), (iii) a contribution to the anisotropy from the rock microfabric. However, stylolithes are mostly observed in sections S3, S4, S5, S6, and S9,

where anisotropy is not as well defined. Sections S3 to S5, hold the highest density of fractures, both layer parallel and layer orthogonal (Figure 1 and *Jeanne et al.*, [2013]) and are also the sections where the travel-time scatter is highest. Moreover in S3, a shift of $V_p(\phi)$ is observed to lower values downward but no systematic variation of matrix porosity is observed downward over the same interval. It thus seems likely that the abundance of layer orthogonal fractures in this interval as well as in S4 and S5 contributes both to increase the heterogeneity and to lower the layer parallel velocity. The negative anisotropy ($\varepsilon = -2$ or -3 %) in section S7 and S8 remains puzzling. Although the anisotropy detected is small, it can be considered reliable because of the low scatter of the data in this interval and the consistency of $V_p(\phi)$ for successive shots. This interval is the most porous and holds few macroscopic fractures, which leaves porosity fabric and mineral orientation as the most likely explanations for this anisotropy.

Finally, we found interesting to compare our results with other works conducted on the same carbonates, but at different scales, i.e.: seismic-scale ($\leq 180\text{m}$) (*Bereš et al.* 2013); field-scale ($\leq 13.5\text{m}$; *this study*); and laboratory-scale ($= 2.54\text{cm}$) (*Fournier et al.* 2014). We computed the stiffness coefficient for *Fournier et al.*, [2014], for the same facies as those in the gallery, assuming the samples were isotropic (i.e. $C_{11}=C_{33}$, $C_{13}=C_{11}-2C_{44}$, and $C_{66}=C_{44}$). Table 4 shows the stiffness coefficients estimated by *Fournier et al.* [2014], *Bereš et al.*, [2013] and by the present study.

Table 6.3. Range of the stiffness coefficients for the Urgonian limestones

	<i>Bereš et al.</i> , [2013]	This study	<i>Fournier et al.</i> , [2014]
C_{11} ($\times 10^9$)	44,9 - 36,9	108,0 – 41,4	110,4 - 26,8
C_{13} ($\times 10^9$)	19,7 - 18,3	52,5 – 6,1	52,7 - 9,2
C_{33} ($\times 10^9$)	69,2 - 65,9	99,6 – 43,4	C_{11}
C_{44} ($\times 10^9$)	19,7 - 18,3	30,3 – 13,7	34 - 7,9
C_{66} ($\times 10^9$)	15,4 - 14,8	30,4 – 12,5	C_{44}

Expectedly, the coefficients show an increased variability when the scale decreases, this can be easily explained, if the averaging effect of the scale is accounted. Indeed, different parameters such as facies, grains sorting, and diagenesis are all responsible of the heterogeneity of carbonate rock at smaller scale. Hence the smaller the samples the greater the probability of sampling particular features. Accordingly, the elastic properties are averaged with the increasing size of investigation area. Nevertheless, even when major fractures are present in the sections, our stiffness coefficients are closer to the laboratory ones than that from seismic-scale. This may suggest that the meter-scale is the scale where fractures start to be sampled but do not dominate the signal, which enables to capture both signatures of the matrix and the fractures. In addition, the faults present in the area (Jeanne 2012), and which did not affect our measurements (no fault between the tested boreholes), but were unavoidably measured by *Bereš et al.*, [2013], may have played a role even bigger in lowering the velocities than the fractures sets alone. For example *Al-Harrasi et al.*, [2011] related the anisotropy in the Natih carbonate reservoir (Oman) the rock type and proximity to major faults. So that, the coefficients presented in this study may be representative of the rock matrix and of the fractured rock, whereas at seismic-scale, the presence of major faults may have obliterated the effects of the matrix (and perhaps of the fractures sets), hence, the seismic-scale coefficients may be more representative of the faulted rock mass.

6.7 Conclusion

In this study, we developed two acoustic-probes in order to characterize, in situ, a microporous carbonate series from meter to decameter scale. At the first order, the average velocity is controlled by the porosity of the matrix, while the standard deviation from that mean value is related to the anisotropy. This weak anisotropy is only weakly related to the fracturing, but is complicated by variations in the fractures density. In addition, the acoustic velocities measured at the meter-scale

are the signature of both the rock matrix, and the fractures sets, but at greater scale some faults with highly deformed cores, may impact the velocities dramatically up to provoke a loss of the information about the matrix. This study thus highlights the scale effect between a micrometer-to-decameter scale and a hectometer-to-kilometer scale in this carbonate formation. Another interesting conclusion of this study is to highlight the effects of the seismic source location on the measured anisotropy in heterogeneous media. This effect may disappear with the averaging effect of an increasing scale. However one should be aware of this effect when considering crosshole data with sparse shots in contrasted formations.

Conclusions and perspectives

During this work, we studied the petrophysical and elastic properties of a carbonate reservoir at three different scales, namely the plugs (centimeter), the cores (decimeter), and the field (multi-meter) scales. According to the assumption generally used in seismic exploration, plug-scale elastic properties should be representative of the seismic scale properties. Here, we show that upscaling plug-scale properties is far from being that simple. We show that the estimation of the elastic wave velocity and of the anisotropy suffer from scale effects, even for scale difference as small as centimeter to decimeter. This is due to the fact that the greater the scale the higher the impact of the heterogeneities and of fracturing. Despite the fact that the plugs scale properties seem to give the average values of the P- and S-wave velocity, it only gives the properties of the intact matrix. At even larger scale, the matrix properties may be overwhelmed by that of the fracturing and/or the heterogeneity.

In our work, we showed that the intact matrix properties still dominate at our field scale (max distance covered by a ray ~ 2.5 m), but in some case they were significantly altered by fracturing (anisotropy up to $\sim 15\%$). This ~ 500 m/s variation of P- or S-wave velocity is huge considering that the volume of rock studied does not allow to investigate the impact of large-scale heterogeneities such as bedding contrasts, sedimentary bodies, or more importantly damaged fault zones, fracture corridors etc. All these examples can possibly have a larger impact on the velocities than the fracture-sets considered here. As a result it may exist a threshold scale above which the acoustic wave velocity may be completely dominated by the effects of fracturing/faulting and large-scale heterogeneities.

Conducting multi-scale acoustic investigations as proposed here, but at field scales ranging from meter to hectometer may allow to determine the representative volume of rock needed to ensure matching interpretation of “geologically-explained” elastic properties and the seismic data. This will require to tackle, beforehand, the issue of wave attenuation by adapting the frequencies to the scale studied. However, this work offers several perspectives that may be grouped into short term, and mid-to-long term objectives.

The short term perspectives could involve further processing of the data collected during the PhD. For example, in this thesis we analyzed the data in terms of acoustic wave velocities and velocity anisotropy. The next stage of the processing (cf. paper in preparation) will include, first, the estimation of the anisotropy using the travel-times instead of the velocity. This new approach of the dataset should allow us to mitigate the uncertainties introduced by the length of the raypath in our calculation. Indeed, during the study, we have been assuming straight raypaths for simplification, but we found out that the studied carbonates were anisotropic. The presence of anisotropy indicates that straight raypaths are unlikely (at least in some cases). Secondly, we proposed a tomography of the reservoir using a probabilistic approach, and assuming isotropy. Since we demonstrated the presence of anisotropy, the next logical step is computing the anisotropic tomography using a deterministic approach. Thirdly, it would be worth modeling the seismic wave propagation in the formation, using the a priori knowledge we gained from this study. For example the model may integrate the velocity variation induced by the porosity gradient, and the varying strength of anisotropy induced by the fracturing gradient. Forward modeling of the wave propagation through a detailed stratigraphic grid giving the elastic properties (including anisotropy) may be a suitable method to achieve this. A further objective, will be to carry out full-waveform inversion using our data. This method goes beyond the classic tomography techniques

which use only the travel time kinematics, by using additional information provided by the amplitude and phase of the seismic waveform.

The developments at mid-term to long term include the modifications or adaptations needed to improve the methodology proposed in this thesis. The first part concerns the laboratory scale. For example, the acoustic measurement in the acoustic tank could be improved to enable anisotropy characterization in several directions. Indeed, our measurements have been carried out only in the horizontal plane. This gave us access to the azimuthal anisotropy, but not to the potential anisotropy caused by the tilted layering. Coupling the azimuthal (horizontal plane) and multi-dip (other than horizontal) can be achieved by modifying the angle of the transducer during the experiment. Our laboratory study lacks for S-wave velocity at the core scale, mainly because we used hydrophones that were not able to record the S-wave through water. A straightforward solution to address this issue would be to use contact transducers instead, which will enable to record both P- and S-wave and also the converted modes. Potentially, offering to carry-out full waveform inversion at the cores scale as well.

At the plugs scale, some improvements can be made to characterize the anisotropy. Despite it couldn't be finely characterized because of the mean size of the heterogeneities in our samples, the anisotropy of finer (heterogeneous) samples may be measured using techniques such as the Resonant Ultrasound Spectroscopy (RUS). This technique relies on the fact that solid objects have natural frequencies at which they vibrate when mechanically excited. The natural frequency depends on the elastic properties, size, and shape of the object. The RUS exploits this property of solids to determine the elastic tensor of the material. The great advantage of this technique is that the entire elastic tensor is obtained in a single rapid measurement.

The second part of the mid-term developments could lead to the second-generation prototypes of field acoustic probes. Indeed, one of the main constraints during the probes conception was that we had to use an existing apparatus (TDAS16). On the one side, this tool enabled to (relatively) rapidly set up the crosshole experiment. But on the other side offered little control, and no flexibility on the physical parameter such as the type of source signal, the frequency range etc. Moreover the transducers are specifically designed for P-wave measurements even if they also measure the S-wave. However, the absence of dedicated two-component shear wave transducers limited drastically our interpretation of the anisotropy of shear wave. For example in the most interesting case i.e., strongest anisotropy (S9, cf. acoustic logging) we suspected shear wave splitting to occur. Unfortunately we were not able to distinguish the pure shear and the quasi shear modes of the S-wave, so we couldn't interpret further the data. In the future, another acquisition system should be employed for better control of the signal and to enable proper analyses of the frequency content of the signal recorded at the field scale.

Despite the effort we deployed to ensure an optimal contact between the transducers and the borehole wall, some improvements are necessary. On the one hand the transducer-to-borehole adapters allowed to measure signals with enough amplitudes, they shifted the transducers bandwidth, increasing by the way the uncertainty about the source signal. This problem can be solved in the next generation of probes by designing specifically tailored transducers. Some other sources could be added to the reception probe (at the top or bottom) to improve the ray (angular coverage, and avoid gap in the data (e.g. we had to model the velocity data normal to the layers because of insufficient coverage).

Finally, the survey design must be rethought to embrace all the possibilities offered by meter to (several) decameter scaled reservoir characterization. This requires to conduct the survey using

different seismic frequencies ranging from hertz to kilohertz, and overlapping bandwidth. The measurement grids (defined by the transducer arrays) are ideally subsets of each other. So both high and low frequency signals can be recorded for every part of the reservoir, and compared afterwards. The acoustic survey can be coupled with other geophysical methods such as Ground Penetrating Radar (GPR) and Electrical Resistivity Tomography (ERT) in order to scope out the petrophysical properties.

References

- Adam, Ludmila, Michael Batzle, K T Lewallen, and K van Wijk. 2009. "Seismic Wave Attenuation in Carbonates." *Journal of Geophysical Research Solid Earth* 114 (B6): B06208. doi:10.1029/2008JB005890.
- Agar S., S M Geiger, ed. 2015. *Fundamental Controls on Fluid Flow in Carbonates. Current Workflows to Emerging Technologies*. Geological Society of London. <http://geoscienceworld.org/content/9781862396838/9781862396838>.
- Al-Harrasi, O H, A Al-Anboori, A Wüstefeld, and J -M Kendall. 2011. "Seismic Anisotropy in a Hydrocarbon Field Estimated from Microseismic Data." *Geophysical Prospecting* 59 (2): 227–43. doi:10.1111/j.1365-2478.2010.00915.x.
- American Petroleum Institute. 1998. "Recommended Practices for Core Analysis." In *API Recommended Practice 40, Second Edition*, 1–236.
- Anselmetti, Flavio S, and Gregor P Eberli. 1993. "Controls on Sonic Velocity in Carbonates." *Pure and Applied Geophysics* 141 (2–4): 287–323.
- . 1999. "The Velocity-Deviation Log: A Tool to Predict Pore Type and Permeability Trends in Carbonate Drill Holes from Sonic and Porosity or Density Logs." *AAPG Bulletin* 83 (3): 450–66.
- . 2001. "Sonic Velocity in Carbonates— A Combined Product of Depositional Lithology and Diagenetic Alterations." In *Subsurface Geology of a Prograding Carbonate Platform Margin, Great Bahama Bank*, Subsurface:193–216. SEPM Society for Sedimentary Geology. doi:10.2110/pec.01.70.0193.
- Anselmetti, Flavio S, Gregor P Eberli, and D Bernoulli. 1997. "Seismic Modeling of a Carbonate Platform Margin (Montagna Della Maiella, Italy): Variations in Seismic Facies and Implications for Sequence Stratigraphy." In *Palaz, I. and Marfurt K.J. (Eds.), Carbonate Seismology, SEG Geophysical Developments Series, 6*, 373–406.
- Anselmetti, Flavio S, Stefan Luthi, and Gregor P Eberli. 1998. "Quantitative Characterization of Carbonate Pore Systems by Digital Image Analysis." *AAPG Bulletin* 82 (10): 1815–36.
- Anselmetti, Flavio S, Gian A Von Salis, Kevin J Cunningham, and Gregor P Eberli. 1997. "Acoustic Properties of Neogene Carbonates and Siliciclastics from the Subsurface of the Florida Keys : Implications for Seismic Reflectivity." *Marine Geology* 144 (97): 9–31.
- Assefa, Solomon, Clive Mccann, and Jeremy Sothcott. 2003. "Velocities of Compressional and Shear Waves in Limestones." *Geophysical Prospecting* 51 (1): 1–13.
- Backus, George E. 1962. "Long-Wave Elastic Anisotropy Produced by Horizontal Layering." *Journal of Geophysical Research* 67 (11): 4427–40. doi:10.1029/JZ067i011p04427.
- Baechle, Gregor T, Arnout Colpaert, Gregor P Eberli, and Ralf J Weger. 2008. "Effects of Microporosity on Sonic Velocity in Carbonate Rocks." *The Leading Edge* 27: 1012–18.
- Baechle, Gregor T, Gregor P Eberli, Ralf J Weger, and Jose Luis Massafferro. 2009. "Changes in Dynamic Shear Moduli of Carbonate Rocks with Fluid Substitution." *Geophysics* 74 (3): E135–47.
- Bakulin, Andrey, Vladimir Grechka, and Ilya Tsvankin. 2000a. "Estimation of Fracture Parameters from Reflection Seismic data—Part I: HTI Model due to a Single Fracture Set."

- Geophysics* 65 (6): 1788–1802. doi:10.1190/1.1444863.
- . 2000b. “Estimation of Fracture Parameters from Reflection Seismic data—Part II: Fractured Models with Orthorhombic Symmetry.” *Geophysics* 65 (6): 1803–17. doi:10.1190/1.1444863.
- Baud, Patrick, Alexandra Rolland, Michael Heap, Tao Xu, Marion Nicolé, Thomas Ferrand, Thierry Reuschlé, Renaud Toussaint, and Nathalie Conil. 2016. “Impact of Stylolites on the Mechanical Strength of Limestone.” *Tectonophysics* 690 (Part A). Elsevier B.V.: 4–20. doi:10.1016/j.tecto.2016.03.004.
- Bera, Bijoyendra, Sushanta K. Mitra, and Douglas Vick. 2011. “Understanding the Micro Structure of Berea Sandstone by the Simultaneous Use of Micro-Computed Tomography (Micro-CT) and Focused Ion Beam-Scanning Electron Microscopy (FIB-SEM).” *Micron* 42 (5). Elsevier Ltd: 412–18. doi:10.1016/j.micron.2010.12.002.
- Bereš, Ján, Hermann Zeyen, Guy Sénéchal, Dominique Rousset, and Stéphane Gaffet. 2013. “Seismic Anisotropy Analysis at the Low-Noise Underground Laboratory (LSBB) of Rustrel (France).” *Journal of Applied Geophysics* 94: 59–71. doi:10.1016/j.jappgeo.2013.04.008.
- Berryman, James G. 1979. “Long-Wave Elastic Anisotropy in Transversely Isotropic Media.” *Geophysics* 44 (5): 896–917.
- . 2008. “Exact Seismic Velocities for Transversely Isotropic Media and Extended Thomsen Formulas for Stronger Anisotropies.” *Geophysics* 73 (1): D1–10. doi:10.1190/1.2813433.
- Berryman, James G, Vladimir Y Grechka, and Patricia A Berge. 1999. “Analysis of Thomsen Parameters for Finely Layered VTI Media.” *Geophysical Prospecting* 47 (6): 959–78. doi:10.1046/j.1365-2478.1999.00163.x.
- Biot, M. A. 1956a. “Theory of Propagation of Elastic Waves in a Fluid- Saturated Porous Solid. I. Low Frequency Range.” *J. Acoust. Soc. Am.* 28 (2): 168–78. doi:10.1121/1.1908241.
- . 1956b. “Theory of Propagation of Elastic Waves in a Fluid Saturated Porous Solid. I. High Frequency Range.” *Journal of the Acoustical Society of America* 28 (2): 179–91. doi:10.1121/1.1908239.
- Borgomano, Jean, Jean-Pierre Masse, Mukerrem Fenerci-Masse, and François Fournier. 2013. “Petrophysics of Lower Cretaceous Platform Carbonate Outcrops in Provence (SE France): Implications for Carbonate Reservoir Characterisation.” *Journal of Petroleum Geology* 36 (1): 5–42.
- Brown, Stephen R, and Christopher H Scholz. 1985. “Closure of Random Elastic Surfaces in Contact.” *Journal of Geophysical Research Solid Earth* 90 (B7): 5531–45.
- . 1986. “Closure of Rock Joints.” *Journal of Geophysical Research* 91 (B5): 4939–48.
- Cheadle, Scott P, R James Brown, and Don C Lawton. 1991. “Orthorhombic Anisotropy: A Physical Seismic Modeling Study.” *Geophysics* 56 (10): 1603–13. doi:10.1190/1.1442971.
- Chen, Chien-Chih, Chung-Cherng Lin, Stanislav V Sinogeikin, and Jay D Bass. 2001. “Elasticity of Single-Crystal Calcite and Rhodochrosite by Brillouin Spectroscopy.” *American Mineralogist* 86 (11–12): 1525–29.
- Choquette, P.W., and L.C. Pray. 1970. “Geological Nomenclature and Classification of Porosity in Sedimentary Carbonates.” *American Association of Petroleum Geologists Bulletin* 54 (2): 207–50.
- Christensen, N I, and D L Szymanski. 1991. “Seismic Properties and the Origin of Reflectivity from a Classic Paleozoic Sedimentary Sequence, Valley and Ridge Province, Southern Appalachians.” *Geological Society of America Bulletin* 103 (2): 277–89.
- Conin, Marianne, Sylvain Bourlange, Pierre Henry, Aurelien Boiselet, and Philippe Gaillot. 2014.

- “Distribution of Resistive and Conductive Structures in Nankai Accretionary Wedge Reveals Contrasting Stress Paths.” *Tectonophysics* 611. Elsevier B.V.: 181–91. doi:10.1016/j.tecto.2013.11.025.
- Cordua, Knud S., Lars Nielsen, Majken C. Looms, Thomas Mejer Hansen, and Andrew Binley. 2009. “Quantifying the Influence of Static-like Errors in Least-Squares-Based Inversion and Sequential Simulation of Cross-Borehole Ground Penetrating Radar Data.” *Journal of Applied Geophysics* 68 (1). Elsevier B.V.: 71–84. doi:10.1016/j.jappgeo.2008.12.002.
- Cordua, Knud Skou, Thomas Mejer Hansen, and Klaus Mosegaard. 2012. “Monte Carlo Full-Waveform Inversion of Crosshole GPR Data Using Multiple-Point Geostatistical a Priori Information.” *Geophysics* 77 (2): H19–31. doi:10.1190/geo2011-0170.1.
- Crampin, Stuart. 1981. “A Review of Wave Motion in Anisotropic and Cracked Elastic-Media.” *Wave Motion* 3 (4): 343–91. doi:10.1016/0165-2125(81)90026-3.
- Dunham, R J. 1962. “Classification of Carbonate Rocks according to Depositional Texture.” In *Classification of Carbonate Rocks: American Association of Petroleum Geologists Memoir*, edited by W E Ham, 108–21.
- Dvorkin, Jack, and Amos Nur. 1996. “Elasticity of High-Porosity Sandstones: Theory for Two North Sea Datasets.” *Geophysics* 61 (5): 1363–70.
- Eberli, Gregor P, Flavio S Anselmetti, Jeroen A M Kenter, Donald F McNeill, and Leslie A Melim. 2001. “Calibration of Seismic Sequence Stratigraphy with Cores and Logs.” In *Subsurface Geology of a Prograding Carbonate Platform Margin, Great Bahama Bank*, Subsurface:241–65. SEPM Society for Sedimentary Geology.
- Eberli, Gregor P, Gregor T Baechle, Flavio S Anselmetti, and Michael L Incze. 2003. “Factors Controlling Elastic Properties in Carbonate Sediments and Rocks.” *The Leading Edge* 22: 654–60.
- Fournier, François, and Jean Borgomano. 2007. “Geological Significance of Seismic Reflections and Imaging of the Reservoir Architecture in the Malampaya Gas Field (Philippines).” *AAPG Bulletin* 91 (2): 235–58. doi:10.1306/10160606043.
- . 2009. “Critical Porosity and Elastic Properties of Microporous Mixed Carbonate-Siliciclastic Rocks.” *Geophysics* 74 (2): E93–109.
- Fournier, François, Philippe Leonide, Kévin Biscarrat, Arnaud Gallois, Jean Borgomano, and Anneleen Foubert. 2011. “Elastic Properties of Microporous Cemented Grainstones.” *Geophysics* 76 (6): E211–26.
- Fournier, François, Philippe Léonide, Luuk Kleipool, Renault Toullec, John J.G. Reijmer, Jean Borgomano, Thomas Klootwijk, and Jeroen Van Der Molen. 2014. “Pore Space Evolution and Elastic Properties of Platform Carbonates (Urgonian Limestone, Barremian–Aptian, SE France).” *Sedimentary Geology* 308 (1). Elsevier B.V.: 1–17.
- Galmudi, Doron, Jack Dvorkin, and Amos Nur. 1999. “Elastic-Wave Velocities in Sandstones with Non-Load-Bearing Clay.” *Geophysical Research Letters* 26 (7): 939–42.
- Gardner, G H F, Louis Wright Gardner, and Alvin Ray Gregory. 1974. “Formation Velocity and Density - The Diagnostic Basics for Stratigraphic Traps.” *Geophysics* 39 (6): 770–80.
- Grechka, Vladimir, and Mark Kachanov. 2006. “Effective Elasticity of Fractured Rocks: A Snapshot of the Work in Progress.” *Geophysics* 71 (6): W45–58. doi:10.1190/1.2360212.
- Guéguen, Yves, and Joël Sarout. 2009. “Crack-Induced Anisotropy in Crustal Rocks: Predicted Dry and Fluid-Saturated Thomsen’s Parameters.” *Physics of the Earth and Planetary Interiors* 172 (1–2): 116–24. doi:10.1016/j.pepi.2008.05.020.
- Guglielmi, Yves, Frédéric Cappa, Jean-philippe Avouac, Pierre Henry, and Derek Elsworth. 2015.

- “Seismicity Triggered by Fluid Injection – Induced Aseismic Slip.” *Science* 348 (6240): 1224–26.
- Hansen, Thomas Mejer, Knud Skou Cordua, Bo Holm Jacobsen, and Klaus Mosegaard. 2014. “Accounting for Imperfect Forward Modeling in Geophysical Inverse Problems — Exemplified for Crosshole Tomography.” *Geophysics* 79 (3): H1–21. doi:10.1190/geo2013-0215.1.
- Hansen, Thomas Mejer, Knud Skou Cordua, Majken Caroline Looms, and Klaus Mosegaard. 2013. “SIPPI: A Matlab Toolbox for Sampling the Solution to Inverse Problems with Complex Prior Information: Part 2-Application to Crosshole GPR Tomography.” *Computers and Geosciences* 52. Elsevier: 481–92. doi:10.1016/j.cageo.2012.10.001.
- Hansen, Thomas Mejer, Knud Skou Cordua, and Klaus Mosegaard. 2012. “Inverse Problems with Non-Trivial Priors: Efficient Solution through Sequential Gibbs Sampling.” *Computational Geosciences* 16 (3): 593–611. doi:10.1007/s10596-011-9271-1.
- . 2014. “A General Probabilistic Approach for Inference of Gaussian Model Parameters from Noisy Data of Point and Volume Support.” *Mathematical Geosciences* 47 (7). Springer Berlin Heidelberg: 843–65. doi:10.1007/s11004-014-9567-5.
- Hansen, Thomas Mejer, Knud Skou Cordua, Majken Caroline Looms, and Klaus Mosegaard. 2013. “SIPPI: A Matlab Toolbox for Sampling the Solution to Inverse Problems with Complex Prior Information: Part 1-Methodology.” *Computers and Geosciences* 52. Elsevier: 470–80. doi:10.1016/j.cageo.2012.09.004.
- Helbig, Klaus. 1983. “Elliptical Anisotropy – Its Significance and Meaning.” *Geophysics* 48 (7): 825–32.
- Helbig, Klaus, and Leon Thomsen. 2005. “75-plus Years of Anisotropy in Exploration and Reservoir Seismics: A Historical Review of Concepts and Methods.” *Geophysics* 70 (6): 9ND–23ND. doi:10.1190/1.2122407.
- Hudson, J. A. 1981. “Wave Speeds and Attenuation of Elastic Waves in Material Containing Cracks.” *Geophysical Journal of the Royal Astronomical Society* 64 (1): 133–50. doi:10.1111/j.1365-246X.1981.tb02662.x.
- Hudson, J. A. 1980. “Overall Properties of a Cracked Solid.” *Mathematical Proceedings of the Cambridge Philosophical Society* 88 (2): 371–84. doi:10.1017/S0305004100057674.
- Huuse, M., and D. A. Feary. 2005. “Seismic Inversion for Acoustic Impedance and Porosity of Cenozoic Cool-Water Carbonates on the Upper Continental Slope of the Great Australian Bight.” *Marine Geology* 215 (3–4): 123–34.
- Jeanne, Pierre. 2012. “Architectural, Petrophysical and Hydromechanical Properties of Fault Zones in Fractured-Porous Rocks: Compared Studies of a Moderate and a Mature Fault Zones (France).” Aix-Marseille Université.
- Jeanne, Pierre, Yves Guglielmi, and Frédéric Cappa. 2012. “Multiscale Seismic Signature of a Small Fault Zone in a Carbonate Reservoir: Relationships between VP Imaging, Fault Zone Architecture and Cohesion.” *Tectonophysics* 554–557 (July): 185–201.
- . 2013. “Dissimilar Properties within a Carbonate-Reservoir’s Small Fault Zone, and Their Impact on the Pressurization and Leakage Associated with CO₂ Injection.” *Journal of Structural Geology* 47 (February). Elsevier Ltd: 25–35.
- Jeanne, Pierre, Yves Guglielmi, Juliette Lamarche, Frédéric Cappa, and Lionel Marié. 2012. “Architectural Characteristics and Petrophysical Properties Evolution of a Strike-Slip Fault Zone in a Fractured Porous Carbonate Reservoir.” *Journal of Structural Geology* 44 (1): 93–109.

- Johnston, J E, and N I Christensen. 1995. "Seismic Anisotropy of Shales." *Journal of Geophysical Research Solid Earth* 100 (B4): 5991–6003. doi:10.1029/95JB00031.
- Kenter, Jeroen A M, Flavio S Anselmetti, P H Kramer, H Westphal, and M G M Vandamme. 2002. "Acoustic Properties Of 'young' carbonate Rocks , ODP Leg 166 and Boreholes Clino And Unda , Western Great Bahama Bank." *Journal of Sedimentary Research* 72 (1): 129–37.
- Kenter, Jeroen A M, Hendrik Braaksma, Klaas Verwer, and Xavier M T van Lanen. 2007. "Acoustic Behavior of Sedimentary Rocks : Geologic Properties versus Poisson ' S Ratios." *The Leading Edge* 26 (4): 436–44.
- Kenter, Jeroen A M, Bruce W Fouke, and Marc Reinders. 1997. "Effects of Differential Cementation on the Sonic Velocities of Upper Cretaceous Skeletal Grainstones (SouthEastern Netherlands)." *Journal of Sedimentary Research* 67 (1): 178–85.
- Kenter, Jeroen A M, F F Podladchikov, Marc Reinders, Sjierk J Vander Gaast, Bruce W Fouke, and Mark D Sonnenfeld. 1997. "Parameters Controlling Sonic Velocities in a Mixed Carbonate-Siliciclastics Permian Shelf-Margin (Upper San Andres Formation, Last Chance Canyon, New Mexico)." *Geophysics* 62 (2): 505–20.
- King, M S, L R Myer, and J J Rezowalli. 1986. "Experimental Studies of Elastic-Wave Propagation in a Columnar-Jointed Rock Mass." *Geophysical Prospecting* 34 (8): 1185–99.
- Kisslinger, Carl. 1950. "Velocity of Longitudinal Waves in Some Paleozoic Formations in the Vicinity of St. Louis, Missouri." *Transaction American Geophysical Union* 31 (2): 169–73.
- . 1953. "The Effect of Variations in Chemical Composition on the Velocity of Seismic Waves in Carbonate Rocks." *Geophysics* 18 (1): 104–15.
- Knight, Rosemary, and Jack Dvorkin. 1992. "Seismic and Electrical Properties of Sandstones at Low Saturations." *Journal of Geophysical Research Solid Earth* 97 (B12): 17.425-17.432.
- Kuster, Guy T, and M Nafi Toksoz. 1974. "Velocity and Attenuation of Seismic Waves in Two-Phase Media: Part II. Experimental Results." *Geophysics* 39 (5): 607–18. doi:10.1190/1.1440451.
- Lamarche, Juliette, Arthur P C Lavenu, Bertrand D M Gauthier, Yves Guglielmi, and Océane Jayet. 2012. "Tectonophysics Relationships between Fracture Patterns , Geodynamics and Mechanical Stratigraphy in Carbonates (South-East Basin , France)." *Tectonophysics* 581. Elsevier B.V.: 231–45.
- Lavenu, Arthur P C. 2013. "Relationships between Fracture Pattern and Geodynamics in Carbonates. Role of Depositional Facies, Diagenesis and Rock Mechanical Properties." Aix-Marseille Université.
- Leonide, Philippe, Jean Borgomano, Jean-Pierre Masse, and Stefan Doublet. 2012. "Relation between Stratigraphic Architecture and Multi-Scale Heterogeneities in Carbonate Platforms: The Barremian–lower Aptian of the Monts de Vaucluse, SE France." *Sedimentary Geology* 265–266 (July): 87–109.
- Léonide, Philippe, François Fournier, John J.G. Reijmer, Hubert Vonhof, Jean Borgomano, Jurrien Dijk, Maelle Rosenthal, Manon van Goethem, Jean Cochard, and Karlien Meulenaars. 2014. "Diagenetic Patterns and Pore Space Distribution along a Platform to Outer-Shelf Transect (Urgonian Limestone, Barremian–Aptian, SE France)." *Sedimentary Geology* 306 (June). Elsevier B.V.: 1–23.
- Looms, Majken C., Thomas Mejer Hansen, Knud S. Cordua, Lars Nielsen, Karsten H. Jensen, and Andrew Binley. 2010. "Geostatistical Inference Using Crosshole Ground-Penetrating Radar." *Geophysics* 75 (6): J29–41. doi:10.1190/1.3496001.
- Louis, Laurent, Christian David, V. Metz, P. Robion, B. Menéndez, and C. Kissel. 2005.

- “Microstructural Control on the Anisotropy of Elastic and Transport Properties in Undeformed Sandstones.” *International Journal of Rock Mechanics and Mining Sciences* 42 (7–8 SPEC. ISS.): 911–23. doi:10.1016/j.ijrmms.2005.05.004.
- Louis, Laurent, F. Humbert, P. Robion, P. Henry, M. Knuth, and W. Likos. 2012. “Data Report: Joint Analysis of Acoustic and Magnetic Suceptibility Anisotropies in the Nankai Accretionary Prism.” In *H. Tobin, M. Kinoshita, J. Ashi, S. Lallemand, G. Kimura, E.J. Screaton, Moe Kyaw Thu, H. Masago, D. Curewitz, and the Expedition 314/315/316 Scientists*. Vol. 314/315/31. Washington DC: Integrated Ocean Drilling Program Management International, Inc. doi:10.2204/iodp.proc.314315316.216.2012.
- Louis, Laurent, Philippe Robion, and Christian David. 2004. “A Single Method for the Inversion of Anisotropic Data Sets with Application to Structural Studies.” *Journal of Structural Geology* 26 (11): 2065–72. doi:10.1016/j.jsg.2004.03.005.
- Lubbe, R, and M H Worthington. 2006. “A Field Investigation of Fracture Compliance.” *Geophysical Prospecting* 54 (3): 319–31.
- Manificat, Guillaume, and Yves Guéguen. 1998. “What Does Control Vp/Vs in Granular Rocks?” *Geophysical Research Letters* 25 (3): 381–84.
- Martínez, Jaime Meléndez, and Douglas R. Schmitt. 2013. “Anisotropic Elastic Moduli of Carbonates and Evaporites from the Weyburn-Midale Reservoir and Seal Rocks.” *Geophysical Prospecting* 61 (2): 363–79. doi:10.1111/1365-2478.12032.
- Masse, J.-P., and J. Philip. 1976. “Paléogéographie et Tectonique Du Crétacémoyen En Provence : Révision Du Concept D’isthme Durancien.” *Revue de Géographie Physique et de Géologie Dynamique* 18 (1): 49–66.
- Masse, Jean-Pierre. 1976. “Les Calcaires Urgoniens de Provence. Stratigraphie, Paléontologie, Les Paléoenvironnements et Leur Évolution.” Université de Provence.
- . 1993. “Early Cretaceous Dasycladales Biostratigraphy from Provence and Adjacent Regions (South of France, Switzerland, Spain). A Reference for Mesogean Correlations.” *Boll. Soc. Paleontol. Ital. Spec* 1: 311–24.
- . 1999. “New Dasycladale Species from the Lower Cretaceous of Provence (S.E. France).” *Revue de Micropaléontologie* 42 (3): 231–43.
- Masse, Jean-Pierre, and J Allemann. 1982. “Relations Entre Les Séries Carbonatées de Plate-Forme Provençale et Sarde Au Crétacé Inférieur.” *Cretaceous Research* 3: 19–33.
- Masse, Jean-Pierre, and Mukerrem Fenerci-Masse. 2006. “Carbonate Production by Rudist Bivalves. The Record of Late Barremian Requiiniid Communities from Provence (SE France).” *Palaeogeography, Palaeoclimatology, Palaeoecology* 234 (2–4): 239–57. doi:10.1016/j.palaeo.2005.10.010.
- . 2011. “Drowning Discontinuities and Stratigraphic Correlation in Platform Carbonates. The Late Barremian–early Aptian Record of Southeast France.” *Cretaceous Research* 32 (6): 659–84.
- . 2013a. “Bioevents and Palaeoenvironmental Changes in Carbonate Platforms: The Record of Barremian ‘Urgonian’ Limestones of SE France.” *Palaeogeography, Palaeoclimatology, Palaeoecology* 386 (September). The Authors: 637–51. doi:10.1016/j.palaeo.2013.06.029.
- . 2013b. “Drowning Events, Development and Demise of Carbonate Platforms and Controlling Factors: The Late Barremian–Early Aptian Record of Southeast France.” *Sedimentary Geology* 298 (December). Elsevier B.V.: 28–52. doi:10.1016/j.sedgeo.2013.09.004.

- Matonti, C., Yves Guglielmi, S. Viseur, P. O. Bruna, J. Borgomano, C. Dahl, and L. Marie. 2015. "Heterogeneities and Diagenetic Control on the Spatial Distribution of Carbonate Rocks Acoustic Properties at the Outcrop Scale." *Tectonophysics* 638 (1). Elsevier B.V.: 94–111. doi:10.1016/j.tecto.2014.10.020.
- Matonti, Christophe. 2015. "Exploration Géophysique Des Processus de Fracturation et de Réactivation Dans Les Carbonates À L'échelle Métrique."
- Mavko, Gary, Tapan Mukerji, and Jack Dvorkin. 2009. *The Rock Physics Handbook*. 2nd ed. Cambridge University Press, Cambridge.
- Mayo, Sheridan, Matthew Josh, Yakov Nesterets, Lionel Esteban, Marina Pervukhina, Michael Ben Clennell, Anton Maksimenko, and Chris Hall. 2015. "Quantitative Micro-Porosity Characterization Using Synchrotron Micro-CT and Xenon K-Edge Subtraction in Sandstones, Carbonates, Shales and Coal." *Fuel* 154. Elsevier Ltd: 167–73. doi:10.1016/j.fuel.2015.03.046.
- McCann, D M, P Grainger, and C McCann. 1975. "Inter-Borehole Acoustic Measurements and Their Use in Engineering Geology." *Geophysical Prospecting* 23 (1): 50–69.
- Melim, Leslie A, Flavio S Anselmetti, and Gregor P Eberli. 2001. "The Importance of Pore Type on Permeability of Neogene Carbonates, Great Bahama Bank." In *Subsurface Geology of a Prograding Carbonate Platform Margin, Great Bahama Bank*, Subsurface:217–38. SEPM Society for Sedimentary Geology. doi:10.2110/pec.01.70.0217.
- Moos, Daniel, and Mark D. Zoback. 1983. "In Situ Studies of Velocity in Fractured Crystalline Rocks." *Journal of Geophysical Research Solid Earth* 88 (B3): 2345–58.
- Moss, Steve, and Maurice E Tucker. 1995. "Diagenesis of Barremian-Aptian Platform Carbonates (the Urgonian Limestone Formation of SE France): Near-Surface and Shallow-Burial Diagenesis (Pages 853–874)." *Sedimentology* 42 (6): 853–74.
- Nur, Amos, and Jack Dvorkin. 1998. "Time-Average Equation Revisited." *Geophysics* 63 (2): 460–64.
- Nur, Amos, and Gene Simmons. 1969. "The Effect of Saturation on Velocity in Low Porosity Rocks." *Earth and Planetary Science Letters* 7: 183–93.
- Paulsson, B N P, N G W Cook, and T V McEvelly. 1985. "Elastic-Wave Velocities and Attenuation in an Underground Granitic Repository for Nuclear Waste." *Geophysics* 50 (4): 551–70.
- Rafavich, F, C H St C Kendall, and T P Todd. 1984. "The Relationship between Acoustic Properties and the Petrographic Character of Carbonate Rocks." *Geophysics* 49 (10): 1622–36.
- Rao, Ying, Yanghua Wang, Shumin Chen, and Jianmin Wang. 2016. "Crosshole Seismic Tomography with Cross-Firing Geometry." *Geophysics* 81 (4): R139–46.
- Raymer, L L, E R Hunt, and John S Gardner. 1980. "An Improved Sonic Transit Time-To-Porosity Transform." In *SPWLA Twenty-First Annual Logging Symposium*. Society of Petrophysicists and Well-Log Analysts.
- Rüger, Andreas. 1997. "P-Wave Reflection Coefficients for Transversely Isotropic Media with Vertical and Horizontal Axis of Symmetry." *Geophysics* 62 (3): 713–22.
- Saleh, Azzeldeen A, and John P Castagna. 2004. "Revisiting the Wyllie Time Average Equation in the Case of near-Spherical Pores." *Geophysics* 69 (1): 45–55. doi:10.1190/1.1649374.
- Serra, Oberto. 1984. *The Fundamentals of Well-Log Interpretation 1. The Acquisition of Logging Data*. Part A. Vol. 15. Amsterdam: Elsevier B.V. doi:10.1126/science.143.3606.560-a.
- Smith, A H, and A W Lawson. 1954. "The Velocity of Sound in Water as a Function of Temperature and Pressure." *Journal of Chemical Physics* 22 (3): 351–59.

- Stafleu, Jan, Arnout J W Everts, and Jeroen A M Kenter. 1994. "Seismic Models of a Prograding Carbonate Platform: Vercors, South-East France." *Marine and Petroleum Geology* 11 (5): 514–527.
- Stierman, Donald J., and Robert L. Kovach. 1979. "An in Situ Velocity Study: The Stone Canyon Well." *Journal of Geophysical Research Solid Earth* 84 (B2): 672–78.
- Storvoll, Vidar, and Knut Bjørlykke. 2004. "Sonic Velocity and Grain Contact Properties in Reservoir Sandstones." *Petroleum Geoscience* 10 (3): 215–26.
- Thomsen, Leon. 1986. "Weak Elastic Anisotropy." *Geophysics* 51 (10): 1954–66. doi:10.1190/1.1442051.
- Todd, Terry, and Gene Simmons. 1972. "Effect of Pore Pressure on the Velocity of Compressional Waves in Low-Porosity Rocks." *Journal of Geophysical Research* 77 (20): 3731–43.
- Tsvankin, Ilya. 1997. "Reflection Moveout and Parameter Estimation for Horizontal Transverse Isotropy." *Geophysics* 62 (2): 614–29. doi:10.1190/1.1444170.
- . 2001. *Seismic Signature and Analysis of Reflection Data in Anisotropic Media*. Edited by Klaus Helbig and Sven Treitel. First edit. Pergamon.
- . 2012. *Seismic Signatures and Analysis of Reflection Data in Anisotropic Media, Third Edition*. Society of Exploration Geophysicists. doi:10.1190/1.9781560803003.
- Tsvankin, Ilya, James Gaiser, Vladimir Grechka, Mirko van der Baan, and Leon Thomsen. 2010. "Seismic Anisotropy in Exploration and Reservoir Characterization: An Overview." *Geophysics* 75 (5): 75A15–75A29. doi:10.1190/1.3481775.
- Tsvankin, Ilya, and Leon Thomsen. 1994. "Nonhyperbolic Reflection Moveout in Anisotropic Media." *Geophysics* 59 (8): 1290–1304. doi:10.1190/1.1443686.
- Tucker, Maurice E, and V Paul Wright. 1990. *Carbonate Sedimentology*. Oxford, UK: Blackwell Publishing Ltd. doi:10.1002/9781444314175.
- Tutuncu, Azra N, Jack Dvorkin, and Amos Nur. 1997. "Influence of Cementation and Permeability on Wave Velocities in Poorly Consolidated Sands." *Journal of Rock Mechanics & Mining Sciences* 34 (3–4): 313.e1–313.e13.
- Vandeginste, Veerle, Cédric M John, and Christina Manning. 2013. "Interplay between Depositional Facies, Diagenesis and Early Fractures in the Early Cretaceous Habshan Formation, Jebel Madar, Oman." *Marine and Petroleum Geology* 43 (1). Elsevier Ltd: 489–503. <http://linkinghub.elsevier.com/retrieve/pii/S0264817212002462>.
- Vernik, Lev, and Amos Nur. 1992. "Petrophysical Classification of Siliciclastics for Lithology and Porosity Prediction from Seismic Velocities." *AAPG Bulletin* 76 (9): 1295–1309. <http://aapgbull.geoscienceworld.org/content/76/9/1295.short>.
- Verwer, Klaas, Hendrik Braaksma, and Jeroen A M Kenter. 2008. "Case History Acoustic Properties of Carbonates : Effects of Rock Texture and Implications for Fluid Substitution." *Geophysics* 73 (2): B51–65.
- Wang, Chi -Yuen. 1966. "Velocity of Compressional Waves in Limestones, Marbles and a Single Crystal of Calcite to 20 Kilobars." *Journal of Geophysical Research* 71 (14): 3543–47.
- Wang, Zhijing. 1997. "Seismic Properties of Carbonate Rocks." In *Palaz, I. and Marfurt K.J. (Eds.), Carbonate Seismology, SEG Geophysical Developments Series, 6 Carbonate Seismology*, 29–52.
- . 2001. "Y2K Tutorial: Fundamentals of Seismic Rock Physics." *Geophysics* 66 (2): 398–412.
- . 2002a. "Seismic Anisotropy in Sedimentary Rocks, Part 1: A Single Plug Laboratory Method." *Geophysics* 67 (5): 1415–22.

- . 2002b. “Seismic Anisotropy in Sedimentary Rocks, Part 2: Laboratory Data.” *Geophysics* 67 (5): 1423–40.
- Wentworth, Chester K. 1922. “A Scale of Grade and Class Terms for Clastic Sediments.” *The Journal of Geology* 30 (5): 377–92. doi:10.1086/622910.
- Winkler, Kenneth W. 1983. “Contact Stiffness in Granular Porous Materials: Comparison between Theory and Experiment.” *Geophysical Research Letters* 10 (11): 1073–76.
- Worthington, M H, and R Lubbe. 2007. “The Scaling of Fracture Compliance.” In *Lonergan, L., Jolly, R. J. H., Rawnsley, K. & Sanderson, D. J. (Eds) Fractured Reservoirs. Geological Society, London, Special Publications, 270:73–82.*
- Wyllie, Malcolm Robert Jesse, Alvin Ray Gregory, and Louis Wright Gardner. 1956. “Elastic Wave Velocities in Heterogeneous and Porous Media.” *Geophysics* 21 (1): 41–70.
- Xu, Shiyu, and Michael A Payne. 2009. “Modeling Elastic Properties in Carbonate Rocks.” *The Leading Edge* 28 (1): 66–74.
- Yin, Hezhu, Gary Mavko, Tapan Mukerji, and Amos Nur. 1995. “Scale Effects on Dynamic Wave Propagation in Heterogeneous Media.” *Geophysical Research Letters* 22 (23): 3163–66.
- Yoshioka, Naoto, and Christopher H Scholz. 1989. “Elastic Properties of Contacting Surfaces under Normal and Shear Loads: 1. Theory.” *Journal of Geophysical Research Solid Earth* 94 (B12): 17,681-17,690.
- Zampetti, V, U Sattler, and Hendrik Braaksma. 2005. “Well Log and Seismic Character of Liuhua 11-1 Field, South China Sea; Relationship between Diagenesis and Seismic Reflections.” *Sedimentary Geology* 175 (1–4): 217–36.
- Zimmer, Michael A, Manika Prasad, Gary Mavko, and Amos Nur. 2007a. “Seismic Velocities of Unconsolidated Sands : Part 1 — Pressure Trends from 0 . 1 to 20 MPa.” *Geophysics* 72 (1): E1–13.
- . 2007b. “Seismic Velocities of Unconsolidated Sands : Part 2 — Influence of Sorting- and Compaction-Induced Porosity Variation.” *Geophysics* 72 (1): E15–25.

Appendix

Articles

Dawin Baden, Yves Guglielmi, Pierre Henry, Ginette Saracco, Lionel Marié, and Seiji Nakagawa (2017- *under 2nd round of review*), **Scale dependency of velocity anisotropy in heterogeneous carbonates**, *submitted in Geophysics*. [cf. Chapter 4]

Dawin Baden, Yves Guglielmi, Pierre Henry, Ginette Saracco, and Lionel Marié (2017- *under revision after a 1st round of review*), **Field characterization of a fractured-carbonate formation using crosshole acoustic waves anisotropy**, *submitted in Journal of Geophysical Research Solid Earth*. [cf. Chapter 5]

Dawin Baden, Yves Guglielmi, Pierre Henry, Ginette Saracco, Lionel Marié, (*in preparation*), **Anisotropy and effects of heterogeneities in fractured carbonate reservoirs**, *Targeted journal: Geophysical Research Letters*

Proceedings

Dawin Baden, Pierre Henry, Ginette Saracco, Lionel Marié, Alain Tonetto, Yves Guglielmi, Seiji Nakagawa, Gérard Massonnat, and Jean-Paul Rolando (2017) **How seismic anisotropy changes with scale**. SEG Technical Program Expanded Abstracts 2017: pp. 305-309.
<https://doi.org/10.1190/segam2017-17587710.1>

How seismic anisotropy changes with scale

Dawin Baden*, Pierre Henry, Ginette Saracco, Lionel Marié, and Alain Tonetto, Aix-Marseille Université, CNRS, CEREGE, IRD; Yves Guglielmi, and Seiji Nakagawa, Lawrence Berkeley National Laboratory; Gérard Massonnat, Jean-Paul Rolando, Total Exploration & Production

Summary:

Physical properties of carbonate rocks cannot be fully captured from laboratory-sized samples. Indeed, heterogeneous facies distribution and/or diagenetic alterations may lead to significant variations in petrophysical properties within few meters. In carbonates, diagenetic transformations are tightly related to nature of fluids flowing through the formations, e.g. via fractures network. Consequently, reservoir properties may have patchy distribution, and may not be correlatable (e.g. using facies distribution or wells-logs correlations) within few meters. Our works aim at characterizing carbonates anisotropy at different scales, and are subject of two presentations at SEG's 87th Annual Meeting. This abstract deals with the second part of our approach, that's to say characterizing impact of diagenetic alteration on reservoir properties and seismic anisotropy, from centimeter to multi-meter scale. This part of the works integrate data from centimeter-scale (mini-cores), decimeter-scale (5" cores), multi-meter (ultrasonic crosshole), and hectometer-scale (seismic), which have been measured at suitable frequency ranges (1MHz, 250kHz, 50kHz, and 1–100Hz, respectively). Although anisotropy is measurable at every scales, its origins vary according to scale. In this study, it is shown that matrix of porous samples are weakly anisotropic as a result of inter-crystalline pores. At centimeter-scale, anisotropy can also be related to: (1) patchy distribution of some physical properties, (2) local cracks distribution, and (3) thick single fractures. The lack of correlation between stiffness components from seismic-scale measurements, and laboratory to multi-meter scale ones emphasizes the fact that, when fracturing dominates, measured anisotropy is dominated by fracture/fault related anisotropy and matrix-related anisotropy may be lost. So that, scale effect must be handled carefully in anisotropy analyses, especially for carbonate formations.

Introduction:

This study is consecutive to a series of published works aiming at characterizing both reservoir and elastic properties of Lower Cretaceous limestone from the Urgonian platform of Provence (SE, France). References describing the characteristics of this platform in terms of facies, and biostratigraphy are available e.g. (Leonide et al. 2012). These microporous bioclastic limestones are analogues of different hydrocarbon reservoirs in Middle East, e.g. Kharab and Shuaiba formations (Borgomano et al. 2013). In addition, several published databases document coupled porosity, and elastic waves velocities measurements from the Urgonian platform (Fournier and Borgomano 2009; Fournier et al. 2011; Fournier et al. 2014; Borgomano et al. 2013). In these works, the authors used conventional laboratory approach, i.e. velocity measurements carried out on 1" to 1.5" mini-cores, under effective stress; and they discussed "effective media theory", and the concept of "pore aspect ratio" extensively. Nevertheless, a known limitation of these approaches is the implicit assumption of medium's isotropy. Despite this assumption is generally true at plug scale, it is rarely the case at larger scale. Carbonate rocks are often fractured and may have either "facies-related" or "patchy" porosity distribution that may lead to seismic anisotropy.

The works presented here focus on the impact of up-scaling onto elastic properties of carbonates rocks. Ultrasonic measurements have been carried out onto laboratory-sized samples, and the results are compared to published works, and to a crosshole acoustic survey (cf. our first presentation).

Geological context:

The studied formations are located within vadose zone of "Fontaine de Vaucluse" aquifer system. LSBB (Low Noise Underground Laboratory) GAS-gallery gives access to the 30° southward-dipping layers, and five vertical fully-cored boreholes (~20m deep) were drilled as part of previous works (Jeanne 2012; Jeanne, Guglielmi, and Cappa 2013; Jeanne, Guglielmi, and Cappa 2012; Jeanne et al. 2012).

The present study focuses on analyzing elastic properties of six 5" cores (C01 to C06), which are representative of different layers intersected by the boreholes (Figure 1). The facies sampled are inner-platform facies i.e. low to moderate energy, muddy or peloidal carbonate sands with abundant rudists. Cores analyses emphasized two facies groups:

- (1) Calcarenites (grainstone to rudstone),
- (2) Calcilutites (wackestone to packstone).

Reservoir properties of this facies are related to diagenesis (Léonide et al. 2014), hence, we do not describe them any further in this abstract, instead, we give extensive description of two cores selected to exemplify our works (i.e. C03 & C04). C03 was selected because it shows gradual transition within a same facies. It is a bioclastic grainstone to rudstone with abundant centimeter scaled rudists fragments and foraminifera. The transition is materialized by the relative abundance of macroscopic bioclasts (rudists), the top of C03 has higher density of macroscopic fragments, whereas bottom has only sand scaled bioclasts. We did not observe any variations in the matrix, and thin sections show large rudists fragments packed into a fine grained matrix, grains size is <300µm, and matrix

How seismic anisotropy changes with scale

texture ranged from packestone to grainstone (Figure 2). The micrite in C03 is compact, with low intercrystalline pores. Expectedly, porosity (<1%) and permeability (<1mD) values are as bad as guessed from SEM images. Absence of macroscopic pores (i.e. other than fractures), and tightness of micrite crystals explain the poor reservoir quality. Another important feature of C03 is partly-open fractures and cracks crossing the sample.

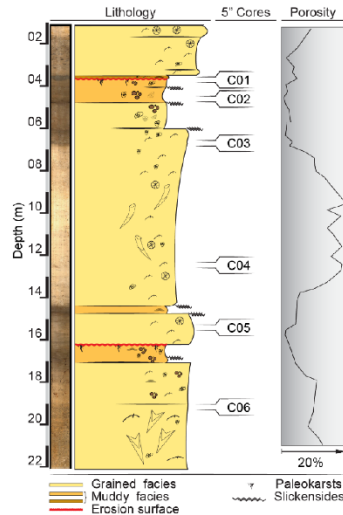


Figure 1. Synthetic lithology and porosity logs of studied formations, and localization of cores C01 to C06.

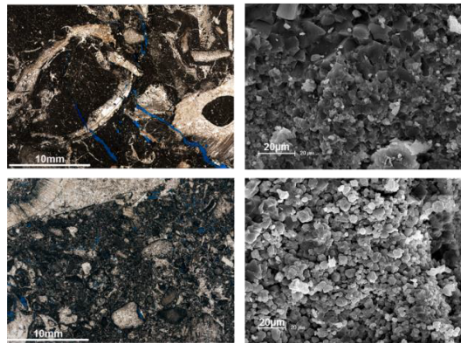


Figure 2. Stained thin-sections (left) and SEM imaging (right) of cores C03 (top) and C04 (bottom). Notice the contrast in muddy crystals shapes and inter-crystalline pores between the non-porous C03 and porous C04.

The footprint of fracturing, is visible on thin sections, since fractures' porosity, significantly increases the overall porosity.

C04 represents the most porous interval in studied formation, its porosity is about 15% but may reach up to 20%, and its permeability ranges from 2 to 3.5mD. C04 facies is a bioclastic grainstone to rudstone with large rudists' fragments. The thin sections show grain size ranging from 200µm, for the finest, to 2mm for the largest (Figure 2). Macroscopic pores both moldic and vuggy, are frequent, but the overall porosity, is dominated by intercrystalline porosity within the micrite (microporosity). SEM images show that micrite crystals are larger than that of the non-porous samples. The micrite crystals are loosely packed, euhedral, and heterogeneous in size, (i.e. 1 to 5µm), while intercrystalline pores are abundant, and relatively well connected because of either poor sorting, or low contact area between micrite crystals.

Material and methods:

Ultrasonic measurements were carried out in two parts. Firstly, the 5" cores were preliminarily saturated, then flooded in an acoustic tank, 20°C tap water was used during all steps. We do not give an extensive description of the experimental set up in this abstract, but Figure 3 shows the experiment.

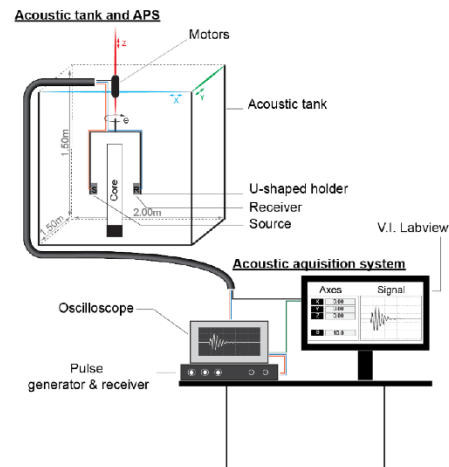


Figure 3. Experimental set up for ultrasonic analyses on 5" cores. The instrumentation included: 250-kHz IMASONIC immersion transducers, oscilloscope TEKTRONIX-DPO4034, pulse generator–receiver PANAMETRICS-5058PR. During acquisition transducers rotate around the sample. The rotation step ($\Delta\theta$), is 5°, and for a given transversal-section, 72 signals (stacked: $\times 64$) are recorded. After that the transducers are moved 1cm up ($\Delta Z=1\text{cm}$), then the process is repeated.

How seismic anisotropy changes with scale

Secondly, three 1.5" mini-cores (plugs) were drilled out of each 5" core. The mini-cores were taken in directions normal, parallel, and 45° to beddings, then wave velocities were measured using pairs of P- and S-wave PANAMETRICS ultrasonic transducers (1MHz). Good surface contact was ensured by using a thin lead foil at each interface, and by applying surface contact force using a vise.

The data were investigated using model of transversely isotropic (TI). For TI materials, the stiffness tensor (C_{IJ}) written in Voigt's notation, requires only five independent components to fully describe the elasticity (equation (1)).

$$C_{IJ} = \begin{pmatrix} c_{11} & c_{12} & c_{13} & & & \\ c_{12} & c_{11} & c_{13} & & & \\ c_{13} & c_{13} & c_{33} & & & \\ & & & c_{44} & & \\ & & & & c_{44} & \\ & & & & & c_{66} \end{pmatrix}, \quad c_{66} = \frac{c_{11} - c_{12}}{2} \quad (1)$$

After equation (2), components of C_{IJ} can be obtained from the density (ρ), and five velocity measurements including both quasi-longitudinal (V_p), and pure-shear (V_{sh}) phase-velocities (Mavko, Mukerji, and Dvorkin 2009).

$$\begin{aligned} c_{11} &= \rho V_{p(90^\circ)}^2 \\ c_{33} &= \rho V_{p(0^\circ)}^2 \\ c_{44} &= \rho V_{sh(0^\circ)}^2 \\ c_{66} &= \rho V_{sh(90^\circ)}^2 \end{aligned} \quad c_{13} = -c_{44} + \left(\begin{aligned} &4\rho^2 V_{p(45^\circ)}^4 - 2\rho V_{p(45^\circ)}^2 \\ &\times (c_{11} + c_{33} + 2c_{44}) \\ &+ (c_{11} + c_{44})(c_{33} + c_{44}) \end{aligned} \right)^{1/2} \quad (2)$$

Thomsen (1986) definition for weak TI media states the conditions $|\epsilon| \ll 1$ and/or $|\gamma| \ll 1$ must hold, and the author also suggested an approximation of P-wave phase velocity $V_p(\theta)$ for weak TI material, using P-wave velocity (noted α in equation (3)), and three constants, namely ϵ , γ , and δ , given by following formulas:

$$\begin{aligned} V_p(\theta) &\approx \alpha \left(1 + \delta \sin^2 \theta \cos^2 \theta + \epsilon \sin^4 \theta \right) \\ \alpha &= \sqrt{c_{33}/\rho} \quad \epsilon = (c_{11} - c_{33})/2c_{33} \quad \gamma = (c_{66} - c_{44})/2c_{44} \quad (3) \\ \delta &= \left((c_{13} + c_{44})^2 - (c_{33} - c_{44})^2 \right) / (2c_{33}(c_{33} - c_{44})) \end{aligned}$$

For mini-cores, components of C_{IJ} were computed using equation(2). Regarding mini-cores size, any anisotropy at this scale is related either to matrix, or micro-cracks, but not to macroscopic fractures. For 5" cores we fitted $V_p(\theta)$ models, using equation (3), onto velocity data for each transversal section. This gave us an estimation of quantities α , ϵ , and δ . Finally, these quantities (Thomsen's parameters) and/or the stiffness coefficients, were compared to results obtained on mini-cores (1.5"), cores (5"), and crosshole survey (meter to multi-meter).

Results and Discussion:

The results of the "mini-core approach" are given in Table 1. C_{IJ} components are nearly identical for non-porous samples (i.e. C01, C02, C03, and C05), whereas they are significantly lower for porous ones (i.e. C04, C06).

Referring to Table 2, these values are consistent with C_{IJ} components obtained from 1" mini-cores and crosshole ultrasonic survey, but they are significantly higher than that from seismic scale measurements.

Focusing on C03 and C04 in Table 1, one can see that shear anisotropy (γ) is <1%, therefore it is negligible. Conversely, ϵ is very low for C03 (2.3%), but is significant for C04, where it reaches ~12%. This results emphasizes that at matrix scale, porous samples can show significant P-wave anisotropy, whereas non-porous ones are nearly isotropic. Consequently, intercrystalline pores may be responsible for most of observed anisotropy.

Table 1. Results of the analyses on mini-cores.

	C01	C02	C03	C04	C05	C06
C_{11}	107.9	110.3	109.0	29.5	101.5	56.6
C_{13}	41.6	55.5	29.1	7.5	61.3	21.8
C_{33}	107.1	100.7	104.3	38.6	106.8	58.2
C_{44}	28.6	28.9	27.6	10.9	26.8	16.6
C_{66}	28.7	29.0	27.5	10.7	26.7	16.6
ρ	2649	2660	2618	2306	2650	2388
ϵ	0,004	0,048	0,023	-0,118	-0,025	-0,014
γ	0,003	0,001	-0,002	-0,008	-0,002	-0,001
δ	-0,074	0,137	-0,167	-0,201	0,080	-0,053

$C_{IJ} \times 10^9$; ρ (kg/m³)

Up-scaling analyses to 5" cores, one can see in most cases, P-wave velocities are low anisotropic in the transverse plane, i.e. ϵ range between =5%, for given transversal-section, (Figure 4, and Figure 5). When particular features such as fractures or large cemented-bioclasts (e.g. recrystallized corals and rudists) occur, P-wave velocities become clearly anisotropic, and ϵ can reach up to $\pm 20\%$. CT scan imaging show that in non-porous samples (e.g. C03) anisotropy (in transverse plane) is related to fractures and cracks only, and its magnitude can be related to either high density of thin cracks, or thick single-fracture.

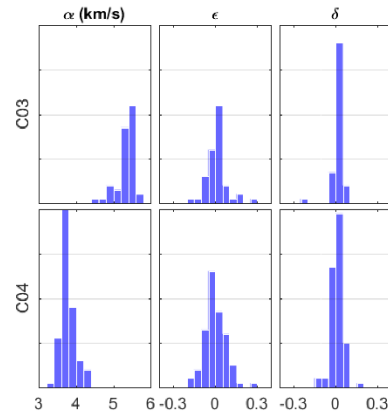


Figure 4. Estimation of α , ϵ , and δ using curve fitting of $V_p(\theta)$ on the 5" cores data (cf. transversal-section). The count is given by ordinate axes [0, 40].

How seismic anisotropy changes with scale

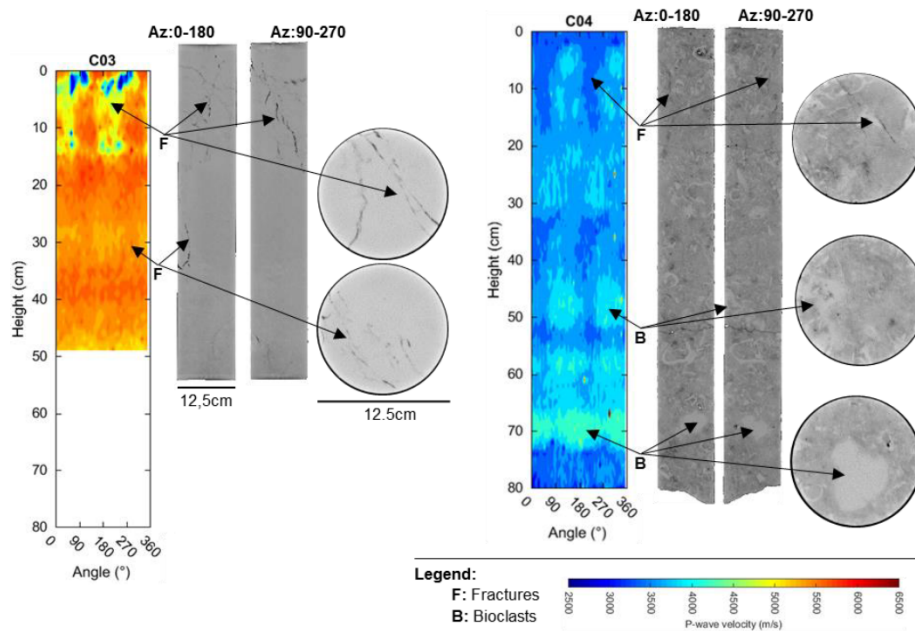


Figure 5. P-wave velocity maps and CT scan images of C03 & C04. Maps are 2D version (i.e. unrolled) of the 3D acquisition grid. The CT scan slices (longitudinal, and transversal) are commented to emphasize impact of bioclasts and fractures on recorded velocities. The gray level gives an idea of actual density, e.g. white→dense→non-porous.

In porous sample (e.g. C04) anisotropy in transverse plane can be related to either density contrasts within porous matrix, or inclusion of macro-fossils (Figure 5). In first case, P-wave velocity can stay close to mini-cores values, but in the second case it can be significantly higher than that of matrix alone.

Table 2. Ranges for C_{ij} ($\times 10^9$) in Urgonian limestone.

	[1]	[2]	[3]	[4]
C_{11}	44,9 - 36,9	96,3 - 39,5	110,3 - 29,5	110,4 - 26,8
C_{13}	19,7 - 18,3	43,5 - 12,1	61,3 - 07,5	52,7 - 09,2
C_{33}	69,2 - 65,9	93,5 - 35,3	107,1 - 38,6	C_{11}
C_{44}	19,7 - 18,3	28,7 - 15,3	28,9 - 10,9	34 - 07,9
C_{66}	15,4 - 14,8	26,7 - 12,3	29 - 10,7	C_{44}

[1] Beres et al., (2013); [2] Baden et al. (submitted);
[3] This study (mini-cores: 1.5"); [4] Fournier et al., (2014).

Conclusion:

Our multi-scale approach integrated data from centimeter-scale (1", 1.5" mini-cores), decimeter-scale (5" cores), multi-meter (ultrasonic crosshole), and hectometer-scale (seismic), these data were collected using frequency ranges suitable for the scales investigated, i.e. 1MHz, 250kHz, 50kHz, and 1-100Hz, respectively.

Although anisotropy is measurable at every scales, causes of that anisotropy can vary, or interfere with each other, according to scale. The data showed that porous matrix could be weakly anisotropic, at plug-scale, inter-crystalline pores may be the reason (Fournier et al. 2014). At centimeter-scale, patchy distribution of some physical properties (e.g. density) and/or local fractures/cracks distribution, produce anisotropy in the transverse plane, meaning similar consequences may be expected in the vertical plane. Effects of minerals/pores orientation and local fractures distribution are also visible at multi-meter scale, they are expressed by anisotropy being tightly correlated to beddings. However, when fracturing dominates signal from matrix anisotropy may be overlapped by fracture-related anisotropy. As shown by lack of correlation between C_{ij} components from seismic-scale measurements, and laboratory to multi-meter scale ones (Table 2). Therefore scale effect must be handled carefully in anisotropy analyses, especially for carbonate formations.

Acknowledgements:

This works were supported by two Research programs: II-CUBE project (ANR-12-SEED-0006), D. Baden's PhD grant; and ALBION-HPMSCa project, funded by TOTAL.

How seismic anisotropy changes with scale

Bibliography (not to be included in the abstract)

- Bereš, Ján, Hermann Zeyen, Guy Sénéchal, Dominique Rousset, and Stéphane Gaffet. 2013. "Seismic Anisotropy Analysis at the Low-Noise Underground Laboratory (LSBB) of Rustrel (France)." *Journal of Applied Geophysics* 94: 59–71. doi:10.1016/j.jappgeo.2013.04.008.
- Borgomano, Jean, Jean-Pierre Masse, Mukerrem Fencerci-Masse, and François Fournier. 2013. "Petrophysics of Lower Cretaceous Platform Carbonate Outcrops in Provence (SE France): Implications for Carbonate Reservoir Characterisation." *Journal of Petroleum Geology* 36 (1): 5–42.
- Fournier, F, and J Borgomano. 2009. "Critical Porosity and Elastic Properties of Microporous Mixed Carbonate-Siliciclastic Rocks" 74 (2).
- Fournier, François, Philippe Leonide, Kévin Biscarrat, Arnaud Gallois, Jean Borgomano, and Anneleen Foubert. 2011. "Elastic Properties of Microporous Cemented Grainstones." *Geophysics* 76 (6): F211–26.
- Fournier, François, Philippe Léonide, Luuk Kleipool, Renault Toullec, John J.G. Reijmer, Jean Borgomano, Thomas Klootwijk, and Jeroen Van Der Molen. 2014. "Pore Space Evolution and Elastic Properties of Platform Carbonates (Urgonian Limestone, Barremian–Aptian, SE France)." *Sedimentary Geology* 308 (July). Elsevier B.V.: 1–17.
- Jeanne, Pierre. 2012. "Architectural, Petrophysical and Hydromechanical Properties of Fault Zones in Fractured-Porous Rocks: Compared Studies of a Moderate and a Mature Fault Zones (France)." Aix-Marseille Université.
- Jeanne, Pierre, Yves Guglielmi, and Frédéric Cappa. 2012. "Multiscale Seismic Signature of a Small Fault Zone in a Carbonate Reservoir: Relationships between VP Imaging, Fault Zone Architecture and Cohesion." *Tectonophysics* 554–557 (July): 185–201.
- . 2013. "Dissimilar Properties within a Carbonate-Reservoir's Small Fault Zone, and Their Impact on the Pressurization and Leakage Associated with CO₂ Injection." *Journal of Structural Geology* 47 (February). Elsevier Ltd: 25–35.
- Jeanne, Pierre, Yves Guglielmi, Juliette Lamarche, Frédéric Cappa, and Lionel Marié. 2012. "Architectural Characteristics and Petrophysical Properties Evolution of a Strike-Slip Fault Zone in a Fractured Porous Carbonate Reservoir." *Journal of Structural Geology* 44 (1): 93–109.
- Leonide, Philippe, Jean Borgomano, Jean-Pierre Masse, and Stefan Doublet. 2012. "Relation between Stratigraphic Architecture and Multi-Scale Heterogeneities in Carbonate Platforms: The Barremian–lower Aptian of the Monts de Vaucluse, SE France." *Sedimentary Geology* 265–266 (July): 87–109.
- Léonide, Philippe, François Fournier, John J.G. Reijmer, Hubert Vonhof, Jean Borgomano, Jurrien Dijk, Maelle Rosenthal, Manon van Goethem, Jean Cochard, and Karlien Meulenaars. 2014. "Diagenetic Patterns and Pore Space Distribution along a Platform to Outer-Shelf Transect (Urgonian Limestone, Barremian–Aptian, SE France)." *Sedimentary Geology* 306 (June). Elsevier B.V.: 1–23.
- Mavko, Gary, Tapan Mukerji, and Jack Dvorkin. 2009. *The Rock Physics Handbook*. 2nd ed. Cambridge University Press, Cambridge.
- Thomsen, Leon. 1986. "Weak Elastic Anisotropy." *Geophysics* 51 (10): 1954–66.

Dawin Baden, Pierre Henry, Ginette Saracco, Lionel Marié, and Yves Guglielmi (2017), **Investigation of anisotropy in non-saturated and heterogeneous carbonate series using crosshole acoustic techniques**. SEG Technical Program Expanded Abstracts 2017: pp. 310-315. <https://doi.org/10.1190/segam2017-17587284.1>

Investigation of anisotropy in non-saturated and heterogeneous carbonate series using crosshole acoustic technics

Dawin Baden*, Pierre Henry, Ginette Saracco, and Lionel Marié, Aix-Marseille Université, CNRS, CEREGE, IRD; Yves Guglielmi, Lawrence Berkeley National Laboratory

Summary:

Physical properties of carbonate rocks cannot be fully captured from laboratory-sized samples. Indeed, heterogeneous facies distribution and/or diagenetic alterations may lead to significant variations in petrophysical properties within few meters. In carbonates, diagenetic transformations are tightly related to nature of fluids flowing through the formations, e.g. via fractures network. Consequently, reservoir properties may have patchy distribution, and may not be correlatable (e.g. using facies distribution or wells-logs correlations) within few meters. Our works aim at characterizing carbonates anisotropy at different scales, and are subject of two presentations at SFG's 87th Annual Meeting. This abstract deals with the first part of our approach, that's to say characterizing impact of diagenetic alteration on reservoir properties and seismic anisotropy, from meter to multi-meter scale. Crosshole acoustic-survey has been carried out using ultrasonic frequencies (50kHz), and vertical-resolution of 10cm. The main conclusions are: (1) multi-meter crosshole surveys, enable measuring elastic properties of both matrix, and fractured-matrix. Wave velocities measured at multi-meter scale are comparable to that from laboratory measurements, and this analogy is attributed to poor likelihood of finding dense fractures-sets –which would drastically change elastic moduli– at reduced scale. (2) Weak anisotropy is detected, varying between +10% (slow axis perpendicular to strata) and -2% (slow axis parallel to strata), and likely results from combination of matrix anisotropy (mineral orientation and pore geometry) and fractures effects. (3) In heterogeneous layered formations, variation of mean velocity with source and receivers locations significantly impact anisotropy parameters estimated by curve fitting. One should be aware of this potential bias, while interpreting crosshole surveys with sparse data, especially in carbonate formations.

Introduction:

This study is consecutive to a series of published works aiming at characterizing both reservoir and elastic properties of Lower Cretaceous limestone from the Urgonian platform of Provence (SE, France). References describing the characteristics of this platform in terms of facies, and biostratigraphy are available e.g. (Leonide et al. 2012). These microporous bioclastic limestones are analogues of different hydrocarbon reservoirs in Middle East, e.g. Kharaiib and Shuaiba formations (Borgomano et al. 2013). In addition, several published databases document coupled porosity, and elastic waves velocities measurements from the Urgonian (Fournier and Borgomano 2009; Fournier et al. 2011; Fournier et al. 2014; Borgomano et al. 2013). In these works, the authors used conventional laboratory approach, i.e. velocity measurements carried out on 1" to 1.5" mini-cores, under effective stress; and they discussed "effective media theory", and the concept of "pore aspect ratio" extensively. Nevertheless, a known limitation of these approaches is the implicit assumption of medium's isotropy. Despite this assumption is generally true at the plug scale, it is rarely the case at larger scale. Carbonate rocks are often fractured and may have either "facies-related" or "patchy" porosity distribution that may lead to seismic anisotropy.

The works presented here focus on the impact of up-scaling onto elastic properties of carbonates rocks. Crosshole ultrasonic measurements have been carried out *in situ*, and the results are compared to published works, and to our multi-scale laboratory approach (cf. our second presentation).

Geological context:

The study took place in SE France, in an underground facility, namely LSBB (Low Noise Underground Laboratory). The LSBB is a network of sub-horizontal galleries dug in thick Barremian bioclastic limestone, within the vadose zone of "Fontaine de Vaucluse" aquifer system. The study site was located in the GAS-gallery (Figure 1), ~250m below the surface topography, which enables to set up experiments in subsurface conditions, at least in terms of hydrostatic stress, Guglielmi et al., [2015] estimated the main stress to 6MPa. The gallery gives direct access to the 30° southward-dipping layers, and five vertical fully-cored boreholes (~20m deep) named P1 to P5 were drilled in 2009, and were studied as part of previous works (Jeanne 2012; Jeanne, Guglielmi, and Cappa 2013; Jeanne, Guglielmi, and Cappa 2012; Jeanne et al. 2012).

The geological background over the studied interval is summarized in Figure 2. The south-dipping layers intersected by the boreholes are inner-platform facies i.e. low to moderate energy, muddy or peloidal carbonate sands with abundant rudists. The cores' analysis emphasized two main facies types: (1) calcarenites (grainstone to rudstone), and (2) calcilutites (wackestone to packestone). Since the reservoir properties are not related to facies, but instead to diagenesis (Léonide et al. 2014), we do not describe them any further in this abstract. The studied interval can be divided in three mechanical units: two are densely fractured (from 1 to 6m, and from 14 to 21m), and one is moderately fractured (from 6 to 14m). The formation is affected by two sets of sub-vertical fractures (dip ~80°), and oriented N30 and N120. The fractures density is controlled by

Investigation of anisotropy in carbonates

both porosity and the fault zone nearness (Jeanne, Guglielmi, and Cappa 2012; Jeanne, Guglielmi, and Cappa 2013). The open-fractures sets are located mainly in area with gradual porosity changes close to the calcilitites. Under pressure-solution conditions, the calcilitites may have produced carbonate rich fluids (cf. stylolites) that migrated and precipitated nearby, occluding some of the fractures and decreasing locally the overall porosity of the porous layer.

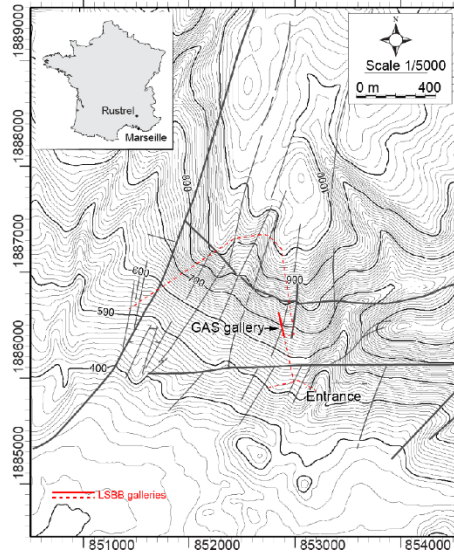


Figure 1. Localization GAS-gallery in the LSBB, and disposition of the boreholes.

Material and methods:

The acoustic logging has been carried out between P4 (Emission Borehole), and P2 (Reception Borehole) located two meters apart, along azimuth N20°. The study was conducted from 1 to 14.5m depth. The acquisition was divided into sections for technical reasons, each section is 1.5m high, and the spacing of the sensor array was 10cm. For each section 256 full-waveforms acoustic signals were recorded. The P- and S-waves travel times were manually picked and were processed, section by section, according to raypaths angles. This approach

emphasized angular dependency of elastic wave velocities, and a correlation with beddings. Data were investigated using a model of anisotropic media, the transverse isotropy (TI). TI media have same properties in one plane (e.g. the x-y plane) and different properties in direction normal to this symmetry plane (e.g. z-axis). If the z-axis is the vertical axis, then the material is a Vertical Transversely Isotropic medium (VTI). For such material, the stiffness tensor (C_{ij}) written in Voigt's notation, requires only five independent components to fully describe its elasticity.

$$C_{ij} = \begin{pmatrix} c_{11} & c_{12} & c_{13} & & & \\ c_{12} & c_{11} & c_{13} & & & \\ c_{13} & c_{13} & c_{33} & & & \\ & & & c_{44} & & \\ & & & & c_{44} & \\ & & & & & c_{66} \end{pmatrix}, \quad c_{66} = \frac{c_{11} - c_{12}}{2} \quad (1)$$

After equation (2), the components of C_{ij} can be obtained from 5 velocity measurements (Mavko, Mukerji, and Dvorkin 2009).

$$\begin{aligned} c_{11} &= \rho V p_{(0^\circ)}^2 \\ c_{33} &= \rho V p_{(0^\circ)}^2 \\ c_{44} &= \rho V sh_{(0^\circ)}^2 \\ c_{66} &= \rho V sh_{(90^\circ)}^2 \end{aligned} \quad (2)$$

$$c_{13} = -c_{44} + \left(4\rho^2 V p_{(45^\circ)}^4 - 2\rho V p_{(45^\circ)}^2 \right)^{\frac{1}{2}} \times (c_{11} + c_{33} + 2c_{44}) + (c_{11} + c_{44})(c_{33} + c_{44})$$

The model of VTI media enables to compute phase velocities for quasi-longitudinal (Vp), quasi-shear (Vsv), and pure-shear (Vsh) modes, see equation below.

$$\begin{aligned} Vp(\theta) &= \left(c_{11} \sin^2 \theta + c_{33} \cos^2 \theta + c_{44} + \sqrt{M} \right)^{\frac{1}{2}} (2\rho)^{-\frac{1}{2}} \\ Vsv(\theta) &= \left(c_{11} \sin^2 \theta + c_{33} \cos^2 \theta + c_{44} - \sqrt{M} \right)^{\frac{1}{2}} (2\rho)^{-\frac{1}{2}} \\ Vsh(\theta) &= \left(\frac{c_{66} \sin^2 \theta + c_{44} \cos^2 \theta}{\rho} \right)^{\frac{1}{2}} \end{aligned} \quad (3)$$

$$M = \left[(c_{11} - c_{44}) \sin^2 \theta - (c_{33} - c_{44}) \cos^2 \theta \right]^2 + (c_{13} + c_{44})^2 \sin^2 2\theta$$

Where ρ is the density, and θ is the phase's angle.

Finally, the phase velocities were converted into group velocities for direct comparison with the field data, and the stiffness components were compared to values documented in literature on Urgonian limestones.

Results and Discussion:

The velocity distribution is consistent with porosity variations within the studied area (Figure 2), and the dipping of the layers ($\sim 30^\circ$), is well figured. The highest velocities [6.5–6.3km/s] are between 1 and 5.5m depth, which is a low porous interval.

Investigation of anisotropy in carbonates

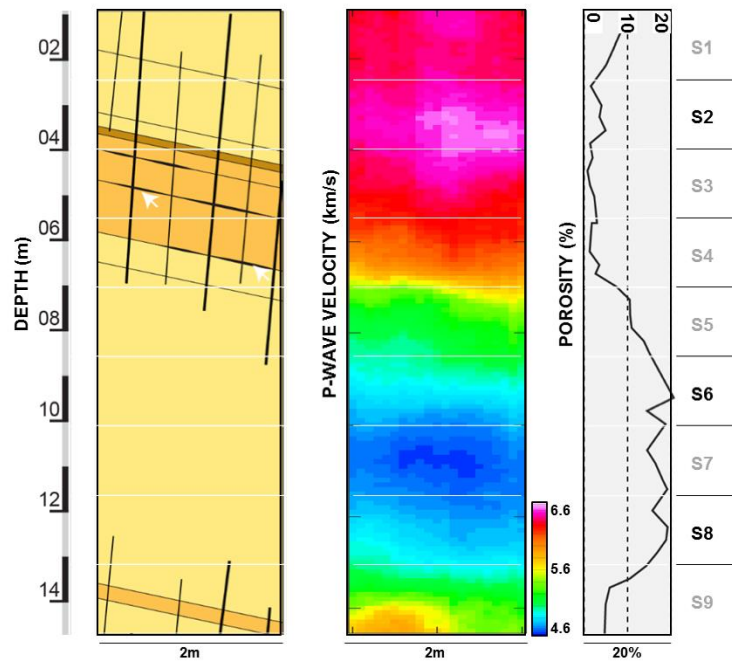


Figure 2. Tomography of inter-borehole space, put in perspective with a schematic view of the geology, and the porosity (adapted from Jeanne et al. (2012)). The tomography of P-wave velocity was computed using the eikonal equation (D. Baden et al. 2017, submitted).

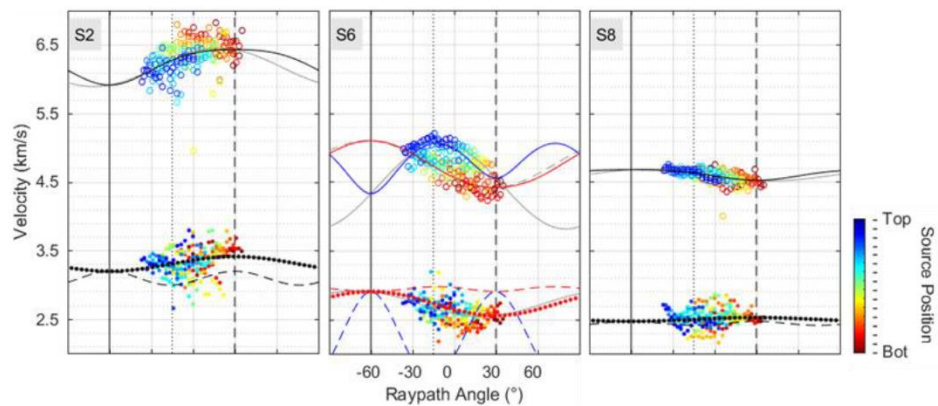


Figure 3. Velocity models computed using the computed stiffness coefficients. The P- and S-wave velocities are figured by open circles and dots, respectively. The solid, the dotted and the dashed models stand for: V_p , V_{sh} , and V_{sv} , respectively. The cosine models (grey) are also plotted for comparison but are not discussed in this abstract.

Investigation of anisotropy in carbonates

The lowest velocities [$\sim 4.6\text{--}4.8\text{km/s}$] are from 9 to 13m, where porosity reaches up to 20%. Two intervals with intermediate velocities $\sim 5.2\text{km/s}$ located between ~ 7 and 8m and from 13 to 14.5m, show porosity variation. Although the tomography have fair consistency with the porosity, yet the anisotropy visible in data (e.g. Figure 3) seems smoothed by such the process.

One can see that transverse isotropy approximation was relevant in this study, since phase velocity models are consistent with experimental data (Figure 3). Taking the example of S2, which is a high velocity interval with P-wave velocity anisotropy $\sim 10\%$. The direction of maximum velocity is 30° which means it follows the stratification. One would expect having slow axis normal to beddings, but in our context, fractures-sets are normal to layers, since they are dry the reduction of elastic modulus is maximum perpendicular to the their orientation (Hudson 1980; Hudson 1981; Rüger 1997; Guéguen and Sarout 2009; Tsvankin 1997). So that, the anisotropy observed in S2 could be explained either by stress relief (and thus opening of fractures-sets), or presence of stylolites (Baud et al. 2015).

The second example, S8, shows despite detected anisotropy is relatively small, the value is reliable. Data from this interval showed great consistency for successive shots, and anisotropy measurements made on the matrix (*cf. our 2nd presentation at SEG's 87th Annual Meeting*), showed that the higher the intercrystalline porosity (i.e. between micrite crystals), the more the matrix was anisotropic. Moreover, this interval have few macroscopic fractures, which leaves porosity fabric and mineral orientation as the most likely explanations for this anisotropy.

The particularity of S6, which is our last example, lies into the fact that there is an obvious influence of the source location on the anisotropy. This interval has increasing porosity values bottomward, plus, it is an area were fractures attenuate as they reach the porous layer. The change in the anisotropy simply show that two anisotropies (matrix and fractures) are convoluted there.

In Table 1, our results are compared to other works conducted on the same carbonates, at seismic-scale ($<180\text{m}$) in Bereš et al. (2013), at field-scale ($\leq 13.5\text{m}$) in this study, and at laboratory-scale ($\approx 2.54\text{cm}$) in Fournier et al. (2014).

Table 1. C_{ij} components for Urganian limestones (Baden et al., @submitted article).

($\times 10^9$)	Bereš et al., [2013]	Baden et al., (submitted)	Fournier et al., [2014]
C_{11}	44,9 - 36,9	108,0 - 41,4	110,4 - 26,8
C_{13}	19,7 - 18,3	52,5 - 6,1	52,7 - 9,2
C_{33}	69,2 - 65,9	99,6 - 43,4	C_{11}
C_{44}	19,7 - 18,3	30,3 - 13,7	34 - 7,9
C_{66}	15,4 - 14,8	30,4 - 12,5	C_{44}

The smaller the sample the higher the coefficients variability, this is explained, by averaging effect of the scale. Indeed, different factors, i.e. facies, grains sorting, and diagenesis cause heterogeneity in carbonate rocks. Hence the smaller the samples the greater the probability of sampling particular

features. Accordingly, elastic properties are averaged with the increasing scale. Interestingly, even if major fractures are present in the sections, our stiffness coefficients are closer to laboratory values than seismic-scale ones. This suggests that at meter-scale, fractures start to be sampled but do not dominate the signal, which enables to capture both signatures of the matrix and the fractures. In addition, the faults present in the LSBB area (Jeanne 2012), and which did not affect our measurements (no fault between the tested boreholes), but which were unavoidably measured by Bereš et al., [2013], may have played a role even bigger in lowering the velocities than fractures-sets alone. For example Al-Harrasi et al. (2011) related the anisotropy in the Natih carbonate reservoir (Oman) the rock type and proximity to major faults. So that, the coefficients presented in this study may be representative of the rock matrix and of the fractured rock, whereas at seismic-scale, major faults may obliterate the effects of the matrix, hence, seismic-scale coefficients may be more representative of faulted rock mass.

Conclusion:

A crosshole acoustic-survey has been carried-out using ultrasonic frequencies (50kHz), and with vertical-resolution of 10cm. This works were conducted in order to characterize, in situ, a microporous carbonate series from meter to decameter scale. The main conclusions can be summarized as follow:

- (1) Crosshole ultrasonic surveys enable measuring elastic properties of both matrix, and fractured-matrix. The wave velocities measured at multi-meter scale are comparable to that from conventional laboratory measurements. This similarity can be attributed to the poor likelihood of finding multiple fractures as the dimensions of investigated area decreases.
- (2) In most cases, a weak anisotropy is detected, varying between +10% (slow axis perpendicular to strata) and -2% (slow axis parallel to strata) and likely results from a combination of matrix anisotropy (mineral orientation and pore geometry) and fractures effects.
- (3) In heterogeneous layered formations, variation of mean velocity with source and receivers locations significantly impact anisotropy parameter estimated by curve fitting. One should be aware of this potential bias, while interpreting crosshole surveys with sparse data, especially in carbonate formations.

Acknowledgements:

This works were supported by two Research programs: H-CUBE project (ANR-12-SEED-0006), D. Baden's PhD grant; and ALBION-HPMSCa project, funded by TOTAL .

Investigation of anisotropy in carbonates

Bibliography (not to be included in the abstract)

- Al-Harrasi, O H, A Al-Anboori, A Wüstefeld, and J-M Kendall. 2011. "Seismic Anisotropy in a Hydrocarbon Field Estimated from Microseismic Data." *Geophysical Prospecting* 59 (2): 227–43. doi:10.1111/j.1365-2478.2010.00915.x.
- Baud, Patrick, Alexandra Rolland, Michael Heap, Tao Xu, Marion Nicolé, Thomas Ferrand, Thierry Reuschlé, Renaud Toussaint, and Nathalie Conil. 2015. "Impact of Stylolites on the Mechanical Strength of Limestone." *Tectonophysics* 690 (Part A). Elsevier B.V.: 4–20. doi:10.1016/j.tecto.2016.03.004.
- Bereš, Ján, Hermann Zeyen, Guy Sénéchal, Dominique Rousset, and Stéphane Gaffet. 2013. "Seismic Anisotropy Analysis at the Low-Noise Underground Laboratory (LSBB) of Rustrel (France)." *Journal of Applied Geophysics* 94: 59–71. doi:10.1016/j.jappgeo.2013.04.008.
- Borgomano, Jean, Jean-Pierre Masse, Mukerrem Fenerci-Masse, and François Fournier. 2013. "Petrophysics of Lower Cretaceous Platform Carbonate Outcrops in Provence (SE France): Implications for Carbonate Reservoir Characterisation." *Journal of Petroleum Geology* 36 (1): 5–42.
- Fournier, François, and Jean Borgomano. 2009. "Critical Porosity and Elastic Properties of Microporous Mixed Carbonate-Siliciclastic Rocks." *Geophysics* 74 (2): E93–109.
- Fournier, François, Philippe Leonide, Kévin Biscarrat, Arnaud Gallois, Jean Borgomano, and Anneleen Foubert. 2011. "Elastic Properties of Microporous Cemented Grainstones." *Geophysics* 76 (6): E211–26.
- Fournier, François, Philippe Léonide, Luuk Kleipool, Renault Toullec, John J.G. Reijmer, Jean Borgomano, Thomas Klootwijk, and Jeroen Van Der Molen. 2014. "Pore Space Evolution and Elastic Properties of Platform Carbonates (Urgonian Limestone, Barremian–Aptian, SE France)." *Sedimentary Geology* 308 (1). Elsevier B.V.: 1–17.
- Guéguen, Yves, and Joël Sarout. 2009. "Crack-Induced Anisotropy in Crustal Rocks: Predicted Dry and Fluid-Saturated Thomsen's Parameters." *Physics of the Earth and Planetary Interiors* 172 (1–2): 116–24. doi:10.1016/j.pepi.2008.05.020.
- Guglielmi, Yves, Frédéric Cappa, Jean-philippe Avouac, Pierre Henry, and Derek Elsworth. 2015. "Seismicity Triggered by Fluid Injection – Induced Aseismic Slip." *Science* 348 (6240): 1224–26.
- Hudson, J. A. 1981. "Wave Speeds and Attenuation of Elastic Waves in Material Containing Cracks." *Geophysical Journal of the Royal Astronomical Society* 64 (1): 133–50. doi:10.1111/j.1365-246X.1981.tb02662.x.
- Ifudon, J A. 1980. "Overall Properties of a Cracked Solid." *Mathematical Proceedings of the Cambridge Philosophical Society* 88 (2): 371–84. doi:10.1017/S0305004100057674.
- Jeanne, Pierre. 2012. "Architectural, Petrophysical and Hydromechanical Properties of Fault Zones in Fractured-Porous Rocks: Compared Studies of a Moderate and a Mature Fault Zones (France)." Aix-Marseille Université.
- Jeanne, Pierre, Yves Guglielmi, and Frédéric Cappa. 2012. "Multiscale Seismic Signature of a Small Fault Zone in a Carbonate Reservoir: Relationships between VP Imaging, Fault Zone Architecture and Cohesion." *Tectonophysics* 554–557 (July): 185–201.
- . 2013. "Dissimilar Properties within a Carbonate-Reservoir's Small Fault Zone, and Their Impact on the Pressurization and Leakage Associated with CO₂ Injection." *Journal of Structural Geology* 47 (February). Elsevier Ltd: 25–35.
- Jeanne, Pierre, Yves Guglielmi, Juliette Lamarche, Frédéric Cappa, and Lionel Marié. 2012. "Architectural Characteristics and Petrophysical Properties Evolution of a Strike-Slip Fault Zone in a Fractured Porous Carbonate Reservoir." *Journal of Structural Geology* 44 (1): 93–109.
- Leonide, Philippe, Jean Borgomano, Jean-Pierre Masse, and Stefan Doublet. 2012. "Relation between Stratigraphic Architecture and Multi-Scale Heterogeneities in Carbonate Platforms: The Barremian–lower Aptian of the Monts de Vaucluse, SE France." *Sedimentary Geology* 265–266 (July): 87–109.
- Léonide, Philippe, François Fournier, John J.G. Reijmer, Hubert Vonhof, Jean Borgomano, Jurrien Dijk, Maëlle Rosenthal, Manon van Goethem, Jean Cochard, and Karlien Meulenaars. 2014. "Diagenetic Patterns and Pore Space Distribution along a Platform to Outer-Shelf Transect (Urgonian Limestone, Barremian–Aptian, SE France)." *Sedimentary Geology* 306 (June). Elsevier B.V.: 1–23.
- Mavko, Gary, Tapan Mukerji, and Jack Dvorkin. 2009. *The Rock Physics Handbook*. 2nd ed. Cambridge University Press, Cambridge.
- Rüger, Andreas. 1997. "P-Wave Reflection Coefficients for Transversely Isotropic Media with Vertical and Horizontal Axis of Symmetry." *Geophysics* 62 (3): 713–22.

Investigation of anisotropy in carbonates

Tsvankin, Ilya. 1997. "Reflection Moveout and Parameter Estimation for Horizontal Transverse Isotropy."
Geophysics 62 (2): 614–29. doi:10.1190/1.1444170.

Abstracts

Dawin Baden, Yves Guglielmi, Ginette Saracco, Sophie Viseur, and Lionel Marié (2014), **High density ultrasonic characterization of carbonates heterogeneities**, in *Résumés de la 24e Réunion des Sciences de la Terre*, p. 309.

6.5.8 (p) High density ultrasonic characterization of carbonates heterogeneities

Dawin Baden¹, Yves Guglielmi¹, Ginette Saracco², Lionel Marié¹,
Sophie Viseur¹

¹*CEREGE, Marseille*

²*CEREGE, Aix-en-Provence*

Characterization of heterogeneities within carbonate rocks remains a key challenge in Oil Industry and for Carbon Geological Storage as well. During CGS operations, heterogeneities have significant impact on fluid flows at near well environment and within the reservoir especially when convective mixing occurs. In this study, we conducted experiments on different sections of a 20 m long and 125 mm wide carbonate core. Sections aimed to be representative of different types of heterogeneities which generally occur in carbonate reservoir units (e.g. petrographic, diagenetic, and tectonic related). Samples were immersed in a 4.5 m³ water tank, and then automated ultrasonic measurements were carried out using 250 kHz immersion transducers. This study was voluntarily based on high density ultrasonic sampling to denote progressive and abrupt variations in the acoustic response of the tested samples. This method successfully allowed detecting heterogeneities in the sample's reservoir properties, such as distinguishing decimeter-scale diagenetic horizons in samples assumed to be homogeneous. It also highlighted the impact of differential diagenesis between shells filling and the packing matrix, footprint of smaller interfaces such as cracks, stylolites and stratigraphic boundary.

Dawin Baden, Yves Guglielmi, Ginette Saracco, Lionel Marié, and Sophie Viseur (2015). **3D modeling of carbonates petro-acoustic heterogeneities**. Geophysical Research Abstracts, Vol 17, EGU2015-9838. EGU General Assembly 2015.

Geophysical Research Abstracts
Vol. 17, EGU2015-9838, 2015
EGU General Assembly 2015
© Author(s) 2015. CC Attribution 3.0 License.



3D modeling of carbonates petro-acoustic heterogeneities

Dawin Baden (1), Yves Guglielmi (1), Ginette Saracco (2), Lionel Marié (1), and Sophie Viseur (1)

(1) CEREGE, Aix-Marseille University, Marseille, France (baden@cerege.fr), (2) CEREGE, Aix-en-Provence, France

Characterizing carbonate reservoirs heterogeneity is a challenging issue for Oil & Gas Industry, CO₂ sequestration and all kinds of fluid manipulations in natural reservoirs, due to the significant impact of heterogeneities on fluid flow and storage within the reservoir. Although large scale (> meter) heterogeneities such as layers petrophysical contrasts are well addressed by computing facies-based models, low scale (< meter) heterogeneities are often poorly constrained because of the complexity in predicting their spatial arrangement.

In this study, we conducted petro-acoustic measurements on cores of different size and diameter ($\varnothing = 1''$, $1.5''$ and $5''$) in order to evaluate anisotropy or heterogeneity in carbonates at different laboratory scales. Different types of heterogeneities which generally occur in carbonate reservoir units (e.g. petrographic, diagenetic, and tectonic related) were sampled. Dry / wet samples were investigated with different ultrasonic apparatus and using different sensors allowing acoustic characterization through a bandwidth varying from 50 to 500 kHz. Comprehensive measurements realized on each samples allowed statistical analyses of petro-acoustic properties such as attenuation, shear and longitudinal wave velocity. The cores properties (geological and acoustic facies) were modeled in 3D using photogrammetry and GOCAD geo-modeler.

This method successfully allowed detecting and imaging in three dimensions differential diagenesis effects characterized by the occurrence of decimeter-scale diagenetic horizons in samples assumed to be homogeneous and/or different diagenetic sequences between shells filling and the packing matrix. We then discuss how small interfaces such as cracks, stylolithes and laminations which are also imaged may have guided these differential effects, considering that understanding the processes may be taken as an analogue to actual fluid drainage complexity in deep carbonate reservoir.

Dawin Baden, Yves Guglielmi, Lionel Marié (2016), **Acoustic Characterization of Sub-Seismic Scaled Heterogeneities in Carbonate Reservoirs: Example of Barremian Microporous Limestone from SE France, an Analog of Middle East Hydrocarbon Reservoirs.** in *AAPG Annual Convention & Exhibition 2016, Calgary, Alberta, Canada.*

PS Acoustic Characterization of Sub-Seismic Scaled Heterogeneities in Carbonate Reservoirs: Example of Barremian Microporous Limestone from Southeast France: An Analog of Middle East Hydrocarbon Reservoirs*

Dawin Baden¹, Yves Guglielmi¹, and Lionel Marié¹

Search and Discovery Article #41989 (2017)**
Posted January 30, 2017

*Adapted from poster presentation given at AAPG Annual Convention & Exhibition, Calgary, Alberta, Canada, June 19-22, 2016

**Datapages © 2017 Serial rights given by author. For all other rights contact author directly.

¹Aix-Marseille Université, Marseille, France (baden@cerege.fr)

Abstract

Carbonate rock physics properties are difficult to assess due to their biogenetic diversity and the overprint of a complex diagenetic history which can alter porous carbonates porosity during the whole life of these reservoirs. Common scales to characterize the latter are seismic profiles and well log data. Despite seismic methods that, in some cases, fail to characterize reservoir units for example because of seismic detection limit (≈ 20 m) or low impedance contrast between two lithified carbonate units, good relationships have been established between elastic properties and reservoir properties of these reservoirs. Nevertheless, elastic properties often in-lab determined, are measured on small-scaled (≥ 2 inch.) samples which are not always representative of the heterogeneity of the sampled units, leading in some cases to wrong interpretations.

In this study, we propose to assess acoustic properties at an intermediate scale in terms of both seismic frequency (SF) and investigated area (IA), between seismic scale (SF:101-102 Hz, IA: km) and laboratory scale (SF:104-106 Hz, IA: cm). We designed, two acoustic probes which enabled us to perform crosshole acoustic measurements up to ultrasonic frequencies (SF: 102-104 Hz), between two wells located in a gallery from an underground laboratory (LSBB†, France). Confining pressure within the wells is ≈ 4 -to-6 MPa and the studied formation are located in the unsaturated zone of the aquifer. The wells were 2 m spaced and 20 m deep. Here we present a HR acoustic log ($\Delta z = 10$ cm) covering an inter-wells area of 30 m² composed of tight and microporous reservoir units of Urganian platform limestones. The key results of this experiment are: (1) Sub-seismic scaled heterogeneities such as diagenetic horizons within a same sedimentary facies or layer and related to porosity variations up to 10% can be successfully characterized using our methodology, (2) Potential diagenesis-induced seismic reflectors can be identified between and within layers under conventional seismic detection limits, and (3) Tight units, regardless to their composition, display different fractures density, they show the same average P-wave velocity but scattering of the values is a function of the underwent deformations. Finally, coupling *in situ* HR acoustic log to conventional lab measurements can fill the gap in terms variations of acoustic response observed between field seismic and synthetic profiles used for the inversion of reservoir properties.